IOWA STATE UNIVERSITY
Digital Repository

Graduate Theses and Dissertations

Graduate College

2010

Yb-based heavy fermion compounds and field tuned quantum criticality

Eundeok Mun
Iowa State University

Follow this and additional works at: http://lib.dr.iastate.edu/etd

 Part of the Physics Commons

Recommended Citation

Mun, Eundeok, "Yb-based heavy fermion compounds and field tuned quantum criticality" (2010). *Graduate Theses and Dissertations*. 11334.
http://lib.dr.iastate.edu/etd/11334

Yb-based heavy fermion compounds and field tuned quantum criticality

by

Eundeok Mun

A dissertation submitted to the graduate faculty

in partial fulfillment of the requirements for the degree of

DOCTOR OF PHILOSOPHY

Major: Condensed Matter Physics

Program of Study Committee:
Paul C. Canfield, Major Professor
Sergey L. Bud'ko
Adam Kaminski
John Lajoie
R. William McCallum
Ruslan Prozorov

Iowa State University

Ames, Iowa

2010

TO THE MEMORY OF MY FATHER AND TO MY MOTHER

TABLE OF CONTENTS

LIST OF TABLES

LIST OF FIGURES

ACKNOWLEDGEMENTS

During the last several years, I have learned not only about physics, but also, more importantly, how to approach and solve physical problems and the importance of collaborations. During the last 5 years, I have spent most of the time in the basement cut off from the sun, so I named myself "the son of darkness", along the same lines, Paul called me "lonely duck". But always there was an invisible window that allowed the sunlight to shine into the dark basement. I would like to thank those numerous people who opened that window to brighten up the darkness.

Foremost, I would like to express my profound appreciation for my advisor Paul C. Canfield for his incredible patience in listening to a foreign accent, his unlimited support for pursuing scientific research, his valuable life lessons, his confidence in all the endeavors and his encouragement to accomplish all the goals, and finally, his invaluable scientific guidance through the entire Ph.D. period.

In the same way, Sergey L. Bud'ko, as an informal co-advisor, deserves my appreciation and deep thanks for helping to take measurements and useful discussion on the various research topics as well as on philosophical ideas. His encouragement, companionship, and support was invaluable for me.

I would like to thank the former colleagues E. Morosan, R. H. T. Wilke, S. Jia, N. Ni, M. Tillman, H. Ryu, G. D. Samolyuk, J. Frederick, S. Moser, S. A. Law, and M. Lampe as well as my present colleagues E. Colombier, R. Hu, A. Thaler, S. Kim, X. Lin, H. Hodovanets, S. Ran, and M. Caudle for valuable scientific discussions, nice help, and pleasant atmosphere.

I would like to also thank M. S. Torikachvili and G. M. Schmiedeshoff for the valuable discussion and the nice help. I am especially grateful to Milton, who was staying with me in

the basement until midnight.

I would like to acknowledge R. Prozorov, M. A. Tanatar, C. Martin, M. Vannette, R. Gorden, and H. Kim, not only for active help in dilution refrigerator measurements, but also for many discussions. I am very grateful to Catalin, who had fruitful discussions about the instrumentation.

I also want to acknowledge A. I. Goldman, A. Kreyssig, S. Nandi, M. Kim, R. W. McCallum, K. Dennis, A. Kaminski, J. Lajoie, Y. Lee, B. Harmon, H. Ko and G. J. Miller for the nice help and discussion. I am very grateful to "damngerman" Andreas for his encouragement and good friendship.

Thanks must go to S. T. Hannahs, E. C. Palm, T. P. Murphy, J. -H. Park, C. Mielke, and V. Zapf at National High Magnetic Field Laboratory and J. R. O'Brien and N. R. Dilley at Quantum Design, Inc. for all their nice help for taking the data and for many discussions on the experiment.

I would like to acknowledge many friends, I.-S. Seo, I.-C. Shin, S.-Y. Noh, S.-K. You, M.-H. Kim, J.-H. Shin, S.-W. Oh, and J.-K. Ju, who have been supporting me in all my endeavors.

The material preparation center in Ames Laboratory has provided the worlds highest purity rare-earth elements to the lab. Therefore, working at Ames Lab during last several years has been a great pleasure for me since I have had an incredible opportunity to study rare-earth based materials with the highest purity rare-earth elements available. I would like to thank people who are working in material preparation center in Ames lab.

Preface

For the last century, rare-earth based intermetallic compounds have provided a wide range of ground states that have been intrigued the condensed matter research community including both local moment and the strongly correlated electron systems. Up until now, huge numbers of binary, ternary, and even quaternary intermetallic compounds have been investigated and the results have been applied to daily life. Rare-earth based intermetallic compounds are composed of metals or nonmetals and rare-earth metals. Rare-earth elements consists of the lanthanides from Lanthanum (La) to Lutetium (Lu) as well as Yttrium (Y) and Scandium (Sc).

The chemical properties of the rare-earth elements in compounds are similar due to their trivalent valence configurations [Elliott, 1972]. Furthermore, the small difference in atomic, or metallic, radii gives rise to the systematic volume change across a series of compounds. Because of the similar chemical properties, when one of the elements of the rare-earth group is part of an intermetallic compound, the other rare-earth elements with the same ligands will have a high probability of forming the same crystal structure. In the past, the similarity of their chemical properties presented considerable difficulties in separating the rare-earth elements to high purity. However, Frank Harold Spedding developed methods for separating individual rare-earth elements in 1942, and since that time the Ames Laboratory has made (and provided) the worlds highest purity rare-earth elements, most recently through the material preparation center (MPC) [MPC].

In contrast to the chemical properties, the physical properties vary remarkably across the rare-earth compounds [Elliott, 1972]. The strong spin-orbit moment, due to the filling up of the $4f$ electron shell, shows a large variation as the rare-earth element proceeds from the Ce

to Yb. The localized character of $4f$ shell, generally situated in the interior of the lanthanide atoms (shielded by the valence electrons), gives rise to the large magnetic moment per atom as well as the strong, single-ion, magnetocrystalline anisotropy of the rare-earths. Rare-earth based intermetallics have received attention since they offer a good opportunity to study the origin and the nature of the $4f$-electron magnetism. An investigation of rare-earth-based intermetallic compounds has received additional attention due to the outstanding quality of permanent magnets, e.g. Sm_2Co_{17} [Ray, 1972] or $Nd_2Fe_{14}B$ [Sagawa, 1984] which is currently widely used in daily life such as loudspeakers, headphones, and drive motors for hybrid and electric vehicles.

Based on the chemical similarity and physical difference, varying the rare-earth elements from La to Lu, including Y, provides a good opportunity to tune the ground state properties through changes in either the volume of the systems or the size or direction of the local moment due to the localized character of f-electron wave function [Canfield, 2008].

A sub-group can be classified by those compounds in which the rare-earth exhibits no magnetic moment, trivalent Y and La, tetravalent Ce, trivalent Eu, divalent Yb, and trivalent Lu. This sub-group of compounds shows no magnetic order and generally simple, metallic behavior. Another sub-group, classified with Ce and Yb, is of particular interest not only because the magnetic trivalent state can transform to a nonmagnetic tetravalent state for Ce and divalent state for Yb, but also because the $4f$ electron can hybridize with the conduction electrons, giving rise to the heavy fermion (HF) behavior.

One of the ultimate goals in the field of condensed matter physics is to understand the interaction between magnetic and electronic degrees of freedom and to find new classes of novel materials, such as high temperature superconductivity (high-T_c cuprates) [Bednorz, 1986], colossal magnetoresistance materials [von Helmolt, 1993], and multiferroic materials [Ramesh, 2007]. Rare-earth-based materials have provided a vast frontier to discover such materials. About 30 years ago, for example, the discovery of superconductivity in $CeCu_2Si_2$ [Steglich, 1979], followed by the discovery of high-T_c cuprates [Bednorz, 1986], opened the new era of strong electron correlations in solids. Since the discovery of these material, great efforts have been

devoted to understand their key mechanisms and use that knowledge to find other classes of novel materials.

Several rare-earth based superconducting compounds such as UBe_{13} [Ott, 1983], $CeCoIn_5$ [Petrovic, 2001], and β-$YbAlB_4$ [Nakatsuji, 2008], including most recently discovered FeAs-based $RFeAsO_{1-x}F_x$ [Kamihara, 2008], have been discovered and instigated hope of unraveling the mechanism for superconductivity in these different classes of materials. The pursuit for new superconductors with higher T_c still continues fervently. HF materials can be an important corner stone for the development of our understanding of the interaction between magnetic and electronic quantum fluctuations because the magnetic and electronic degrees are strongly coupled. Thus, an understanding of the HF physics as part of the f-electron research can push us one step further toward understanding strongly correlated electron systems and hopefully, in the future, allow us to make a connection, through from HF superconductors (f-electron), to high-T_c cuprates (d-electron) systems.

CHAPTER 1.   Introduction

In Ce- and Yb-based compounds, the complex physics of antiferromagnetic (AFM) heavy fermion (HF) metals is mainly governed by the delicate interactions between hybridization, resulting from submerging the $4f$, often magnetic, electrons in a mobile conduction electron sea, and the Ruderman-Kittel-Kasuya-Yosida (RKKY) magnetic interaction [Doniach, 1977]. The relative strength of these interactions give rise to various phenomena like long range magnetic order, intermediate (and/or mixed) valence behavior, unconventional superconductivity, and HF behavior.

The ground state of the HF, Kondo lattice, systems is a Fermi liquid (FL) state comprised of (Landau) quasi-particles. When f-electrons enter a conduction band there is an increased overlap of the electronic state which enhances the hybridization and band widths [Hewson, 1993]. One hallmark of these quasi-particles is the large Sommerfeld coefficient, γ, of the specific heat. At low temperatures, the specific heat of metals is approximated by $C(T) = \gamma T + \beta T^3$, where γT is the electronic specific heat and βT^3 is the lattice (phonon) contribution. For a normal metal γ is of order $1\,\mathrm{mJ/mol \cdot K^2}$, for example copper $\gamma \sim 0.7\,\mathrm{mJ/mol \cdot K^2}$ [Pobell,1996], and for HF materials γ is several hundred to several thousand times larger than that for normal metals [Stewart, 1984]. The magnetic susceptibility, $\chi(T)$, of HF compounds at high temperatures follows the Curie-Weiss form, $\chi(T) = C/(T - \theta)$, where C is the Curie constant and θ is the Weiss temperature, but at low temperatures tend to saturate at an anomalously high $\chi(0)$ value. In the majority of HF metals, the electrical resistivity, $\rho(T)$, at very low temperatures follows a T^2-dependence, $\rho(T) = \rho_0 + AT^2$ where ρ_0 is the residual resistivity and A represents the quasi-particle scattering cross section. The observed A value for HF metals is on the order of tens of $\mu\Omega\mathrm{cm/K^2}$, and is much larger than that of normal metals in which $A \sim 10^{-3}$

- $10^{-4}\,\mu\Omega\text{cm}/\text{K}^2$.

In addition to these fascinating properties, HF compounds also provide the cleanest evidence for a quantum phase transition [Stewart, 2001]. In HF systems, the electronic states have a characteristic energy that is orders of magnitude smaller than in normal metals because the effective mass, $\epsilon(k) = \hbar^2 k^2/2m^*$, is orders of magnitude larger than the free electron mass. This characteristic low energy scale can be controlled by such nonthermal control parameters as chemical substitution (doping, $\mathbf{x}$), magnetic field ($\mathbf{H}$), and pressure ($\mathbf{P}$).

At low temperatures, the thermodynamic and transport properties of HF systems have been shown to be in remarkable agreement with the FL descriptions. The validity of FL theory in metals, without long range order, was generally unquestioned in the community until strange metallic behaviors were observed in HF systems tuned by varying $\mathbf{x}$, $\mathbf{H}$, $\mathbf{P}$ such as $\rho(T) \propto AT$ and $C(T)/T \propto -\log(T)$ [Stewart, 2001]. This strange metallic behavior, so-called non Fermi liquid (nFL) behavior, have been explored in a moderate number of Ce-based intermetallic compounds and to only a small extent in Yb-based materials. For instance a field tuned quantum critical point (QCP) has been limited to two cases, only among stoichiometric compounds, in particular YbRh$_2$Si$_2$ [Gegenwart, 2002] and YbAgGe [Bud'ko, 2004]. The question "why Ce is popular and Yb so rare ?" may be answered simply due to the lack of known Yb-based HF compounds. In general, Yb ions in intermetallic compounds show more localized character than Ce and prefers to form Yb^{2+} state which is the same as non magnetic Lu. Additionally, roughly speaking, the Yb-based intermetallic compounds may not be prepared easily by arc melting due to the high vapor pressure of Yb, and so limits the rapid synthesis and discovery of new materials. The goal of this work then is to study Yb-based HF physics across the QCP.

The outline of the dissertation is as follows: Chapter 2 presents a brief description of the experimental methods used in this study and gives details of crystal growth via high temperature solution, focusing on the particular procedures used for growing the YbPtBi single crystals. Chapter 3 presents the theoretical framework for this thesis. This chapter begins with the theory of the Kondo effect, which gives rise to the HF phenomena, followed by a summary of the FL theory; theoretical reviews of quantum criticality are also presented.

The experimental data are presented and discussed in chapters 4, 5, and 6. Chapter 4 focus on a thermoelectric power (TEP) study of YbT_2Zn_{20} (T = Fe, Ru, Os, Ir, Rh, and Co) [Torikachvili, 2007]. The discovery of these compounds formally doubled the number of known examples of the Yb-based HF compounds. The Kondo interaction of these systems is much larger than inter-site RKKY exchange ($T_K \gg T_{RKKY}$) and hence no long range magnetic order was observed down to 20 mK. Mainly, the Kondo and crystalline electric field (CEF) energy scales in these systems are inferred and the strong correlations between the zero temperature limit of the electronic specific heat and the TEP are presented. In Chapter 5, the results of TEP measurements for YbAgGe are given as an example of $T_K > T_{RKKY}$. The HF metal YbAgGe, with a Kondo temperature of $T_K \sim 25$ K, orders antiferromagnetically below ~ 1 K. The existence of a magnetic field-induced QCP has been inferred by suppressing the AFM order to sufficiently low temperature (~ 20 mK) by a magnetic field applied both in the hexagonal **ab**-plane and along the **c**-axis [Bud'ko, 2004]. In this study the TEP measurements only for $\mathbf{H} \parallel \mathbf{ab}$ are investigated and compared to earlier studies. Chapter 6 presents thermodynamic and transport measurements of the face centered cubic YbPtBi [Fisk, 1991]. A huge low temperature Sommerfeld coefficient, $\gamma \simeq 8$ J/mol·K^2, characterizes YbPtBi as an extreme limit of the HF cases. This system also shows AFM ordering (spin density wave) below $T_N = 0.4$ K that is located below the estimated Kondo temperature of $T_K \sim 1$ K which is the case as $T_K \sim T_{RKKY}$. The discussion is mainly focused on establishing the full $H - T$ phase diagram and quantum criticality in this system. Finally, Chapter 7 summarizes the main findings of this work and outlines directions for further investigations as extensions of these studies of quantum criticality.

CHAPTER 2.   Experimental methods

2.1   Sample growth and characterization

2.1.1   Synthesis

There are several techniques such as Czochralski, Bridgeman, floating zone methods [Pamplin, 1975; Brice, 1986], and high temperature solution growth [Fisk, 1989; Canfield, 1992; Canfield, 2001; Canfield, 2010], that can be used to grow single crystals. Among these techniques, the RPtBi (R = Yb, and Lu) samples studied in this dissertation were prepared using a molten metal, high temperature solution growth method with an excess of Bi flux [Canfield, 1991]. Since the Bi flux itself is one of the constituent elements of the compounds the technique is called self-flux growth.

Since no ternary phase diagram for YbPtBi is available and the method for growing single crystals of RPtBi (R = rare-earth) was reported in Ref. [Canfield, 1991], several trials to improve the quality of samples were attempted based on the binary phase diagram. No other ternary compounds with Yb, Pt, and Bi, except YbPtBi, have been reported to date. Figures 2.1 (a), (b), and (c) show the binary phase diagrams of Bi-Yb, Bi-Pt, and Pt-Yb [Okamoto, 2000], respectively, where both Yb and Pt can be dissolved into Bi over 40 % at 800 °C there is plenty of opportunity to grow single crystals using excess Bi. In addition to the eutectic region near 90% of Yb in Bi-Yb binary phase diagram, there is an eutectic region near 87.5 % of Yb in Pt-Yb binary phase diagram. This eutectic region could also be used to grow single crystals using high temperature solution method. In this case, since Yb is a main flux in ternary melt, sometimes extra Yb^{3+} magnetic residue makes a problem in the physical property measurements when Yb flux is included inside the sample or solidified on the sample
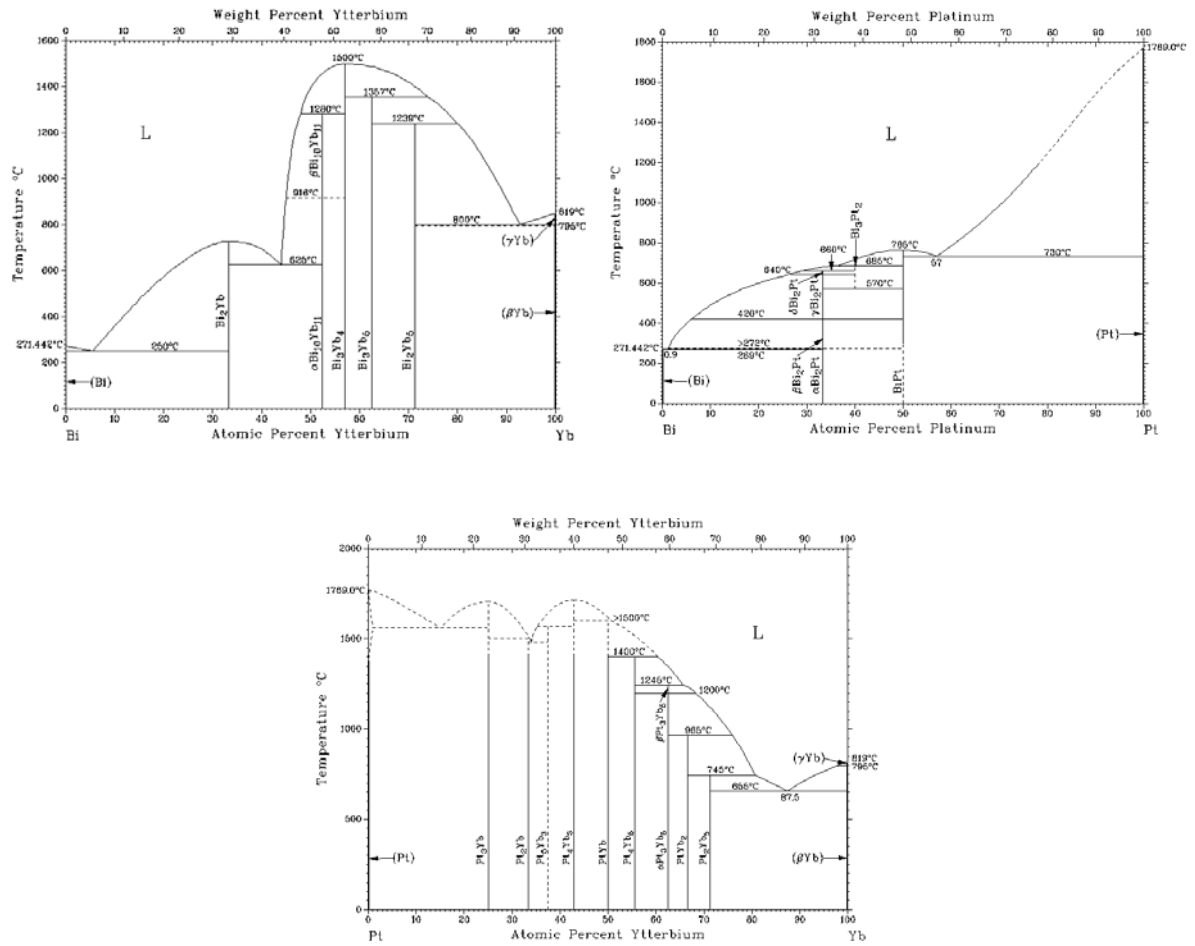
Figure 2.1   Binary phase diagram of (a) Bi-Yb, (b) Bi-Pt, and (c) Pt-Yb [Okamoto, 2000].

surface. Thus, we avoided the Yb-riched ternary melt to grow single crystals. Because of the $YbBi_2$ phase and the reaction between rare-earth element and alumina crucible, the maximum ratio of Yb in ternary melt was limited up to 12% of Yb. Since the binary phase diagram of Bi-Lu is similar to Bi-Yb, similar procedures were used for growing LuPtBi samples.

The constituent elements were placed in an alumina crucible and sealed in a silica tube under a partial pressure of Ar (Fig. 2.2 (d)). For YbPtBi, a starting molar proportion of $0.04 \leq x \leq 0.12 : 0.04 \leq y \leq 0.12 : 0.76 \leq z \leq 0.92$ ($Yb_x : Pt_y : Bi_z$) of the constituent elements was used to grow samples. The starting molar compositions are plotted in ternary phase diagram, together with the reported binary compounds and the desired YbPtBi, as shown in Fig. 2.2 (a). The YbPtBi samples can be grown in a wide range of the Bi-riched ternary melt.

The growth of YbT_2Zn_{20} (T = Fe, Ru, Os, Ir, Rh, and Co) and YbAgGe are discussed in detail in Ref. [Jia, 2007; Torikachvili, 2007] and Ref. [Morosan, 2004], respectively. The samples used for this work were grown as described in these references.

The temperature profile for the YbPtBi growth was optimized with data from the differential thermal analysis (DTA) using a PerkinElmer Pyris DTA 7 differential thermal analyzer, where ultra high purity Ar process gas, a Zr metal getter, and an Al_2O_3 crucibles were used. For the experiments, the sample, loaded inside an Al_2O_3 crucible with initial composition of $Yb_{0.1}Pt_{0.1}Bi_{0.8}$, was heated and cooled two times between room temperature and $1200\,^{\circ}C$ at $10\,^{\circ}C$/min. In Fig. 2.2 (b), the obtained DTA curves are plotted. In the both heating cycles a clear, endothermic event occurred near $270\,^{\circ}C$ corresponding to Bi melting. In the cooling cycles, the DTA curves showed an exothermic peak between $760 \sim 790\,^{\circ}C$, corresponding to the crystalization of the YbPtBi and an another exothermic peak near $260\,^{\circ}C$ corresponding to the solidification of Bi. Except for unknown features near $600\,^{\circ}C$ during the first heating, probably related to the Pt and Yb melting, no other significant endo- or exthothermic peaks were observed in this DTA experiments.

Based on the DTA data, the temperature of the furnace was raised to $1100\,^{\circ}C$ and after homogenizing the mixture for 2 hours, the melt solution was cooled down to $900\,^{\circ}C$ over 10
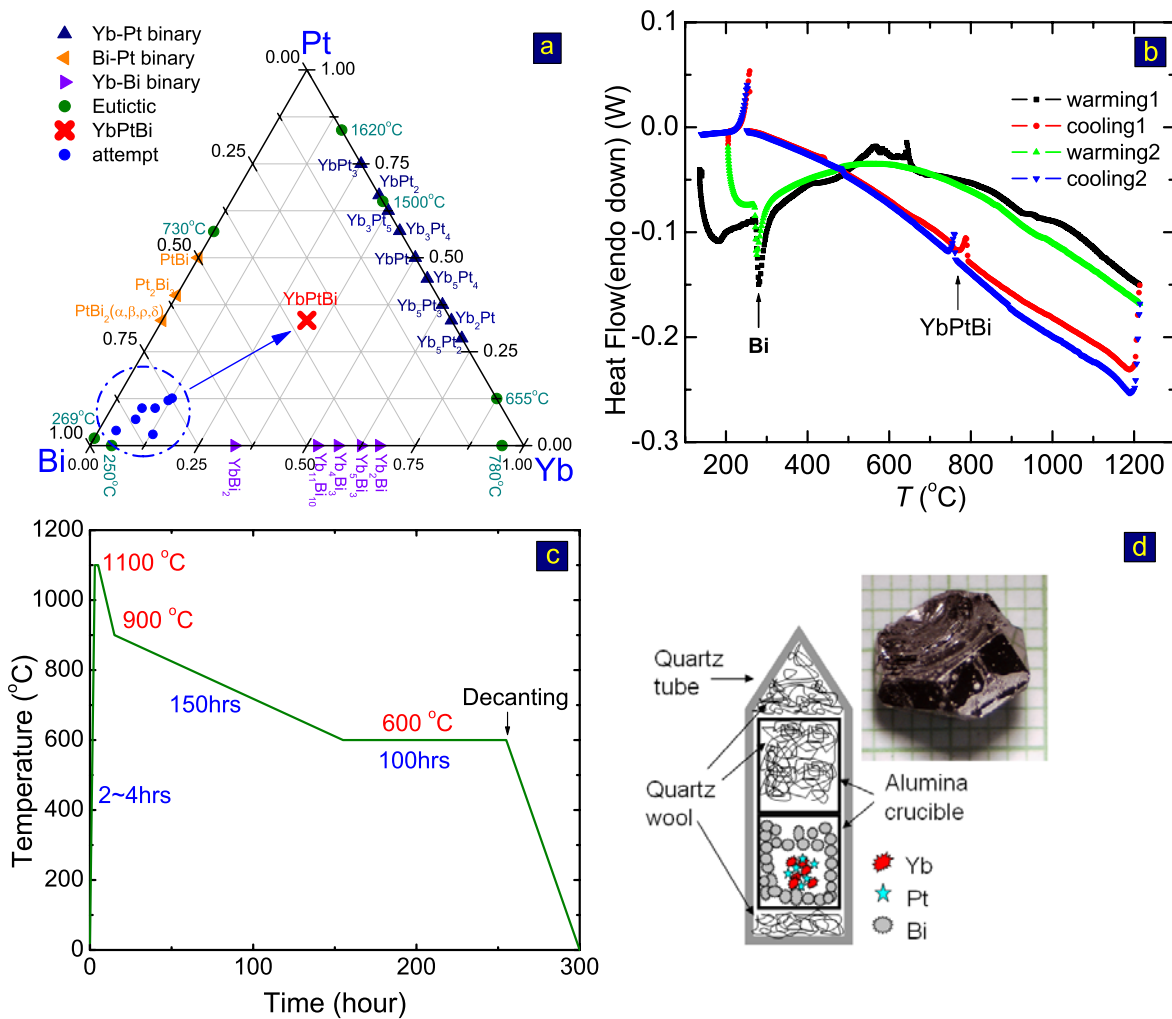
Figure 2.2 (a) Ternary phase diagram of YbPtBi. Solid dots mark the initial compositions used for the growth of YbPtBi. (b) DTA curves for YbPtBi, used initial composition of $Yb_{0.1}Pt_{0.1}Bi_{0.8}$, measured upon heating and cooling with a $10\,^\circ C/min$ rate. (c) Temperature profile for the growth of single crystals of YbPtBi from the Bi flux. (d) Schematic diagram of the ampoule. When the constituent elements are loaded inside alumina crucible, small pieces of Yb and Pt elements are surrounded by Bi elements. The picture of single crystal of YbPtBi over a millimeter grid is included. The droplets on the surface are residual flux.

hours and finally, slowly cooled down to 600 °C over 150 hours. Before decanting the excess solution using a centrifuge, the samples, still submerged in the melt were annealed at 600 °C for over 100 hours (see Fig. 2.2 (c)) in an attempt to minimize residual defects. The nucleation of the samples in the crucible is completely random, and generally yielded either lots of small crystals or a few (2 or 3) big crystals with typical dimensions of $5 \times 5 \times 5$ mm^3. The as grown samples are a bit sensitive in air, probably sensitive to moisture. In air the surface of samples starts to become dark after one week. Based on these observations, the samples were kept in vacuum.

It is worth noting that the probability of growing larger samples seemed to depend on the size of the initial constituent elements. When (i) small pieces of elements were used and (ii) Yb and Pt elements are close each other and surrounded by Bi, larger sized crystals were obtained. The second condition is just suspect, it has not proven yet. However, since there is a chance of reaction between Yb and alumina crucible, it is best to avoid contact between Yb and the crucible. Therefore, all constituent elements, Yb, Pt, and Bi, were cut roughly $0.5 \sim 1$ mm pieces and then placed in the alumina crucible. When the elements were loaded inside the crucible, small pieces of Yb and Pt elements were surrounded by Bi as shown in Fig. 2.2 (d).

2.1.2 Characterization

Powder X-ray diffraction measurements, collected on a Rigaku MiniFlex, were taken at room temperature with Cu K$_\alpha$ radiation in order to confirm the crystal structure, determine values for the lattice parameters, and to check for impurity phases. The X-ray pattern clearly revealed that the flux-grown single crystals are single phase. No secondary phases are detected except small amounts of pure, elemental Bi, that came from small solidified dropplets on the the crystal surface. As shown in Fig. 2.2 (d), well-formed facets are clearly visible. The crystallographic [100] direction is perpendicular to the rectangular shaped surface and the [111] direction is perpendicular to the equilateral triangle surface which were determined from the Laue technique.

2.2 Measurements methods

2.2.1 Magnetization measurements

Magnetization measurements were made in order to characterize the magnetic properties of YbPtBi. The dc magnetization was measured using a Superconducting Quantum Interference Device (SQUID) made by Quantum Design (QD) which can perform measurements in magnetic fields up to 70 kOe, and a temperature range from 1.8 K to 350 K. Generally, the magnetic susceptibility was measured in a 1 kOe magnetic field. The samples were mounted tightly between two straws, an approximately homogeneous background.

2.2.2 Specific heat measurements

The specific heat of YbPtBi was measured in a QD Physical Property Measurements System (PPMS) with ^{3}He option by the relaxation method in the temperature range of 0.4 to 100 K, with a magnetic field applied along the [100] direction. The specific heat measurements at lower temperatures, extended down to 0.05 K, were performed at Quantum Design head quarters, San Diego, California using a PPMS with ^{3}He-^{4}He dilution option. The specific heat of LuPtBi was measured in a QD PPMS by the relaxation method from 1.8 to 100 K.

2.2.3 Thermal expansion and magnetostriction measurements

Thermal expansion and magnetostriction were measured using a capacitive dilatometer [Schmiedeshoff, 2006] constructed from copper, for ^{3}He-setups, and from titanium, for dilution refrigerator setups. The dilatometer was mounted in a ^{3}He cryostat and was operated over a temperature range of 0.3 - 300 K in an applied magnetic field up to 90 kOe at Occidental College, Los Angeles, California. The magnetostriction measurements were extended to temperatures down to 0.02 K and magnetic fields up to 180 kOe in a top loading, ^{3}He-^{4}He dilution refrigerator at the Millikelvin Lab., National High Magnetic Field Laboratory, Tallahassee, Florida. The variation of the sample length was measured in a longitudinal configuration; $\Delta L \parallel H \parallel [100]$.

2.2.4   Electrical and Hall resistivity measurements

The electrical properties of YbPtBi and LuPtBi were characterized by electrical resistivity, $\rho(T, H)$, and Hall resistivity, $\rho_H(T, H)$, measurements. The $\rho(T, H)$ and $\rho_H(T, H)$ measurements as function of temperature from 0.02 to 300 K and magnetic fields up to 140 kOe were performed using the ordinary, ac ($f = 16$ Hz), four-probe method. Below 1 K, $\rho(T, H)$ and $\rho_H(T, H)$ for YbPtBi were measured in an Oxford Instrument ^{3}He-^{4}He dilution refrigerator with a Lakeshore LS370 and a Linear Research LR700 ac resistance bridge. In order to reduce the heating effect, the excitation current, I, was selected to be as low as possible, 10-30 μA, and the magnetic field was swept very slowly, with rate of 100-500 Oe/min. Above 0.4 K, $\rho(T, H)$ and $\rho_H(T, H)$ were measured in a QD PPMS with ^{3}He option. The transverse magnetoresistance measurements were performed in a configuration; $I \perp H$, $I \parallel$ [010] and $H \parallel$ [100]. The Hall resistivity was measured in the following configuration; the Hall voltage was perpendicular to the current ($V_H \perp I$), $V_H \parallel$ [010], and magnetic field ($V_H \perp H$), $H \parallel$ [100]. In order to remove MR contributions in ρ_H due to the misalignments of Hall voltage wires, the polarity of the magnetic field was switched. For LuPtBi, $\rho_H(T, H)$ measurements were performed with $H \parallel$ [111], $I \perp$ [111], and $H \perp I \perp V_H$ configuration.

2.2.5   Thermoelectric power measurements

The transport properties of RPtBi (R = Yb and Lu) as well as YbT$_2$Zn$_{20}$ (T = Fe, Ru, Os, Ir, Rh, and Co), and YbAgGe were further characterized by thermoelectric power (TEP) measurements. The TEP was measured using a dc, alternating heating, technique utilizing two heaters and two thermometers [Mun, 2010]. This specially designed setup was used in a QD PPMS over the temperature range from 2 to 350 K and magnetic fields up to 140 kOe, and in a CRYO Industries of America ^{3}He system from 0.3 to 30 K and up to 90 kOe. Single crystal samples were cut using a wire-saw and then polished down to the desired dimensions with typical geometry factors; the length $l \geq 2$ mm, the thickness 0.1 mm $\leq t \leq 0.2$ mm, and the width 0.1 mm $\leq w \leq 0.2$ mm. The needle-shaped samples were directly attached to the two Cernox thermometers using DuPont 4929N silver paint. Note that the TEP value of the

lead wire (phosphor-bronze) is ignored since the TEP of this wire is negligible. See Appendix for details of measurement setup.

For YbPtBi, the heat current, ΔT, was generated along the [010] direction and magnetic field was applied along the [100] direction. The temperature difference along the samples was kept between $0.03 \sim 0.05\,\mathrm{K}$ below $2\,\mathrm{K}$. For LuPtBi, the TEP measurements were performed with the heat current perpendicular to the [111] direction and magnetic field parallel to the [111] direction, maintaining a transverse configuration; $\mathbf{H} \perp \Delta T$. For $\mathrm{YbT_2Zn_{20}}$ (T = Fe, Ru, Os, Ir, Rh, and Co), the heat current was generated in the (111)-plane of the samples ($\Delta T \parallel (111)$) and the magnetic field was applied along the [111] direction, maintaining a transverse configuration. For T = Fe, Rh, and Co, zero-field TEP measurements were extended down to $0.4\,\mathrm{K}$. The anisotropic TEP measurements for YbAgGe were performed with two different heat current directions, generated in the hexagonal $\mathbf{ab}$-plane and along the $\mathbf{c}$-axis, and the temperature difference along the samples was kept between $0.03 \sim 0.05\,\mathrm{K}$ below $2\,\mathrm{K}$. The magnetic field was applied in the $\mathbf{ab}$-plane for both ΔT directions, maintaining a transverse configuration, $(\mathbf{H} \parallel \mathbf{ab}) \perp (\Delta T \parallel \mathbf{ab})$ and $(\mathbf{H} \parallel \mathbf{ab}) \perp (\Delta T \parallel \mathbf{c})$, in both cases.

CHAPTER 3.   Heavy Fermions and Quantum Criticality

3.1   Heavy Fermions

In this section we will give a general introduction to heavy fermion materials, their physical properties and the basic concepts related to them; Kondo effect in a single ion and in a lattice, crystalline electric field effect, RKKY interaction, Doniach diagram, Fermi liquid theory, and manifestation of Fermi liquid nature in physical properties.

3.1.1   Kondo effect

The Kondo problem goes back to the discovery of a resistivity minimum at low temperatures in metals with dilute, localized d- or f-electron, magnetic impurities. The resistivity minimum was a long standing theoretical puzzle after its first experimental observation in Gold (Au) by de Haas et $al.$ [deHaas, 1934]. Finally, this minimum and the lower temperature increase of the resistivity were successfully explained by Kondo [Kondo, 1964] with a perturbative calculation with in the $s - d$ model framework. The initial motivation for Kondo's calculation of the conductivity was that a possible basis for an explanation of the resistance minimum emerged with the experimental observation of a correlation between the disappearance of a high temperature Curie-Weiss term in the impurity susceptibility (a local moment) below the temperature of the resistivity minimum. Within the $s - d$ model, a magnetic impurity is described by a local spin $\mathbf{S}$ $(S = 1/2)$ exchange coupled to the local conduction electron spin density. Figure 3.1 (a) shows the general behavior observed single impurity, Kondo systems. As temperature decreases the impurity resistivity increases logarithmically and eventually saturates. The local minimum in the sample's resistivity can be obtained from this increasing impurity contribution, $\rho(T) \propto -\log(T)$, combined with the decreasing phonon contribution, $\rho(T) \propto T$. At
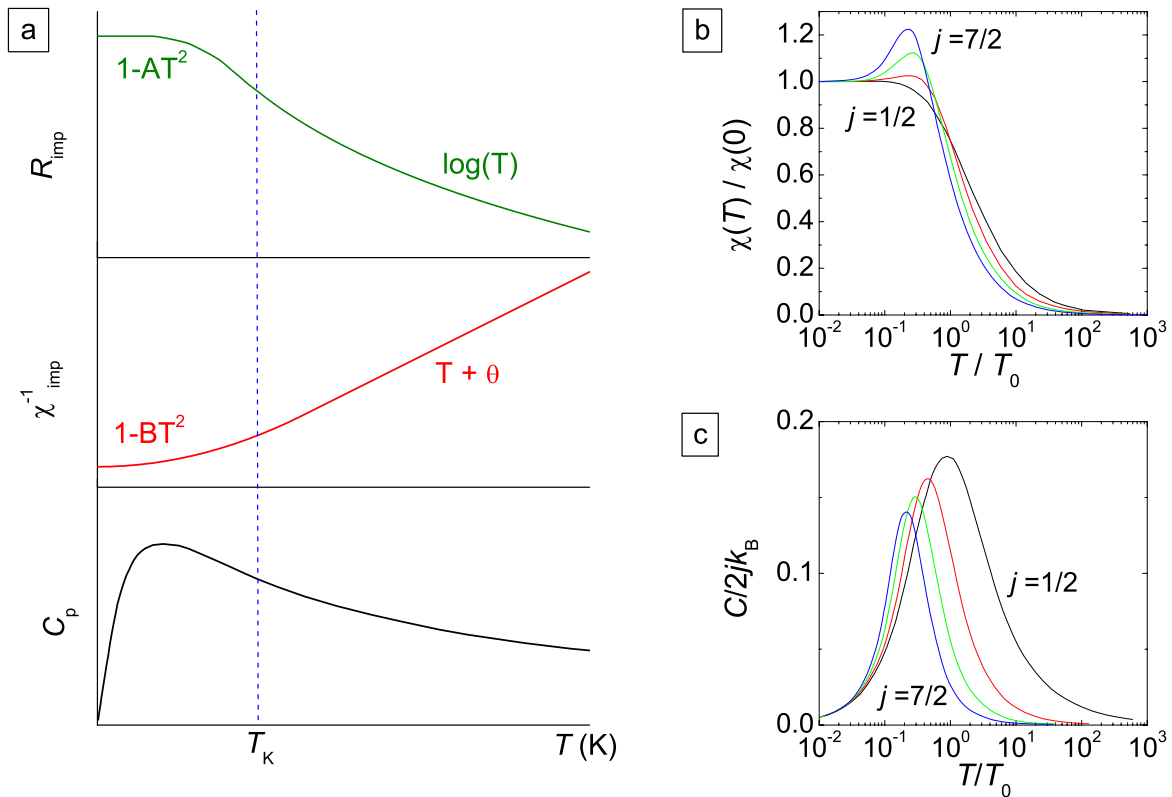
Figure 3.1   (a) Schematic behavior of the impurity contribution characteristic of a typical Kondo alloy (single ion). (b) $\chi(T)/\chi(0)$ vs. $\log(T/T_0)$ for j = 1/2, ..., 7/2 impurities. (c) $C/2jk_B$ vs. $\log(T/T_0)$ for $j = 1/2$, ..., 7/2 impurities. Where T_0 is the characteristic temperature, related to Kondo temperature (T_K = $(2\pi w_N/2j+1)T_0$). Figures (b) and (c) are digitized from the Ref. [Rajan, 1983].

high temperatures, the magnetic susceptibility follows a Curie-Weiss law, $\chi(T) = C/(T - \theta)$, where C is the Curie constant and θ is the Weiss temperature. In the low temperature limit the impurity spin is compensated by the conduction electrons and the impurity susceptibility is finite corresponding to Pauli and Van Vleck contributions. The impurity contribution to the specific heat shows a peak corresponding to a magnetic entropy change of approximately $R\ln(2)$, where $R = N_A k_B$; N_A is the Avogadro number and k_B is the Boltzmann constant. This changes in these data take place gradually on a temperature scale called the Kondo temperature, T_K, below which anomalous properties appear. Note that the Kondo temperature is

not a phase transition temperature but rather characterizes a crossover, and can be defined as [Hewson1993]:

$$T_K = D \exp(-\frac{1}{JN_0}) \tag{3.1}$$

where J is the exchange coupling and N_0 is the density of state at the Fermi level. Many theoretical approaches developed so far, the renormalization group, Fermi liquid, and the Bethe ansatz solutions, have led to rather a complete picture of the ground state and thermodynamic behavior of the $s - d$ model for spin $S = 1/2$ and non-degenerate Anderson model [Hewson, 1993].

When a hybridizing, f-shell, local moment ion such as Ce, Yb, or U is embedded into a metallic host, it is necessary to consider the ground state f-spin degeneracy $N = 2j + 1$. In this limit, the N-fold degenerate Kondo lattice model, Coqblin-Schrieffer model [Coqblin, 1969], and the degenerate (periodic) Anderson model [Hirst, 1978] have been developed and successfully applied to rare-earth (impurity) systems. We now begin a discussion of qualitative features in the Anderson and Kondo lattice models. For small interaction, the periodic Anderson model describes a Fermi liquid with two bands [Hewson, 1993]. The resulting Fermi liquid, formed below a coherence temperature T_{coh}, will have a Fermi volume containing both conduction electrons and local moments.

A quadratic temperature dependence of the electrical resistivity is expected below T_{coh}; for $T > T_{coh}$, conduction electrons interact weakly with a paramagnetic system of localized spins. Ignoring phonon contributions, the resistivity in this region is logarithmically increased as temperature decreases. In the crossover region $T \sim T_{coh}$, the strong Fermi surface fluctuations give rise to a very high resistivity, giving rise to local resistance maximum. Experimentally, this resistivity maximum is often used to defined coherence temperature, and sometimes is considered to be a caliper of the Kondo temperature. Because of local moment ions in periodic lattice, at high temperatures the magnetic susceptibility follows a Curie-Weiss behavior. At low temperatures, much below T_{coh}, the electronic specific heat is proportional to the temperature, $\gamma = C(T)/T|_{T\rightarrow 0} \propto T$, in Kondo lattice system. Recently a mean field approach taken to the Kondo lattice model in the weak coupling limit shows that two energy scales are relevant

for the Kondo lattice system [Burdin, 2000]: one is associated with the onset of local Kondo screening, single impurity Kondo scale ($T_K^s = D\exp(-1/JN_0)F_K(n_c)$); the other is associated with Fermi liquid coherence and the behavior of physical quantities at $T = 0$ ($T_{coh} = D\exp(-1/JN_0)F_{coh}(n_c)$), where F_K and F_{coh} are functions of the filling of the conduction band. These two scales have the same exponential dependence on T_K/D for weak coupling, but very different dependencies on the conduction electron density in the limit $n_c \ll 1$, in which $T_{coh} \ll T_K$.

In the N-fold degenerated Kondo lattice model, $k_B T_K \gg \Delta_{CEF}$, where Δ_{CEF} is the crystalline electric field splitting (see below), a broad local maximum occurs for $N > 3$ in the magnetic susceptibility and the magnetic specific heat. The magnetic susceptibility and specific heat in the Coqblin-Schrieffer model based on the Bethe-ansatz solution are numerically solved by Rajan [Rajan, 1983], and are plotted in Figs. 3.1 (b) and (c), respectively. Recently, these results have been reproduced by Otsuki *et al.* solving the Coqblin-Schrieffer model based on a continuous-time, quantum Monte Carlo method [Otsuki, 2007]. This peak like structure has been observed in many Ce- and Yb-based Kondo lattice system [Hewson, 1993].

3.1.2 Crystalline electric field

Given that the $4f$-electrons in rare-earth ions lie much closer to the nucleus than the $3d$-electrons in transition metal ions, and lie within $5d$ shells, they are shielded from the local environment. As a consequence the spin-orbit interactions are stronger than the crystalline electric field (CEF) interactions for rare-earth atoms. Consider the rare-earth ion with a stable $4f^n$ configuration with a ground state Hund's rule multiplet $|n, L, S\rangle$. This energy level is split by spin-orbit coupling into multiplets, $|n, L, S, j\rangle$ and $|n, L, S, j'\rangle$ with energies E_j, $E_{j'} = E_j + \Delta E_{jj'}$, with $\Delta E_{jj'} > 0$ so that the j multiplet lies lowest (Fig. 3.2 (a)). The degeneracy factor will be denoted by N_j, where $N_j = 2j + 1$. For instance, $j = 5/2$ and j' = 7/2 is appropriate for Ce.

If there is a CEF effect the lowest multiplet $|n, L, S, j\rangle$ is split into multiplets, depending on the point symmetry. Assuming that if the lowest multiple is split into two multiples, $|n, L, S, j, \gamma\rangle$ and $|n, L, S, j, \gamma'\rangle$ as shown in Fig. 3.2 (b), with degeneracies, N_γ and $N_{\gamma'}$, and
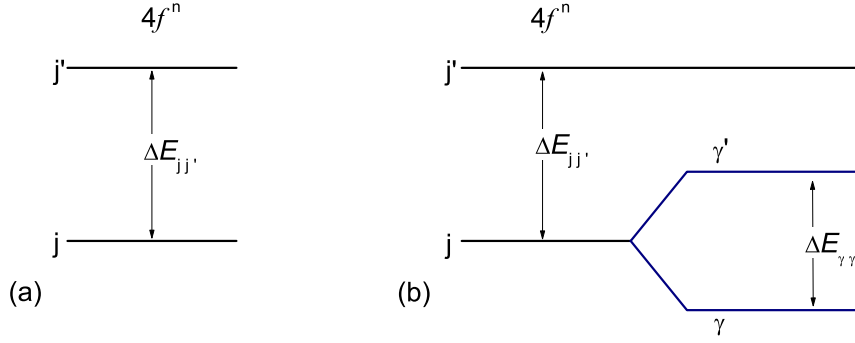
Figure 3.2 Lower multiplets associated with a rare-earth ion in a configu-
ration $4f^n$: (a) two multiplets with a spin-orbit splitting $\Delta E_{jj'}$
and (b) with the lowest multiplet split by a crystalline electric
field with an excitation energy $\Delta E_{\gamma\gamma'}$.

energies (E_γ), $E_{\gamma'} = E_\gamma + \Delta E_{\gamma\gamma'}$, where $E_{\gamma'} > 0$ and $N_\gamma + N_{\gamma'} = N_j$. When $\Delta E_{\gamma\gamma'} \ll T_K$ the low temperature thermodynamics is governed by the energy scale $k_B T_K$, the Kondo temperature associated with the unsplit multiplet, given by N_j. When $\Delta E_{\gamma\gamma'} \gg T_K$, T_K will be appropriate to the lower CEF multiplet with a degeneracy factor N_γ. These results can be applied to Ce case, $j = 5/2$ multiplet split by a cubic CEF into a Γ_7 doublet $(N_{\Gamma7} = 2)$ and a Γ_8 quartet $(N_{\Gamma8} = 4)$. Note that the relevant ratio $k_B T_K / \Delta E_{\gamma\gamma'}$ is important in the Coqblin-Schrieffer regime, but the ratio $\Delta E_{jj'} / \Delta E_{\gamma\gamma'}$ is a relevant ratio in the mixed valence regime. Since the CEF is responsible for lifting the degeneracy of Hund's rule ground state multiplet at low temperatures, it is important to consider CEF effect that eventually affects the magnetic properties of the rare-earth ions in Kondo lattice system .

3.1.3 RKKY interaction

The screening of local moments, required for Fermi liquid behavior in the Kondo lattice, competes with interactions between local moments. Such interactions can be due to direct hopping or exchange between f-orbitals, but are also generated due to the polarization of the conduction electrons. Most local moment systems develop antiferromagnetic, or ferromagnetic, order at low temperatures. A magnetic moment at location $\mathbf{x}_0$ induces a wave of Friedel os-cillations in the electron spin density $\langle \hat{\sigma}(\mathbf{x}) \rangle = -J\chi(\mathbf{x} - \mathbf{x}_0)\langle \mathbf{S}(\mathbf{x}_0) \rangle$ where $\chi(\mathbf{x} - \mathbf{x}_0)$ is the

nonlocal susceptibility of the metal [Coleman, 2008]. The sharp discontinuity in the occupancies $f(\epsilon_k)$ at the Fermi surface is responsible for Friedel oscillations in induced spin density that decay with a power law. If second moment is introduced at location $\mathbf{x}$, it couples to this Friedel oscillation with energy $J\langle\mathbf{S}(\mathbf{x})\hat{\sigma}(\mathbf{x})\rangle$, giving rise to the Ruderman-Kittel-Kasuya-Yosida (RKKY) magnetic interaction [Ruderman, 1954; Kasuya, 1956; Yosida, 1957]. This indirect, RKKY interaction, is given in lowest quadratic order in J;

$$H_{RKKY} = -J^2 \chi(\mathbf{x} - \mathbf{x}')\mathbf{S}(\mathbf{x}) \cdot \mathbf{S}(\mathbf{x}') \tag{3.2}$$

where $J_{RKKY}(\mathbf{x} - \mathbf{x}') = J_{RKKY}(r) = -J^2 N_0 \frac{\cos 2k_F r}{k_F r}$, where N_0 is the conduction electron density of states and r is the distance from the local moment setting up the oscillations. In alloys containing a dilute concentration of magnetic transition metal ions, the oscillatory RKKY interaction gives rise to a frustrated, glassy magnetic state known as a spin glass [Mydosh, 1993]. In the Kondo lattice systems, the RKKY interaction typically gives rise to an ordered antiferromagnetic (or ferromagnetic) state with a Néel temperature, T_N, (or Curie temperature, T_c) of the order $J^2 N_0$. In the Kondo screened state, J_{RKKY} is expected to be renormalized, in particular at long distances, but a reliable determination of J_{RKKY} is not available at present.

3.1.4 Heavy fermion state

The term heavy fermion (HF) has been used to describe the low temperature electronic state in a new class of intermetallic compound with electronic density of states as much as 1000 times larger than copper. Since the discovery of heavy fermion behavior in CeAl$_3$ (γ = 1620 mJ/mol·K^2) [Andres, 1975], various ground states, such as superconductors, antiferromagnets, valence fluctuations, and insulators, has been observed in Kondo lattice systems. The lower cut-off ($C(T)/T|_{T\to 0} = \gamma \geq 400$ mJ/mol·K^2) [Stewart, 1984], defining heavy fermions, is somewhat arbitrary as these systems are part of a continuum extending down through Kondo lattice to mixed valence (intermediate valence) systems. The heavy electron state of intermetallic lanthanide and actinide compounds has its origin in the hybridization between the $4f$- and $5f$-electrons and the conduction electrons. In Ce-, Yb-, and U-based metallic systems

the conduction electrons compensate or screen the localized moments of f-electrons where localized electrons together with their screening cloud form quasi-particles. These quasi-particles have a heavy (effective) mass, reflected in the enhanced value of the Sommerfeld coefficient $\gamma = C(T)/T|_{T \to 0}$, Pauli susceptibility $\chi(0)$, and A-coefficient of the T^2 term to the electrical resistivity at low temperatures. When f-electrons enter a conduction band there is an increased overlap of the electronic state which enhances the hybridization and band widths [Hewson, 1993] and the Fermi surface volume expands (within in the approximation of single Fermi surface), and is compensated by the development of a positively charged background [Coleman, 2008].
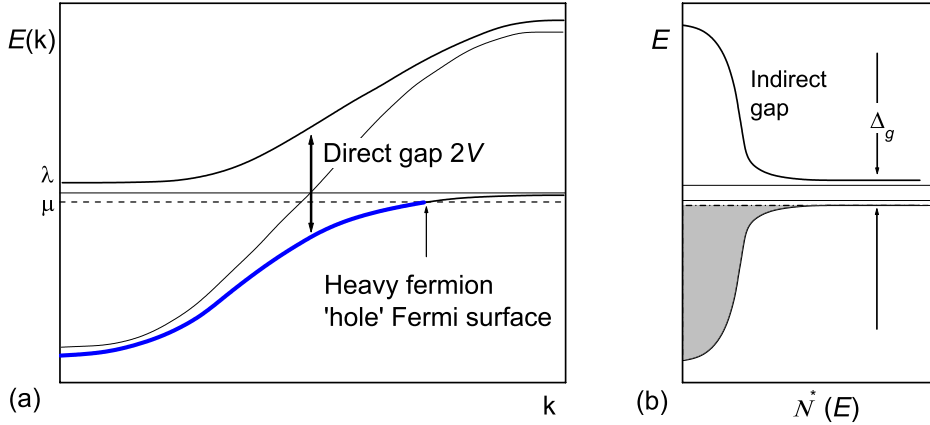
Figure 3.3 (a) Dispersion produced by the injection of a composite fermion into the conduction sea. (b) Renormalized density of states, showing hybridization gap Δ_g [Coleman, 2008].

From the mean field approach to the Kondo lattice model the mass enhancement of the quasi-particles and their hybridization strength can be obtained [Coleman, 2008]. Hybridization between the f-electron states and the conduction electrons builds an upper and lower Fermi band, separated by an indirect hybridization gap of width $\Delta_g = E_g(+) - E_g(-)$, where $E_g(\pm) = \lambda \pm V^2/D_{\mp}$ and $D_{\mp}$ are the top and bottom of the conduction band (Fig. 3.3). The direct gap between the upper and lower bands is $2|V|$, where $|V|$ is the hybridization matrix elements. The energy gap with $N = 2j + 1$ can be written

$$\Delta_g = \frac{\pi n_f}{N e^2} T_K. \tag{3.3}$$

The relationship between the energy of the heavy electrons (E) and the energy of the conduction electrons (ϵ) is given by $\epsilon = E - |V|^2/(E - \lambda)$, so that the density of heavy electron states $N^*(E) = \sum_{k,\pm} \delta(E - E_k^{\pm})$ is related to the conduction electron density of states $N^*(\epsilon)$ by $N^*(E) = N_0 \frac{d\epsilon}{dE} = N^*(\epsilon)(1 + \frac{|V|^2}{(E-\lambda)^2})$, which becomes $N^*(E) \sim N_0(1 + \frac{|V|^2}{(E-\lambda)^2})$ outside hybridization gap and becomes $N^*(E) = 0$ inside hybridization gap. So the hybridization gap has of approximate width of $k_B T_K$. Since the density of state $N^*(0) = N_0 + n_f/(NT_K)$ at the Fermi energy so the mass enhancement of the heavy electrons is then

$$\frac{m^*}{m} = 1 + \frac{n_f}{N_0 NT_K} \sim \frac{n_f D}{NT_K} \tag{3.4}$$

where N_0 is the density of state of electrons in the conduction sea and D is the width of the electron band. Therefore, the mass enhancement is expected either when the band width is very large, $\hbar^2/m^* = \mathrm{d}^2 E(k)/\mathrm{d}k^2$ where $E(k)$ is the energy dispersion, or when the Kondo temperature is very low, $T_K \propto 1/m^*$, which defines a Fermi energy $(k_B T_K)$ that is much smaller than in common metals.

3.1.5   Doniach phase diagram

The competition between the Kondo screening (on-site) and the RKKY (inter-site) interactions governs the phase diagram of the Kondo lattice, called Doniach diagram [Doniach, 1977]. Generally the Fermi liquid competes with a magnetically ordered metal, but in the presence of strong quantum effects and geometric frustration, spin glass and spin liquid states may also occur as a ground state [Coleman, 2007]. Doniach [Doniach, 1977] argued that there are two energy (temperature) scales in the Kondo lattice, the single ion Kondo temperature T_K and T_{RKKY}, given by $T_K = D\exp(\text{-}1/2JN_0)$ and $T_{RKKY} = J^2 N_0$. Figure 3.4 is based on a extension [Coleman, 2008] of the general Doniach phase diagram. When JN_0 is small, then T_{RKKY} is the largest energy scale and an antiferromagnetic state is formed, but, when the JN_0 is large, T_K is the largest energy and a fully screened Kondo lattice ground state becomes stable. For intermediate values of JN_0 a local maximum in T_N occurs.

Although the Doniach diagram provides a qualitative understanding of HF Kondo lattice behavior, there are concerns left over. This diagram is generically a comparison of energy
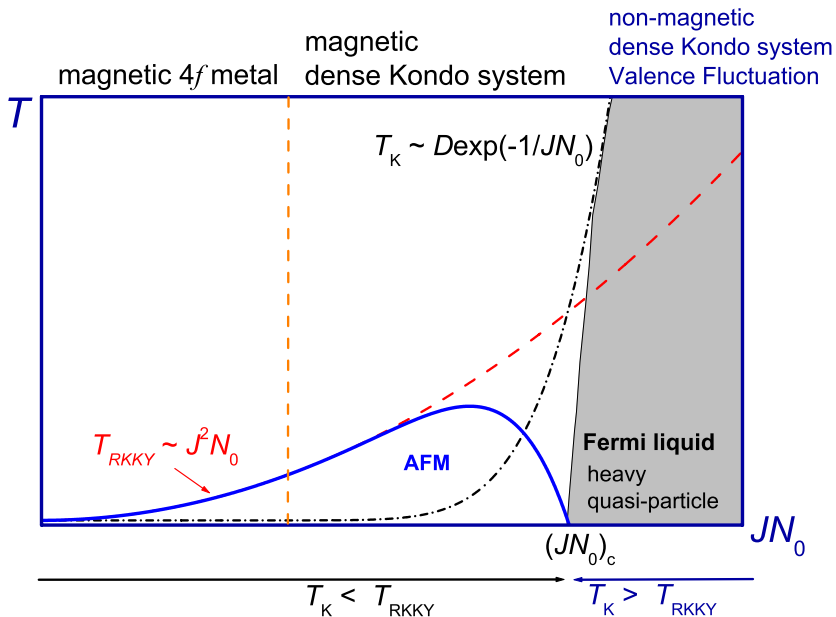
Figure 3.4   Doniach diagram, illustrating the antiferromagnetic (AFM) regime, where $T_K < T_{RKKY}$ and the heavy fermion regime, where $T_K > T_{RKKY}$. Experimental observation indicates that the transition between these two regimes, $(JN_0)_c$, occurs through a quantum critical point [Coleman, 2008].

scales and does not provide a mechanism connecting the heavy fermion to the local moment (AFM) states. In this diagram, fundamentally based on a single impurity model, an artificially large value of the coupling constant JN_0 is required for heavy fermion state. This was later resolved by considering the large f-spin degeneracy ($N = 2j + 1$) of the spin-orbit coupled moments. The degeneracy can be large as $N = 8$ in Yb-based compounds, leading to a Kondo temperature $T_K = D(NJN_0)^{1/N} \exp(-1/NJN_0)$ [Hewson, 1993; Coleman, 2008].

The Doniach diagram implies that there are materials having a critical value of $(JN_0)_c$ (Fig. 3.4) which are located at the interface of magnetic and nonmagnetic behavior; at this point magnetic ordering take place undergoes at exactly zero temperature. The parameter, JN_0, depends on the details of the system. Experimental observation [Stewart, 2001] indicates that the transition between these two regimes is a quantum critical point (QCP). Except for the special case of some material being precisely located at the this critical value, in general it is necessary to tune a system to the QCP using nonthermal control parameters

such as substitution ($\mathbf{x}$), pressure ($\mathbf{P}$), and/or magnetic field ($\mathbf{H}$). Near the critical point of such a quantum phase transition, pronounced deviations from the Fermi liquid behavior have been observed from the finite temperature thermodynamic and transport measurements. Such deviations were considered as a breakdowns of the Fermi liquid state, so called non Fermi liquid (nFL) behavior, caused by quantum fluctuations near the critical point. Experimentally, such nFL behavior associated with an antiferromagnetic QCP involves logarithmic divergence of the specific heat, $C(T)/T \propto$ -log(T), and linear temperature dependence of the resistivity, $\Delta\rho = AT$ [Stewart, 2001]. Generally, the Fermi liquid state, with $\Delta\rho = AT^2$, is typically recovered when the system is tuned away from the QCP.

3.2   Fermi liquid theory

Systems of interacting fermions at low temperature have been of interest since early in the development of condensed matter theory. The Fermi liquid (FL) theory, or Landau theory, a phenomenological theory of interacting fermions, is based on the concept of quasi-particles [Landau, 1957a; Landau, 1957b; Landau, 1959]. It proposed to map the properties of Fermi systems at low temperature onto the physics of dilute gas of strongly interacting fermionic excitations. A microscopic justification and rigorous general mathematical proof for the stability of the FL state have been performed by using a renormalization group (RG) method [Feldman, 1993; Shankar, 1994].

For a noninteracting system, the occupation of the single particle state $|\mathbf{k}\widehat{\sigma}\rangle$ with momentum $\mathbf{k}$ is given by $n_{\mathbf{k}\widehat{\sigma}}^{T=0} = \theta(k_F - k)$, where $\theta(k_F - k)$ is the step function. The Fermi momentum k_F is determined by the density of particles

$$n = \sum_{\mathbf{k}\widehat{\sigma}} n_{\mathbf{k}\widehat{\sigma}}^{T=0} = \frac{k_F^3}{3\pi^2}. \tag{3.5}$$

If the low energy excitation spectrum of the interacting system is in one-to-one correspondence with the Fermi liquid spectrum, and if the ground state retains the full symmetry of the Hamiltonian, the system is termed a normal Fermi liquid [Baym, 1991]. Low energy single particle excitations of the FL, with momentum numbers $\mathbf{k}$ and $\widehat{\sigma}$, are called quasi-particles.

In the ground state, the quasi-particle distribution function is $n_{\mathbf{k}\widehat{\sigma}}$. The energy of a quasi-particle, $\epsilon_{\mathbf{k}\widehat{\sigma}}$, is defined as the amount of energy by which the total energy E of the system increases, if a quasi-particle is added to the unoccupied state $|\mathbf{k}\widehat{\sigma}\rangle$, $\epsilon_{\mathbf{k}\widehat{\sigma}} = \frac{\partial E}{\partial n_{\mathbf{k}\widehat{\sigma}}}$, where $\partial n_{\mathbf{k}\widehat{\sigma}}$ is the corresponding change of the distribution function. As a consequence of the interaction, the single particle energies depend on the state of the system $\epsilon_{\mathbf{k}\widehat{\sigma}}\{n_{\mathbf{k}'\widehat{\sigma}'}^{T=0}\} = v_F(k - k_F)$ for an isotropic system at small energies, with the Fermi velocity $v_F = k_F/m^*$. The effective mass, m^*, determines the density of states N_0 per spin at the Fermi level,

$$N_0 = \frac{m^* k_F}{\pi^2} \tag{3.6}$$

For isotropic systems, with short range interaction, the FL interaction function ($f_{\mathbf{k}\widehat{\sigma}\mathbf{k}'\widehat{\sigma}'}$) depends only on the angle between $\mathbf{k}$ and $\mathbf{k}$' and on the relative spin orientation of $\widehat{\sigma}$ and $\widehat{\sigma}'$, and hence is parameterized as [Baym, 1991]

$$f_{\mathbf{k}\widehat{\sigma}\mathbf{k}'\widehat{\sigma}'} = \frac{1}{2N_0} \sum_{l=0}^{\infty} P_l(\widehat{\mathbf{k}}, \widehat{\mathbf{k}}')[F_l^s + F_l^a \widehat{\sigma}\widehat{\sigma}'] \tag{3.7}$$

Here $\widehat{\mathbf{k}} = \mathbf{k}/|\mathbf{k}|$, $\widehat{\sigma} = \pm 1$, $P_l(x)$ are the Legendre polynomials, and F_l^s and F_l^a are the dimensionless, spin symmetric and spin antisymmetric, Landau parameters, respectively, which characterize the effect of the interaction on the quasi-particle energy spectrum. In a crystal, the symmetry of the system is reduced to discrete rotations and/or reflections (the elements of the space group of the lattice). As a consequence the band structure $\epsilon_{\mathbf{k}}$ and the FL interaction $f_{\mathbf{k}\widehat{\sigma}\mathbf{k}'\widehat{\sigma}'}$ may be strongly anisotropic. In applications of Fermi liquid theory to metals, it is frequently assumed that an isotropic approximation in 3D or quasi-2D systems can give a reasonable account of the FL properties.

3.2.1 Thermodynamic properties

The equilibrium distribution function $n_{\mathbf{k}\widehat{\sigma}}^0$ at finite temperature follows:

$$n_{\mathbf{k}\widehat{\sigma}}^0 = n_F(\epsilon_{\mathbf{k}\widehat{\sigma}}) = \frac{1}{e^{\epsilon_{\mathbf{k}\widehat{\sigma}}/T} + 1} \tag{3.8}$$

The derivative of the internal energy with respect to temperature yields the specific heat at constant volume. The leading term at $T \ll T_F$ (T_F is the Fermi temperature) is linear

in temperature, as for the free Fermi gas, and given by the (renormalized) density of states $N_0 = m^* k_F / \pi^2$ (Eq. 3.6)

$$C_V = \frac{\pi^2 k_B^2 N_0 T}{3} = \gamma T. \tag{3.9}$$

The spin susceptibility χ at $T \ll T_F$ follow as

$$\chi = \frac{\mu_B^2 N_0}{1 + F_0^a} = \frac{m^*/m}{1 + F_0^a} \chi_0 \tag{3.10}$$

where μ_B is the magnetic moment of electrons, χ_0 is the susceptibility of the free gas, and F_0^a is the dimensionless, spin antisymmetric, Fermi liquid parameters for $l = 0$. χ is affected both by the mass renormalization and by Fermi liquid parameters describing an effective screening of the external fields.

3.2.2 Transport properties

At low temperature $T \ll T_F$, there exists a small number of thermally excited quasi-particles, which interact strongly. The decay rate $1/\tau$ of a quasi-particle on top of the filled Fermi sea is dominated by two particle collision processes; the considered quasi-particle in state $|1\rangle = |\mathbf{k}_1 \hat{\sigma}_1\rangle$ scatters off a partner in state $|2\rangle$, the two particles ending up in the final states $|3\rangle$ and $|4\rangle$.

A full evaluation of $1/\tau$ yields [Baym, 1991]

$$\frac{1}{\tau_{\mathbf{k}}} = (T^2 + \frac{\epsilon_{\mathbf{k}}^2}{\pi^2}) \frac{\pi^3}{64 \epsilon_F} \int_0^1 d\cos(\frac{\theta}{2}) \int_0^{2\pi} \frac{d\phi}{2\pi} [|A_0(\theta, \phi)|^2 + 3|A_1(\theta, \phi)|^2]. \tag{3.11}$$

The quantities A_0 and A_1 are the dimensionless scattering amplitudes in the singlet and triplet channels $[A_{0,1} = N_0 a(1, 2; 3, 4)]$; θ and ϕ parameterize the angle between $\mathbf{k}_1$ and $\mathbf{k}_2$ and the planes $(\mathbf{k}_1, \mathbf{k}_2), (\mathbf{k}_3, \mathbf{k}_4)$, respectively. In 2D systems the prefactor of T^2 in $1/\tau$ is logarithmically enhanced, $1/\tau \sim T^2 \ln(T_F/T)$ [Chubukov, 2005].

The forward scattering limit of the quasi-particle scattering amplitude can be expressed as [Landau, 1959]

$$A^\alpha(\theta, \phi = 0) = \sum_l \frac{F_l^\alpha}{1 + F_l^\alpha/(2l + 1)} P_l(\cos \theta), \tag{3.12}$$

where $\alpha = s$ and a labels the spin symmetric and antisymmetric particle-hole channels, respectively.

In the lowest approximation, the electrical conductivity $\sigma = 1/\rho$, where ρ is the resistivity, is defined as the response of the electrical current density, $\mathbf{j}$, to the screened electric field, $\mathbf{E}$, $\mathbf{j} = \sigma\mathbf{E}$. For a translationly-invariant system, quasi-particle collisions are momentum conserving and the resistivity is zero. The most important source of momentum dissipation at low temperature is impurity/defect scattering. Taking into account that electron-electron collisions $1/\tau_{e-e} \sim T^2$ (Eq. 3.11) at low temperatures, the resistivity is given by

$$\rho(T) = \rho_0 + AT^2 + \cdots. \tag{3.13}$$

Here ρ_0 is the residual resistivity from impurity/defect scattering. The coefficient A is given by a weighted angular average of the squared quasi-particle scattering amplitudes $A \propto (A_{0,1}(\theta, \phi))^2 \propto N_0^2$. Note that in general the transport relaxation time, τ_{tr}, differs from the relaxation time in a particular $\mathbf{k}$ state due to the extra factor $1 - \cos\theta$ (Eq. 3.11).

Whereas in the FL picture, the resistivity coefficient (when the transition amplitude $a(1, 2; 3, 4)$ depends weakly on momentum), the magnetic susceptibility, and the specific heat coefficient are expected to be material dependent since $A \propto N_0^2$, $\chi \propto N_0$, and $\gamma \propto N_0$, ratios of these terms can be constructed so as to be material independent. This is indeed observed for a large number of HF systems, and A/γ^2 is termed the Kadowaki-Woods ratio [Kadowaki, 1986] and $\chi(0)/\gamma$ is called the Wilson ratio [Lee, 1986]. In the following section these FL relations will be discussed in detail.

3.3 Fermi liquid relations

3.3.1 Kadowaki-Woods ratio - A vs. γ

Experimentally, the ratio between the T^2 coefficient of the resistivity (A) and the linear specific heat coefficient (γ) in heavy fermion compounds shows an approximate universal value $A/\gamma^2 \approx 10^{-5}$ $\mu\Omega\text{cm}(\text{mJ/mol·K})^{-2}$, which is know as the Kadowaki-Woods (K-W) ratio [Kadowaki, 1986]. Although it was believed to be universal in heavy fermion systems for a

long time, the K-W relation is violated in many Yb-based systems. Recently, a generalized K-W relation was derived that is applicable for system with general f-orbital degeneracy, N, for Ce- and Yb-based compounds [Tsujii, 2005] as well as some Sm- and Er-based compounds [Kontani, 2005; Kontani, 2008]. By considering the material dependence of N, the variation in K-W ratio values was explained [Kontani, 2005; Kontani, 2008] by the given equations:

$$A = \frac{hk_B^2}{e^2} \frac{3\pi^6}{2\mathbf{k}_F^4 a^3} N(N-1)\Gamma_{loc}^2(0,0)\rho_f^4(0) \tag{3.14}$$

$$\gamma = N_A k_B^2 \frac{\pi^2}{6} N(N-1)\Gamma_{loc}(0,0)\rho_f^4(0)$$

where h is the Plank constant and e is the electron charge; k_F is the Fermi momentum, $\Gamma_{loc}(0,0)$ is the local four-point vertex which represents the effective interaction between quasi-particles; $\rho_f(0)$ is the density of states (DOS) per f-electron at the Fermi energy of which $N\rho_f(0)$ is the total DOS at the Fermi level. Here we will follow the notation given in Ref. [Tsujii, 2005], in the previous section the DOS is given by N_0. Since $\Gamma_{loc}(0,0)$ also depends on N, A and γ are not simply proportional to $N(N-1)$. But a value for A/γ^2 can be deduced as

$$\frac{A}{\gamma^2} = \frac{h}{e^2 N_A^2 k_B^2} \frac{9(3\pi^2)^{-1/3}}{n^{4/3} a^3} \frac{1}{\frac{1}{2}N(N-1)} \approx \frac{1 \times 10^{-5}}{\frac{1}{2}N(N-1)} \tag{3.15}$$

by making several assumptions. For the case of $N = 2$, this formula gives the K-W ratio; A/γ^2 $= 1 \times 10^{-5}$ $\mu\Omega$cm(mJ/mol·K)$^{-2}$ with $h/e^2 = 2.6 \times 10^4$ Ω and assuming $1/n^{4/3}a \approx 4 \times 10^{-8}$ cm. For general N, this gives a set of universal relations given in Ref. [Tsujii, 2005] and shown in Fig. 3.5 as the solid lines for $N = 2, 4, 6$, and 8. In the above equation the free electron model $k_F = (3\pi^2 n)^{1/3}$, n being the carrier concentration, was used. Based on the above the formula unit (f.u.) should include only one rare-earth ion. The K-W ratio is found to depend on n as $n^{-4/3}$. Thus, it is necessary to consider the carrier density for low carrier systems.

For YbPtBi, in zero field and zero pressure, the K-W ratio is located close to the $N = 8$ curve [Torikachvili, 2007]. When the carrier density, 0.04 hole per formula unit (see chapter 6), is considered, the $N = 2, 4, 6, 8$ manifolds shown in Fig. 3.5 shifts to downward with the $N = 2$ line falling well below the data. Both the degeneracy and carrier density can not explain the observed K-W ratio for YbPtBi. The K-W ratio may depend on CEF splitting, low carrier
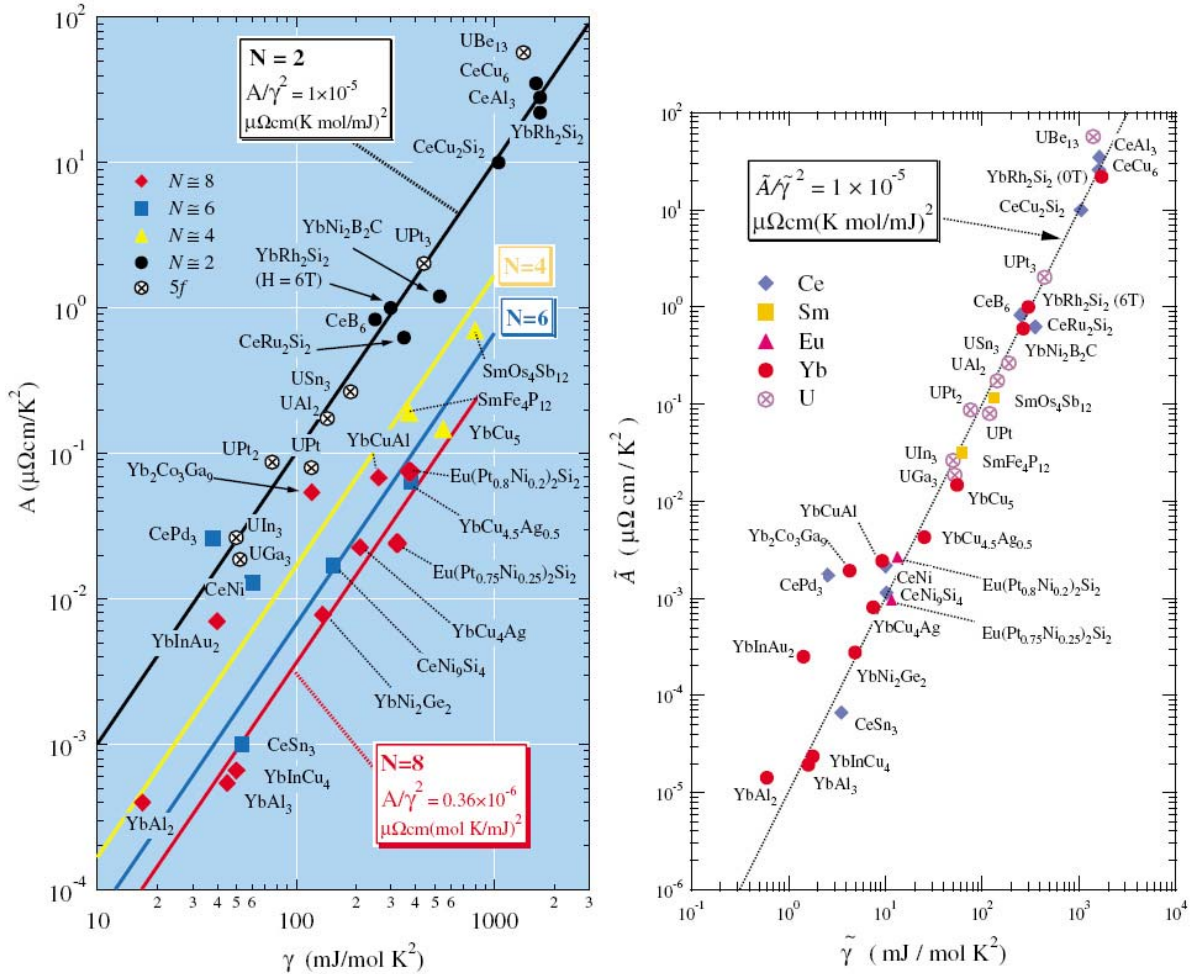
Figure 3.5   Figures are taken from Ref.   [Tsujii, 2005].   Left figure:
A vs. γ of heavy fermion systems with various degener-
acy. The black line corresponds to the Kadowaki-Woods ratio
[Kadowaki, 1986]. Other solid lines are the predicted from the
orbitally degenerate periodic-Anderson model. Colors of this
symbols represent the degeneracy N; black, yellow, blue, and
red indicate $N = 2$, 4, 6, and 8, respectively. Right figure:
The plot of $\widetilde{A}$ and $\widetilde{\gamma}$ of heavy-fermion systems. The dotted line
represents the generalized K-W ratio.

density and details of the multiple Fermi surface. The further discussion of the K-W ratio for YbPtBi will be present in chapter 6.

If the value of N can be determined experimentally, the normalized coefficients $\widetilde{A}$ and $\widetilde{\gamma}$ can be written

$$\widetilde{A} = \frac{A}{\frac{1}{2}N(N-1)} \quad , \quad \widetilde{\gamma} = \frac{\gamma}{\frac{1}{2}N(N-1)}. \tag{3.16}$$

Then the K-W ratio with any N values, $\widetilde{A}/\widetilde{\gamma}^2 = 1 \times 10^{-5}$ $\mu\Omega$cm(mJ/mol·K)$^{-2}$. This generalized K-W ratio does not include any N dependence and should be applicable to arbitrary N systems. The previous K-W relation turned out to be valid only when $N = 2$ (Kramers doublet case due to strong CEF splitting primarily in Ce-based systems). However, a determination of the ground state degeneracy N, or equivalently, the number of states below Kondo temperature T_K, is not trivial due to the CEF splitting (Δ_{CEF}/k_B) of the f-level; for example, the $N = 6$, for Ce^{3+}, and $N = 8$, for Yb^{3+}, levels split into Kramers doublets or quartets depending on point symmetry of the rare-earth ion. The generalized K-W relation is derived only by imposing constraints of large mass enhancements and small charge susceptibility on the microscopic FL theory. This fact illustrates a remarkable advantage of the FL theory for the analysis of strongly correlated systems. Recently, the YbT$_2$Zn$_{20}$ (T = Fe, Ru, Os, Ir, Rh, and Co) system with $2 \leq N \leq 8$, has been reported by Torikachvili $et\,al$ [Torikachvili, 2007]. These system were found to be followed the generalized K-W relation well, and formally doubled the number of examples of Yb-based HF system.

It should be noted that the transition metals Pd and Pt also deviate from the K-W relation. These transition metals are not likely to require the generalized K-W relation, because the N of these metals would be close to 2 due to the quenching of the orbital moment. Indeed $\widetilde{A}/\widetilde{\gamma}^2$ values for these metals is much smaller than the above equation. A. C. Jacko $et\,al$. [Jacko, 2009] introduced a ratio closely related to the K-W ratio, that includes the effects of carrier density and spatial dimensionality and reconciles the values for organic charge-transfer salts, transition metal oxides, heavy fermions, and transition metals (Fig. 3.6).

Jacko $et\,al$. achieve this by considering new parameter, $f_{dx}(n) = \varsigma^2 n N_0^2 \langle v_{0x}^2 \rangle$, where $\langle\rangle$ denotes an average over the Fermi surface, n is the conduction electron density, and ς is a
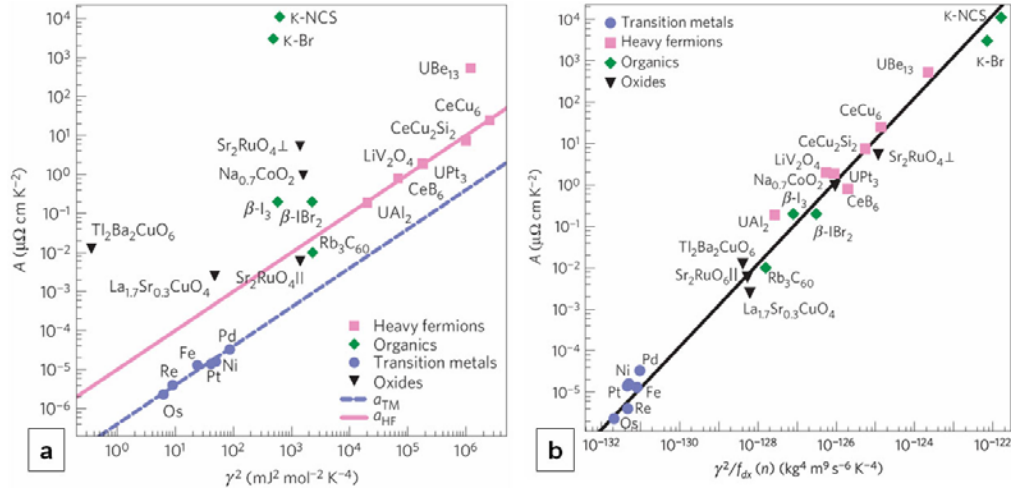
Figure 3.6   Figures taken from Ref. [Jacko, 2009]. (a) The standard Kad-
owaki-Woods plot. It can be seen that the data for the tran-
sition metals and heavy fermions (other than UBe_{13}) fall onto
two separate lines. However, a wide range of other strongly
correlated metals do not fall on either line or between the two
lines. $a_{TM} = 0.4$ $\mu\Omega$cm mol^2 K^{2}mJ^2 is the value of the K-W
ratio observed in the transition metals [Rice, 1968] and $a_{HF} =$
10 $\mu\Omega$cm mol^2 K^{2}mJ^2 is the value seen in the heavy fermions
[Kadowaki, 1986]. (b) Comparison of the ratio defined in equa-
tion $\frac{Af_{dx}(n)}{\gamma^2}$ with experimental data. It can be seen that, in all
of the materials studied, that data are in excellent agreement
with our prediction (line). The abbreviations in the data-point
labels are the same as in left figure. Further details of the data
are given in Supplimentary information [Jacko, 2009].

constant, a more fundamental ratio is proposed:

$$\frac{A}{\gamma^2} f_{dx}(n) = \frac{81}{4\pi\hbar k_B^2 e^2} \tag{3.17}$$

With $f_{dx}(n)$ derived from the band structures, this new relation was applied to a variety of strongly correlated metals, assuming the isotropic materials have isotropic Fermi surfaces and that layered materials have warped, cylindrical Fermi surfaces. As shown in Fig. 3.6 the new ratio is in good agreement with the data for materials investigated, although the range of this log-log plot does itself conceal a fair amount of scatter.

3.3.2 Wilson ratio - $\chi(0)$ vs. γ

The magnetic susceptibilities of all the HFs obey a Curie-Weiss law ($\chi = C/(T - \theta)$) at high temperatures and are large and less temperature dependent at low temperatures, but also display considerable variations. A plot of γ and $\chi(0)$ ($T \to 0$) for a number of HF compounds is given in Fig. 3.7 [Hewson, 1993]. The straight line in the figure corresponds to the Wilson ratio (R_W). This shows that both these quantities are enhanced in a similar way, caused presumably by the f-spin fluctuations. In the N-fold degenerate models, the Coqblin-Schrieffer limit, the magnetic susceptibility of Kondo lattice compounds is given by [Hewson, 1993]

$$\chi = \frac{(g\mu_B)^2 j(j+1)w_N}{3k_B T_K} \tag{3.18}$$

where w_N is the generalization of the Wilson number, given by $w_N = e^{1+C-3/2N}/2\pi\Gamma_N(1 + 1/N)$ [Rasul, 1984]. The electronic specific heat coefficient, γ, deduced from the thermodynamic equations in the Coqblin-Schrieffer limit [Coqblin, 1969] is given by

$$\gamma = \frac{\pi^2 w_N}{3k_B T_K} \frac{N-1}{N}, \tag{3.19}$$

where γ is expressed using high temperature limit of T_K, as defined by Wilson [Rasul, 1984], and this equation is equivalent to Eq. 3.14.

The Wilson ratio in this limit is given by

$$R_W = \frac{\chi/\chi_c}{\gamma/\gamma_c} = \frac{\pi^2 k_B^2}{j(j+1)(g\mu_B)^2} \frac{\chi}{\gamma} = \frac{N}{N-1} \tag{3.20}$$
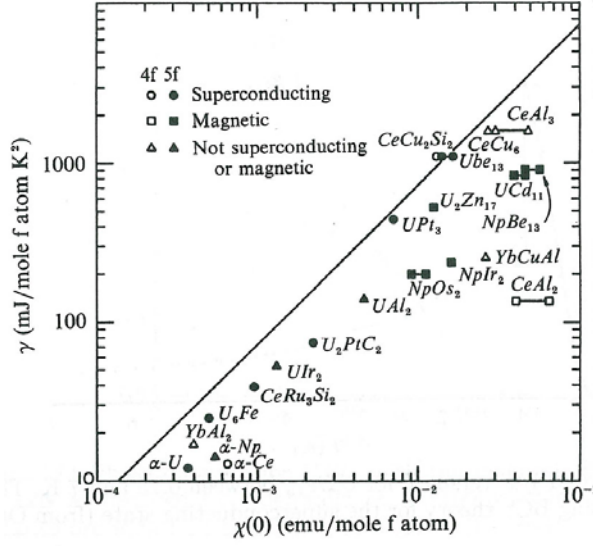
Figure 3.7   Figure taken from Ref. [Hewson, 1993]. A plot of γ and $\chi(0)$
for a number of heavy fermion compounds. The straight line
corresponds to the Wilson ratio for non-interacting electrons
$R_W = 1$ (original figure from Ref. [Lee, 1986]. The compound
Ube$_{13}$ is a typo, should be UBe$_{13}$.

hence $R_w = 2$ for $N = 2$, and $R_w = 1$ for $N \to \infty$. The degeneracy (N) dependence of the R_W was derived earlier than the generalized K-W relation, however, it has not been tested, partly due to the experimental difficulties associated with measuring $\chi(0)$ down to low temperatures, and partly caused by the nature of the ground state susceptibility, which is more sensitive to the ground state wave function than specific heat and resistivity. The ground state susceptibility is determined by the eigenstates for given j, where the degenerate eigenstate splits into several new eigenstates for given point symmetry in a solid. The wavefunction of these eigenstates is the quantum mechanical admixture, consisting $\sum_m \alpha \mid \pm j_m \rangle$. Therefore, the proper ground state wave function should be taken account to extracted the $\chi(0)$ as well as the measurement should be performed at sufficiently low temperature. By considering the ground state N, likely inferred from the K-W ratio, the different manifolds, with different ratio of R_W, are expected on γ vs. $\chi(0)$ plot for Ce, Yb, and U-based compounds.

More generally, there is a generalization of the FL relation [Hewson, 1993],

$$R_W = \frac{N}{N - 1 + j(j+1)(g\mu_B)^2 \chi_{c,imp}/3\chi} \tag{3.21}$$

which reduces to $N/(N-1)$ in the localized limit $\chi_{c,imp} \to 0$. From the FL theory, the specific heat coefficient (3.9) and the spin susceptibility (3.10) are found as

$$\gamma = \frac{\pi^2 k_B^2}{3} \widetilde{N}_0 \quad , \quad \chi = \frac{\mu_B^2 \widetilde{N}_0}{1 + F_0^a} \tag{3.22}$$

where $\widetilde{N}_0$ is the renormalized total density of states at the Fermi level $\widetilde{N}_0 = N_0^c(0) + N_0^f(0)/Z$ with $N_0^{c,f}(0)$, the densities of states of conduction electrons and f-electrons, respectively, and Z is the quasi-particle weight factor in FL theory. The factor $R_W = 1/(1 + F_0^a)$ often called the generalized Wilson ratio, where χ expresses the effect of quasi-particle interactions in terms of the Landau parameter F_0^a.

For a finite magnetic field, $C(T)$ can also be expressed in terms of $\chi(T)$ by using the thermodynamic relation,

$$\frac{\partial^2 C(T,H)}{\partial H^2} = T \frac{\partial^2 \chi(T,H)}{\partial T^2} \tag{3.23}$$

where $C(T,H)$ and $\chi(T,H)$ is the specific heat and magnetic susceptibility, respectively, as function of temperature and magnetic field. For $T \ll T_K$, in the limit of $T \to 0$,

$$\left(\frac{\partial^2 \chi(T,H)}{\partial T^2}\right)_{0,0} = \left(\frac{\partial^2 \gamma(H)}{\partial H^2}\right)_0 . \tag{3.24}$$

Using the independence of the χ/γ ratio of the magnetic field,

$$\frac{\partial^2 \gamma(H)}{\partial H^2} = \frac{4\pi^2 k_B^2}{3(g\mu_B)^2} \frac{\partial^2 \chi(0,H)}{\partial T^2}, \tag{3.25}$$

thus $\gamma(H)$ can be obtained from the magnetic susceptibility.

3.3.3 Faraday number - $S(T)/T$ vs. $C(T)/T$ in the $T = 0$ limit

There is a third ratio connecting two distinct consequences of strong correlations among electrons; the thermoelectric power (TEP) of a free electron gas is linear as a function of temperature; $S(T) = \alpha T$. Moreover, the magnitude of the coefficient α is directly proportional to the density of states at Fermi energy. A dimensionless ratio links the coefficient of TEP to the electronic specific heat through the Faraday number q and the ratio is equal to -1 for free electrons. A strong correlation between $S(T)/T|_{T\to 0}$ and γ was recently found to hold for

several systems including HF compounds [Behnia, 2004]. Figure 3.8 shows the experimental verification of this correlation for electron and hole-like carriers. In the following the diffusion TEP for free electron and N-fold degenerate Anderson model [Newns, 1987; Houghton, 1987] will be briefly summarized [Behnia, 2004].
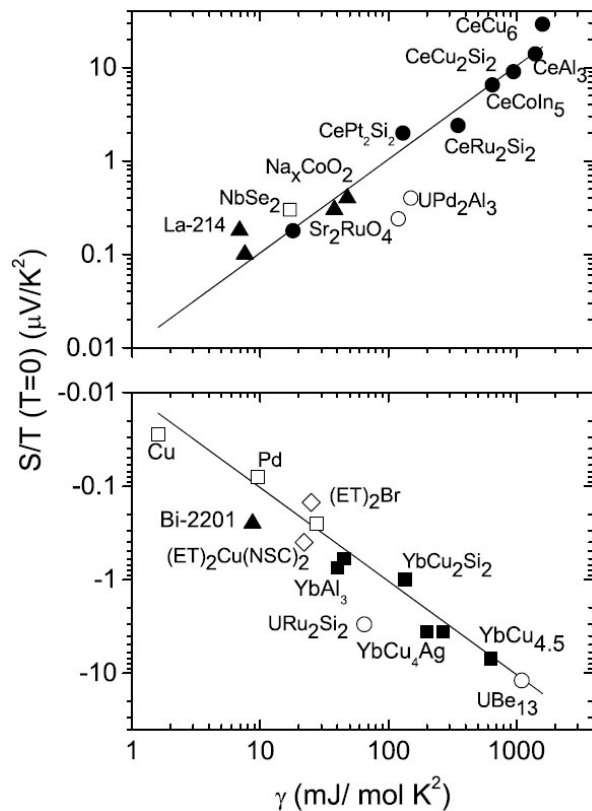
Figure 3.8   Figures taken from Ref. [Behnia, 2004]. S/T versus γ for several compounds. Solid circles (squares) represent Ce (Yb) heavy fermion systems. Uranium-based compounds are represented by open circles, metallic oxides by solid triangles, organic conductors by open diamonds, and common metals by open squares. The two solid lines represent $\pm\gamma/(eN_{Av})$. Details are in Ref. [Behnia, 2004].

In a Boltzmann equation, the TEP, also known as the Seebeck coefficient, is given by

$$S = -\frac{\pi^2}{3}\frac{k_B^2 T}{e}\left(\frac{\partial \ln \sigma_\epsilon}{\partial \epsilon}\right)_{\epsilon_F} \tag{3.26}$$

here e is the elementary charge and ϵ_F is the Fermi energy.

Inserting the dc conductivity ($\sigma(\epsilon)$) of the system for $\epsilon = \epsilon_F$ into above equation yields

$$S = -\frac{\pi^2}{3}\frac{k_B^2 T}{e}\left[\left(\frac{\partial \ln \tau(\epsilon)}{\partial \epsilon}\right)_{\epsilon_F} + \frac{\int d\mathbf{k}\delta(\epsilon_F - \epsilon(\mathbf{k}))\mathbf{M}^{-1}(\mathbf{k})}{\int d\mathbf{k}\delta(\epsilon_F - \epsilon(\mathbf{k}))v(\mathbf{k})v(\mathbf{k})}\right] \qquad (3.27)$$

where $\mathbf{k}$ is the electron wavevector, $\tau(\epsilon)$ is the scattering time and $\mathbf{M}^{-1}$ is the inverse of the effective mass tensor. This expression contains information on both transport and thermodynamic properties of the system, and demonstrates the difficulty of interpreting the temperature dependence of TEP. The scattering time and its energy dependence are only present in the first term of the right hand side of the equation. The second term is purely thermodynamic.

In the simple case of a free electron gas, the second term of equation 3.27 is equal to $3/2\epsilon_F$. Moreover, in the zero-energy limit, the energy dependence of the scattering time can be expressed as a simple function: $\tau(\epsilon) = \tau_0 \epsilon^\zeta$ which yields $(\partial \ln \tau(\epsilon)/\partial \epsilon)_{\epsilon=\epsilon_F} = \zeta/\epsilon_F$ for the first term. Although the most simple case is an energy independent relaxation time $\tau(\epsilon) = \tau_0$ ($\zeta = 0$), a conceivable case is $\zeta = $ -1/2, that corresponds to a constant mean free path (l); $\tau = l/v \propto \epsilon^{-1/2}$. This leads to a very simple expression for the TEP of the free electron gas:

$$S = -\frac{\pi^2}{3}\frac{k_B^2}{e}\frac{T}{\epsilon_F}\left(\frac{3}{2} + \zeta\right). \qquad (3.28)$$

This expression gives an estimation of the magnitude of TEP in real metals. It also indicates that, whenever the Fermi energy is replaced by a different, smaller energy scale, the coefficient is expected to increase. The Fermi energy is related to the carrier concentration n and to the density of states $N_0(\epsilon)$. For free electrons, the link is given by $N_0(\epsilon_F) = 3n/2\epsilon_F$. Using this expression, TEP can be written as

$$S = -\frac{\pi^2}{3}\frac{k_B^2 T}{e}\frac{N_0(\epsilon_F)}{n}\left(1 + \frac{2}{3}\zeta\right) = \alpha T \qquad (3.29)$$

This equation is similar to the familiar expression for the electronic specific heat of free electrons, $C_{el} = -\frac{\pi^2}{3}k_B^2 T N_0(\epsilon_F) = \gamma T$. In this regime, as pointed by Ziman [Ziman, 1972], TEP probes the specific heat per electron (fundamentally reflecting entropy considerations). In other words (and assuming $\zeta = 0$): $S = C_{el}/ne$, where the units are V/K for TEP, J/Km^{-3} for C_{el}, and m^{-3} for n. However, in order to compare different compounds, it is useful to express $\gamma = C_{el}/T$ in J/mol·K^2 units.

In order to focus on the S/C_{el} ratio, a dimensionless quantity can be defined,

$$q = \frac{S}{T} \frac{N_A e}{\gamma} \tag{3.30}$$

where the constant $N_A e = 9.6 \times 10^5$ C/mol is called the Faraday number. For a free electron gas with $\zeta = 0$ (the simplest case), q is equal to -1. In the case of an energy independent mean free path, implying $\zeta = -1/2$, q becomes equal to -2/3. If the free electrons are replaced by free holes (that is assuming a spherical Fermi surface in both cases) then q becomes equal to +1 or +2/3.

In HF compounds, the effective mass, m^*, of quasi-particles is enhanced mainly due to Kondo effects. A characteristic temperature scale, $T_K \propto 1/m^*$, appears which defines a Fermi energy $\epsilon_F = k_B T_K$ much smaller than in ordinary metals (replacing the Fermi energy in Eq. 3.28). Thus, highly enhanced value of the linear coefficient of TEP, α, is expected. The magnitude of $S(T)/T$ in the zero-temperature limit and its eventual correlation with γ in HF compound has been shown in Refs. [Newns, 1987; Houghton, 1987]. At $T = 0$, with the expression for the impurity density of states at the Fermi level (f-electron $\rho_f(0)$) and the localized f-electron number n_f, $S(T)$ follows [Hewson, 1993]

$$S(T) = \frac{2\pi^3 k_B^2 T}{3eN} \cot\left(\frac{\pi n_f}{N}\right) N \rho_f(0) \left(1 - \frac{\partial \Sigma}{\partial \epsilon}\right)_{\epsilon=0} + O(T^3) \tag{3.31}$$

Thus, for the N-fold degenerate Anderson model, ignoring higher order terms,

$$\lim_{T \to 0} \left[\frac{S(T)}{\gamma T}\right] = \frac{2\pi}{eN} \cot(\frac{\pi n_f}{N}) \tag{3.32}$$

The values of γ and $n_f(T = 0)$ can be calculated from the Bethe ansatz results. This equation is the same as Eq. 3.30, with a factor difference of $N/2\pi \cot(\frac{\pi n_f}{N})$. In the N-fold degenerate models for Ce and Yb impurities the sign of the TEP coefficients differ: for Ce impurities, the Kondo resonance lies above the Fermi level and is only fractionally occupied, $n_f(0)/N$, for $0 < n_f(0) < 1$ and $N = 6$ (without CEF splittings), so the density of states at the Fermi level is steeply rising and the coefficient is positive; for Yb, which is the particle-hole image of the Ce case, the Kondo resonance lies below the Fermi level with a fraction of n_f/N holes above, where $0 < n_f^h < 1$ and $N = 8$, so the coefficient is then negative.

At low temperatures the TEP measurements have been limited due to experimental difficulties. In general, the TEP ($S = -\Delta V/\Delta T$) signal is extremely small, much less than sub-μV for given ΔT at low temperatures, and difficult to experimentally detect. For HF compounds, however there is a possibility to probe the TEP signal at low temperatures due to the enhanced TEP value. For instance, as shown in Fig. 3.8, $|S(T)/T| \sim 10\,\mu\text{V/K}^2$ for HF compounds can be measured; at $T = 1\,\text{K}$, experimentally the TEP voltage $\Delta V = 0.5\ \mu\text{V/K}$ can be easily measured with $\Delta T = 0.05\,\text{K}$ (5% of given temperature). Even in HF compounds, because $S \rightarrow 0$ when $T \rightarrow 0$, it is extremely difficult to measure TEP in dilution temperature region ($\sim 20\,\text{mK}$). Therefore, the zero temperature limit of $S(T)/T$ may need to be extrapolated from higher temperature measurements. In the following chapter we will test the FL relation between γ vs. $S(T)/T|_{T\rightarrow 0}$ with $\text{YbT}_2\text{Zn}_{20}$ (T = Fe, Ru, Os, Ir, Rh, and Co) HF system [Torikachvili, 2007], since this relation has been relatively less investigated, as far as we know, compared to K-W and Wilson ratio.

3.4 Quantum criticality

In this section we will introduce both existing experimental evidence and theoretical concepts for quantum phase transitions, with particular emphasis on the antiferromagnetic (AFM) quantum critical point (QCP). The first part of this section deals with the concept of quantum phase transition. Next the critical exponents and scaling properties applicable to quantum phase transition are presented and the experimental observation of AFM QCP is introduced for HF compounds. Then the current theoretical models for quantum phase transition are summarized; the Hertz-Moriya-Milllis theory, known as the spin density wave (SDW) scenario and the breakdown of quasi-particle at the quantum critical point, known as the Kondo breakdown scenario, including local quantum criticality. Finally, a new perspective of quantum criticality, global phase diagram particularly applied to the field tuned AFM QCP materials, will be briefly reviewed with regards to YbRh_2Si_2 and YbAgGe. A more detailed introduction to the material YbAgGe and experimental results on it will be presented in Chapter 5.

3.4.1 Quantum phase transition

Phase transitions are classified into discontinuous (first order) and continuous (second order) transitions. At a first order phase transition, the two phases coexist at the transition temperature, good examples are ice and water at 0°C or water and steam at 100°C. In contrast, at a continuous phase transition, the two phases do not coexist. An important example is the ferromagnetic transition of iron at 770°C, above which the magnetic moment vanishes. The transition point of a continuous phase transition is also called the critical point. A continuous phase transition can be characterized by an order parameter; this is a thermodynamic quantity that is zero in one (disordered) phase and nonzero in the other (ordered) phase. Very often the choice of an order parameter for a particular phase transition is obvious as, e.g. for the ferromagnetic transition, where the total magnetization is an order parameter. However, in some cases finding an appropriate order parameter is not trivial.

In order to introduce the concept of quantum phase transition and describe the consequence of this, we will use the concept introduced by Sachdev [Sachdev, 1999] and follow his approach. The following quoted sentence [Sachdev, 1999] describes the central concept of quantum phase transition, which we will use.

> "Consider a Hamiltonian, $\mathsf{H}(g)$, whose degrees of freedom reside on the sites of a lattice, and which varies as a function of a dimensionless coupling g. Let us follow the evolution of the ground state energy of $\mathsf{H}(g)$ as a function of g. ... We shall identify *any point of nonanalyticity in the ground state energy of the infinite lattice system as a quantum phase transition*: The nonanalyticity could be either the limiting case of an avoided level-crossing or an actual level-crossing. ... Actually our focus shall be on a limited class of quantum phase transitions-those that are *second order*. *Loosely speaking, these are transitions at which the characteristic energy scale of fluctuations above the ground state vanishes as* g *approaches* g_c. ... It is important to notice that the discussion above refers to singularities in the ground state of the system. So *strictly speaking, quantum phase transitions occurs only at zero temperature,* $T = 0$. ... Because all experiments are necessarily

at some nonzero, though possibly very small, temperature, a central task of the theory of quantum phase transitions is to describe the consequences of this $T = 0$ singularity on physical properties at $T > 0$. It turns out that *working outward from the quantum critical point at* g $=$ g$_c$ *and* $T = 0$ *is a powerful way of understanding and describing the thermodynamic and dynamical properties of numerous systems over a broad range of values of* |g - g$_c$| *and* T."

Phase transitions at $T = 0$ are dominated by quantum effects, in contrast to classical phase transitions at $T > 0$, even though both may occur in the same physical system. Figure 3.9 (a) and (b) illustrates two possibilities for the $T > 0$ phase diagram of a system near a quantum critical point. In the first case, order only exists at $T = 0$ and all $T > 0$ properties are analytic as a function of g near g $=$ g$_c$. In this case there will be no true phase transition in any real experiment carried out at finite temperature.

In the second case, there is a line of second order phase transitions for $T > 0$ that terminates at the $T = 0$ quantum critical point at g $=$ g$_c$, shown in Fig. 3.9 (b), in which some key distinctions between classical and quantum criticality are illustrated. The vicinity of the phase transition line, $\hbar\omega \ll k_B T$, can be described by the theory of second order phase transitions in classical systems. The phase transition can be tuned by varying the values of |g - g$_c$| and T, and therefore the QCP can be determined as the endpoint of a line of finite temperature transitions at g $=$ g$_c$ and $T = 0$. Thus, complementary information about the quantum phase transition can be obtained from the $T > 0$ phase transition in terms of a purely classical model. In a classical systems the phase transitions are driven by thermal fluctuations which have no fluctuation at $T = 0$. In contrast, quantum systems have fluctuations driven by the Heisenberg uncertainty principle even in the ground state, and these fluctuation can drive interesting phase transitions at $T = 0$. In the quantum disordered regime the physics is dominated by quantum fluctuations. In the quantum critical region, both thermal and quantum fluctuations are important, where unusual power laws and nFL behavior are observed at finite temperatures. The boundaries of quantum critical region are determined by the condition $k_B T > \hbar\omega \propto$ |g - g$_c$|$^{z\nu}$ [Sachdev, 1999], where both z and ν are critical exponent. In most of the experimental
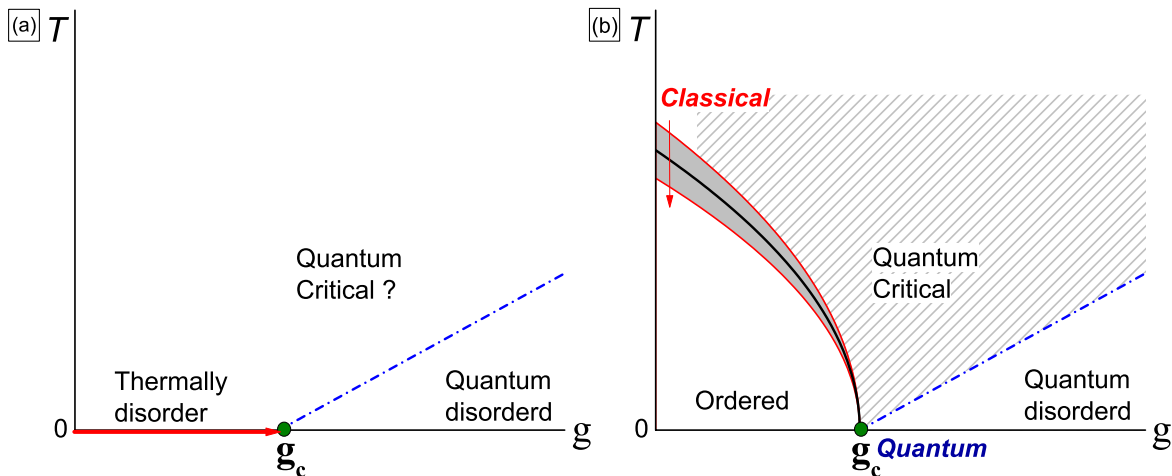
Figure 3.9   Schematic phase diagram for two possibilities for the $T > 0$ phase diagram near a quantum phase transition. The horizontal axis represents the control parameter (g) used to tune through the quantum phase transition, and the vertical axis is the temperature (T). (a) Order is only present at $T = 0$. The shaded area indicate the boundaries of the quantum critical region; the boundaries (crossover line) are given by $k_B T \propto |g \text{ - } g_c|^{z\nu}$. (b) Order can also exist at finite temperature, which are second order phase transitions terminating at the quantum critical point. The solid line marks the finite temperature boundary between the ordered and disordered phases. Close to this line the critical behavior is classical. The ordered state can be suppressed to $T = 0$ (g_c) by nonthermal control parameters (g) such as pressure, doping, and magnetic field.

examples shown a QCP the phase diagram is similar to the second (Fig. 3.9 (b)), where the phase diagram has been constructed for various ordered state such as antiferromagnetic and superconducting. A QCP can be generally approached in two different ways as either g → g_c for T near 0 or $T \to 0$ near g = g_c.

From now on we will use a limited criterion for a AFM QCP as following: A continuous phase transition should be present at finite temperature and this transition should be suppressed to $T = 0$ by using nonthermal control parameters. At a certain point, close to g_c, a signature of strong quantum fluctuation, such as nFL behavior, should be observed. Lastly the QCP can also be decided by extrapolating the finite temperature behavior to $T = 0$, for

Table 3.1   Commonly used critical exponents for magnets, where the order parameter is the magnetization, m, and the conjugate field is a magnetic field, H. $t = |T - T_c|/T$ denotes the distance from the critical point and d is the space dimensionality [Cowan, 2005].

	Exponent	Definition	Conditions
Specific heat	α	$C \propto |t|^{-\alpha}$	$t \to 0$, $H = 0$
Order parameter	β	$m \propto (-t)^{\beta}$	$t \to 0$ from below $H = 0$
Susceptibility	γ	$\chi \propto |t|^{-\gamma}$	$t \to 0$, $H = 0$
Critical isotherm	δ	$H \propto |m|^{\delta}$	$t = 0$, $H \to 0$
Correlation length	ν	$\xi \propto |t|^{-\nu}$	$t \to 0$, $H = 0$
Correlation function	η	$g(r) \propto |r|^{-d+2-\eta}$	$t = 0$, $H = 0$
Dynamic	z	$\tau_c \propto \xi^z$	$t \to 0$, $H = 0$

instance, using scaling behavior with critical exponent.

3.4.2   Critical exponent and scaling invariant

One of the most remarkable features of continuous (classical) phase transitions is universality [Cowan, 2005]; the critical exponents are the same for entire classes of phase transitions that may occur in very different physical systems. These universality classes are determined only by the symmetries of the order parameter and by the space dimensionality of the system. The mechanism behind the universality is the divergence of the correlation length. If the critical point is approached, the spatial correlations of the order parameter fluctuations become long-ranged. Close to the critical point the correlation length, ξ, diverges as $\xi \propto |t|^{-\nu}$ where ν is the critical exponent and t is a dimensionless measure of the distance from the critical point, if the transition occurs at a non-zero temperature, T_c, it can be defined as $t = |T - T_c|/T_c$. In addition to the long-range correlations in space there are analogous long-range correlations of the order parameter fluctuations in time. The typical time scale for the decay of such fluctuations is the correlation (or equilibration) time, τ_c. As the critical point is approached the correlation time diverges as $\tau_c \propto \xi \propto |t|^{-\nu z}$, where z is the dynamical critical exponent. At the phase transition point, the correlation length and time are infinite, fluctuations occur on all length and time scales, and the system is said to be scale invariant. As a consequence, all observables have power law dependencies on the external parameters. The set of corresponding

exponents, so called critical exponents, completely characterizes the critical behavior near a particular phase transition.

For example, the order parameter of a classical ferromagnet is the magnetization $\mathbf{m}(\overrightarrow{\mathbf{r}})$. The external parameters are the reduced temperature, $t = |T - T_c|/T_c$, and the external magnetic field, $\mathbf{H}$, conjugate to the order parameter. Close to the critical point the correlation length is the only relevant length scale and therefore, the physical properties can be described by the homogeneity relation for the singular part of the free energy density, $f(t, H) = b^{-d} f(t b^{1/\nu}, H b^{y_B})$. Here d represents the dimensionality and y_B is another critical exponent, which is related to δ by $y_B = d\delta/(1 + \delta)$ [Vojta, 2003]. The scale factor, b, is an arbitrary positive number. A corresponding thermodynamic quantities can be obtained by differentiating $f(t, H)$.

In addition to the critical exponents ν, y_B, and z, there are a number of other exponents [Vojta, 2003]: α, β, γ, and δ. These exponents describe the singularities in the heat capacity, order parameter, susceptibility, and equation of state, respectively, in terms of the reduced temperature t. The definitions of the most commonly used critical exponents are summarized in Table 3.1, where it should be noted that the exponents are not independent each other. The four thermodynamic exponents, α, β, γ, and δ, can all be obtained from the free energy, which contains only two independent exponents. They are connected by scaling relations: $2 - \alpha = 2\beta + \gamma$ and $2 - \beta = \beta(\delta + 1)$. Similarly, the exponents for the correlation length and correlation function are connected by two hyperscaling relations; $2 - \alpha = d\nu$ and $\gamma = (2 - \eta)\nu$.

In general for a quantum phase transition, the energy scale E, eigenvalue of Hamiltonian $\mathsf{H}(g)$, defined at $T = 0$ for $g \neq g_c$ vanishes as $\mathsf{E} \sim J|g - g_c|^{z\nu}$ as g approaches g_c [Sachdev, 1999]. Here J is the energy scale of a characteristic microscopic coupling. In addition to a vanishing energy scale, second order, quantum phase transitions have a diverging characteristic length scale ξ; $1/\xi \sim \Lambda|g - g_c|^{\nu}$ where Λ is an inverse length scale of order the inverse lattice spacing. Thus the characteristic energy scale, taking the ratio of exponents, vanishes as the z-th power of the characteristic inverse length scale $\mathsf{E} \sim \xi^{-z}$.

In the vicinity of a QCP, various physical properties show singularities which can be char-

acterized by critical exponents [Ma, 1976]. Critical exponents, having no dependence of the detailed microscopic nature of the system, are, by the dimensionality of the system and the degrees of freedom, associated with the long-range correlations in the ordered phase. At the QCP ξ and τ_c scales diverge like $\xi \sim g^{-\nu}$ and $\tau_c \sim g^{-\nu z}$ for $g \to 0$. Thus the scaling form can be written in terms of r, where r measures the distance to the critical point;

$$r = \frac{\delta_0 - \delta_c}{\delta_c}. \tag{3.33}$$

The parameter δ_0 depends on temperature and tunes the system through the phase transition. If the system is tuned by varying pressure, magnetic field, or chemical substitution, then $r = (P - P_c)/P_c$, $(H - H_c)/H_c$, or $(x - x_c)/x_c$, here P_c, H_c, and x_c are their critical values. By approaching g_c at $T = 0$ a universal divergence in the low temperature limit has been observed in many systems, especially for HF metals. For example, the AFM transition at finite temperature can be suppressed to $T = 0$ by magnetic field. The phase boundary of the ordered phase, tuned through the QCP, follows $T_N \propto (-r)^\psi$, $\psi = z/(d + z - 2)$. Hence, the phase line is expected to be $T_N \propto (-\frac{H - H_c}{H_c})^{2/3}$ for $d = 3$ and $z = 2$ [Stewart, 2001].

3.4.3 Experimental observation

As a general consideration, a quantum phase transition is most easily probed by changing not the temperature, but some other parameter in the Hamiltonian of the system. This parameter might be the charging energy in Josephson-junction arrays (which controls their superconductor-insulator transition) [Chaikin, 1995; Sondhi, 1997], doping in the parent compound of a high T_c superconductor (which destroys the AFM spin order) [Dagotto, 1994; Maple, 1998; Orenstein, 2000; Sachdev, 2000], the magnetic field in a quantum-Hall sample (which controls the transition between quantized Hall plateaus) [Das Sarma, 1996], or the transverse magnetic field in rare-earth magnetic insulators (which controls Ising spin variables) [Bitko, 1996], as well as pressure, doping, and magnetic field in HF materials and transition metal alloys (which controls the ground state between ordered and disordered states) [Stewart, 2001; Löhneysen, 2007].
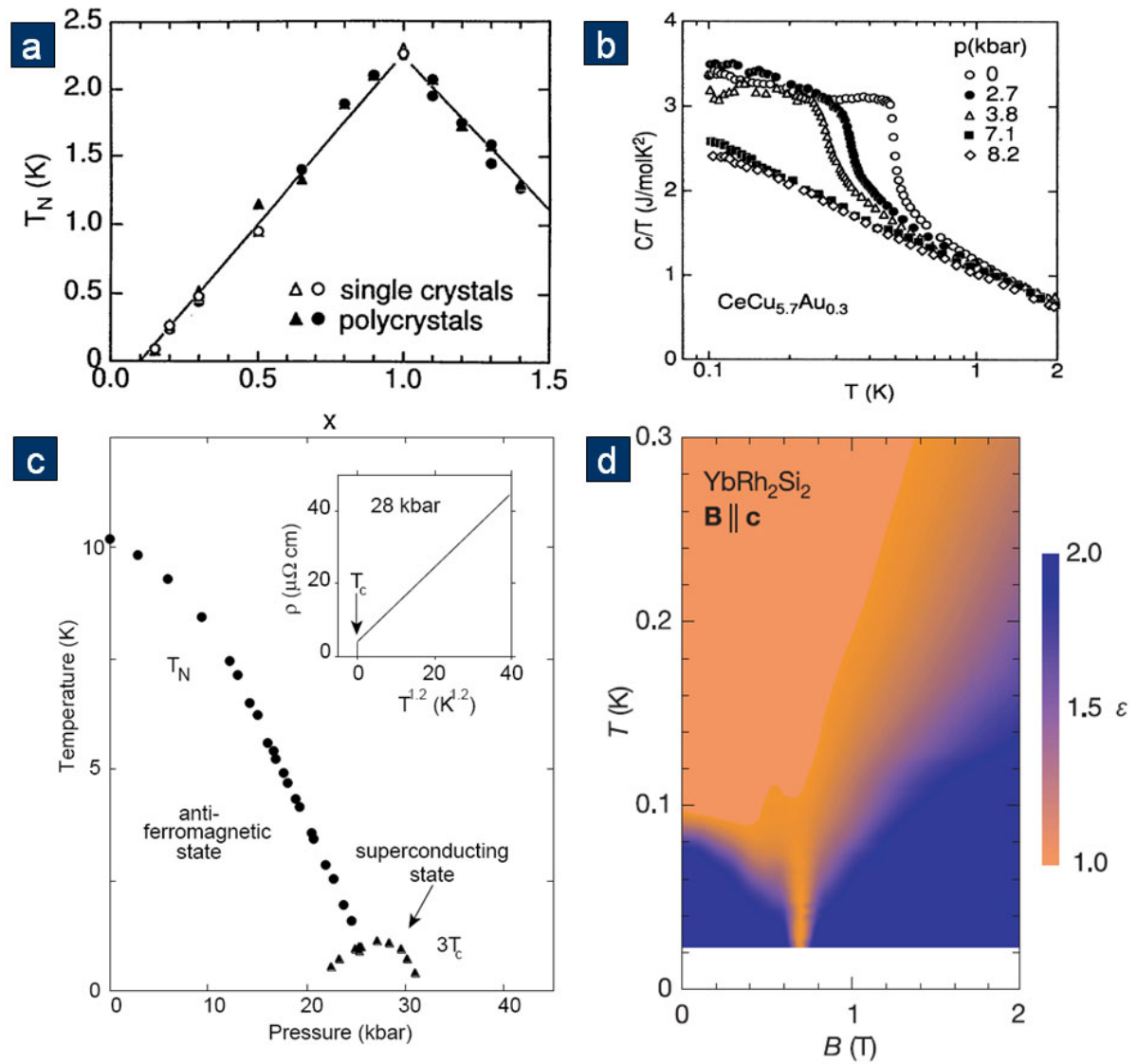
Figure 3.10   Quantum critical points in HF metals. (a) Doping dependence of the phase diagram of $CeCu_{6-x}Au_x$ system [Pietrus, 1995]. (b) $C(T)/T$ vs. $\log(T)$ of the AFM $CeCu_{5.7}Au_{0.3}$ as a function of pressure [Bogenberger, 1995]. The $C(T)/T$ data for 7.1 kbar and 8.2 kbar show more than a decade in temperature agreement with -$\log(T)$ in the vicinity of the QCP. (c) Temperature vs. pressure phase diagram for $CePd_2Si_2$ [Mathur, 1998]. Superconductivity appears below T_c in a narrow window where the T_N tends to $T = 0$. Inset shows the normal state resistivity above T_c varies as $T^{1.2}$ over wide range of temperature. (d) $YbRh_2Si_2$ tuned by magnetic field [Custers, 2003]. The evolution of the exponent ε in $\Delta\rho = AT^\varepsilon$ is shown by blue ($\varepsilon = 2$) and orange ($\varepsilon = 1$) regions.

Whereas quantum criticality is currently being investigated in a number of strongly correlated system, among these systems it has been most systematically studied in AFM HF metals which have several specific merits. Since a large effective mass is a characteristics of HF systems, the relevant energy scales are small; a low energy scale give rise to relatively easy tuning of the ground state by external parameters. When the external, nonthermal control parameter is varied, its affects can be understood, qualitatively, by considering how it changes the relevant energy scales; Kondo and RKKY interaction, within Doniach diagram picture. Explicit observation of AFM QCPs has been achieved in a number of HF metals, including $CeCu_{6-x}Au_x$ [Pietrus, 1995] tuned by chemical substitution, $CePd_2Si_2$ [Julian, 1998; Mathur, 1998] tuned by pressure, and $YbRh_2Si_2$ [Trovarelli, 2000; Gegenwart, 2002] and $YbAgGe$ [Bud'ko, 2004] tuned by magnetic field. Most of these systems have allowed systematic studies of quantum critical behavior through transport and thermodynamic measurements. A comprehensive review of quantum criticality, including nFL behavior, in a large variety of HF systems up through the year 2000 has been given by Stewart [Stewart, 2001].

One of the most intensively studied materials among AFM QCP systems is the $CeCu_{6-x}Au_x$ system. $CeCu_6$ has been established as a HF system showing no long range magnetic order down to $20\,mK$ [Amato, 1987; Onuki, 1987]. By doping in Au atoms [Pietrus, 1995], where Au occupies the $Cu(2)$ position in the $CeCu_6$ structure, AFM order in $CeCu_{6-x}Au_x$ is induced beyond a critical concentration $x_c \sim 0.1$ as shown in Fig. 3.10 (a). The Néel temperature, T_N, for $0.1 \leq x \leq 1$ varies linearly with x. For $x < x_c$, the electrical resistivity, $\rho(T)$, increases at low temperature as $\rho(T) = \rho_0 + AT^2$ which is expected for a FL for $T \to 0$ [Löhneysen, 1998]. For $x_c = 0.1$ a linear temperature dependence of $\rho(T)$ is observed between $20\,mK$ and $0.6\,K$, signaling nFL behavior. A pronounced nFL behavior in specific heat measurements, $C(T)/T = a\ln(T_0/T)$, was also observed between 0.06 and $\sim 2.5\,K$ for $x_c = 0.1$ [Lohneysen, 1996; Löhneysen, 1998]. Pronounced nFL behavior has also been observed with Ag doping [Heuser, 1998; Scheidt, 1999]. As an alternate route to induce nFL behavior, using pressures up to $9\,kbar$ to suppress AFM order in $CeCu_{5.7}Au_{0.3}$ has also been investigated. As shown in Fig. 3.10 (b), the $C(T)/T$ data indicate a $-\log(T)$ dependence in the vicinity of the

critical pressure.

At ambient pressure, $CePd_2Si_2$ manifests the AFM order below $10\,K$ with a relatively small ordered moment of $\sim 0.7\,\mu_B$ [Grier, 1984]. This AFM order can be suppressed to $T \to 0$ by increasing pressure, and superconductivity in a very narrow window is induced in the $T - P$ region close to the inferred critical pressure (Fig. 3.10 (c)) leading the authors to infer that the superconductivity is magnetically mediated [Julian, 1998; Mathur, 1998]. The resistivity does not exhibit the standard T^2-dependence expected of a FL, where the detailed power law analysis showed that near P_c the resistivity varies as $T^{1.2}$ over wide range of temperature (inset, Fig. 3.10 (c)).

In $YbRh_2Si_2$, presumed AFM ordering is continuously suppressed by an external magnetic field, leading to a field tuned AFM QCP [Trovarelli, 2000; Gegenwart, 2002] as shown in Fig. 3.10 (d) [Custers, 2003]. By increasing the magnetic field the AFM ordering temperature is suppressed to $T \to 0$, and FL behavior is recovered away from the QCP. Quantum criticality is also indicated by a linear temperature dependence of the electrical resistivity and a logarithmic temperature dependence of $C(T)/T$ in specific heat, i.e. nFL behavior close to H_c. A further study of the quantum criticality has also been accomplished with Ge-, Ir-, and Co-doped samples [Custers, 2003; Friedemann, 2009], tuning each of these related systems by magnetic field.

Quantum phase transition experiments have been accompanied by extensive theoretical studies, which will be introduced in the following section, focused specifically on AFM QCP. From an experimental perspective, measurements can never be extended down to zero temperature, thus QCPs are inferred from finite temperature results, but carried out down to sufficiently low temperatures. A few of the experimental strategies use to find AFM QCP from thermodynamic and transport measurements are:

- $T_N \to 0$ at $g = g_c$: By varying a control parameter the AFM transition should be suppressed to $T = 0$.

- nFL behavior: At the QCP a pronounced nFL behavior is one of signatures of quantum fluctuations, i.e. behavior that deviates from the FL behavior, e.g., from a constant

specific heat coefficient and a T^2-dependence of the resistivity at low temperatures.

- scaling behaivor: Scaling analysis is one of tools used to find a QCP. Since the order parameter correlation length diverges near the quantum phase transition as $\xi \sim |r|^{-\nu}$, by tracking the finite temperature behavior toward $T \to 0$, the QCP can be found. For example, the AFM transition temperature can be tracked by $T_N \sim (-r)^\psi$ and the coefficient A of the T^2 resistivity diverges as $A \sim 1/(\text{g - g}_c)^\alpha$, approaching QCP from paramagentic phase, where the exponent $\alpha \approx 1$ has been observed for many system.

- tracking T_K: Based on recent theoretical work, a mechanism for quantum criticality can be identified by tracking the characteristic energy scale of Kondo temperature at finite temperature (see below). In this approach, however, it still remains a difficulty to identify the Kondo temperature due to its crossover nature (T_K does not define a phase transition).

3.5 Theoretical models

We begin with briefly by reviewing the basic concepts of small moment ordering, which belong to both intinerant magnetism and spin density wave models of field-induced QCP, that are necessary for the later discussion. Following this, the two theoretical models, being currently used to explain AFM QCP will be reviewed: the spin density wave, and the Kondo breakdown, scenarios.

3.5.1 Spin Density Wave instabilities

A spin density wave (SDW) is an AFM ground state of metals for which the density of the conduction electron spins is spatially modulated [Gruner, 1994a]. The development of a SDW breaks translation symmetry, violating the translational invariance in solid, due to the consequence of electron-electron interactions. The ground state is characterized by a periodic modulation of the spin density, the period $\lambda = \pi/\mathbf{k}_F$ being related to a wave vector, $\mathbf{k}_F$, that nests parts (or all) of the Fermi surface. The AFM order can be represented schematically as

$\Delta S(\mathbf{r}) = \Delta S_0 \cos(2\pi/\mathbf{q}\cdot\mathbf{r}+\phi)$, where $\Delta S(\mathbf{r})$ denotes the spatially dependent spin modulation, which occurs along the direction $\mathbf{r}$. The wavelength λ of SDW is determined by the Fermi surface of the conduction electrons and in general is not a multiple of the lattice period a and instead is incommensurate. In fact, the ratio λ/a can change with temperature, external pressure, doping, and other parameters.
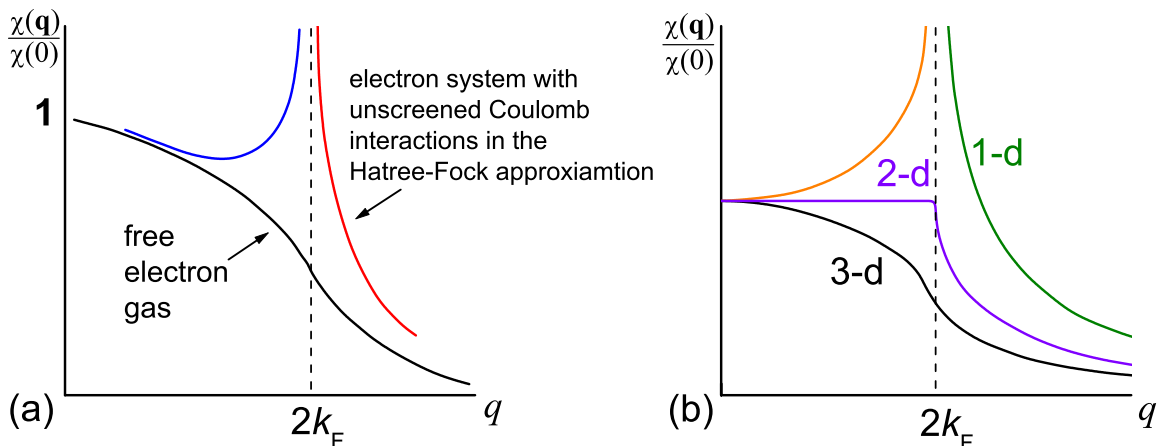
Figure 3.11   (a) Effect of electron-electron interactions on the susceptibility. (b) Effect of dimensionality on the free electron generalized electronic susceptibility.

It has been shown that in the Hatree-Fock approximation that the susceptibility, $\chi(\mathbf{q})$ for $\mathbf{q} \neq 0$, diverges as $q \to 2k_F$ [Overhauser, 1962], as shown in Fig. 3.11 (a). The effects of screening and electron correlations, however, tend to suppress this divergence [White, 1983]. Consequently, a spin density wave can form only under special conditions, which can be understood in a simply way by considering the behavior of the noninteracting electronic susceptibility $\chi_0(q)$ in one, two, and three dimensions as shown in Fig. 3.11 (b). Lower dimensional systems are more likely to become unstable with respective to SDW formation. The reason for this is related to the nesting of the corresponding states. In one and two dimensions Fermi surfaces are geometrically simpler and a single wave vector can nest more (or all) of the Fermi surface.

SDW are observed in metals and alloys; the canonical example is chromium and its alloys, where the AFM ordering is directly related to the band structure of chromium [Fawcett, 1994].

SDWs also occur as ground state in strongly anisotropic systems, for example, the psudo-one dimensional organic conductors [Gruner, 1994]. In analogy to the magnetic order of antiferro-magnets below Néel temperature, the electron gas becomes unstable for temperatures below an ordering temperature, T_{SDW}, and enters a collectively ordered ground state of an itinerant antiferromagnet. The reason of the instability of the electron gas at the transition to the SDW ground state is the so-called nesting of the Fermi surface.

Nesting of the Fermi surface is essential to SDW formation. Nesting describes the required property of the reciprocal space that allows parts of the Fermi surface with electron or hole character to map on top of each other by a single translation with the wavevector k_F. This allows a gap to open at the Fermi surfaces involved with the nesting. The most obvious case is for pseudo-one dimension, where the Fermi surface consists of two points at k_F [Gruner, 1994]. In two or three dimensions a complete nesting by just a single k_F-vector is no longer as likely, but different parts of the Fermi surface can be mapped by different k_F-vectors in a more or less perfect way.

The spin density wave state, in a sense of Fermi-surface-related instability, has many similarities to other broken symmetry ground states of metals, such as superconductivity and the charge density wave (CDW) [Gruner, 1994a]. Within the framework of a mean field description, the ground states develop below a second order phase transition temperature with many of the same thermodynamic signatures as that of the BCS superconducting ground state within the framework of weak coupling theories. A gap develops in the single particle excitation spectrum, with the zero temperature gap related (again within the framework of weak coupling theory) to the transition temperature through the same relation $2\Delta = 3.5k_BT_c$. In all case, furthermore, the ground state is that of the coherent superposition of pairs; pairs of electrons for the superconducting state, pairs of electrons and holes with parallel spins for the CDW state; and pairs of electrons and holes with opposite spins for the SDW ground state. Consequently, the CDW ground state is nonmagnetic, while the SDW ground state has a well defined long range magnetic order with magnons being the collective excitations of the ground state. The small effective mass for SDW, expected to be the same as the band mass, may lead

to quantum effects [Gruner, 1994a]. The ground state of SDW has a well defined magnetic character. Consequently, transport and magnetic measurements, together with local probes have been used to evaluate the essential characteristics of the ground state.

3.5.2 Spin Density Wave scenario of field-induced QCP

A large class of HF materials, which have localized magnetic moments coupled to a separate set of conduction electrons, has been successfully explained in a framework of Doniach's model [Doniach, 1977; Continentino, 1989]. When the intersite exchange interaction dominates ($T_K < T_{RKKY}$), magnetic order typically occurs; the moments do not participate in the Fermi surface of the metal, and thus the saturation moment in the ordered state is large and comparable to the atomic moment. When the onsite Kondo effect is larger ($T_K \gtrsim T_{RKKY}$), the low temperature physics can be well described by FL theory with renormalized quasi-particle masses [Hewson, 1993]; in this case the saturation moment in the ordered state is usually very small in HF systems. Often the magnetism inferred from experiments is very weak, where the ordered moment per site is much smaller than the microscopic local moment that actually occupies each site; for example, small ordered moments, much less than $1\,\mu_B$ have been observed in Ce-based HF compounds, where the microscopic local moment is expected to be $2.14\mu_B$ per Ce site [Kittel, 1996]. Therefore, the ordered magnetism can be considered as the consequence of a spin density wave that develops out of the parent heavy FL state, where such a small ordered moment is expected in a SDW state. This is the reason why these apparently the local moment systems as can be treated spin density wave states. Within this phenomenological concept, several attempts to explain a strong quantum fluctuation in AFM QCP have been developed, known as the spin density wave scenario (or Hertz-Moriya-Millis theory [Hertz, 1976; Millis, 1993; Moriya, 1995]).

The SDW scenario is based on the assumption that, in a HF system, below an energy scale of T_K, the low energy excitations are heavy quasi-particles and their collective excitations [Hertz, 1976; Millis, 1993; Moriya, 1973]. The traditional approach to an itinerant AFM QCP describes its universal properties in terms of a Ginzburg-Landau-Wilson (GLW)

Table 3.2   Temperature dependences from the spin fluctuation theories of nFL behavior of Hertz-Millis [Hertz, 1976; Millis, 1993]and Moriya *et al* [Moriya, 1995]., for the specific heat, susceptibility, and resistivity in the low temperature limit. The dependences of the magnetic ordering temperature T_N (AFM) and T_c (FM) and two crossover lines (T_I and T_{II}) on the critical parameter g_c from the Hertz-Millis theory.

| | Hertz/Millis | | | |
| | AFM | AFM | FM | FM |
	$z=2, d=3$	$z=2, d=2$	$z=3, d=3$	$z=3, d=2$
C/T	$\gamma - a\sqrt{T}$	$c\log(T_0/T)$	$c\log(T_0/T)$	$T^{-1/3}$
$\Delta\chi$	$T^{3/2}$	$\chi_0 - dT$		
$\Delta\rho$	$T^{3/2}$	T	T	
$T_{N/C}$	$(g_c - g)^{2/3}$	$(g_c - g)$	$(g_c - g)^{4/3}$	$(g_c - g)$
T_I	$(g - g_c)$	$(g - g_c)$	$(g - g_c)^{3/2}$	$(g - g_c)^{3/2}$
T_{II}	$(g - g_c)^{2/3}$	$(g - g_c)$	$(g - g_c)^{3/4}$	$(g - g_c)$
	Moriya			
	AFM	AFM	FM	FM
	$d=3$	$d=2$	$d=3$	$d=2$
C/T	$\gamma_0 - a\sqrt{T}$	$-\log(T)$	$-\log(T)$	$T^{-1/3}$
χ_q	$T^{-3/2}$	$-\log(T)/T$	$T^{-4/3}$	$-T^{-1}/\log(T)$
$\Delta\rho$	$T^{3/2}$	T	$T^{5/3}$	$T^{4/3}$

functional of the order parameter and its fluctuations, ϕ^4 theory, in $d_c^+ = d + z$ dimensions [Hertz, 1976; Millis, 1993], where d is the spatial dimension (typically 3 or 2) and $z = 2$ corresponds to the dynamical exponent. The results of this model (Hertz and Millis) depend on the dimension d, the critical exponent z, the reduced temperature t, and a control parameter g, which is related to a Hamiltonian parameter such as pressure, doping, or magnetic field [Hertz, 1976; Millis, 1993]. The nFL behavior for antiferromagnets and ferromagnets in this framework are summarized in Table 3.2 [Stewart, 2001]. A self consistent renormalization study of the spin fluctuations near magnetic phase transitions [Moriya, 1995] gives several theoretical predictions about the nFL behavior. Application of this model to HF systems leads, in only a few cases, to a satisfactory description of the low temperature properties (e.g. $Ce_{1-x}La_xRu_2Si_2$ [Kambe, 1996]). Likewise, in $CeCu_2Si_2$, transport and thermodynamic measurements [Gegenwart, 1998] have indicated that its field tuned QCP belongs

to this SDW category, but mainly itinerant d-electron systems are explainable within this model [Yeh, 2002; Norman, 2003; Fawcett, 1970; Moriya, 1985; Pfleiderer, 2001].
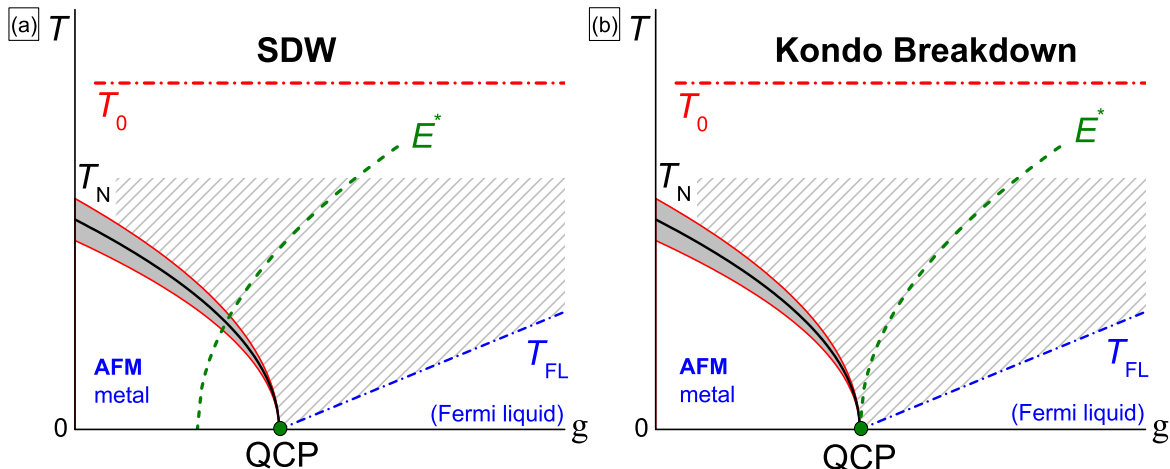
Figure 3.12   Schematic phase diagram showing two classes of quantum critical points, illustrating quantum criticality of (a) the spin density wave (SDW) scenario and (b) Kondo breakdown scenario [Gegenwart, 2008]. T_N represents the AFM ordering temperature and T_{FL} indicates the onset of the low temperature Fermi liquid regime. T_0 represents the characteristic energy scale, signifying the initial crossover from the high temperature local moment behavior to the beginning of the low temperature Kondo screening in a Kondo lattice system. The E^* marks an energy scale separating between small (left side of E^*) and large Fermi surface (right side of E^*). The horizontal axis represents the control parameter (g) used to tune through the quantum phase transition, and the vertical axis is the temperature (T). In heavy fermion metals the antiferromagnetic (AFM) transition can be suppressed to $T = 0$ (g_c) by non-thermal control parameters (g) such as pressure, doping, and magnetic field. For g > g_c a Fermi liquid behavior is recovered.

A crucial aspect of the SDW scenario is that the paramagnetic energy scale T_K remains finite at the QCP [Gegenwart, 2008], implying that the heavy quasi-particles survive near the QCP. Therefore, for such a transition one does not expected the Kondo temperature to change significantly while the system is tuned through the QCP by varying control parameter. The schematic phase diagram of this scenario is shown in Fig. 3.12 (a), where the characteristic

energy scale T_0 represents the Kondo temperature [Gegenwart, 2008]. In view of the current experimental tools, the issue of defining the Kondo temperature is not trivial, partly due to the crossover character of Kondo temperature, and partly because standard quantities such as resistivity and specific heat do not measure Kondo temperature directly. For example, the Kondo temperature can be inferred from the coherence temperature, where resistivity shows a significant drop followed by a logarithmic temperature dependence as temperature decrease. Also the magnetic specific heat shows a broad local maximum which roughly reflects the Kondo temperature. However, when CEF effects are significant, $T_K \geq \Delta_{CEF}/k_B$, there are difficulties in extracting Kondo temperature because of broadening of these features.

For a long time the SDW scenario has been applied to experimental results. However, in three dimensions this class of theories fails to explain the simultaneous linear temperature dependence of the resistivity and the -log(T) dependence of the specific heat coefficient observed in experiments as well as the divergent Grüneisen ratio[Kim, 2008] and Fermi surface reconstruction, changing from small to large Fermi surface across the QCP, inferred by Hall effect measurements [Paschen, 2004]. Although, in a multiband system, there also needs to be careful interpretation of Hall effect measurements, since the Hall coefficient depends on the carrier density and mobility as the weighted sum over each band's contribution [Ziman, 1960].

3.5.3   Breakdown of Kondo effect

In contrast to the SDW scenario of quantum criticality, the Kondo temperature in the "Kondo-breakdown" scenario of quantum criticality vanishes at the QCP and the quantum critical behavior is dominated by local magnetic fluctuations [Schröder, 1998; Schröder, 2000]. The $CeCu_{6-x}Au_x$ system motivated this new theoretical approach to local quantum criticality [Si, 2001; Si, 2003], since it is one of the intensively characterized HF systems exhibiting nFL behavior.

Although the behaviors of $C(T)/T \propto \log(T_0/T)$ and $\Delta\rho(T) \propto T$ in $CeCu_{6-x}Au_x$ at the QCP were reported [Lohneysen, 1996; Löhneysen, 1998], the phase boundary of T_N can be described by SDW scenario via 2D critical fluctuations [Millis, 1993], see Table 3.2 for $d = 2$ and $z =$

2, these are not thought to be appropriate for $CeCu_{6-x}Au_x$ system. $CeCu_{6-x}Au_x$ exhibit 3D AFM ordering, and the anisotropy of the electrical resistivity along different crystallographic directions is less than factor of 3. Therefore $CeCu_{6-x}Au_x$ might be treated as 3D AFM metal. For 3D itinerant fermion systems the SDW scenario predict $C(T)/T = \gamma_0 - \beta\sqrt{T}$ and $\Delta\rho(T)$ $\sim T^{3/2}$ for antiferromagnets ($z = 2$) (see also Table 3.2) and T_N should depend on the control parameter, $g_x = x - x_c$ for doping and $g_P = P - P_c$ for pressure, as $T_N \sim |g|^\psi$ with $\psi = z/z(d + z - 2) = z/(z + 1)$. In $CeCu_{6-x}Au_x$ system $\psi = 1$ for both g_x and g_P [Rosch, 1997]. Note that the dimensionality of this compound is still under debate, because of conflicting inelastic neutron scattering results [Stockert, 1998].

Inelastic neutron scattering experiments, for $x_c = 0.1$, showed that the unusual type of scaling of the dynamical susceptibility of $CeCu_{6-x}Au_x$ at the QCP is not consistent with the SDW scenario. The experimental data indicate anomalous E/T scaling: $\chi^{-1}(q, E, T) = 1/c[f(q) + (-iE + aT)^\alpha]$ with an anomalous scaling exponent $\alpha \approx 0.75$ [Schröder, 1998; Schröder, 2000]. Based on these experiments a new theoretical concept was proposed with the idea that the Kondo effect breaks down at the QCP.

Although many proposals have been developed, the model proposed by Si *et al.* [Si, 2001; Si, 2003], called the local quantum criticality, seems to be in agreement with experiments for $CeCu_{6-x}Au_x$ system. Note that among the currently available theoretical models only the local quantum criticality model provides the E/T scaling of the dynamical susceptibility, although it needs to also be tested by other microscopic models. The quantum criticality of $CeCu_6$ system is also tuned by other control parameters (pressure and magnetic field) (for pressure, see Fig. 3.10 (b)). Tuning the system through the QCP by both the pressure and doping shows the characteristics of local quantum criticality [Scheidt, 1999]. For field tuned transitions the behavior appears to be consistent with the properties of an SDW QCP with $d = 3$ [Löhneysen, 2001; Stockert, 2007]. Thus, the quantum criticality depends on not only the systems, but also control parameters.

The name "local quantum criticality" refers to the localization of the electronic excitations associated with the f-moments in which a destruction of Kondo screening of the f-moments

coincides with the magnetic transition of the Kondo lattice. Thus, the breakdown of the Kondo effect, vanishing at the QCP, should be associated with Fermi surface fluctuations (instabilities).

In the SDW scenario of quantum criticality, the quasi-particle system undergoes a SDW instability at the QCP and the Kondo temeprature remains finite across the quantum phase transition. Recently, however, experimental results have indicated that the signature of heavy quasi-particles does not survive near the QCP. This may occur due to magnetic coupling to the surrounding moments or possibly due to fluctuations of the Fermi volume involved with onset of Kondo screening in an Anderson lattice system [Si, 2001; Coleman, 2001; Senthil, 2003].

Originally, based mainly on results from $YbRh_2Si_2$, the nature of the Kondo breakdown was suggested to involve multiple energy scales. These multiple energy scales collapse to zero as the system is tuned through the QCP and it has been proposed that the Fermi surface changes from a large to a small one when the QCP is crossed from the paramagnetic side [Gegenwart, 2008]. In Fig. 3.12 T_0 represents the initial crossover into Kondo screened state. For $T \gg T_0$ a Kondo lattice behaves as individual local moments, following the Curie-Weiss behavior. Because of the difficulties of extracting T_0, the temperature of $0.4R\ln(2)$ entropy per local moment is generally defined as T_0 [Gegenwart, 2008]. The line associated with the scale E^* separates between the incomplete Kondo screened state (left side of E^*) and complete Kondo screened state (right side of E^*). Thus, the E^* line marks the crossover from small to large Fermi surface. The left side of E^* the local moments do not participate in the Fermi surface formation. As shown in Fig. 3.12 (a), when the two lines, T_N and E^*, are intersect, the QCP belongs to the SDW scenario. When E^* terminates at the same value of the control parameter as the AFM phase boundary, the QCP falls in the Kondo breakdown scenario (Fig. 3.12 (b)) [Gegenwart, 2008].

Using the $z = 3$ quantum criticality (Kondo breakdown scenario), which describes the dynamics of hybridization fluctuation, both the logarithmically divergent specific heat coefficient and the power law divergence of the thermal expansion coefficient are explained successfully, giving rise to the divergent Grüneisen ratio with an exponent 2/3 [Kim, 2008]. However, for

the Ge-doped and Co-doped $YbRh_2Si_2$ cases [Friedemann, 2009] these multiple energy scales seem to yield more complex picture (see below).

3.5.4 Disorder effect

In a recent work, the interplay of disorder and spin fluctuations near a QCP has been found to give $\Delta\rho = AT^n$, with $1 \leq n \leq 1.5$ depending on the amount of disorder [Rosch, 1999]. In the framework of disorder induced QCP, nFL in disordered systems can be considering as arising from the formation of a Griffiths-phase[Griffiths, 1969]. By invoking Griffiths phases, a number of measurable quantities in nFL systems were predicted to have power law behavior when disorder is present; $C(T)/T \propto \gamma + \sqrt{T}$, $\Delta\chi(T) \propto T^{-3/2}$, and $\Delta\rho \propto T^{3/2}$ [Castro Neto, 1998].

A number of HF systems such as $CePd_2Si_2$ [Mathur, 1998], $CeNi_2Ge_2$ [Julian, 1996], and $CeCu_2Si_2$ [Gegenwart, 1998], are good candidates to be described within the conventional scenario, but the qualitative trends can also be well described by the theory taking the disorder effects into account: $\Delta\rho(T) \propto T^{3/2}$ in the more dirty systems and $\Delta\rho(T) \propto T^n$ with n close to 1 in the cleaner systems [Rosch, 1999]. In the cleaner systems an anomalous behavior in the transport (not in thermodynamics) is predicted even at some distance away from the QCP. Therefore it is important to use the cleanest systems to investigate quantum criticality and thus pressure and magnetic field will be better choices for control parameters.

3.5.5 High temperature approach

Rather than considering the quantum fluctuation at low temperature, near QCP via nFL behavior and scaling invariance, careful examination of high temperature energy scale may provide good opportunities to select the proper model for quantum critical scenarios, since the high temperature signature is distinctly different between SDW and Kondo breakdown scenario. Recently this approach has been taken with the high resolution ultraviolet photoemission spectroscopy of the $CeCu_{6-x}Au_x$ system [Kroha, 2010]. Although there obviously is uncertainty in estimating the Kondo temperature, a sudden decrease of the Kondo temperature was observed at/or very close to the quantum critical concentration (x_c). This drop is

consistent with the theoretically expected signature of the Kondo breakdown scenario. In Ref. [Kroha, 2010] the Kondo temperature was defined as E^* in Fig. 3.12. In this case the phase diagram is close to Fig. 3.12 (b), where the characteristic energy scale terminates to QCP. This supports the idea that the quantum phase transition in $CeCu_{6-x}Au_x$ follows the local quantum criticality scenario, but this conclusion needs to be tested carefully.

3.5.6 New perspective - global phase diagram

Recently, a new perspective on the mechanism for quantum criticality, including a proposed "global" phase diagram has been developed. We will summarize it briefly, based on the Ref. [Coleman, 2010; Custers, 2010], since this model has been applied to field tuned AFM QCP. The earlier work and its references can be found in Ref. [Rech, 2006; Coleman, 2007].
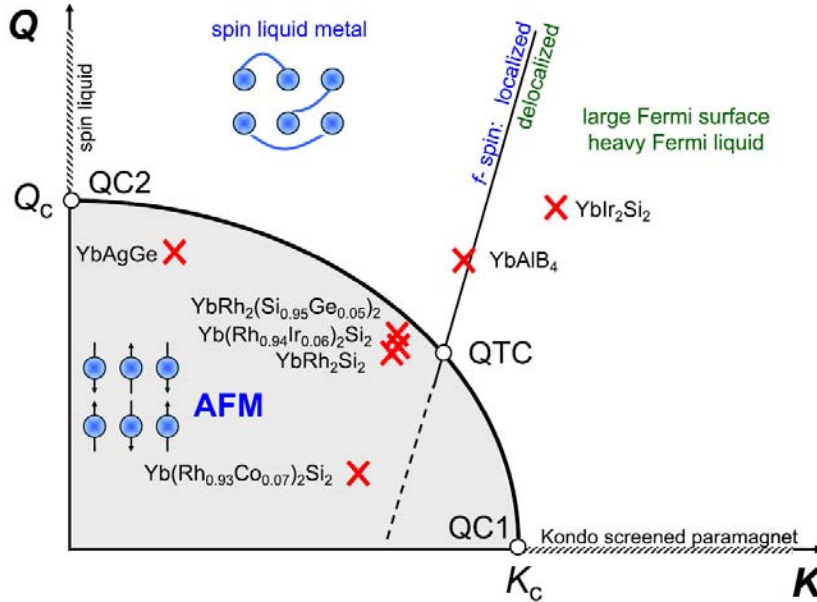
Figure 3.13   Figure taken from Ref. [Custers, 2010]: Generic phase diagram displaying the combined effects of Kondo coupling (**K**) and magnetic frustration, or quantum zero-point motion (**Q**). The f-electron localization and the phase line intersect at a quantum tetra-critical point (QTC). For the location of compounds in the phase diagram (red cross), see Ref. [Custers, 2010].

A two-dimensional phase diagram (Fig. 3.13) can be constructed from the ratio $K =$

T_K/J_H the Kondo temperature, T_K, and the nearest neighbor RKKY interaction, J_H, and the quantum zero point motion of the local moments Q, where Q can be increased by increasing the amount of frustration in the coupling between the local moments. This is an extension of the Doniach diagram [Doniach, 1977]. As K is increased, a quantum phase transition takes place at some value K_c (QC1) as shown in Fig. 3.13. When $K = 0$ local moments are coupled together on a lattice by a short-range AFM Heisenberg interaction, and for $Q = 0$, this lattice would develop an AFM ground state. However, by adding a frustrated, second neighbor coupling, between the spins (reducing the moment size), the strength of the quantum zero point spin fluctuation can be increased. At some critical value Q_c, there is a quantum phase transition where long range magnetic order melts under the influence of zero point spin fluctuations to form a spin liquid (see QC2 in Fig. 3.13). For the general case $K \neq 0$ and $Q \neq 0$, QC1 and QC2 are linked with a single phase boundary. At small K and Q, a common AFM phase exists. The paramagnetic spin liquid at large Q has a small Fermi surface and the paramagnetic, heavy FL at large K has a large Fermi surface, where these can be separated by zero temperature phase transition.

This extended Doniach like diagram has been used to parameterize the magnetic field tuning experiments on pure, Ir-, Co-, and Ge-doped $YbRh_2Si_2$, $YbIr_2Si_2$, YbAgGe, and $YbAlB_4$ (see Fig. 3.13) [Custers, 2010]. For the $YbRh_2Si_2$ family, except for $YbIr_2Si_2$, there is a field tuned temperature scale, T^* (E^* in Fig. 3.12), where various anomalies are seen in the thermodynamic and transport measurements such as Hall coefficient, susceptibility, and magnetostriction. The anomalies corresponding to T^* are shown to sharpen up at the critical field H^* when $T \to 0$. The H^* has been interpreted as the point at which the magnetic field causes the modification from a small to a large Fermi surface. The ground state of $YbIr_2Si_2$ is a paramagnetic FL state which is stable up to $80\,\mathrm{kbar}$ [Yuan, 2006]. At the lowest temperature no signature of T^* was found in magnetic field dependent Hall effect measurements [Kriegisch, 2008]. Thus, $YbIr_2Si_2$ was placed tentatively to the right of the f-spin localization line. In Fig. 3.13, $YbAlB_4$ was placed at the edge of the spin liquid metal phase, since this system enters a FL phase with small magnetic field. For YbAgGe, a larger magnetic field is

required to suppress the AFM order. Beyond the AFM QCP, YbAgGe was shown to pass through a finite magnetic field range with a linear temperature dependence of the resistivity (nFL region), which is very similar to subsequent work on Ge-doped $YbRh_2Si_2$. For YbAgGe, detailed descriptions of physical properties are give in the chapters below with references there in.

In $YbRh_2Si_2$, the field induced T^* scale and the T_N (AFM phase boundary) converge at a single QCP, however, these have recently been proposed to separate in Ir- and Ge-doped systems [Friedemann, 2009], manifesting similar features as those seen at high magnetic fields in YbAgGe. A central question, raised from the proposed Doniach-like diagram, is what are the characteristics of proposed spin liquid metal and what is the nature of the spin liquid phase that is predicted to develop in Ir- and Ge-doped (not for Co-doped) $YbRh_2Si_2$ and YbAgGe system.

3.5.7   Field tuned QCP - $YbRh_2Si_2$ and YbAgGe

Schematic $H-T$ phase diagrams of $YbRh_2Si_2$ with Ir, Co, and Ge-doped [Friedemann, 2009] and YbAgGe [Bud'ko, 2005a] are plotted in Fig. 3.14 which clearly shows the evolution of the various energy and crossover scales; AFM ordering temperature T_N, a crossover T^*, and a FL region below T_{FL}. These scales were evidenced from several thermodynamic and transport measurements. For $YbRh_2Si_2$ (Fig. 3.14 (a)), all these scales converge to one critical field at $T = 0$ (QCP). For Ir-doped sample (Fig. 3.14 (b)), the T_N is suppressed below $0.02\,\mathrm{K}$, whereas in the case of Co-doped sample (Fig. 3.14 (c)) the T_N is enhanced to $0.41\,\mathrm{K}$. The T^* scale does not change the position in the phase diagram. Therefore, it was inferred that T^* is separated from T_N for Ir-doped sample, whereas T^* intersects with T_N for Co-doped sample. In both cases T^* and T_{FL} seem to converge to the same critical field at $T = 0$.

Interestingly, both T^* and T_{FL} for Ge-doped sample (Fig. 3.14 (d)) are separated from T_N but both of them vanish at the same field. For YbAgGe (Fig. 3.14 (e)), in addition to T_N, T^*, and T_{FL} there is one more characteristic crossover scale T_{Hall}; T_{Hall} and T^* were initially based on the sharp variation of the Hall coefficient [Bud'ko, 2005a]. As seen in Fig. 3.14 the
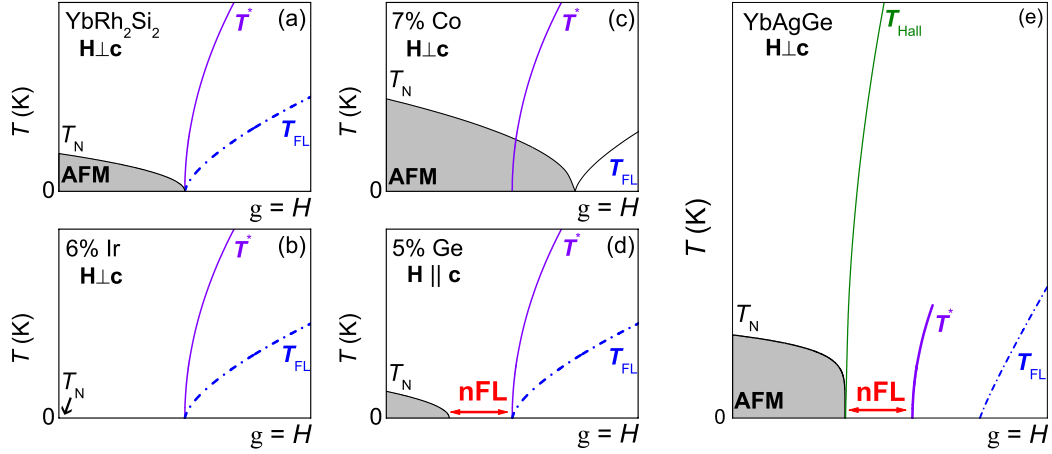
Figure 3.14 Schematic $H-T$ phase diagram of YbRh$_2$Si$_2$ with Ir, Co, and Ge substitution and YbAgGe. In these systems a magnetic field (H) was selected as a control parameter g. Figures are based on the results in Ref. [Friedemann, 2009] for (a) YbRh$_2$Si$_2$, (b) Yb(Rh$_{1-x}$Ir$_x$)$_2$Si$_2$, and (c) Yb(Rh$_{1-x}$Co$_x$)$_2$Si$_2$; in Ref. [Custers, 2010] for (d) YbRh$_2$(Si$_{1-x}$Ge$_x$)$_2$; in Ref. [Bud'ko, 2005a] for (e) YbAgGe. The T_N represents the antiferromagnetic phase boundary. The crossover temperature to the Fermi liquid state, T_{FL}, is based on the quadratic temperature dependence in the electrical resistivity $\Delta\rho(T) = AT^2$. The crossover temperature, T^*, was evidence from several thermodynamic and transport measurements. For YbAgGe and Ge doped YbRh$_2$Si$_2$ the non Fermi liquid (nFL) behavior, $\Delta\rho(T) = AT$, is observed for a wide range of magnetic field, and therefore T_{FL} is separated from the T_N. See details in text.

$H-T$ phase diagram of YbAgGe is quite different compared to YbRh$_2$Si$_2$ family. However, if T_N and T_{FL} only are considered, the $H-T$ phase diagram of YbAgGe is similar to the case of Ir- and Ge-doped YbRh$_2$Si$_2$. If nFL behavior is only considered, the features in the phase diagram of Ge-doped YbRh$_2$Si$_2$ are very similar to those of YbAgGe; both of them show the nFL behavior in a wide range of magnetic field, separating T_{FL} from T_N.

Although there are qualitative differences, the extended Doniach like diagram seems to incorporate these materials. From the Fig. 3.13, when AFM order in YbAgGe is tuned by magnetic field, the system moves in the direction of increasing K. Thus, the AFM order is suppressed by intersecting the phase boundary linked by QC1 and QC2, and the nFL behavior

corresponds to the region between the phase boundary and the line at which the f-spin changes from localized to delocalized. The T^* feature may correspond to the f-spin localization line. However, the nature of crossover T_{Hall} and T^* lines in YbAgGe still need to be clarified.

With the current interest in Kondo breakdown scenario, including local quantum criticality, a central question that has to be resolved is what is the direct experimental signature of the Kondo breakdown, distinguished it from other possible routes to quantum criticality. For example, a crossover scale, T^*, was detected in a number of transport and thermodynamic measurements in agreement with the predictions of the Kondo breakdown scenario. In particular, Hall effect measurements are consistent with a jump, and are interpreted as a change from a small to a large Fermi surface, at the QCP in YbRh$_2$Si$_2$ [Paschen, 2004]. Generally, in HF metals, the interpretation of the transport measurements is not easy due to the multi-band contributions. Addressing this issue is not trivial due to the absence of low temperature angle resolved photoemission spectroscopy which is restricted to higher temperatures $T \gg T_N$ and de Haas van Alphen experiments which are restricted to high magnetic fields $H \gg H_c$. In addition, standard quantities, which are accessible down to mK order such as resistivity and specific heat, do not measure T_K directly due to the crossover character.

In YbAgGe a wide range of nFL region appears to lie between the AFM and the heavy electron state. Therefore, it is important to more carefully study the region between T_{Hall} and T^*. In the later section we will investigate further this region by means of thermoelectric power (TEP) measurements. In addition, when the higher temperature energy scale T_K as shown in Fig. 3.12, is identified, a Kondo breakdown scenario can be distinguished experimentally from a SDW instability by tracking the evolution of T_K at least qualitatively. Since the TEP is known to be particularly sensitive to Kondo and CEF effects, and to various physical quantities related to the DOS at the Fermi level [Blatt, 1976], the evolution of T_K will also be traced by TEP measurements for YbAgGe (see chapter 5).

CHAPTER 4.   Thermoelectric Power of the YbT_2Zn_{20} (T = Fe, Ru, Os, Ir, Rh, and Co) Heavy Fermion Compounds

4.1   Introduction

In a heavy fermion (HF) Kondo lattice system, the ground state is a Fermi-liquid (FL) state constituting the Landau quasi-particles. In Ce-, Yb-, and U-based intermetallic systems the conduction electrons compensate or screen the localized moments of the f-electrons where localized electrons together with their screening cloud form quasi-particles. These quasi-particles have heavy masses, reflected in an enhanced value of the Sommerfeld coefficient, γ = $C(T)/T|_{T \to 0}$, at low temperatures. When f-electrons so strongly couple with conduction band there is an increased overlap of the electronic state which enhances the hybridization and band widths [Hewson, 1993].

The FL state in HF Kondo lattice systems shows strong correlations among physical quantities. One such correlation is the Kadowaki-Woods (K-W) ratio, a relation between the electrical resistivity $(\rho(T) - \rho_0 = AT^2)$ and specific heat $(C(T) = \gamma T)$ [Kadowaki, 1986; Miyake, 1989], given by the universal ratio $A/\gamma^2 = 1.0 \times 10^{-5}$ $\mu\Omega cm/(mJ/mol \cdot K)^2$. Recently, systematic deviations of the K-W ratio in many HF systems (especially for Yb-based compounds) have been explained by Tsujii et $al.$, taking into account the ground state degeneracy $(N = 2j+1)$ [Tsujii, 2003; Kontani, 2004; Tsujii, 2005]. A FL state is also characterized by the Wilson ratio (R_W) which links γ to the Pauli susceptibility $\chi(0)$ [Weigman, 1983; Auerbach, 1986; Lee, 1986], which is given by $R_W = \pi^2 k_B^2 \chi(0)/(j(j + 1)g^2 \mu_B^2 \gamma^2)$, where k_B, g, and μ_B are the Boltzman constant, Lande's factor, and Bohr magneton, respectively [Hewson, 1993]. In addition to the R_W and K-W ratio, the zero temperature limit of the thermoelectric power (TEP), $S(T)/T = \alpha$, for several correlated materials has shown a strong correlation with γ via

the dimensionless ratio $q = N_A e S / \gamma T = N_A e \alpha / \gamma$ [Behnia, 2004], where N_A is the Avogadro number and e is the carrier charge.

For Yb-based HF systems, the electrical resistivity and TEP reveal complex temperature dependencies with a local extrema. In general, these extrema are related to Kondo scattering associated with the ground state and excited states of the CEF energy levels [Bhattacharjee, 1976; Lassailly, 1985; Maekawa, 1986]. The characteristic temperature of the local maximum shown in $\rho(T)$ and the local minimum developed in $S(T)$ allow for an estimate of the Kondo temperature, T_K, and the crystalline electric field (CEF) splitting, Δ / k_B, as relevant energy scales in Yb-based HF systems.

In this chapter, TEP measurements on YbT_2Zn_{20} (T = Fe, Ru, Os, Ir, Rh, and Co) are presented as functions of temperature and magnetic field to evaluate the correlation between specific heat and TEP in the zero temperature limit. These compounds crystallize in the cubic $CeCr_2Al_{20}$-type structure ($F d \overline{3} m$, No.227) [Thiede, 1998] and have been reported to be HF metals with no long range order down to $20\,mK$ [Torikachvili, 2007]. In the FL regime it has been shown that the R_W and K-W ratios in this family follow the theoretical predictions with different ground state degeneracies. The TEP data of YT_2Zn_{20} (T = Fe, Co) are also presented for comparison. YFe_2Zn_{20} is one of the examples of a nearly ferromagnetic Fermi liquids (NFFL) with a highly enhanced magnetic susceptibility value at low temperatures [Jia, 2007], whereas YCo_2Zn_{20} shows normal metallic behavior.

4.2   Results

Figure 4.1 shows the TEP data for YFe_2Zn_{20} and YCo_2Zn_{20}. The temperature-dependent TEP, $S(T)$, of these compounds is similar to normal metallic systems. At $300\,K$, $S(T)$ of both compounds is positive and has an absolute value of $\simeq 9\,\mu V/K$ for YFe_2Zn_{20} and $\simeq 5\,\mu V/K$ for YCo_2Zn_{20}, and then decrease monotonically to below $25\,K$ with decreasing temperature. With further cooling, $S(T)$ of YCo_2Zn_{20} passes through a broad peak ($\sim \Theta_D/12$ [Jia, 2008], where Θ_D is the Debye temperature) expected to be due to phonon-drag [Blatt, 1976]. On the other hand, $S(T)$ of YFe_2Zn_{20} shows a local minimum around $14\,K$ ($\sim \Theta_D/23$ [Jia, 2008]) that is
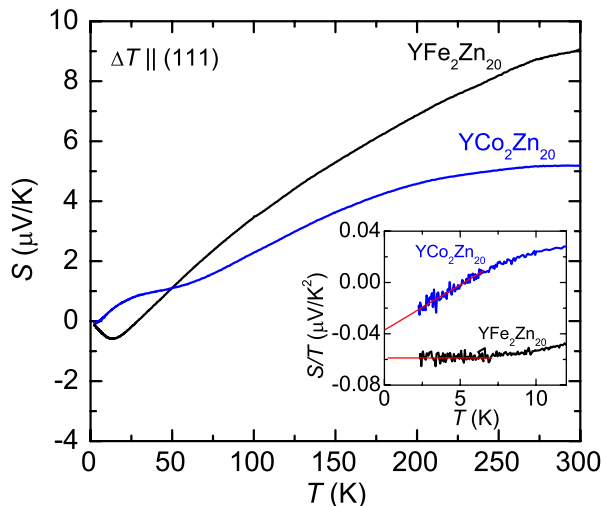
Figure 4.1   Temperature-dependent   thermoelectric   power, $S(T)$,   of YFe$_2$Zn$_{20}$ and YCo$_2$Zn$_{20}$ along $\Delta T \parallel (111)$. Inset: $S(T)/T$ vs. T below 12 K. Solid lines are guide to eye.

not currently understood. The absolute value of the TEP for YFe$_2$Zn$_{20}$ is much smaller than other NFFL systems. A signature of the spin fluctuation temperature, T_{sf}, has been inferred from a shoulder in AFe$_4$Sb$_{12}$ (A = Ca, Sr, and Ba) data [Takabatake, 2006] and as a minimum developed in RCo$_2$ (R = Y, Sc, and Lu) data [Gratz, 2001]. The minimum developed near 14 K may be related to the signature of spin fluctuation, combined with phonon-drag in the YFe$_2$Zn$_{20}$ system. In the $T \rightarrow 0$ K limit, $S(T)/T$ of YFe$_2$Zn$_{20}$ is larger than that of YCo$_2$Zn$_{20}$ as shown in the inset of Fig. 4.1.

In zero field, the $S(T)$ data of the YbT$_2$Zn$_{20}$ (T = Fe, Ru, Os, Ir, Rh, and Co) compounds are plotted in Fig. 4.2. In contrast to the isostructural Y-based compounds, $S(T)$ of the Yb-based compounds exhibits a large, negative minimum (between -70 and -40 μV/K) and the sign of $S(T)$ changing above 150 K from negative to positive (not observed in this temperature range for T = Ir). The absolute TEP values of Yb-based compounds are much larger than Y-based compounds at low temperatures, while they have a similar order of magnitude compared to Y-based compounds around 300 K. A negative, highly enhanced value of the TEP, over the temperature region measured, is typical of those found in other Yb-based Kondo lattice systems [Foiles, 1981; Andreica, 1999; Deppe, 2008].
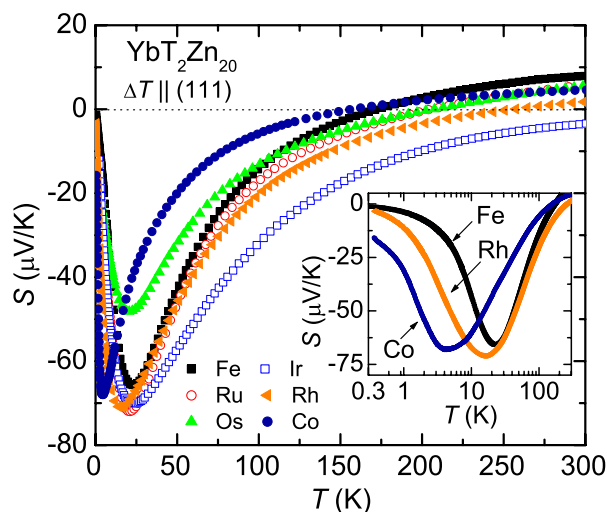
Figure 4.2   Temperature-dependent thermoelectric power, $S(T)$, of
YbT$_2$Zn$_{20}$ (T = Fe, Ru, Os, Ir, Rh, and Co) in zero applied
magnetic field. Inset: $S(T)$ vs. log(T) for T = Fe, Rh, and Co.

Figure 4.3 shows the low temperature $S(T)$ of YbT$_2$Zn$_{20}$. For T = Fe and Ru, a broad minimum of $\sim$ -70 μV/K is shown at the temperature $T_{min}^S \sim 22$ K. For T = Os, Ir and Rh, a similar broad minimum develops at a temperature of $T_{min}^S \sim 16$-23 K, where the width of the peak is wider than that for T = Fe and Ru. For T = Co, $S(T)$ shows a similar temperature dependence but with the minimum shifted to $T_{min}^S \sim 4$ K and it also shows slope changes around ~ 1 K and ~ 8 K. The width of the minimum for T = Co is narrower than that for the other members of this family. Above 10 K, the absolute value of the TEP for T = Co reduces rapidly as the temperature increases and the sign of the TEP changes from negative to positive close to 150 K. For comparison, $S(T)$ curves for T = Co together with T = Fe and Rh are plotted on a semi-logarithmic scale in the inset of Fig. 4.2. A smaller local minimum ($\sim$ -48 μV/K) is observed for YbOs$_2$Zn$_{20}$. It is not clear at present if this is related to the electrical resistivity measurement that showed a larger residual resistivity in YbOs$_2$Zn$_{20}$ compared to other members (T = Fe, Ru, Ir, and Rh) [Torikachvili, 2007]. $S(T)$ of YbIr$_2$Zn$_{20}$ is negative over the whole temperature range measured, the sign change from negative to positive being expected around ~ 400 K, based on a linear extrapolation of $S(T)$ above 250 K. Below 10 K (or 3 K for T = Co), $S(T)$ data for all compounds show a tendency of approaching zero and reveal
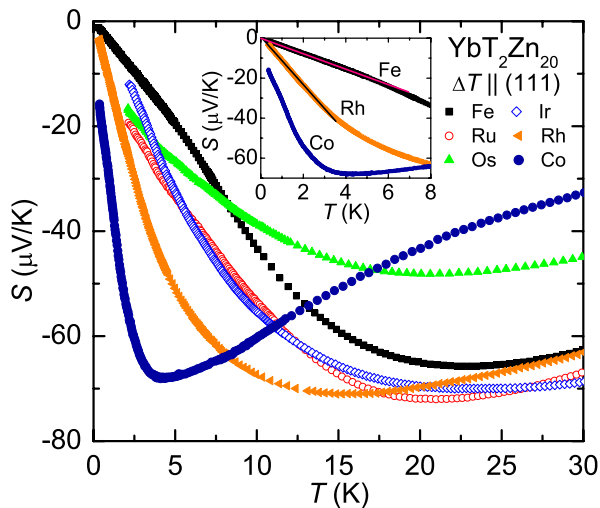
Figure 4.3   Low temperature $S(T)$ of YbT_2Zn_{20} compounds in zero applied
magnetic field. Inset: $S(T)$ for T = Fe, Rh, and Co below 8 K.
Solid lines on the top of the data for T = Fe and Rh are guide
to eye.

linear temperature dependencies, $S(T) = \alpha T$. Since the TEP was measured down to 0.4 K for

T = Fe, Rh, and Co, the linear temperature dependence of $S(T)$ is even more clearly revealed

for these compounds as shown in the inset of Fig. 4.3.

Figure 4.4 presents $S(T)/T$ of YbT_2Zn_{20} below 10 K. Since no signature of any kind of

long range order down to 20 mK has been observed in the electrical resistivity measurements

[Torikachvili, 2007], the zero temperature limit of $S(T)/T$ can be reliably estimated by ex-

trapolating $S(T)$ from 2 K (or 0.4 K) to $T = 0$, where the inferred $S(T)/T|_{T\to 0}$ values for

T = Fe, Ru, Os, Ir, and Rh range between -3.8 $\sim$ -10 $\mu V/K^2$. For T = Co, $S(T)/T$ value

at 0.4 K reaches -42 $\mu V/K^2$ and is still decreasing (see inset of Fig. 4.4). By using a linear

extrapolation, $S(T)/T|_{T\to 0}$ value for T = Co is found to be $\sim$ -57 $\mu V/K^2$.

In Fig. 4.5 (a), the results of $S(T)$ measurements at $H = 0$ and 140 kOe are shown for T

= Fe, Ru and Ir. For clarity, the absolute value of the TEP is shifted by -20 $\mu V/K$ for T =

Ru and -40 $\mu V/K$ for T = Ir. A slight change of T_{min}^{S} and a reduction of absolute value are

seen for the $H = 140$ kOe data. Above 100 K, $S(T)$ for $H = 140$ kOe remains essentially the

same as $S(T)$ for $H = 0$. In the zero temperature limit for $H = 140$ kOe data (Fig. 4.5 (b)),
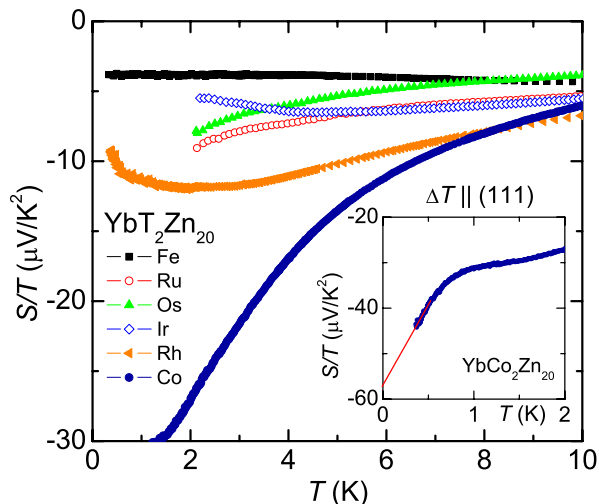
Figure 4.4　$S(T)/T$ vs. T for YbT_2Zn_{20} below 10 K in zero applied magnetic field. Inset: $S(T)/T$ vs. T for $YbCo_2Zn_{20}$. The solid line represents the linear extrapolation curve to $T = 0$.

whereas $S(T)/T$ for T = Ru remain essentially the same, $S(T)/T$ at 140 kOe for T = Fe and Ir is decreased from $\sim$-3.8 to $\sim$-6.4 $\mu V/K^2$ and from $\sim$-4 to $\sim$-6.6 $\mu V/K^2$, respectively. In the inset of Fig. 4.5 (a), the TEP measured at $T = 2.2$ K is plotted as a function of magnetic field for T = Fe, Ru, and Ir, where $\Delta S = S(H) - S(0)$. An interesting point of this result is the appearance of a maximum around ~ 70 kOe for T = Fe and Ru and a minimum around ~ 100 kOe for T = Ir. For T = Ir the local minimum field shown in TEP is roughly matched with the metamagnetic-like anomaly seen around $H = 120$ kOe in magnetization isotherms, $M(H)$, [Yoshiuchi, 2009] for $\mathbf{H} \| [110]$. For T = Fe and Ru the $M(H)$ data at $T = 2$ K do not show any signature of metamagnetic-like behavior up to 70 kOe [Mun, 2010c], with $M(H)$ being linear in magnetic field for both compounds. In order to clarify this point, it is necessary to measure $M(H)$ for magnetic fields higher than 70 kOe, to see whether the anomaly in $S(H)$ is related to features in magnetization or electronic data.

In zero field, the electrical resistivity, $\rho(T)$, of YbT_2Zn_{20} (T = Fe, Ru, Os, Ir, Rh, and Co) data taken from Ref. [Torikachvili, 2007] and isostructural LuT_2Zn_{20} data taken from Ref. [Mun, 2010a] are plotted in Figs. 4.6 (a) and (b), respectively. Upon cooling, $\rho(T)$ of $YbCo_2Zn_{20}$ indicates a clearly local maximum ($T_{max}^{\rho} = 2.4$ K) followed by the logarithmic
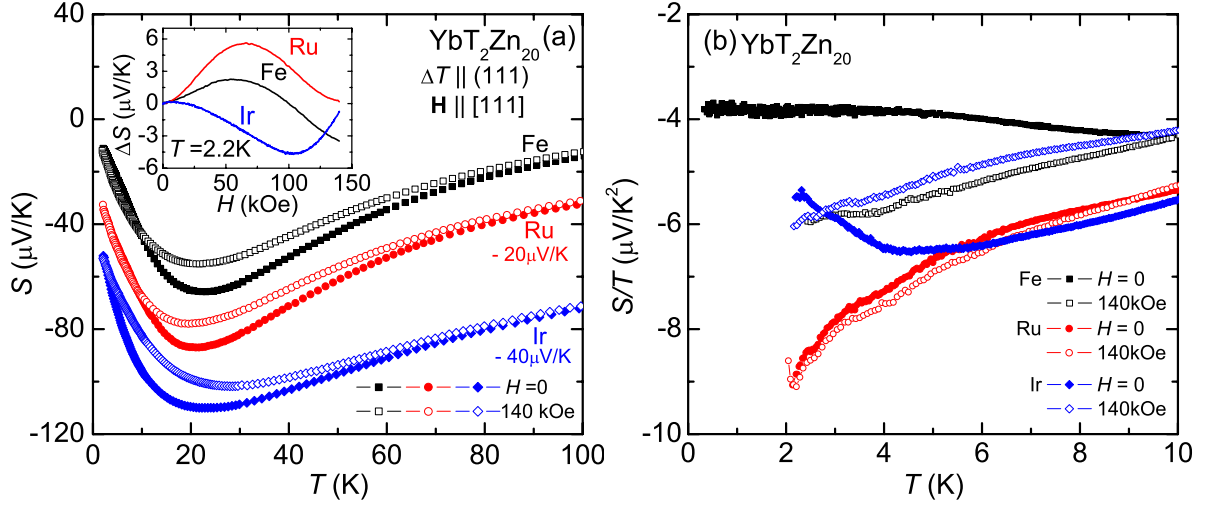
Figure 4.5   (a) $S(T)$ of YbT$_2$Zn$_{20}$ (T = Fe, Ru, and Ir) at $H=0$ (closed symbols) and 140 kOe (open symbols). For clarity, the data for T = Ru and T = Ir are shifted by -20 μV/K and -40 μV/K, respectively. Inset: $\Delta S = S(H) - S(0)$ at 2.2 K for T = Fe, Ru, and Ir. (b) $S(T)/T$ vs. T for YbT$_2$Zn$_{20}$ (T = Fe, Ru, and Ir) below 10 K at $H=0$ (closed symbols) and 140 kOe (open symbols).

temperature dependence ($-\log(T)$) as temperature decreases (inset (a)), which is typical of a Kondo lattice system, whereas $\rho(T)$ data for the other members of this family (T = Fe, Ru, Os, Ir, and Rh) decreases linearly and follows a sharp drop due to the coherent Kondo scattering. In order to see the T_{max}^{ρ} for T = Fe, Ru, Os, Rh, and Ir, $\Delta\rho(T)$ of YbT$_2$Zn$_{20}$ compounds has been obtained by subtracting $\rho(T)$ of isostructural LuT$_2$Zn$_{20}$ compounds, where the relation $\Delta\rho(T) = [\rho(T)\text{-}\rho_0](\text{YbT}_2\text{Zn}_{20})$ - $[\rho(T)\text{-}\rho_0](\text{LuT}_2\text{Zn}_{20})$ was used because of the larger ρ_0 value of Lu-based than Yb-based compounds. The obtained $\Delta\rho(T)$ is plotted in Fig. 4.6 (c), which clearly shows T_{max}^{ρ} for all compounds followed by the $-\log(T)$ dependence. At $T = 2$ K, the magnetoresistance (MR) of YbT$_2$Zn$_{20}$ (T = Fe and Ru), is plotted as $(\rho(H)\text{-}\rho(0))/\rho(0)$ vs. H in Fig. 4.6 (d), and it is positive up to 140 kOe without showing any noticeable anomaly.
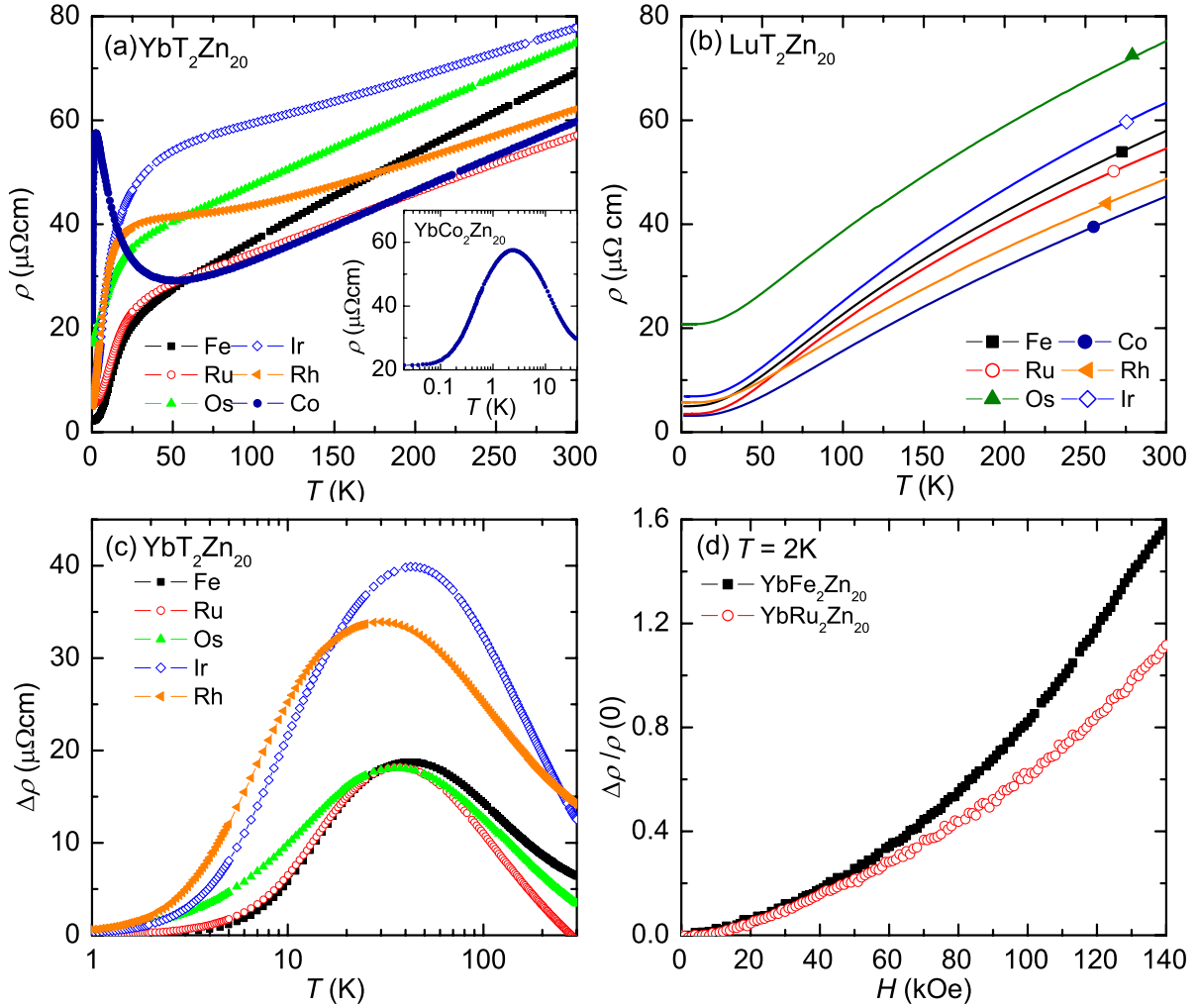
Figure 4.6   (a) Temperature-dependent electrical resistivity, $\rho(T)$, of
YbT$_2$Zn$_{20}$ (T = Fe, Ru, Os, Ir, Rh, and Co). Inset shows
$\rho(T)$ of YbCo$_2$Zn$_{20}$ in a semi-logarithmic scale. Data are
taken from Ref. [Torikachvili, 2007]. (b) $\rho(T)$ of LuT$_2$Zn$_{20}$
(T = Fe, Ru, Os, Ir, Rh, and Co, taken data from Ref.
[Mun, 2010a].   (c) $\Delta\rho(T)$ of YbT$_2$Zn$_{20}$, where $\Delta\rho(T)$ =
$(\rho(T) - \rho_0)$ (YbT$_2$Zn$_{20}$) - $(\rho(T) - \rho_0)$ (LuT$_2$Zn$_{20}$). (d) Mag-
netoresistance, $(\rho(H) - \rho(0))/\rho(0)$, of YbT$_2Zn_{20}$ (T = Fe and
Ru) at T = 2 K.

4.3 Discussion

Based on earlier thermodynamic and transport measurements [Torikachvili, 2007] of this family, $S(T)$ data for YbT_2Zn_{20} (T = Fe, Ru, Os, Ir, Rh, and Co) can be understood qualitatively by considering the Kondo (T_K) and CEF (Δ/k_B) effects. The compounds in this series appear to be a set of model Kondo lattice systems with varying energy scales: T_K and Δ/k_B. In Fig. 4.7 (a), the Kondo temperature, T_K^γ, determined from γ [Torikachvili, 2007] and local minimum temperature, T_{min}^S, observed in the zero field $S(T)$ data are plotted as a function of the transition metal, T. The change of T_{min}^S from T = Fe to T = Co correlates strongly with changing T_K by varying the transition metal, especially for T = Os, Ir, Rh, and Co.
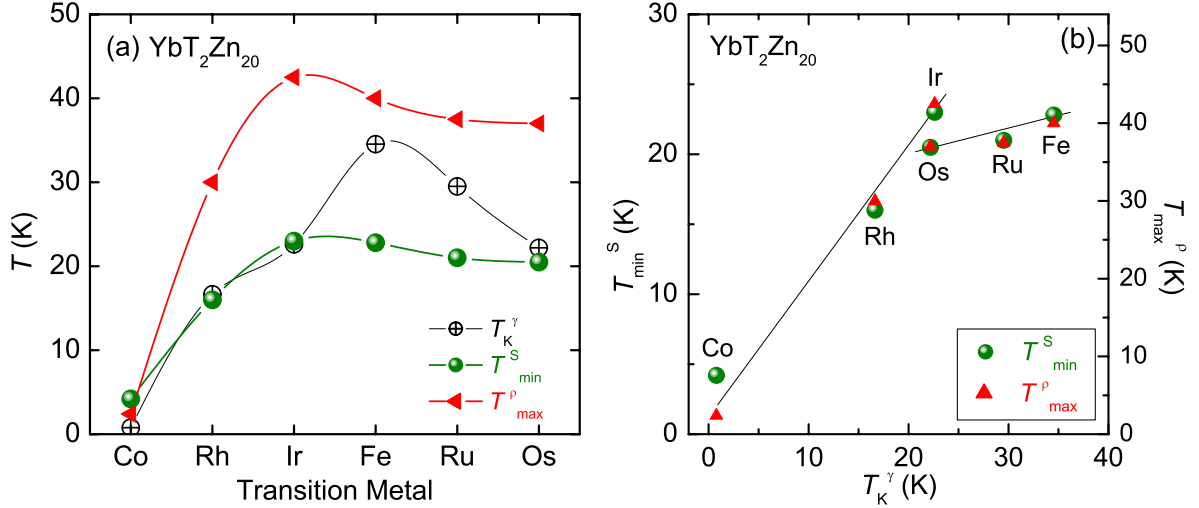
Figure 4.7 (a) Relevant characteristic temperatures in YbT_2Zn_{20} (T = Fe, Ru, Os, Ir, Rh, and Co). A Kondo temperature (T_K^γ) calculated from γ, a local maximum temperature (T_{max}^ρ) obtained from the resistivity, and a local minimum temperature (T_{min}^S) developed in $S(T)$ are plotted as a function of transition metal. T_K^γ values are taken from Ref. [Torikachvili, 2007]. (b) Plots of T_{min}^S (left) and T_{max}^ρ (right) vs. T_K^γ. Solid lines are guide to the eye.

A similar trend can be found in the previously published electrical resistivity, $\rho(T)$, results [Torikachvili, 2007]. For T = Co, $\rho(T)$ manifests a clear local maximum, T_{max}^ρ, around $2.4\,\mathrm{K}$ followed by a logarithmic temperature dependence as temperature decreases. Whereas T_{max}^ρ is clear in the $\rho(T)$ data for T = Co, $\rho(T)$ data from the other members of this family only show

a clear local maximum after subtracting the resistivity data of the isostructural LuT_2Zn_{20} (T = Fe, Ru, Os, Ir, and Rh) compounds. The local maximum temperatures, T^ρ_{max}, taken from Ref. [Mun, 2010a] are plotted in Fig. 4.7 (a). Although the absolute value of the peak temperatures are different, a systematic variation of T^ρ_{max} follows the same trends of T^S_{min} and T^γ_K for varying transition metals.

In a Kondo lattice system, a single minimum developed in $S(T)$ is expected when T_K is either close to or higher than Δ/k_B. Typically, an intermediate valence system such as $YbAl_3$ [Foiles, 1981] and $YbCu_2Si_2$ [Andreica, 1999] and a fully degenerate Kondo lattice system such as $Yb_2Pt_6Al_{15}$ [Deppe, 2008] exhibit a single minimum in the TEP, developing below T_K. When $T_K < \Delta/k_B$, more than one peak has been frequently observed in the TEP [Andreica, 1999; Huo, 2001; Wilhelm, 2004; Köhler, 2008]. The low temperature extremum is usually located close to T_K, and the high temperature extremum located at 0.4-0.6 Δ/k_B is attributed to Kondo scattering off of the thermally populated CEF levels, which is in agreement with theoretical predictions [Bhattacharjee, 1976; Maekawa, 1986; Bickers, 1985; Mahan, 1997; Zlatić, 2003; Zlatić, 2005]. Therefore, the peak position can represent T_K and Δ/k_B as relevant energy scales in Kondo lattice systems.

For the YbT_2Zn_{20} family, T_K and the ground state degeneracy play important roles in the thermodynamic and transport properties. By considering the ground state degeneracy ($N=8$ for T = Fe and Ru, and $N=4$ for T = Os, Rh, Ir, and Co [Torikachvili, 2007]) it is expected that $T_K \gtrsim \Delta/k_B$ for T = Fe and Ru and $T_K \lesssim \Delta/k_B$ for T = Os, Ir, Rh, and Co. Based on this, for T = Fe and Ru, it is reasonable to assume that T^S_{min} and T^ρ_{max} simply reflect T_K; with the fully degenerate case corresponding to $N=8$. For T = Os, Ir, Rh, and Co, the two extrema in the $S(T)$ data associated with Kondo scattering on the ground state and thermally populated CEF levels could be expected, however, only one broad peak structure is developed for T = Os, Ir, Rh, and Co. We thus expect that a single broad minimum is produced by merging more than one peak structure due to the relatively small CEF level splitting ($T_K \sim \Delta/k_B$). A strong correlation between the two local extrema T^ρ_{max} and T^S_{min} develops and remains robust even when dependence on T_K appears to break down (Fig. 4.7 (b)). It is worth noting that

(i) $T_{max}^{\rho} \sim 2\,T_{min}^{S}$ for T = Fe, Ru, Os, Ir, and Rh and (ii) for T = Os, Ir, Rh, and Co $T_{min}^{S} \sim T_K$ and $T_{max}^{\rho} \sim 2\,T_K$.

As shown in Fig. 4.5 the magnetic field dependence of the TEP observed in YbT_2Zn_{20} (T = Fe, Ru, and Ir) is anomalous. In the simplest case of a two band model, the carrier density of electrons, n_e, and holes, n_h, can be taken as $\frac{1}{2}n = n_e = n_h$. The diffusion TEP in magnetic field with several assumptions [Sondheimer, 1948] can be expressed as

$$\Delta S = S(H) - S(0) = -S(0)\frac{\Upsilon^2 H^2 \zeta(1+\zeta)}{1+\Upsilon^2 H^2 \zeta^2}$$

where $\Upsilon = 1/nec\rho(0)$, and $\zeta = L_n/L_0$ with $L_n = \frac{1}{3}(\pi k_B/e)^2$ and $L_0 = \kappa(0)/\sigma(0)T$ (Lorentz number); $\sigma(0) = 1/\rho(0)$ and $\kappa(0)$ are the electrical conductivity and thermal conductivity, respectively, in zero magnetic field. At low temperatures $L_0 = L_n$, $\rho(0) = \rho_0$ (the residual resistivity), and the diffusion TEP in zero magnetic field is proportional to the temperature, $S(0) \propto T$. Therefore, for simple metals $\Delta S = 0$ when $T = 0$, and for very low temperatures $\Delta S \propto T$. At high temperatures $L_0 = L_n$, and $S(0)$ and $\rho(0)$ are both proportional to temperature, so that ΔS tends to zero like $1/T$ as $T \to \infty$. In general, the change in the TEP will be too small to be detected at room temperature. Since the magnetoresistance (MR) for T = Fe and Ru is positive and increases monotonically at $2\,K$ for $\mathbf{H} \parallel [111]$ up to $140\,kOe$ [Mun, 2010a], the change of the TEP (ΔS) should increase or saturate with increasing magnetic field. The field dependence of the TEP is not consistent with the MR results. Generally, the phonon-drag itself is not sensitive to the applied magnetic field [Blatt, 1976], so it is clear that neither conventional phonon-drag nor diffusion TEP of conduction electrons can account for the magnetic field dependence of the TEP in these compounds. Thus, multiple factors, such as the Kondo effect and CEF contributions, have to be considered. In order to understand the observed behavior in more detail, a theoretical analysis of the TEP as a function of field for this systems will be necessary.

Earlier thermodynamic and transport measurements [Torikachvili, 2007] showed that the R_W and K-W ratios of YbT_2Zn_{20} agree well with the FL picture of the HF ground state. A clear dependence of the A/γ^2 ratio on the degeneracy N is shown in the inset of Fig. 4.8, where the A and γ values are taken from Ref. [Torikachvili, 2007] and lines for degeneracies N are based
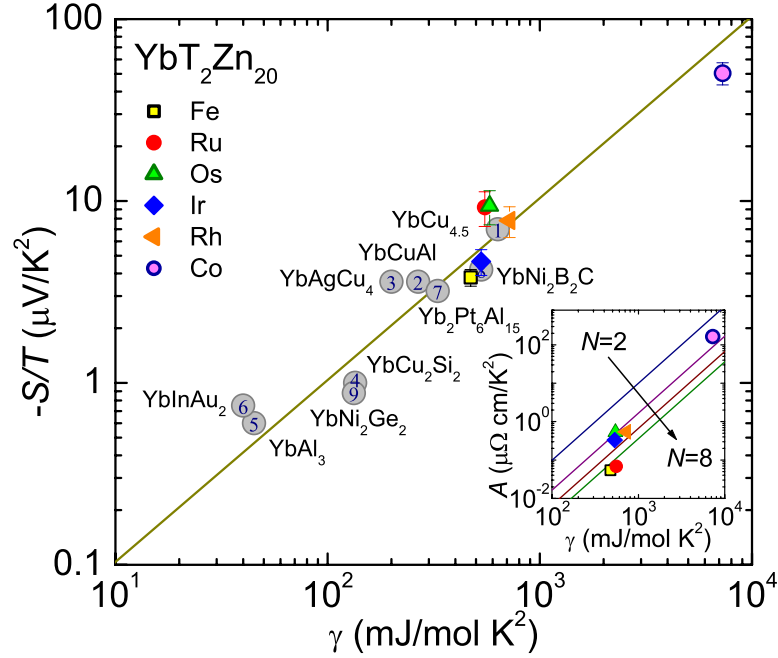
Figure 4.8 $-S(T)/T|_{T\to 0}$ vs. γ (log-log) plot of YbT_2Zn_{20} (T = Fe, Ru, Os, Ir, Rh, and Co).   The zero temperature limit of $S(T)/T$ and γ for (1) $YbCu_{4.5}$, (2) YbCuAl, (3) $YbAgCu_4$, (4) $YbCu_2Si_2$, (5) $YbAl_3$, and (6) $YbInAu_2$ are taken from the table of Ref.   [Behnia, 2004]. $S(T)/T$ and γ of (7) $Yb_2Pt_6Al_{15}$ are taken from Ref.   [Deppe, 2008]. $S(T)/T$ and γ of (8) $YbNi_2B_2C$ and (9) $YbNi_2Ge_2$ are taken from Refs. [Li, 2006; Bud'ko, 1999; Mun, 2010a], respectively.   The solid line represents $\gamma/(eN_A)$.   Inset: Kadowaki-Woods plot (log-log plot of A vs. γ) of YbT_2Zn_{20}.   Symbols are taken from Ref. [Torikachvili, 2007] and solid lines correspond to $N = 2, 4, 6,$ and 8 based on Ref.   [Tsujii, 2005], respectively.

on Ref. [Tsujii, 2005]. A Fermi liquid state can also be characterized by the ratio between γ and the zero temperature limit of $S(T)/T$ [Behnia, 2004; Grenzebach, 2006; Zlatić, 2007]: a "quasi universal" ratio $q = N_A e S/\gamma T$ remains close to $q = \pm 1$ for metals and the sign of q depends on the type of carriers. Although for strongly correlated electronic materials like HF systems, a single band and single scattering process is not generally thought to be sufficient for explaining the strong correlation effects, given that $C(T)/T$ and $S(T)/T$ are most sensitive to the position of the heavy band, a quasi universal ratio is expected to hold at low temperatures [Miyake, 2005; Kontani, 2003].

The experimental correlation between the zero temperature limit of $S(T)/T$ and γ for YbT$_2$Zn$_{20}$ (T = Fe, Ru, Os, Ir, Rh, and Co) is presented in Fig. 4.8, where the phonon-drag effect is ignored since it is small. For comparison, data for several other Yb-based HF compounds are also plotted in the same figure [Behnia, 2004a]. The calculated q values of Yb-based compounds vary from -0.77 for T = Fe to -1.4 for T = Rh, which are close to the value q = -1, expected for hole-like charge carriers. As shown in the figure, each data point is close to a line represented by q = -1 which means that the zero temperature limit of $S(T)/T$ is strongly correlated to γ due to the enhanced density of state at the Fermi level; the larger density of states at the Fermi level results in a larger γ and $S(T)/T|_{T\rightarrow 0}$.

4.4   Summary

The thermoelectric power measurements on the YbT$_2$Zn$_{20}$ (T = Fe, Ru, Os, Ir, Rh, and Co) compounds are in agreement with the behavior observed in many heavy fermion Kondo lattice systems. The evolution of the local minimum in $S(T)$ and the local maximum (coherence temperature) in $\rho(T)$ with variation of the transition metals can be understood based on the energy scale of Kondo temperature in conjunction with the influence of the crystalline electric field splitting. The large value of $S(T)/T$ in the zero temperature limit can be scaled with the electronic specific heat coefficient, γ, which is reflected by a strong correlation via the universal ratio $q = N_A eS/\gamma T$ and confirms the validity of Fermi-liquid descriptions.

CHAPTER 5.   Thermoelectric Power Investigations of YbAgGe across the Quantum Critical Point

5.1   Introduction

Intensive study of strongly correlated electronic systems (SCES) has revealed the existence of quantum phase transitions from ordered states to disordered states driven by non-thermal control parameters such as chemical doping, pressure, and magnetic field [Gegenwart, 2008]. In the quantum critical regime, these systems can manifest non-Fermi liquid (nFL) behavior: the exponent of electrical resistivity, $\Delta\rho = AT^n$, has $n < 2$ and the electronic specific heat coefficient, $\gamma = C(T)/T|_{T\to 0}$, is either singular, so the effective mass diverges in the zero temperature limit, $C(T)/T \propto$ -log(T), or has a non-analytic dependence on temperature, so the effective mass is finite $C(T)/T \propto$ -$\sqrt{T}$ [Stewart, 2001]. Among SCES, nFL behavior near a quantum critical point (QCP) has explicitly been identified for heavy fermion (HF) metals such as CeCu$_{6-x}$Au$_x$ [Löhneysen, 1994] which becomes magnetic when the Au atom is replaced Cu site ($x \sim 0.1$); CePd$_2$Si$_2$ [Mathur, 1998] in which the Néel temperature, T_N, is suppressed and superconductivity is induced by applying pressure; and YbRh$_2$Si$_2$ [Trovarelli, 2000] and YbAgGe [Bud'ko, 2004] both of which have antiferromagnetic (AFM) order which is suppressed by the application of an external magnetic field. When the system is tuned away from (beyond) the QCP, resistivity and specific heat indicate a recovery of the Fermi liquid (FL) state.

Systematic thermodynamic and transport measurements of YbAgGe have shown that the behavior of this compound in the vicinity of the QCP differs from that of other examples of field-induced quantum criticality. The hexagonal HF metal YbAgGe, with a Kondo temperature of $T_K \sim 25$ K, orders antiferromagnetically below ~ 1 K [Bud'ko, 2004; Katoha, 2004]. The $H-T$ phase diagram of YbAgGe for $\mathbf{H} \parallel \mathbf{ab}$ is shown in Fig. 5.1, constructed from the electrical resis-
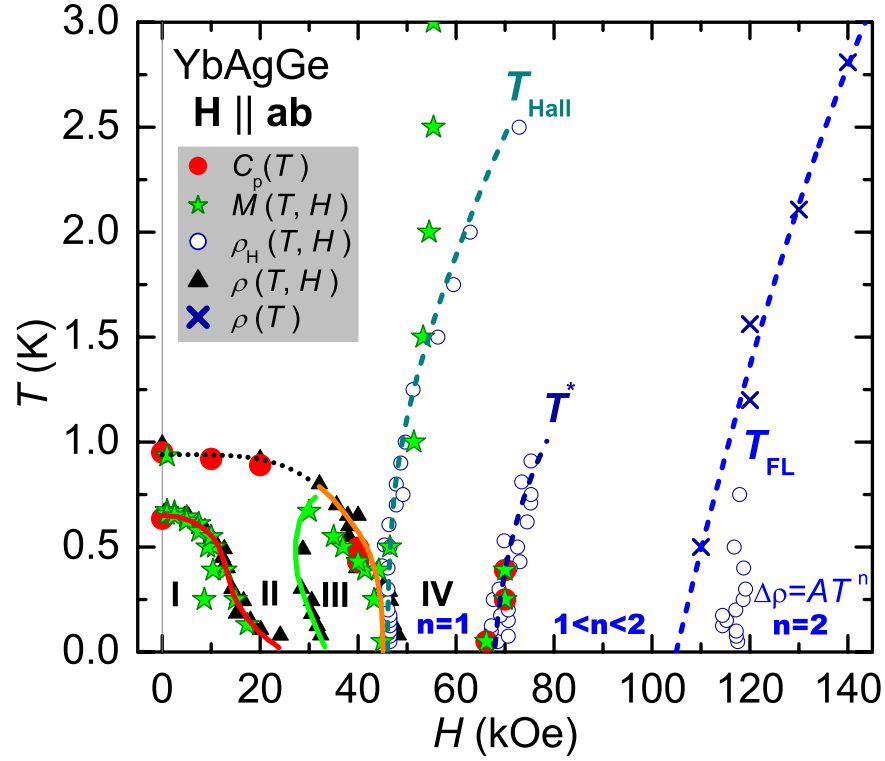
Figure 5.1 $H - T$ phase diagram of YbAgGe for $\mathbf{H} \parallel \mathbf{ab}$, constructed from the specific heat $C_p(T)$ [Bud'ko, 2004; Tokiwa, 2006], magnetizaion $M(T, H)$ [Tokiwa, 2006], Hall resistivity $\rho_H(T, H)$ [Bud'ko, 2005a], and resistivity $\rho(T, H)$ [Bud'ko, 2004; Niklowitz, 2006] measurements. Thick solid- and dotted-lines represent the magnetic phase boundaries. Dashed-lines T_{Hall} and T^* are the crossover lines determined from the thermodynamic and transport measurements. The Fermi liquid region denoted by the dashed, T_{FL} crossover line was determined from the region satisfying $\Delta\rho = AT^2$. See text for details.

tivity ($\rho(T, H)$) [Bud'ko, 2004; Niklowitz, 2006], magnetizaion ($M(T, H)$) [Tokiwa, 2006], specific heat ($C_p(T)$) [Bud'ko, 2004; Tokiwa, 2006], and Hall resistivity ($\rho_H(T, H)$) [Bud'ko, 2005; Bud'ko, 2005a] measurements. Thermodynamic and transport measurements show that there is a first order transition below $0.6\,\mathrm{K}$ in zero field [Bud'ko, 2004; Tokiwa, 2006; Umeo, 2004] as well as either AFM order below $0.8 \sim 1\,\mathrm{K}$ or a crossover region between $0.6 \sim 1\,\mathrm{K}$. The AFM order can be suppressed by applying magnetic field of $H_c \geq 45\,\mathrm{kOe}$. Inside the AFM state, for $H < H_c$, there are three different regions. The first order phase boundary of region I is clearly evidenced from $\rho(T, H)$ and $M(T, H)$ with hysteresis. The lower field side of the phase boundary of region III was inferred primarily from $\rho(H)$ measurements, whereas the top and higher field side of the phase boundary are observable in all thermodynamic and transport measurements, without any detectable hysteresis. The top boundary of region II, denoted by the dotted-line, has been inferred from broad features in $C_p(T)$ and $\rho(T)$ measurements. However, as magnetic field increases this top boundary evolves into clear, sharp features that form the high field side of region III.

The crossover lines, T_{Hall} and T^*, were inferred from the slope changes in $\rho_H(H)$ data [Bud'ko, 2005; Bud'ko, 2005a] and supported by features in $M(T, H)$ and $C_p(T)$ [Tokiwa, 2006] data. A detailed power law analysis of $\rho(T)$ [Niklowitz, 2006], $\rho(T) = \rho_0 + AT^n$, results that the exponent $n = 1$ for $45 \lesssim H \lesssim 70\,\mathrm{kOe}$ (region IV in Fig. 5.1), the exponent n gradually increases from 1 to 2 for $70 \lesssim H \lesssim 100\,\mathrm{kOe}$, and ultimately the FL region, denoted by the T_{FL} line in Fig. 5.1, emerges for $H > 100\,\mathrm{kOe}$, satisfying $\Delta\rho = AT^2$ [Niklowitz, 2006]. Note for $\mathbf{H} \,\|\, \mathbf{c}$ that the AFM order can also be suppressed for $H \sim 90\,\mathrm{kOe}$ and FL state is recovered for $H > 150\,\mathrm{kOe}$ [Bud'ko, 2004; Niklowitz, 2006].

When a QCP is approached, either by varying temperature or magnetic field, from the FL state, a strong nFL signatures were observed; $\Delta\rho(T) = AT$ in region IV and $C(T)/T \propto$ -$\log(T)$ is clearly found for $H \simeq 80\,\mathrm{kOe}$. The magnetic structure has been identified from the neutron scattering experiments [Fåk, 2005; Fåk, 2006; McMorrow, 2008]; in zero field the magnetic structure described by a commensurate propagation vector $\mathbf{k}_1 = (1/3, 0, 1/3)$ [Fåk, 2005], in region II the magnetic structure changes to incommensurate with $\mathbf{k}_2 = (0, 0, 0.324)$ [Fåk, 2006],

and in region III the magnetic structure, with small staggered moment, is similar as those in region I [McMorrow, 2008], where the small ordered moment between 0.15 and 0.4 μ_B per Yb ion is either perpendicular or parallel to the **c**-axis.

In this chapter, we report the thermoelectric power (TEP) measurements on YbAgGe. Systematic measurements of the TEP through out the $H - T$ phase space of a field-induced QCP have been limited to few cases, only among stoichiometric compounds, in particular YbRh$_2$Si$_2$ [Hartmann, 2010] and CeCoIn$_5$ [Izawa, 2007]. In order to clarify the anisotropic TEP response, measurements of TEP in this work were performed with two different heat current directions.

5.2   Results

The temperature-dependent TEP, $S(T)$, of YbAgGe for both $\Delta T \parallel \textbf{ab}$ and $\Delta T \parallel \textbf{c}$ measured for $H = 0$ and $140\,\mathrm{kOe}$ are plotted in Fig. 5.2; for comparison $S(T)$ data for isostructural LuAgGe and TmAgGe are displayed in the inset. The $S(T)$ plot for LuAgGe is typical of those found in normal metals, consistent with resistivity and Hall coefficient measurements [Bud'ko, 2005; Morosan, 2004]. At high temperatures the absolute value of TEP for TmAgGe is smaller than that of LuAgGe, however the slope, $\mathrm{d}S(T)/\mathrm{d}T$, is similar for both compounds. In contrast to LuAgGe, the $S(T)$ data of TmAgGe manifest a broad peak around $25\,\mathrm{K}$, followed (upon warming) by sign change from positive to negative at $53\,\mathrm{K}$.

For YbAgGe, above $25\,\mathrm{K}$, a qualitatively similar temperature dependence for both ΔT-directions is seen for $S(T)$ in zero and high magnetic field, which is negative and reveals a broad local minimum around $T_{min} \sim 85\,\mathrm{K}$ with the TEP values between $-20 \sim -30\,\mu\mathrm{V/K}$, typical of those found in other Yb-based, Kondo lattice systems [Köhler, 2008]. At low temperatures the observed $S(T)$ is anisotropic; in zero field, $S(T)$ for $\Delta T \parallel \textbf{c}$ remains negative over the whole temperature range measured, whereas $S(T)$ for $\Delta T \parallel \textbf{ab}$ manifests sign reversals at $T_{SR} = 21$ and $9.5\,\mathrm{K}$. Sign changes at similar temperatures have been observed in ρ_H measurements [Bud'ko, 2005; Bud'ko, 2005a].

Figures 5.3 (a) and (b) show the low temperature $S(T)$ for $\Delta T \parallel \textbf{ab}$ and $\Delta T \parallel \textbf{c}$, respec-
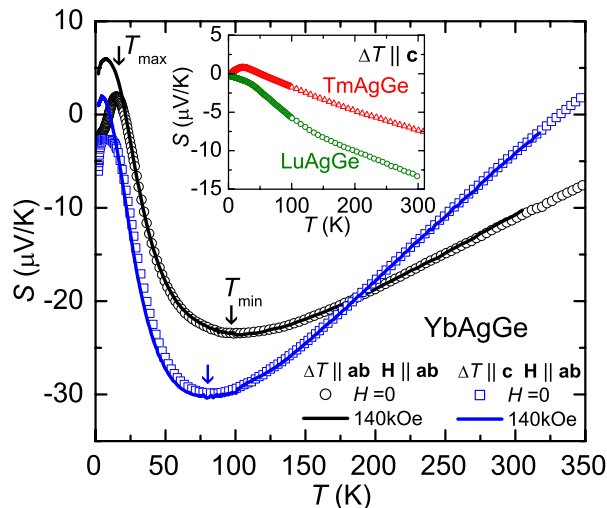
Figure 5.2 $S(T)$ of YbAgGe for $\Delta T \parallel \mathbf{ab}$ and $\Delta T \parallel \mathbf{c}$ at $H = 0$ (symbols) and $140 \, \mathrm{kOe}$ (lines), applied along hexagonal $\mathbf{ab}$-plane ($\mathbf{H} \parallel \mathbf{ab}$) in a transverse configuration, $\mathbf{H} \perp \Delta T$, for both heat flow directions. Arrows indicate the local minimum (T_{min}) and maximum (T_{max}) temperature. Inset: $S(T)$ of LuAgGe and TmAgGe at $H = 0$.

tively, in selected fields. In zero field the observed $S(T)$ data manifest rich and complex structures involving sign reversals, T_{SR} (not marked in Fig. 5.3), a clear maximum centered at $T_{max} \sim 15 \, \mathrm{K}$, a gradually decreasing TEP followed by plateau region (T_0), followed at lower temperature by a sharp drop, and finally a weak slope change and an abrupt change associated with the long range magnetic order $T_N \sim 0.8 \, \mathrm{K}$ and $T_{N1} \sim 0.65 \, \mathrm{K}$, respectively. As magnetic field increases, $S(T)$ reveals systematic changes of these anomalies: T_N, T_{N1}, T_{max}, and T_{SR}. The evolution of these features with magnetic field will be discussed in detail below. Similar features are apparent in the $\Delta T \parallel \mathbf{ab}$ and $\Delta T \parallel \mathbf{c}$ data sets. The biggest difference is that a clear positive peak at T_{max} develops for $\Delta T \parallel \mathbf{ab}$, whereas a shoulder occurs for $\Delta T \parallel \mathbf{c}$.

Below T_{max}, an inflection point around $T_0 \sim 5 \, \mathrm{K}$, determined as the local maximum in $\mathrm{d}S(T)/\mathrm{d}T$, is observed in zero field for both ΔT-directions. This characteristic temperature is also evident in the bulk magnetic susceptibility which shows a broad peak around $5 \, \mathrm{K}$ along $\mathbf{H} \parallel \mathbf{ab}$ [Morosan, 2004]. Neutron scattering experiments [Fåk, 2005] show that the characteristic energy scale $\Gamma_{\mathbf{q}}$ at the AFM zone boundary has a discontinuity at $T \sim 5 \, \mathrm{K}$. Whereas $\Gamma_{\mathbf{q}}$

Figure 5.3   Low-temperature $S(T)$ of YbAgGe for $\Delta T \parallel \mathbf{ab}$ (a) and $\Delta T \parallel \mathbf{c}$
(b) in selected fields, $H = 0$, 40, 50, 60, 70, 80, 90, 110 (only for
$\Delta T \parallel \mathbf{ab}$), 140 kOe (bottom to top), applied along the $\mathbf{ab}$-plane
in a transverse configuration ($\mathbf{H} \perp \Delta T$) for both heat flow di-
rections. Symbols and lines are taken from ^{4}He and ^{3}He mea-
surement setup, respectively. The local maximum temperature
T_{max}, inflection point T_0, magnetic order T_N and T_{N1}, and field-
-induced local maximum T^* are marked by arrows. Inset: (a)
Low-temperature $S(T)$ for $\Delta T \parallel \mathbf{ab}$ at $H = 0$, taken data both
warming up and cooling down the temperature. Arrow indicates
the phase transition temperature T_{N1}. Inset: (b) Low-temper-
ature $S(T)$ for $\Delta T \parallel \mathbf{c}$ at $H = 0$, taken data both warming up
and cooling down the temperature. Arrows indicate the phase
transition temperature T_{N1} and the local minimum tempera-
ture corresponding to T_N.

at the AFM zone center increases rapidly without any discontinuity as temperature increases, following $\sqrt{T}$ behavior usually shown in HF compounds such as $CuCu_6$ [Aeppli, 1986]. This particular $\mathbf{q}$-dependence of the strong antiferromagnetic spin fluctuations, may be a responsible for anisotropic TEP at low temperature, as well as the inflection at temperature T_0. Anisotropic TEP may also be related to the different scattering rate due to the anisotropic Fermi surface.

For $H > 70\,\mathrm{kOe}$ the development of local maximum at T^* can be clearly seen in $S(T)$ for both ΔT-directions, although it more clearly develops for $\Delta T \parallel \mathbf{c}$ than for $\Delta T \parallel \mathbf{ab}$. This maximum shifts to higher temperature as magnetic field increases. At least up to $90\,\mathrm{kOe}$ it seems to be clear that T_{max} is magnetic field-independent and T^* is approximately proportional to the magnetic field. At higher fields, above $110\,\mathrm{kOe}$, these two peaks merge into one peak structure. Note that a similar development of such a peak structure has also been observed in specific heat measurements in the similar temperature and magnetic field regime [Bud'ko, 2004; Tokiwa, 2006].

As is suggested in earlier studies, YbAgGe shows a broad feature at $T_N \sim 0.8$-$1\,\mathrm{K}$ and a sharp, first order phase transition at $T_{N1} \sim 0.65\,\mathrm{K}$ which manifest clear hysteresis in resistivity and magnetization measurements [Niklowitz, 2006; Tokiwa, 2006]. As shown in the inset of Fig. 5.3 (a) in zero field the $S(T)$ data for $\Delta T \parallel \mathbf{ab}$ show a sharp jump below $\sim 0.7\,\mathrm{K}$ (T_{N1}) without hysteresis within our measurement resolution ($\Delta T \sim 30\,\mathrm{mK}$). For $\Delta T \parallel \mathbf{c}$ (inset to Fig. 5.3 (b)) a broad local minimum is located near $T_N \sim 0.8\,\mathrm{K}$ and a sharp jump upward occurs at $T_{N1} \sim 0.6\,\mathrm{K}$. When magnetic field is applied, the shape of the anomaly at T_{N1} broadens and develops a clear hysteresis as it shifts to lower temperatures (see Fig. 5.4 below). The iso-magnetic field ($S(T)$) and isothermal ($S(H)$) data can be used to establish a $H - T$ phase diagram. The TEP response to a magnetic phase transition has not been well established and, in the case of AFM compounds, sometimes TEP shows no clear indication of the phase transition [Hartmann, 2010; Sakurai, 2002]. Hence, we present all $S(T)$ data for $\Delta T \parallel \mathbf{ab}$ in Fig. 5.4 and outline the criterion we have established for tracking transitions.

As shown in Fig. 5.4 (a), a sudden jump at T_{N1} is clearly seen for $H < 15\,\mathrm{kOe}$, that
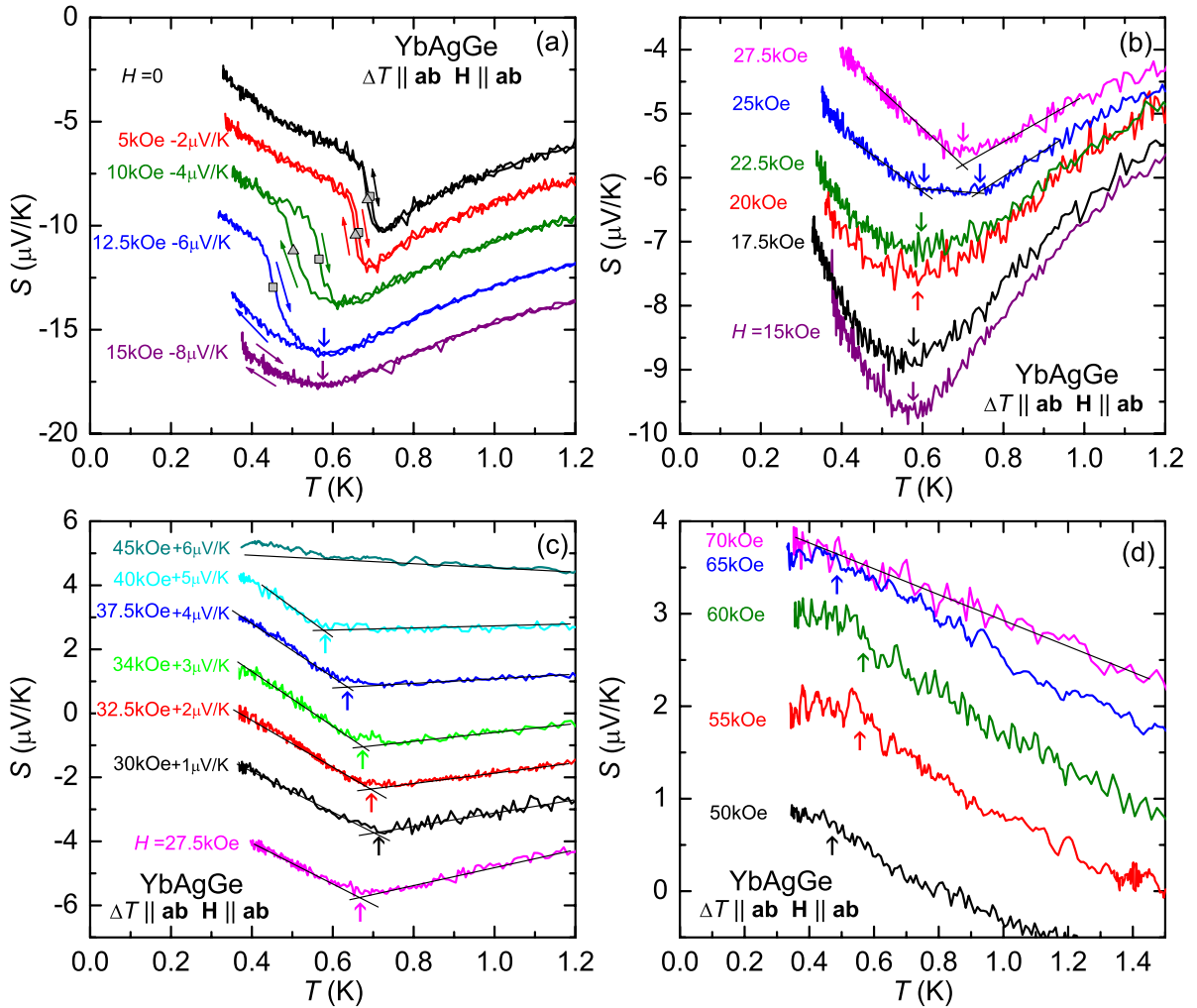
Figure 5.4   Low-temperature $S(T)$ of YbAgGe for $\mathbf{H} \parallel \mathbf{ab}$ and $\Delta T \parallel \mathbf{ab}$
($\mathbf{H} \perp \Delta T$). $S(T)$ curves in (a), (b), (c), and (d) correspond
to the region I, II, III, and IV in Fig. 5.1, respectively. $S(T)$
curves in (a) and (c) are shifted for clarity.   (a) Squares and
triangle symbols indicate phase transition temperatures deter-
mined from $dS(T)/dT$ and the arrows represent the local min-
imum. The data, taken for both warming and cooling the tem-
perature, are plotted. Arrows in (b), (c), and (d) indicate the
local minimum and slope change. The data are presented only
taken upon warming the temperature. Solid lines are guides to
the eye. See text for details.

corresponds to the boundary of region I in Fig. 5.1. Initially, the data were taken upon warming from the base temperature to $T > 1.5\,$K and then the data were collected upon cooling down to base temperature, allowing for evaluation of hysteresis. The critical temperature for this phase line was determined from the minimum of $\mathrm{d}S(T)/\mathrm{d}T$. The T_{N1} in zero field is suppressed to lower temperature and the hysteresis becomes significant as magnetic field increases. Note that a very large splitting between warming and cooling curves below $\sim 0.5\,$K is observed for $H = 12.5\,$kOe and a broad local minimum near $0.6\,$K begins to develop. The determined phase transition temperatures are plotted below in Fig. 5.8 as solid up-triangles for warming and solid down-triangles for cooling. As magnetic field increases (region II) the abrupt jump in $S(T)$ changes to a broad local minimum first seen for $H = 12.5\,$kOe (arrow in Fig. 5.4 (a)) and seen evolving in Fig. 5.4 (b). In this plot, only the data taken upon warming are plotted because no detectable hysteresis was observed for $H \geq 15\,$kOe, for example, as seen for $H = 15\,$kOe curves in Fig. 5.4 (a). It is not clear at present whether this minimum is a phase transition or a crossover. This minimum is denoted by solid circles in Fig. 5.8 below. At $H = 25\,$kOe two slope changes are observed near $0.6\,$K and $0.75\,$K. For higher fields, $25 < H < 45\,$kOe (Fig. 5.4 (c)), the broad minimum in region II becomes sharp and the slope change shifts to lower temperature with increasing magnetic field. This sharp slope change is indicated by arrows in Fig. 5.4 (c) and plotted in Fig. 5.8 (below) as solid squares.

For still higher fields, $45 < H < 70\,$kOe (Fig. 5.4 (d)), there is a weak slope change below $0.6\,$K. The slope change is most clearly seen in the $H = 55\,$kOe data and is indicated by arrows in Fig. 5.4 (d), and is represented in Fig. 5.8 (below) as stars. Note for $H = 70\,$kOe data, $S(T)$ increases linearly as temperature decreases without any slope change below $1.5\,$K. In this field regime, no clear feature of a phase transition has been detected in any of the earlier studies [Bud'ko, 2004; Niklowitz, 2006; Tokiwa, 2006; Bud'ko, 2005a]. However, a broad feature occurs in the magnetization and specific heat data [Tokiwa, 2006]. For further increasing magnetic field ($H > 70\,$kOe) a local maximum T^* develops as shown in Fig. 5.3 (a). The position of T^* was determined from a Gaussian curve fit to the $S(T)$ data and plotted in Fig. 5.8 (below) as the cross-symbols.
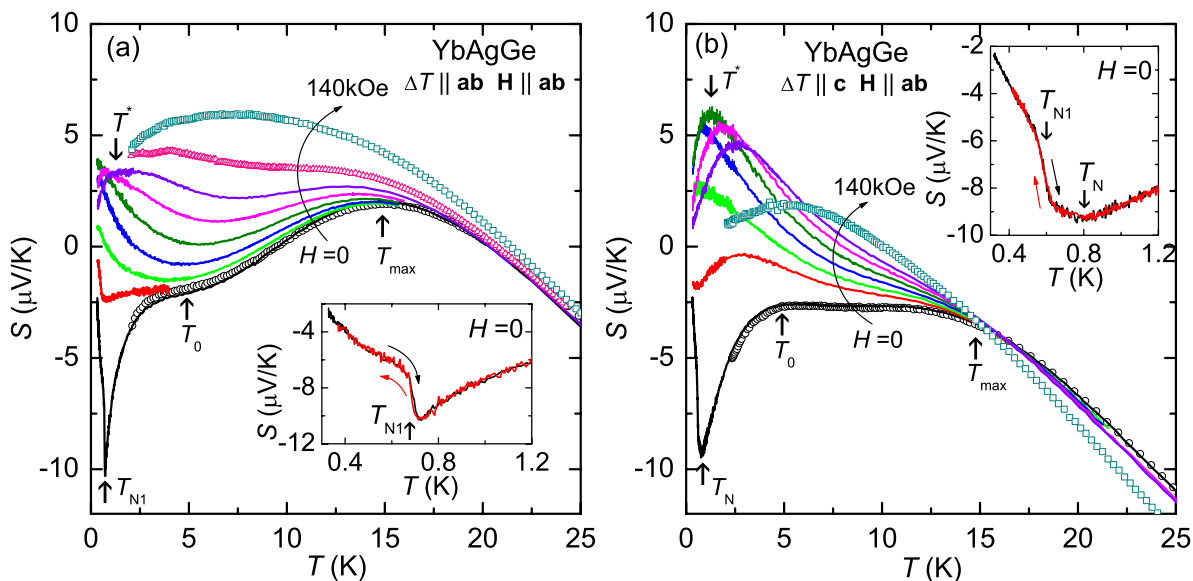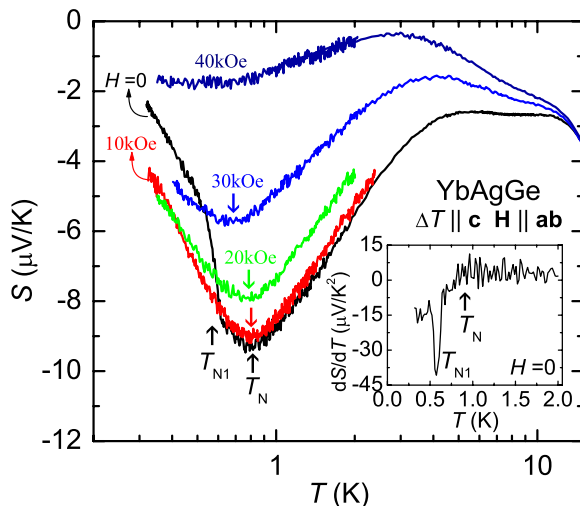
Figure 5.5   Low-temperature $S(T)$ of YbAgGe for $\mathbf{H} \parallel \mathbf{ab}$ and $\Delta T \parallel \mathbf{c}$. In zero-field up-arrows indicate the abrupt jump (T_{N1}) and local minimum (T_N), respectively, determined from $\mathrm{d}S(T)/\mathrm{d}T$ (inset). Down-arrows indicate the local minimum temperatures corresponding to the T_N. Inset: $\mathrm{d}S(T)/\mathrm{d}T$ at $H = 0$.

One of the most striking features of the $S(T)$ measurements is the different manifestations of the magnetic phase transitions for the two different directions of heat flow. When the AFM ordering takes place, $S(T)$ for $\Delta T \parallel \mathbf{c}$ manifests a broad minimum at $\sim 0.8\,\mathrm{K}$ which is close to the temperature identified as T_N from earlier studies of $C_p(T)$, $\rho(T)$, and $M(T)$ [Bud'ko, 2004; Tokiwa, 2006] and an abrupt jump without measurable hysteresis at $T_{N1} \sim 0.6\,\mathrm{K}$ as shown in the inset of Fig. 5.3 (b). As magnetic field increases (Fig. 5.5), T_N shifts to lower temperature and it is completely suppressed for $H > 50\,\mathrm{kOe}$, whereas the feature identified as T_{N1} fades away very rapidly and is not detected for $H > 10\,\mathrm{kOe}$. The evolution of T_N with varying magnetic field are shown in Fig. 5.5, where the arrows are determined from $\mathrm{d}S(T)/\mathrm{d}T$ (inset, Fig. 5.5). These phase boundaries are plotted in Fig. 5.8 as open up-triangles for T_N and open circle for T_{N1}. Note for the $H = 40\,\mathrm{kOe}$ curve that the local minimum at this magnetic field is not discernible, instead $S(T)$ flattens below $\sim 0.6\,\mathrm{K}$.

Figures 5.6 (a) and (b) show the field-dependent TEP, $S(H)$, at selected temperatures. $S(H)$ measurements provide orthogonal cuts through the $H-T$ phase diagram (Fig. 5.1) and shed further light on some of the features observed in $S(T)$. For $\Delta T \parallel \mathbf{ab}$ at $T = 0.4\,\mathrm{K}$ (Fig.
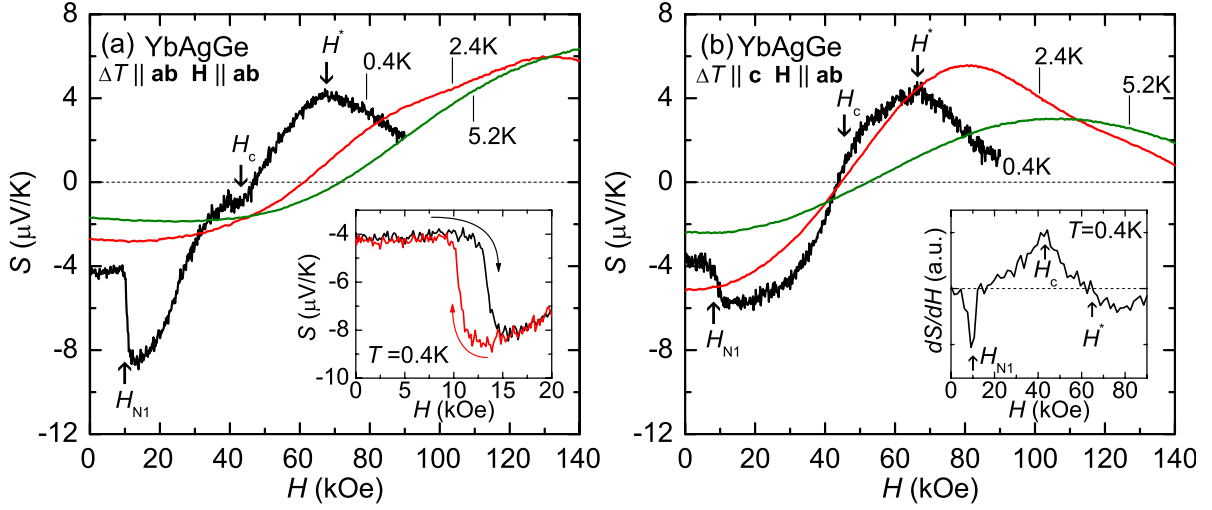
Figure 5.6 $S(H)$ of YbAgGe for $\Delta T \parallel \mathbf{ab}$ (a) and $\Delta T \parallel \mathbf{c}$ (b) at selected temperatures of 0.4, 2.4, and 5.2 K, and for magnetic field applied along $\mathbf{H} \parallel \mathbf{ab}$ in a transverse configuration ($\mathbf{H} \perp \Delta T$). Arrows indicate phase transitions (H_c and H_{N1}) and local maximum field (H^*), determined from $\mathrm{d}S(H)/\mathrm{d}H$. Inset: (a) $S(H)$ for $\Delta T \parallel \mathbf{ab}$ at 0.4 K, taken data with both increasing and decreasing magnetic field. (b) $\mathrm{d}S(H)/\mathrm{d}H$ for $\Delta T \parallel \mathbf{c}$ at 0.4 K.

5.6 (a)), $S(H)$ data show a sudden jump at $H_{N1} = 13$ kOe which is hysteretic (inset) and a slope change around $H_c = 42$ kOe. In addition, a broad maximum appears at $H^* \sim 68$ kOe. Note that H_{N1}, H_c, and H^* were determined from $\mathrm{d}S(H)/\mathrm{d}H$ analysis by a sharp peak, slope change (or minimum), and $\mathrm{d}S(H)/\mathrm{d}H = 0$, respectively. Although an anisotropic response of $S(H)$ to the magnetic field is observed for the two different directions of heat flow, the characteristic magnetic fields for the long range magnetic order and the crossover field H^* remain qualitatively the same for both ΔT-directions: for $\Delta T \parallel \mathbf{c}$ at $T = 0.4$ K shown in Fig. 5.6 (b), $S(H)$ data show distinct features at ~ 10 kOe and ~ 67 kOe corresponding to H_{N1} and H^* for $\Delta T \parallel \mathbf{ab}$, respectively. A very weak slope change around 42 kOe corresponding to H_c for $\Delta T \parallel \mathbf{ab}$ is also observed, where the derivative $\mathrm{d}S(H)/\mathrm{d}H$ (inset) clearly shows a slope change (or maximum) around 42 kOe. The phase transition fields, H_{N1} and H_c, for $\Delta T \parallel \mathbf{c}$ are represented by open-triangles ($\triangleright$) in Fig. 5.8. Note that the lower field boundary of region III in Fig. 5.1 was not observed in TEP measurements for either ΔT-direction, where $S(H)$ varies

without any kink or significant slope change from 15 to 40 kOe. For $\Delta T \parallel \mathbf{c}$, the H^* evolve in basically the same way as for $\Delta T \parallel \mathbf{ab}$. Note that $S(H)$ for $\Delta T \parallel \mathbf{c}$ shows an additional broad feature near ~ 90 kOe for $T = 2.4$ K curve.
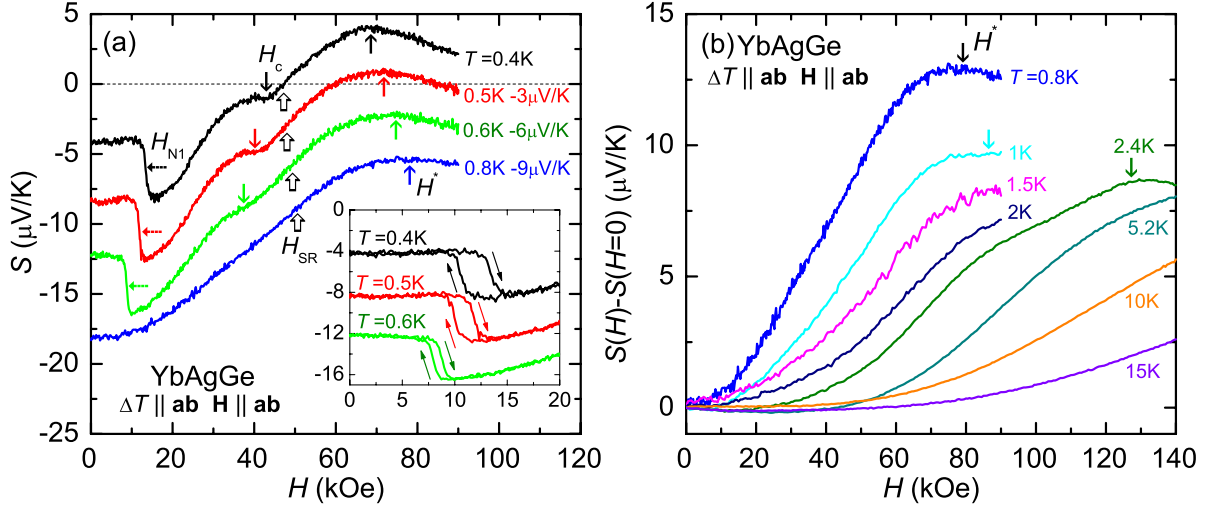
Figure 5.7 $S(H)$ of YbAgGe for $\Delta T \parallel \mathbf{ab}$ and for magnetic field applied along $\mathbf{H} \parallel \mathbf{ab}$ in a transverse configuration ($\mathbf{H} \perp \Delta T$). (a) $S(H)$ at 0.4, 0.5, 0.6, and 0.8 K, taken data with increasing magnetic field. Curves for $T = 0.5$, 0.6, 0.8 K are shifted for clarity. Arrows indicate phase transitions H_{N1} ($\leftarrow$) and H_c ($\downarrow$), a sign reversal ($\Uparrow$), and a local maximums H^* ($\uparrow$). Inset: hysteresis curves of $S(H)$ measurements at $T = 0.4$, 0.5, and 0.6 K. (b) Normalized TEP ($S(H) - S(H = 0)$) as a function of H at $T = 0.8$, 1, 1.5, 2, 2.4, 5.2, 10 and 15 K. Arrows indicate a local maximum H^*.

The evolution of H_{N1}, H_c, and H^* for $\Delta T \parallel \mathbf{ab}$ are shown in Figs. 5.7 (a) and (b). As temperature increases H_{N1} and H_c shift to lower magnetic fields and H^* moves to higher magnetic fields. The arrows, $\leftarrow$, $\downarrow$, and $\uparrow$, are represented by symbols, $\blacktriangleright$, $\blacklozenge$, and $+$, respectively, in Fig. 5.8. When the temperature is lowered, the hysteresis at H_{N1} is more pronounced as shown in the inset of Fig. 5.7 (a).

Since TEP in zero field manifests a sign reversal at low temperatures and the possibility of a sign reversal at the QCP has been proposed [Kim, 2010], it is of interest to see the evolution of the TEP sign change as the system is tuned by magnetic field (Fig. 5.7 (a)). For $\Delta T \parallel \mathbf{ab}$ the negative TEP sign in zero field changes to positive for $H_{SR} > 47$ kOe at 0.4 K. The H_{SR} at

0.4 K shifts to higher fields as temperature increases, indicated by the large, open arrows in Fig. 5.7 (a). The sign reversal temperatures obtained from $S(T, H)$ measurements for $\Delta T \parallel \mathbf{ab}$ are plotted in Fig. 5.8 as ×-symbols. Note that the sign reversal of TEP for $\Delta T \parallel \mathbf{c}$ is essentially similar to that for $\Delta T \parallel \mathbf{ab}$ below 2 K. At 0.4 K the TEP sign for $\Delta T \parallel \mathbf{c}$ changes from negative to positive for $H > 44$ kOe (Fig. 5.6 (b)).

5.3 Discussion

At low temperatures, TEP measurements on YbAgGe indicate complex sign variations as temperature and magnetic field vary. For $\Delta T \parallel \mathbf{ab}$, in zero field (Fig. 5.3 (a)) the sign reversal in $S(T)$ occurs at $T_{SR} = 21$ and 9.5 K. As magnetic field increases T_{SR} shown at 21 K moves to slightly higher temperatures, T_{SR} at 9.5 K moves down and a third sign reversal occurs at lower temperatures: $H_{SR} = 47$ kOe at 0.4 K (Fig. 5.7 (a)). For $\Delta T \parallel \mathbf{c}$, in zero field TEP remains negative for all $T < 300$ K (Fig. 5.2), but, at low temperatures, it moves gradually to positive with increasing magnetic field, becoming positive for $H_{SR} > 44$ kOe at 0.4 K (Fig. 5.6 (b)). Similar behavior, but with opposite sign change, has been observed in ρ_H measurements [Bud'ko, 2005; Bud'ko, 2005a]. As temperature decreases, the Hall coefficient, ρ_H/H, remains positive down to 50 mK for $\mathbf{H} \parallel \mathbf{ab}$ and the Hall voltage along (approximately) the $\mathbf{c}$-axis, whereas a sign reversal from positive to negative is observed for $\mathbf{H} \parallel \mathbf{c}$ and the Hall voltage in the $\mathbf{ab}$-plane. At this stage it is difficult to explain low temperature sign reversal for both $S(T)$ and ρ_H/H which may arise from the multisheet Fermi surface of electrons and holes with different mobilities. The conductivity change is mainly determined by the change in the electron velocity at the Fermi level and the sign of the derivative of density of states (DOS) does not depend on the sign of the velocity but depends on the curvature of the dispersion of quasi-particles [Blatt, 1976; Ziman, 1960]. This may explains the discrepancy of sign between TEP and Hall coefficients of YbAgGe; $S > 0$ and $\rho_H/H < 0$ at high temperatures. At low temperatures, an explanation of the complex sign reversal in the TEP is not simple because one should be considered all band contribution with a relevant weight of heavy and light carriers.

TEP is known to be particularly sensitive to Kondo (T_K) and crystalline electric field (CEF, Δ_{CEF}) effects, and to various physical quantities related to the DOS because of the energy dependence formula at the Fermi level [Blatt, 1976]: $S = -\frac{\pi^2 k_B^2 T}{3e}(\frac{\partial ln\sigma(\varepsilon)}{\partial \varepsilon})_{\varepsilon_F}$, where e is the elementary charge, ε_F is the Fermi energy, and $\sigma(\varepsilon)$ is the transport integral. Although TEP can probe various salient energy scales, the interpretation of its temperature and magnetic field dependence is often difficult, even for simple metals. Since a quantitative analysis of TEP is very difficult, we assumed that the present TEP data reflect the remaining $4f$ magnetic contribution of trivalent Yb-ions, especially the position of the local extrema, the large absolute value, and the abrupt change associated with long range magnetic order.

The characteristic temperatures, T_{max} and T_{min}, allow for the evaluation of T_K and Δ_{CEF} as relevant energy scales in YbAgGe. In zero field, T_{max} and T_{min}, as shown in Fig. 5.2, can be related to Kondo scattering associated with the CEF ground state and the excited CEF multiplet levels, respectively. For HF Kondo lattice compounds, in general, it has been shown that the lower temperature maximum is close to T_K and the higher temperature minimum develops roughly within 0.3-0.6 Δ_{CEF}, which is in agreement with theoretical predictions [Bhattacharjee, 1976; Lassailly, 1985; Alami, 1999; Zlatić, 2005]. Inelastic neutron scattering experiments on YbAgGe have proposed the CEF level scheme with doublet levels located approximately at 0-140-230-330 K [Matsumura, 2004]. This scheme is consistent with the specific heat analysis (0-110-190-335K) involving combined Kondo effect ($T_K = 24$ K) and electronic Schottky contributions [Katoha, 2004]. Thus, the doublet ground state and T_K are well separated from the first excited CEF level. From the TEP measurements shown in Fig. 5.2 an estimate of the energy level splitting lies between 140 and 280 K with respect to the ground state doublet. The lower end of this range, $T_{min} \sim 0.6\,\Delta_{CEF}$, is very close to the value obtained in the inelastic neutron scattering and specific heat analysis. Thus, we conclude that T_{min} with the large, negative, absolute value can be attributed to Kondo scattering on an excited CEF multiplet of Yb^{3+}.

In general a phonon-drag contribution to the TEP appears between 0.1-0.3 Θ_D with a broad peak structure [Blatt, 1976; Elliott, 1972], where Θ_D is the Debye temperature. For

YbAgGe with $\Theta_D \sim 300\,\mathrm{K}$ [Morosan, 2004], T_{max} is far below the expected temperature due to the phonon-drag. For comparison, the TEP plots of the isostructural compounds, LuAgGe and TmAgGe, do not manifest any conspicuous signatures of phonon-drag either (inset to Fig. 5.2). LuAgGe has a slope change around $35\,\mathrm{K}$ ($\sim 0.12\,\Theta_D$), and TmAgGe, $S(T)$ shows a broad peak around $25\,\mathrm{K}$ expected due to either phonon-drag or CEF splitting. The absolute TEP value of both compounds is small compared to that of YbAgGe and the temperatures of anomalies seen for both compounds are higher than T_{max} for YbAgGe. Therefore, we expect that the origin of T_{max} is not the phonon-drag.

On the other hand, it seems reasonable that T_{max} is caused by the Kondo effect. In a number of HF compounds the Kondo effect manifests itself as a maximum in $S(T)$ in the vicinity of the T_K [Maekawa, 1986; Bickers, 1987; Očko, 2004]. In a similar way the resistivity curve of YbAgGe displays a characteristic behavior in which the resistivity decreases rapidly below $\sim 100\,\mathrm{K}$ expected due to the CEF effect and shows a hump below $25\,\mathrm{K}$ related to the development of coherent quasi-particles [Morosan, 2004]. We therefore assume that T_{max} in TEP measurements represents the crossover temperature (T_K) from local moment to HF behavior. A similar order of magnitude of T_K is also estimated from the specific heat and neutron scattering experiments. However, T_K obtained from TEP is smaller than the one obtained from the specific heat. Since T_K is not a phase transition temperature but a crossover, a different crossover temperature, but of similar order of magnitude, can be expected from different measurements.

Figure 5.8 shows the $H-T$ phase diagram based on the TEP measurements. All data points inferred from $S(T)$ track well the data inferred from $S(H)$ data. The closed-symbols are taken from $\Delta T \parallel \mathbf{ab}$ and open-symbols are taken from $\Delta T \parallel \mathbf{c}$, respectively. The TEP data are plotted on the top of the lines from Fig. 5.1. The clear agreement between TEP data and earlier thermodynamic and transport results indicates that TEP measurements can be a useful tool to refine and extend the $H-T$ phase diagram. The sign reversal ($\times$), shown for $45 < H < 65\,\mathrm{kOe}$, and local maximum ($+$), shown for $H > 70\,\mathrm{kOe}$, are taken from $\Delta T \parallel \mathbf{ab}$. The phase boundary of region I, showing the hysteresis from both $S(T)$ and $S(H)$ measurements, is consistent with
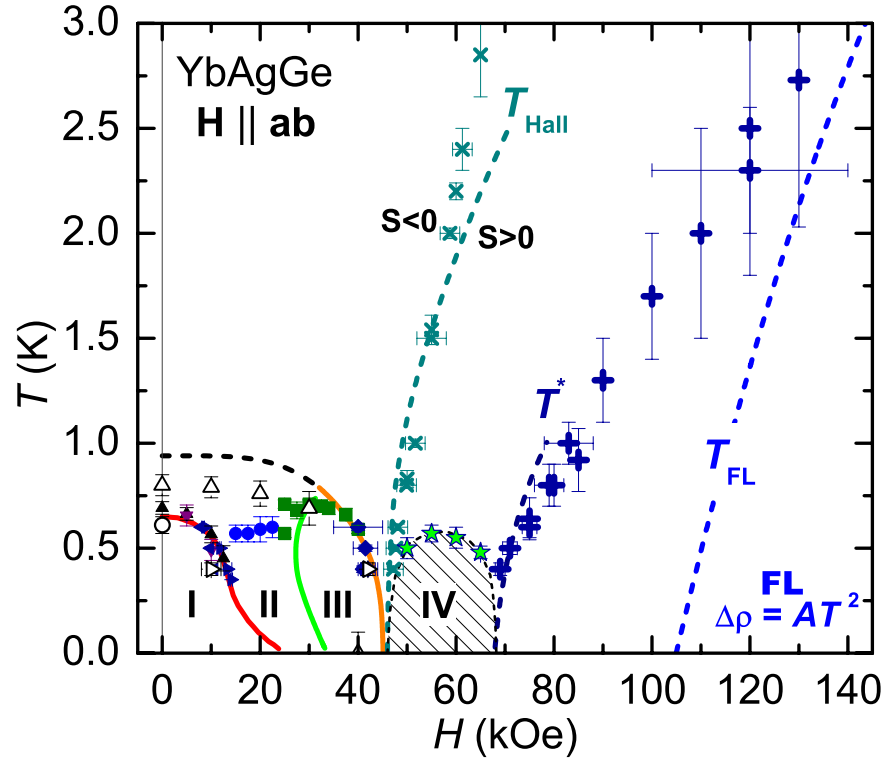
Figure 5.8 $H - T$ phase diagram of YbAgGe for $\mathbf{H} \,\|\, \mathbf{ab}$. Solid sym-
bols are inferred from $\Delta T \,\|\, \mathbf{ab}$ data and open symbols are
inferred from $\Delta T \,\|\, \mathbf{c}$ data, plotted on the top of phase and
crossover lines in Fig. 5.1; $\blacktriangle$ ($\triangle, \circ$) from up-sweeps in T, $\blacktriangledown$
from down-sweeps in T, $\blacktriangleright$ ($\triangleright$) from up-sweeps in H, $\blacktriangleleft$ from
down-sweeps in H, and other symbols ($\bullet$, $\blacksquare$, $\blacklozenge$, $\bigstar$, $\times$, $+$) from
up-sweeps in T and H. The $\times$-symbols indicate the sign re-
versal on TEP from negative to positive. The $+$-symbols cor-
respond to the local maximum developed in $S(T, H)$. The FL
region was taken from earlier $\rho(T)$ ($\Delta\rho = AT^2$) measurements
[Bud'ko, 2004; Niklowitz, 2006].

earlier studies. The top of region II, reflected by a broad local minimum in $S(T)$, may not be a phase transition but a crossover, since any clear signature of the phase transition in this temperature and magnetic field region has not been observed from earlier thermodynamic and transport measurements. The top and higher field boundary of region III are clearly seen in both $S(T)$ and $S(H)$ data; this phase transition line tends to go toward zero for $H_c \sim 45\,\mathrm{kOe}$.

The upper boundary (T_N) of region I and II was determined from the local minimum in $S(T)$ for $\Delta T \parallel \mathbf{c}$ (Fig. 5.5). It is clear that no signature of the upper boundary is observed for $\Delta T \parallel \mathbf{ab}$, which is similar to resistivity results [Niklowitz, 2006]. By contrast, the observed TEP for $\Delta T \parallel \mathbf{c}$ indicates both T_N and T_{N1} in zero field, which is very similar to the specific heat measurements [Bud'ko, 2004; Tokiwa, 2006]. As magnetic field increases, T_N shifts to lower temperature and seems to be suppressed for $H > 45\,\mathrm{kOe}$, merging together with the high magnetic field boundary of region III and the T_{Hall} crossover line.

In earlier versions of the YbAgGe $(H - T)$ phase diagram [Bud'ko, 2004; Niklowitz, 2006; Tokiwa, 2006; Bud'ko, 2005; Bud'ko, 2005a] two well separated crossover lines, T_{Hall} and T^*, were seen and the long range magnetic order was suppressed to zero at $H_c \simeq 45\,\mathrm{kOe}$. The T_{Hall} line is well matched with the sign reversal of the TEP and T^* follows the local maximum observed in $S(T, H)$ measurements (Fig. 5.8). The T^* shifts to higher temperature as magnetic field increases and the peak position roughly follows an anomaly shown in $C_p(T)$ measurements [Tokiwa, 2006]. Importantly, upon decreasing temperature $(T \to 0)$, the features associated with these crossover lines, obtained from all the thermodynamic and transport measurements, converge to the same magnetic field values of $H_c \sim 45\,\mathrm{kOe}$ and $H^* \sim 70\,\mathrm{kOe}$. Hence, it is expected that, when $T \to 0$, the sign of TEP will changes from negative to positive at $\sim 45\,\mathrm{kOe}$ for both ΔT-directions and a peak structure in $S(H)$ data will be developed at $\sim 70\,\mathrm{kOe}$ since the feature at H^* sharpens as temperature decreases.

It has been observed that the TEP measurements of $YbRh_2Si_2$ with a longitudinal configuration $(\mathbf{H} \parallel \Delta T)$ manifest a sign reversal across the field-induced QCP [Hartmann, 2010]. A recent theoretical work [Kim, 2010] proposed the possibility of such TEP sign reversal at the QCP and was applied to the $YbRh_2Si_2$. The sign reversal for $YbRh_2Si_2$ is present inside the

AFM state and terminates at the critical field, whereas the sign reversal for YbAgGe emerges at the critical field and persists up to high temperature. For $CeRu_2Si_2$ [Aoki, 1998], the positive TEP in zero field also changes sign above the metamagnetic field for $\Delta T \parallel \mathbf{c}$. Therefore, it is suggestive that the sign reversal can be an additional tool to probe and identify a QCP. Clearly, further theoretical and experimental investigations of this issue are required.

In addition to reproducing the earlier phase diagram in region I, II, and III, the TEP measurements also delineate a new region: IV. The high temperature boundary of the dome-like area, located between T_{Hall} and T^* crossover line (region IV, Fig. 5.8), was determined by a slope change of $S(T)$ (Fig. 5.4 (d)). In this region the temperature dependences and large absolute values of the TEP are significantly different from that expected for the normal metal. Thus, the observed TEP in region IV suggests an unconventional magnetic or electronic origin.

Between the T_{Hall} and T^* crossover lines hints of such a dome-like region were seen as broad features in earlier $M(H)$ and $C_p(T)$ studies, but not identified as a possible transition. For instance, upon increasing magnetic field, the magnetization divided by magnetic field, $M(H)/H$, shows a considerable decrease passing through this region [Tokiwa, 2006]. More significantly, the power law analysis of resistivity [Niklowitz, 2006] indicates a strong nFL behavior, $\rho(T) \propto T$, in this dome-like area, where the boundary of maximum temperatures satisfying $\Delta\rho \propto T$ coincides with the boundary of the region IV. Therefore, the detection of this newly identified, dome-like region appears to be robust in YbAgGe. When the magnetic field increases from AFM (region III) to this region with $\rho(T) \propto T$ (region IV), the lower field boundary of the dome-like region manifests as sudden jump in $M(H)/H$ and $C(T)/T$, as a sharp peak in magnetostriction (λ_{ab}) [Schmiedeshoff, 2010] and ρ_H/H, and as a sign change in $S(H)$, however the higher field boundary of the dome-like region manifests itself as a smooth evolution of $M(H)/H$, $C(T)/T$, λ_{ab}, and ρ_H/H and as a peak structure in $S(H)$. It is not clear at this point if the dome-like region is a magnetic field induced metamagnetic phase or electronic structure change (e.g. topology change of Fermi-surface). To clarify this mysterious region further microscopic measurements, such as neutron scattering experiments, will be needed.

It is worth noting that although this region has not been identified at ambient pressure, a similar region in the $H - T$ phase diagram has been identified in recent pressure measurements [Kubo, 2010]. At 0.95 GPa, region IV appears in the high magnetic field region between $\sim$ 45 and $\sim 65\,\text{kOe}$ and with increasing pressure (1.5 and 2.2 GPa) a new phase region between ~ 65 and $\sim 90\,\text{kOe}$ also develops. This behavior in the $H - T - P$ phase space has been associated with the partial release of the magnetic frustration in the quasi-kagome lattice of Yb ions under pressure [Kubo, 2010]. Note that recently, a finite range of nFL behavior, separating FL region from AFM state, has been observed from Ge- and Ir-doped $YbRh_2Si_2$ [Friedemann, 2009; Custers, 2010].
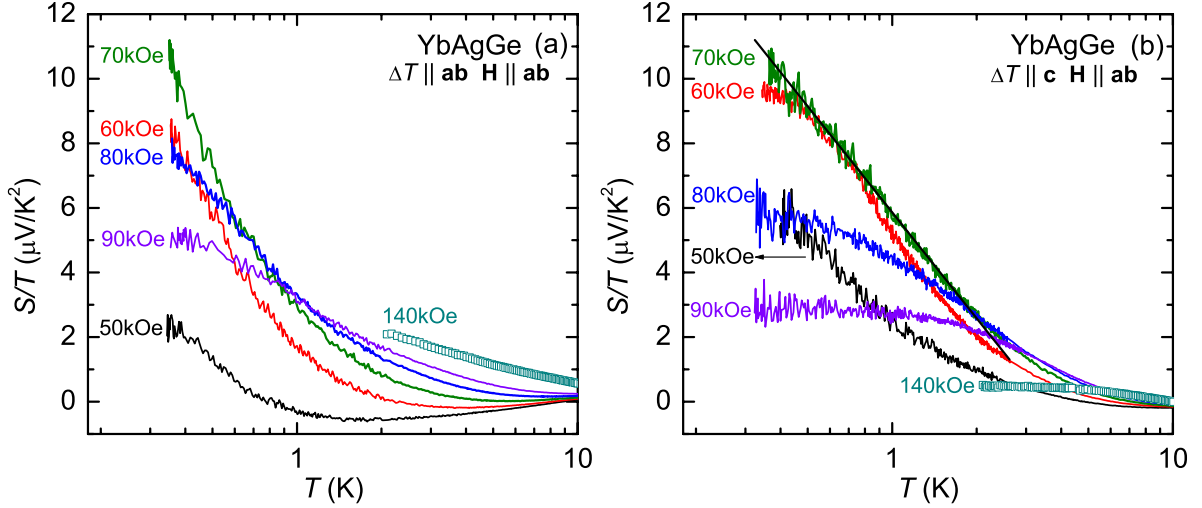
Figure 5.9 $S(T)/T$ of YbAgGe on a $\log(T)$ scale for both (a) $\Delta\,T \parallel \mathbf{ab}$ and (b) $\Delta\,T \parallel \mathbf{c}$ in selected magnetic fields, applied along $\mathbf{H} \parallel \mathbf{ab}$ in a transverse configuration ($\mathbf{H} \perp \Delta T$). Solid line in (b) on the top of 70 kOe data is a guide to the eye.

Inside the dome-like region IV, the TEP deviates from standard FL behavior, $S(T) = \alpha T$, where the observed $S(T)/T$ for both ΔT-directions does not show a tendency of saturation at low temperatures. As shown in Figs. 5.9 (a) for $\Delta\,T \parallel \mathbf{ab}$ and (b) for $\Delta\,T \parallel \mathbf{c}$, $S(T)/T$ increases inside region IV as magnetic field increases, reaching the maximum around 70 kOe, and then decrease with further increase of the magnetic field. It should be noticed that at $H = 70\,\text{kOe}$, $S(T)/T$ for $\Delta\,T \parallel \mathbf{c}$ manifests a clear, logarithmic temperature dependence as a signature of nFL

behavior over about an order of magnitude in temperature. This is consistent with the specific heat results that also manifest $C(T)/T \propto -\log(T)$ at similar fields [Bud'ko, 2004]. However, $S(T)/T$ for $\Delta T \parallel \mathbf{ab}$ increases more slowly than that for $\Delta T \parallel \mathbf{c}$ when temperature is lowered below 10 K. In order to clarify the existence of the logarithmic temperature dependence for $\Delta T \parallel \mathbf{ab}$ and to explore possibly of larger temperature range of such behavior, it is necessary to measure TEP below 0.3 K. Logarithmic temperature dependencies of specific heat and TEP in YbRh$_2$Si$_2$ [Hartmann, 2010] and CeCu$_{6-x}$Au$_x$ [Benz, 1999] has been observed in the vicinity of QCP, which are supported from the theoretical calculations based on the two-dimensional spin-density wave scenario [Paul, 2001]. In addition, the $\log(T)$ divergence is also explained by the $Z = 3$ quantum criticality of Fermi surface fluctuations of the Kondo breakdown scenario [Kim, 2010].

As shown in Fig. 5.1, a finite range of nFL behavior with $\Delta \rho = AT$ down to 75 mK appears between the T_{Hall} and T^* crossover lines and the FL behavior is recovered for $H > 100$ kOe [Niklowitz, 2006]. Between the T^* and T_{FL} crossover lines the exponent of resistivity increases from 1 to 2 as magnetic field increases. Therefore, the wide range of nFL behavior is robust in YbAgGe, in contrast to the general expectation of the field-tuned QCP in HF metals of which the FL behavior is recovered when long range magnetic order is suppressed to zero temperature ($T_N \rightarrow 0$). On the other hand, particularly for $\Delta T \parallel \mathbf{c}$, the TEP is proportional to the temperature below T^* crossover line. The constant α corresponding to a saturation of $S(T)/T$ is seen at least up to 1 K for $H = 90$ kOe and up to ~ 4 K for 140 kOe (Fig. 5.9 (b)). The observed large value of α in the zero temperature limit is characteristic of the HF state. The range with constant α is enlarged upon increasing field and the absolute value of α decreases, in agreement with the results of $C(T)/T$ [Bud'ko, 2004; Tokiwa, 2006]. Based on the constant α, reflecting the FL region, the crossover temperature (T_{FL}) from nFL to FL obtained from TEP does not coincide with the one determined from resistivity measurements [Niklowitz, 2006]. From the TEP results for $\Delta T \parallel \mathbf{c}$, AFM order and the FL state are not directly connected by a QCP, but are separated by the dome-like region IV. In order to clearly address this discrepancy between resistivity and TEP results as well as the anisotropic TEP

response for different heat current directions, it is necessary to measure TEP with magnetic field higher than 90 kOe and temperature down to mili-Kelvin range. Note that $S(T)/T$ for $\Delta T \parallel \mathbf{ab}$ is continuously suppressed for $H > 70$ kOe, indicating a tendency of saturation of α.

Up to this point several qualitative correlations between TEP and specific heat have been mentioned. More quantitatively, many HF compounds have shown correlations between $C(T)/T$ and $S(T)/T$ in the zero temperature limit, linking these two quantities via the dimensionless ratio $q = \frac{S N_A e}{\gamma T} \sim \pm 1$, where N_A is the Avogadro number and the constant $N_A e$ is called the Faraday number [Behnia, 2004]. Within the framework of the FL picture, both TEP and specific heat are linearly proportional to the temperature, leading to the low temperature saturation of $S(T)/T = \alpha$ and $C(T)/T = \gamma$. Fundamentally, this correlation can be linked to entropy considerations because the entropy is carried by the heat current due to temperature and electric potential gradients.

Since we are currently limited to TEP data down to 0.35 K, we compare $C(T)/T$ to $S(T)/T$ at $T = 0.4$ K. As shown in Fig. 5.10 (a), although $S(T)/T$ data (left axis) show somewhat different magnetic field dependence between $\Delta T \parallel \mathbf{ab}$ and $\Delta T \parallel \mathbf{c}$, especially for $H < 45$ kOe, the $S(T)/T$ data sets at $T = 0.4$ K are fundamentally similar. $C(T)/T$ data (right axis) at 0.39 K are taken from the Ref. [Tokiwa, 2006]. Figure 5.10 (b) presents q value as a function of magnetic field. In the vicinity of $H_c \sim 45$ kOe, q is much less than unity $(q \rightarrow 0)$ for both ΔT-directions. Basically the small q value near H_c is due to the small value of α, where the sign of TEP changes from negative to positive. As magnetic field increases, the q value increases inside the dome-like region, and then reaches order of unity at 70 kOe for both ΔT-directions. For $H > 70$ kOe q value for $\Delta T \parallel \mathbf{ab}$ remains close to the order of unity, whereas q value for $\Delta T \parallel \mathbf{c}$ decreases as magnetic field increases. The separation of q values is due to $S(H)/T$ data heading back toward to zero, amplifying of a relatively small difference between the $\Delta T \parallel \mathbf{ab}$ and $\Delta T \parallel \mathbf{c}$ data. For comparison with YbRh$_2$Si$_2$ [Hartmann, 2010], it has been observed that the sign of q changes from positive to negative near the QCP; $q > 0$ for $H < H_c$ and $q < 0$ for $H > H_c$. The $S(T)/T$ value of YbRh$_2$Si$_2$ in the zero temperature limit does not scaled well with γ $(q \neq 1)$ in the paramagnetic state. A recent theoretical investigation of
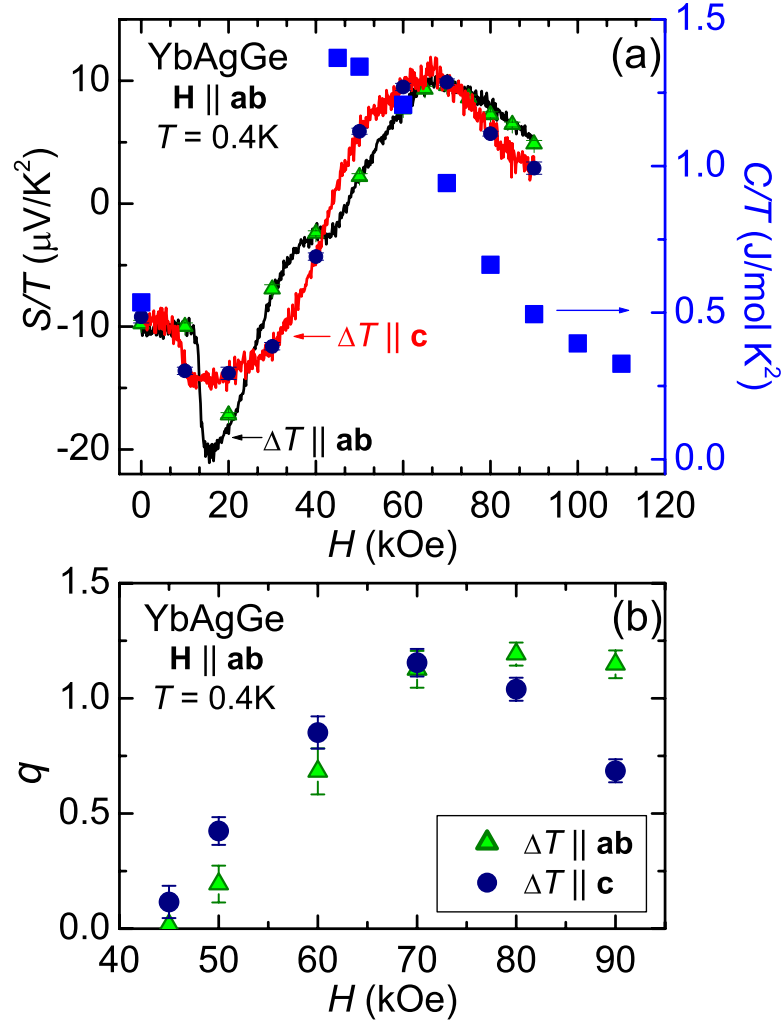
Figure 5.10   (a) $S(H)/T$ of YbAgGe at $T = 0.4$ K for both $\Delta T \parallel \mathbf{ab}$ and $\Delta T \parallel \mathbf{c}$, plotted as a function of magnetic field, applied along $\mathbf{H} \parallel \mathbf{ab}$ in a transverse configuration ($\mathbf{H} \perp \Delta T$). Solid symbols (triangles and circles) are taken from temperature sweeps $S(T)/T$. Sommerfeld coefficient ($C(T)/T$, right axis) at 0.39 K was taken from the previous specific heat measurements [Tokiwa, 2006]. (b) The estimated q values at $T = 0.4$ K for both $\Delta T \parallel \mathbf{ab}$ and $\Delta T \parallel \mathbf{c}$, plotted as a function of H.

the ratio q shows that q decreases considerably toward antiferrromagnetic (AFM)-QCP but does not change significantly for a ferrromagnetic-QCP [Miyake, 2005]. At this stage, we can not offer a decisive comparison between theoretical work and our results because the ratio q is compared at finite temperature of $T = 0.4$ K and manifests an anisotropic response for different ΔT-directions; both further theoretical investigations and experimental measurements down to sub-mK range are needed. Based on our results, one should notice that the observed sign of q is negative in zero field and positive for $H > H_c$ due to the sign of TEP. In zero field it has been shown that the sign of q is positive for Ce-based compounds and negative for Yb-based compounds [Behnia, 2004]. In the presence of the magnetic field the observed sign of q for YbAgGe does not follow the general trend, thus further investigations including theoretical work are needed to clarify the discrepancy.

In this part experimental results of YbAgGe will be compared to theoretical predictions of quantum criticality which were particularly applied to the magnetic field tuned quantum phase transition of YbRh$_2$Si$_2$. Currently available scenarios of quantum criticality can be divided into two categories. The first one is the conventional spin density wave (SDW) scenario [Hertz, 1976; Millis, 1993; Moriya, 1995; Moriya, 1973] and the second one is the Kondo breakdown [Senthil, 2003; Senthil, 2004; Paul, 2007; Paul, 2008], including local quantum criticality [Si, 2001; Si, 2003], scenario (see Chapter 3). In the first scenario, the quasi-particle system undergoes a SDW instability at the QCP with the Kondo temperature (T_K) remaining finite across the quantum phase transition. Thus, heavy quasi-particles survive near the QCP while the system is tuned through the QCP by varying control parameter. In the second, Kondo breakdown scenario, the central question should be, what is the direct experimental signature of the breakdown of the Kondo effect that distinguishes it from the alternate route to quantum criticality? For example, in particular for only YbRh$_2$Si$_2$ [Paschen, 2004], Hall effect measurements were proposed as a signature of breakdown of quasi-particles, where an abrupt jump was predicted in the Hall coefficient, interpreted as change from small to large Fermi surface, at QCP. In the SDW scenario, the Hall coefficient changes continuously upon entering the AFM state [Paschen, 2006], which was observed in Cr$_{1-x}$V$_x$ [Yeh, 2002; Norman, 2003; Lee, 2004]

($3d$-electron system). This issue is not trivial to address due to the absence of low temperature angle resolved photoemission spectroscopy which is generally restricted to high temperatures $T \gg T_N$ and quantum oscillation (such as de Haas-van Alphen) experiments which is generally restricted to high magnetic fields $H \gg H_c$. In addition, so far the local quantum critical scenario is restricted to only $CeCu_{6-x}Au_x$ [Schröder, 1998; Schröder, 2000] and the Kondo breakdown scenario is only based on main results of $YbRh_2Si_2$ [Paschen, 2004].

It has remained difficult to unambiguously identify the quantum critical scenario from the low temperature behavior. Thus, rather than considering the quantum fluctuation at low temperature, near QCP via nFL behavior and scaling invariance, careful examination of high temperature energy scale (T_K) may provide a good opportunity to select the proper model for quantum criticality, since the high temperature signature is distinctly different between SDW and Kondo breakdown scenario. Recently, the quantum criticality has been tested by considering the high temperature scale of T_K in $CeRu_2(Si_{1-x}Ge_x)_2$ [Okane, 2009] and $CeCu_{6-x}Au_x$ [Kroha, 2010] systems. An investigation of the Fermi surface near QCP of $CeRu_2(Si_{1-x}Ge_x)_2$ by soft x-ray angle resolved photoelectron spectroscopy suggested that SDW quantum criticality is more appropriate than Kondo breakdown scenario, where the absence of the clear change of the Fermi surfaces across the QCP was observed. An ultraviolet photoemission spectroscopy measurements of $CeCu_{6-x}Au_x$ proposed that the quantum phase transition is dominated by the local quantum critical scenario, where the sudden decrease of T_K was seen near QCP. Note that in both cases the measurements was performed around $15 \sim 20\,\mathrm{K}$, which is comparable or much higher than T_K.

Figures 5.11 (a) and (b) show the evolution of T_{max} for both heat flow directions as a function of magnetic field. The local maximum was determined from the Gaussian fit to $S(T)$ vs. $\log(T)$ plots. The large uncertainty is mainly due to the merging of the two, T_{max} and T^*, peaks at higher magnetic fields. As discussed above T_{max} can be assumed to reflect the T_K. The estimate T_K remains finite for both heat flow directions as the magnetic field is varied across the whole magnetic field range, suggested that this is consistent with SDW scenario. When the Kondo breakdown scenario is considered, the TEP should collapse below certain
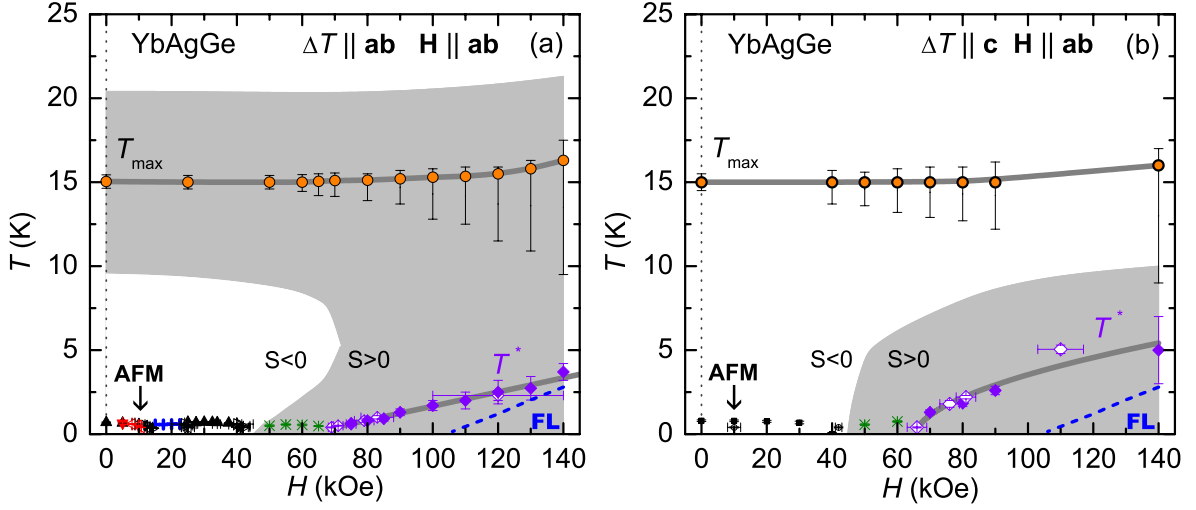
Figure 5.11   High temperature phase diagram of YbAgGe for $\mathbf{H} \parallel \mathbf{ab}$: (a)
$\Delta T \parallel \mathbf{ab}$ ($\mathbf{H} \perp \Delta T$) and (b) $\Delta T \parallel \mathbf{c}$. T_{max} (T_K) and T^* rep-
resent crossover scales determined from the $S(T, H)$. The FL
region was taken from earlier $\rho(T)$ ($\Delta\rho = AT^2$) measurements
[Bud'ko, 2004; Niklowitz, 2006]. The shaded area indicates
$S(T) > 0$, determined from the crossover point $S(T, H) =$
0. See text and Fig. 5.8 for AFM phase boundaries.

energy scale ($T^* \sim E^*$ in Ref. [Gegenwart, 2008], see the figure in chapter 3) associated with

the Fermi surface reconstruction and the sign of the TEP should change in the low temperature

limit [Kim, 2010]. For the case of YbAgGe, although the sign of TEP changes across the T_{Hall}

crossover line, the TEP does not collapse, which is consistent with SDW scenario, although this

definitely needs to be verified below 0.35 K. However, the observed nFL behavior, $C(T)/T \propto$ -

$\log(T)$, $S(T)/T \propto$ -$\log(T)$, and $\Delta\rho(T) \propto T$ near 70 kOe, due to the strong quantum fluctuation

can not be explained within the $d = 3$ and $z = 2$ SDW framework [Hertz, 1976; Millis, 1993], but

can be explained within $d = 2$ SDW [Hertz, 1976; Millis, 1993; Moriya, 1995] and $z = 3$ Kondo

breakdown scenario [Paul, 2007; Paul, 2008]. Note that since the anisotropy between hexagonal

$\mathbf{ab}$-plane and $\mathbf{c}$-axis, based on transport measurements, is not very large [Umeo, 2004], YbAgGe

seems to be considered as 3D structure. Note that the in-plane resistivity, ρ_{ab}, is higher than

the c-axis one, ρ_c, with $\rho_{ab}/\rho_c \approx 4.2\text{-}4.7$ for LuAgGe [Samolyuk, 2006].

There is an another issue to consider: The nature of the Kondo breakdown involves multiple

energy scales, which for YbRh$_2$Si$_2$ all converge at the QCP [Gegenwart, 2008]. However, the

Ir- and Ge-doped YbRh$_2$Si$_2$ [Friedemann, 2009; Custers, 2010] show that the crossover energy scale, T^*, can be separated from the AFM state, showing a relatively wide nFL region. When the nFL region is considered, the $H - T$ phase diagram for YbAgGe is similar to that of doped YbRh$_2$Si$_2$ (see schematic phase diagram in Chapter 3). However, the crossover scales are needed to be distinguished among these systems, i.e. are both T_{Hall} and T^* generic for all systems or these are particular for only YbAgGe. In the Kondo breakdown scenario the nFL behavior is based on the presence of a second QCP, which is close to the magnetic (AFM) QCP, where the effective Kondo temperature goes to zero ($T_K \rightarrow 0$) near second QCP. If we assume that these two QCP can be separated e.g. due to the frustration effect for YbAgGe giving rise to the spin liquid state [Coleman, 2007], the T_{Hall} line will be related to the magnetic QCP and T^* can be related to second QCP. This assumption can be supported from the recent proposed Doniach like diagram [Custers, 2010] (see figure in chapter 3). In this case, by applying magnetic field much higher than 140 kOe, the high temperature scale of T_{max} should be breakdown, implying below T^* the heavy quasi-particles do not survive.

Clearly, there is no universal scenario to reconcile all of the experimental results, partly due to the absence of unambiguous experimental tool to probe quantum critical scenario and partly due to the limited experimental examples and biased theoretical approach to only one particular system. This issue will be discussed further below together with YbPtBi.

5.4 Summary and Conclusion

TEP data on YbAgGe have been collected down to $T \sim 0.3$ K and applied magnetic fields up to 140 kOe for $\mathbf{H} \parallel \mathbf{ab}$ and $\Delta T \parallel \mathbf{ab}$ as well as $\Delta T \parallel \mathbf{c}$. In zero field, the TEP data reveal characteristic features of a local minimum ($T_{min} = 85$ K), local maximum ($T_{max} = 15$ K), and an abrupt jump below 1 K, which correspond to the CEF level splitting (Δ_{CEF}), Kondo temperature (T_K), and long range magnetic order, respectively, as relevant energy scales in YbAgGe. The TEP response at the magnetic phase transition is anisotropic for the heat current direction between in the hexagonal $\mathbf{ab}$-plane and along the $\mathbf{c}$-axis. The TEP measurements reproduce the earlier $H - T$ phase diagram and identify an additional dome-like phase between ~ 45

and $\sim 70\,\text{kOe}$, associated with anomalous, $\rho(T) \propto T$, resistivity. Two characteristic crossover lines, constructed mostly from earlier Hall resistivity, are confirmed, clarified, and extended to higher temperature from the TEP results. These crossover lines show a tendency of converging toward to $H_c \sim 45\,\text{kOe}$ and $H^* \sim 70\,\text{kOe}$ in the zero temperature limit. The temperature and magnetic field range of nFL behavior ($\Delta\rho \propto T$) observed in resistivity are well matched with the dome-like area in the phase diagram. For $H = 70\,\text{kOe}$ data, adjacent to the dome-like area, $S(T)/T$ for $\Delta T \parallel \mathbf{c}$ exhibits clearly a logarithmic temperature dependence in agreement with earlier specific heat results $C(T)/T \propto$ -$\log(T)$. The present TEP results, combined with earlier specific heat and resistivity results, show a strong evidence of quantum critical fluctuations around $H \simeq 70\,\text{kOe}$. The ratio of q, reflecting the correlations between $S(T)/T$ and $C(T)/T$, is much less than unity ($q \to 0$) in the vicinity of the $H_c \simeq 45\,\text{kOe}$. As magnetic field increases from H_c the q value is recovered an order of unity at $H^* \simeq 70\,\text{kOe}$. For $H > 70\,\text{kOe}$ the enhanced value of $S(T)/T$ is indicative of the heavy fermion state, supporting previous specific heat and resistivity results.

CHAPTER 6.   Magnetic field tuned QCP of heavy fermion system YbPtBi

6.1   Introduction

The faced-centered cubic (fcc) YbPtBi is a member of RPtBi (R = rare-earth) systems and one of the few stoichiometric Yb-based heavy fermion compounds [Fisk, 1991; Canfield, 1991]. An enormous low temperature Sommerfeld coefficient, $\gamma \simeq 8\,\mathrm{J/mol \cdot K^2}$ [Fisk, 1991], which corresponds to one of highest effective mass values among heavy fermion (HF) systems, is a characteristic of YbPtBi. This system manifests antiferromagnetic (AFM) ordering below $T_N = 0.4\,\mathrm{K}$, below the estimated Kondo temperature of $T_K \sim 1\,\mathrm{K}$ [Fisk, 1991]. The results of electrical resistivity and specific heat measurements suggested that a spin density wave transition occurs below T_N [Movshovich, 1994] with small ordered moment of only $\sim 0.1\,\mu_B$ [Amato, 1992; Robinson, 1994]. It has been proposed that the massive electronic state manages to appear due to either the frustrated (for nearest neighbors) fcc crystal structure suppressing long range order to below the Kondo temperature or the low carrier density, metallic nature leading to an unusually low Kondo temperature [Fisk, 1991; Hundley, 1997], or both.

For an AFM quantum critical point (QCP) in HF systems the conventional theory, so called spin density wave (SDW) scenario, considers itinerant f-electrons on both the ordered and the paramagnetic side of the QCP [Hertz, 1976; Millis, 1993; Moriya, 1995]. The critical SDW fluctuations are responsible for non-Fermi liquid (nFL) behavior in which the electrical resistivity follows $\Delta\rho(T) \propto T^n$ with $n < 2$ ($n = 1.5$ for $d = 3$ and $n = 1$ for $d = 2$). In this scenario, the quasi-particle effective mass is finite $C(T)/T \propto -\sqrt{T}$ at QCP for $d = 3$ critical fluctuations. For $d = 2$ critical fluctuations, the theory predicts a logarithmic divergence of the effective mass $C(T)/T \propto$ -log(T). An essential aspect of the SDW scenario is that the characteristic energy scale, T_K, remains finite across the QCP, thus the

quasi-particles survive in the vicinity of the QCP [Gegenwart, 2008]. An alternate scenario, so-called Kondo breakdown scenario, has proposed that a localization of the f-electrons at the QCP gives rise to a breakdown of the local Kondo energy scale and a dramatic change of the Fermi surface topology [Coleman, 2001; Si, 2001; Si, 2003; Senthil, 2004; Paul, 2008]. The SDW scenario has been applied to many HF compounds such as $CeCu_2Si_2$ [Gegenwart, 1998] and $CeNi_2Ge_2$ [Julian, 1996] and the Kondo breakdown model seems to be favor for Au-doped $CeCu_{6-x}Au_x$ [Schröder, 1998; Schröder, 2000] (specially called a local quantum criticality [Si, 2001; Si, 2003]) and $YbRh_2Si_2$ [Paschen, 2004; Gegenwart, 2008]. However, unfortunately, neither SDW nor the Kondo break down model are sufficient to explain the observed experimental results from these systems.

Magnetic field-induced AFM QCP systems have been limited relatively few examples, only among stoichiometric compounds, in particular $YbRh_2Si_2$ [Trovarelli, 2000; Gegenwart, 2002; Paschen, 2004; Gegenwart, 2007; Friedemann, 2009] and YbAgGe [Bud'ko, 2004; Bud'ko, 2005; Bud'ko, 2005a; Niklowitz, 2006; Tokiwa, 2006]. In addition to strong quantum fluctuations in the vicinity of the QCP, the existence of a new crossover field scale, apparently associated with the QCP, detected from several thermodynamic and transport measurements, has been shown from the extensive study of $YbRh_2Si_2$ [Paschen, 2004; Gegenwart, 2007; Friedemann, 2009] and YbAgGe [Bud'ko, 2004; Bud'ko, 2005]. This was motivated from changes in Hall effect measurements [Paschen, 2004], interpreted as a change of the Fermi surface at the QCP, and more clearly seen in the other HF antiferromagnet, YbAgGe, in an applied magnetic field of $\sim 45\,\text{kOe}$ [Bud'ko, 2005a; Niklowitz, 2006; Tokiwa, 2006], particularly in Hall resistivity data [Bud'ko, 2005a] and extended to higher temperatures via thermoelectric power [Mun, 2010b] measurements. Among magnetic field-tuned QCP systems, YbAgGe shows a wide nFL region characterized by the linear temperature dependence of the resistivity, $\Delta\rho \propto T$ [Niklowitz, 2006]. Recently a similar range of nFL behavior has also been observed in Ge-doped $YbRh_2Si_2$ [Custers, 2010]. Mainly based on the magnetic field-tuned QCP systems, a new mechanism for quantum criticality has been proposed by considering two tuning parameters [Coleman, 2010; Custers, 2010]: (i) the ratio between the Kondo temperature and the

Ruderman-Kittel-Kasuya-Yosida (RKKY) interaction and (ii) the quantum zero-point fluctuations which can be tuned by increasing the amount of frustration, where a Doniach-like, two dimensional, phase diagram can be established with these two tuning parameters (see figure in Chapter 3).

In this chapter, we present systematic measurements of the thermodynamic and transport properties of YbPtBi down to $20\,\mathrm{mK}$ with magnetic fields up to $140\,\mathrm{kOe}$ to establish, delineate, and understand the nature of magnetic field-induced QCP in this canonical system. In the constructed $H - T$ phase diagram for YbPtBi three low temperature regimes emerge: (i) AFM state, characterized by SDW, which can be suppressed to $T = 0$ with a relatively small, external magnetic field of $H_c \sim 4\,\mathrm{kOe}$, (ii) a field induced, anomalous state in which the electrical resistivity follows $\rho(T) \propto T^{1.5}$ between H_c and $\sim 8\,\mathrm{kOe}$, and (iii) a Fermi liquid (FL) state in which $\rho(T) \propto T^2$ for $H \geq 8\,\mathrm{kOe}$. Each region can be distinguished by two crossover scales, emerging near $H_c \sim 4\,\mathrm{kOe}$ and $H^* \sim 7.8\,\mathrm{kOe}$ at $T = 0$. For $H > H^*$, the FL coefficient A of the temperature dependence of resistivity and γ the linear component of the temperature dependence of specific heat are drastically enhanced as $\sim 1/(H - H_c)$ and $\sim 1/(H - H_c)^2$, respectively, when approaching H_c from the high magnetic field side. In contrast to the resistivity results, the electronic specific heat coefficient, $C(T)/T$, does not show any pronounced nFL behavior as either $C(T)/T \propto -\sqrt{T}$ or -log(T) down to $50\,\mathrm{mK}$ near H_c.

6.2   Results

6.2.1   Magnetization

The anisotropic inverse magnetic susceptibilities, $H/M(T)$, of YbPtBi are shown in Fig. 6.1 (a), where the magnetic field was applied along the [100], [110], and [111] directions. The observed magnetic susceptibility is essentially isotropic down to $2\,\mathrm{K}$. Between $10\,\mathrm{K}$ and $250\,\mathrm{K}$, $H/M(T)$ obeys the Curie-Weiss law, $\chi(T) = \mathrm{C}/(T-\theta_p)$, with $\theta_p \simeq$ -2 K and $\mu_{eff} \simeq 4.3\,\mu_B/\mathrm{Yb}^{3+}$ which is close to the free ion value of $4.5\mu_B$ and consistent with earlier studies [Fisk, 1991]. Magnetization isotherms, $M(H)$, of YbPtBi were measured at $1.8\,\mathrm{K}$ for the magnetic field applied along the [100], [110], and [111] direction. The magnetic moment develops a modest
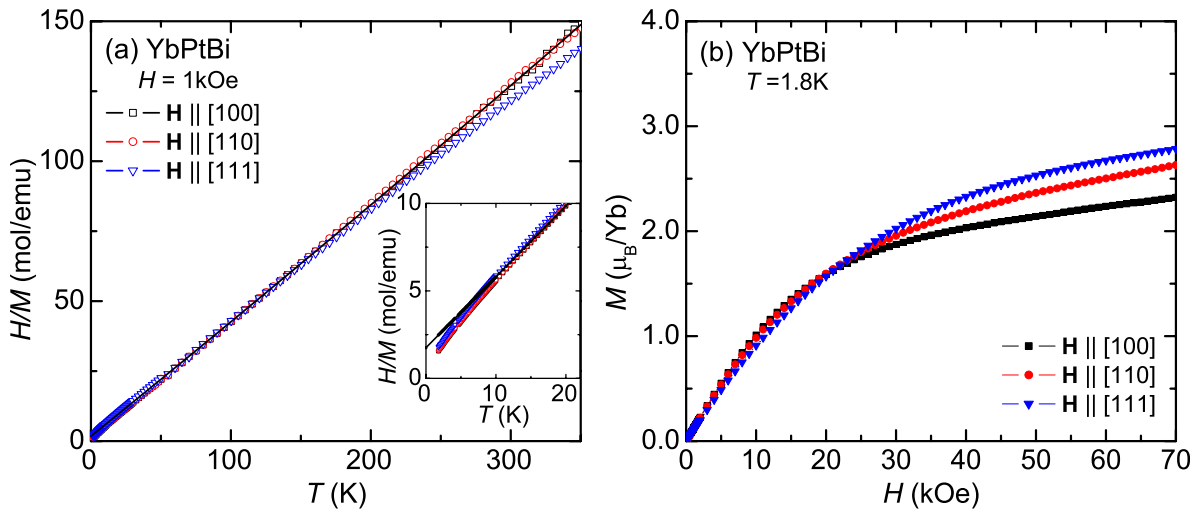
Figure 6.1 (a) Inverse magnetic susceptibility, $H/M(T)$, of YbPtBi, where the magnetic field was applied along [100], [110], and [111] direction. The solid line represents the Curie-Weiss fit to the data for $\mathbf{H} \parallel [100]$. Inset displays $H/M(T)$ at low temperatures. (b) Magnetization isotherms of YbPtBi at $T = 1.8\,\mathrm{K}$ for $\mathbf{H} \parallel [100]$, [110], and [111] direction.

anisotropy for $H > 25\,\mathrm{kOe}$ at $1.8\,\mathrm{K}$ and reaches 2.3-2.8 μ_B/Yb^{3+} at $70\,\mathrm{kOe}$, depending on the magnetic field orientation, which is below the theoretical saturated value of $4\,\mu_B$ for the free Yb^{3+} ion and expected due to the Kondo and crystalline electric field (CEF) effects.

6.2.2 Resistivity

Earlier studies of the low temperature resistivity of YbPtBi found that below $T_N \sim 0.4\,\mathrm{K}$ an unexpected sample-to-sample variation of the resistive anomaly, and even an apparent anisotropy, could develop. It was speculated that strain associated with the sample mounting and hypothesized magnetoelastic effects to these observations. Figure 6.2 shows the electrical resistivity, $\rho(T)$, for several different samples of YbPtBi as a function of temperature with data for different ways attaching the sample to the thermal bath, for cooling. The electrical resistivity curves of samples #3, #10, and #14 are normalized at $1\,\mathrm{K}$ to the resistivity of sample #13, for clarity. The shape of the $\rho(T)$ curve below the AFM ordering temperature, T_N, turns out to be very sensitive to the details of how the sample is attached onto heat sink
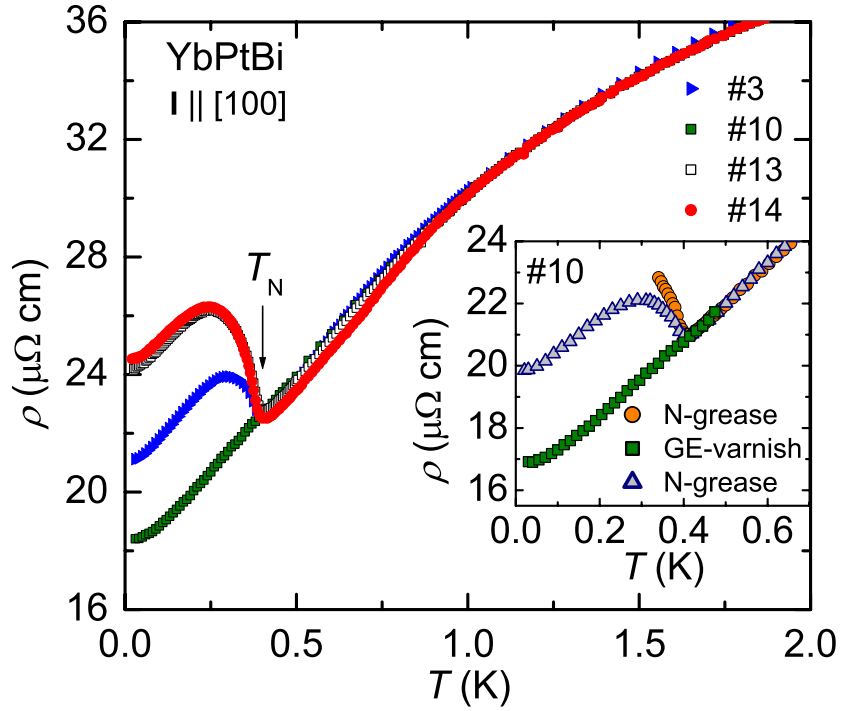
Figure 6.2   Temperature-dependent electrical resistivity, $\rho(T)$, of YbPtBi measured for different sample mount conditions for cooling. $\rho(T)$ curves are normalized to the sample #13 curve at $T = 1\,\mathrm{K}$. Sample #13 and #14 were hanging in vacuum, thus cooled only through high purity, platinum voltage and current lead wires. Samples #3 and #10 were attached to the thermal bath by GE 7301 varnish. The inset shows $\rho(T)$ of sample #10, measured by the following temporal procedure; (i) initially sample was mounted with Apiezon N-grease in ^{3}He cryostat and $\rho(T)$ was measured down to $0.34\,\mathrm{K}$ (circles) in order to see the onset of a sharp phase transition. After cleaning the N-grease (ii) sample was attached to the dilution refrigerator with GE-varnish and $\rho(T)$ was measured (squares, inset and main figure). After cleaning the GE-varnish (iii) sample was mounted with N-grease again in dilution refrigerator and $\rho(T)$ was measured (triangles).

for cooling. Samples #13 and #14, both of which show a sharp increase of $\rho(T)$ below the phase transition, were measured with the sample hanging in vacuum (without being directly affixed to the thermal bath). Thus, these samples were cooled down to 0.02 K through only the platinum voltage and current wires. On the other hand, the electrical resistivity measurements, taken on samples that were mechanically attached to the heat sink, showed unusual behavior. Samples #3 and #10 were attached to the heat sink with GE 7301 varnish (GE-varnish). The $\rho(T)$ curve for sample #3 shows a relatively weak jump below T_N, compared to the results from samples #13 or #14, and no obvious anomaly, corresponding to the AFM phase transition, was observed for sample #10, which manifests a weak slope change, only in a $\mathrm{d}\rho(T)/\mathrm{d}T$ plot.

The degree of sensitivity to mounting conditions can be illustrated, in detail, by the measurement sequence below. Initially $\rho(T)$ data on several samples of YbPtBi were measured down to 0.34 K in ^{3}He cryostat in order to confirm a sharp onset of the phase transition below 0.4 K, where Apiezon N-grease was used to secure the sample to the heat sink. Most of the samples showed a sharp rise of $\rho(T)$ below 0.4 K in which the slope of $\rho(T)$ below 0.4 K was comparable to that of sample #13 in Fig. 6.2. The $\rho(T)$ data for sample #10 is representative and is shown as circles in the inset to Fig. 6.2. Next, from these samples, after cleaning the N-grease off using toluene, eight samples were mounted on a dilution refrigerator cold stage with GE-varnish and $\rho(T)$ was measured down to 0.02 K. The $\rho(T)$ data obtained for sample #10 in this measurement are presented as squares in Fig. 6.2 (and its inset) in which the phase transition is no longer discernible, due to the complete suppression of $\rho(T)$ feature below 0.4 K. All eight samples showed $\rho(T)$ behavior similar that of sample #10. Lastly, after cleaning of the GE-varnish, using ethanol, samples were remounted with Apiezon N-grease to the cold stage of the dilution refrigerator. The $\rho(T)$ data obtained in this measurement for sample #10 are plotted in the inset of Fig. 6.2 as triangles. Interestingly, $\rho(T)$ shows sharp rise below 0.4 K, which is similar to the result of the sample #3. The magnitude of enhancement of $\rho(T)$ below T_N is still smaller than that for the results in vacuum measurements (samples #13 and #14), however much bigger than that for GE-varnish results, where among the eight remounted samples, five of them indicate a sharply rising $\rho(T)$ below 0.4 K. The observed

$\rho(T)$ response for different sample mounting methods may be related to the anisotropic local pressure (strain), generated by different thermal contraction between sample and heat sink via thermal bond (GE-varnish) combined with changes associated with the AFM transition.
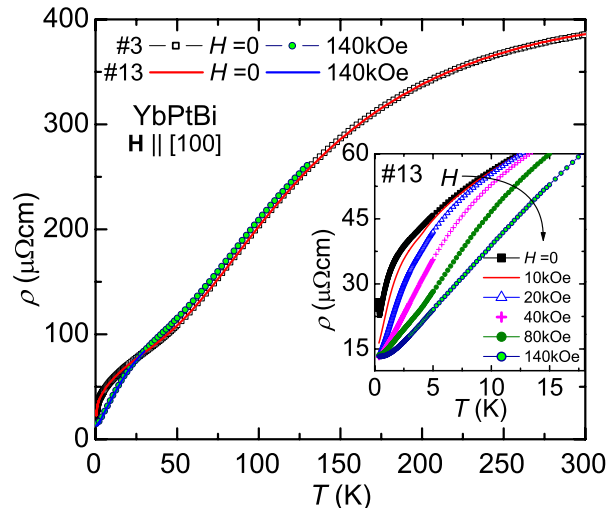
Figure 6.3   Temperature-dependent electrical resistivity, $\rho(T)$, of YbPtBi (for samples #3 and #13) at $H = 0$ and 140 kOe. For $T > 0.35$ K data, samples were mounted in PPMS ^{3}He option with Apiezon N-grease. Inset: $\rho(T)$ of sample #13 for several selected fields.

In the paramagnetic region, $T > T_N$, the electrical resistivity of YbPtBi is not sensitive to either the sample mounting methods for cooling or the sample growth conditions, which was tested with more than 20 samples. All resistivity curves, normalized at 300 K, collapse to a single curve, where the resistivity values at 300 K range between $350 \sim 420$ $\mu\Omega$cm (reflecting our geometric error in evaluating sample dimensions). In Fig. 6.3, as an example, the $\rho(T)$ data of the samples #3 and #13 are plotted for $H = 0$ and 140 kOe, where the $\rho(T)$ curve of the sample #3 is scaled at 300 K to the sample #13. In zero field the two $\rho(T)$ curves are identical above 0.4 K. For $H = 140$ kOe data, two curves also show virtually identical temperature dependencies with an approximately 10% ($1.6\,\mu\Omega$cm) difference at 0.4 K. In zero field, $\rho(T)$ decreases with decreasing temperature, displayed an inflection around 85 K (a maximum in $\mathrm{d}\rho(T)/\mathrm{d}T$), and shows a shoulder-like feature below 5 K as it drops sharply until $T = T_N$. These two characteristic features in $\rho(T)$, around 5 and 85 K, are probably due to the Kondo

and CEF effects. Without correction for the phonon contribution to the resistivity, the local maximum associated with the coherence effect in a Kondo lattice and the logarithmic temperature dependence of $\rho(T)$ can not be resolved. In the inset of Fig. 6.3, $\rho(T)$ data for sample #13 are plotted in various magnetic fields. As magnetic field increases $\rho(T)$ shows a continuous suppression of the low temperature anomaly, developed near $5\,K$, which is no longer visible at least for $H = 140$ kOe. The observed magnetoresistance (MR) for $H = 140$ kOe changes from negative to positive near $25\,K$. In the following, we will mainly present the resistivity results of sample #13 and the results will be compared to those of samples #3 and #14.
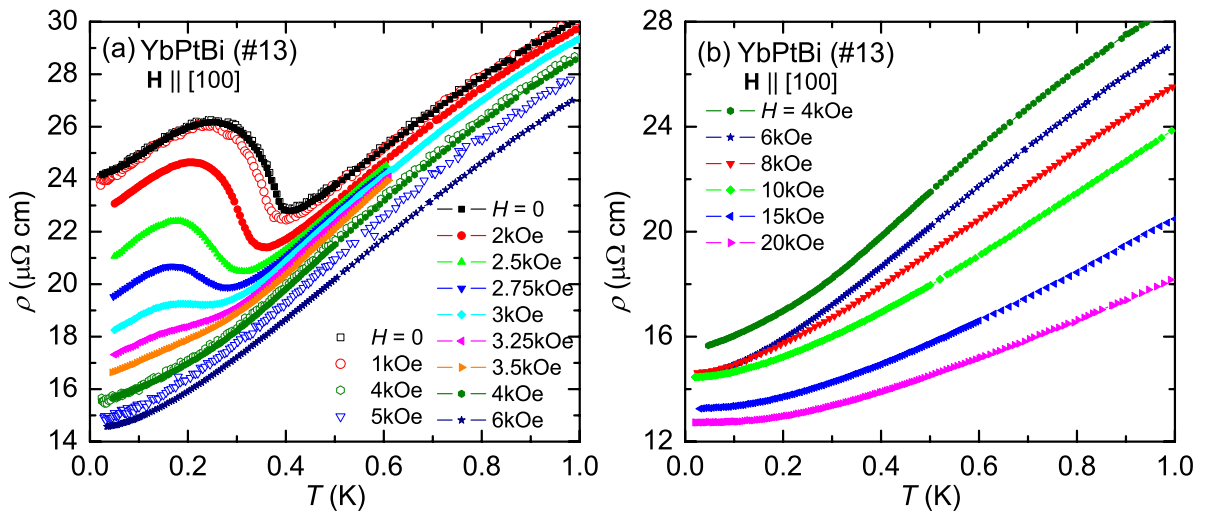
Figure 6.4 Low temperature electrical resistivity ($\rho(T)$, sample #13) of YbPtBi in various magnetic fields applied along the [100] direction (a) for $H \leq 6\,kOe$ and (b) for $4\,kOe \leq H \leq 20\,kOe$. For comparison, $\rho(T)$ data at $H = 4$ and $6\,kOe$ are plotted in both figures. (a) Open- and closed-symbols correspond to the data taken with $3\,\mu A$ and $30\,\mu A$ excitation current, respectively.

Figures 6.4 (a) and (b) show the low temperature $\rho(T)$ of YbPtBi for sample #13. In zero field there is a monotonic quasi-linear decrease with temperature from $1\,K$ down to just above $0.4\,K$, followed by a sharp increase of $\rho(T)$ is observed below $0.4\,K$ (which is consistent with earlier results [Movshovich, 1994]). This behavior is not consistent with that observed for simple, local moment AFM ordering for which $\rho(T)$ decreases below T_N due to a loss of spin

disorder scattering. A sharp rise of the resistivity below $0.4\,\mathrm{K}$ is reminiscent of the resistivity signature of charge density wave (CDW) [Myers, 1999] and spin density wave (SDW) materials [Fawcett, 1988], and of that in AFM materials which form a magnetic superzone gap below T_N [Elliott, 1972]. The bulk magnetic susceptiblity shows that YbPtBi exhibits an AFM order below $0.4\,\mathrm{K}$ [Fisk, 1991] but the μSR [Amato, 1992] and neutron scattering experiments [Robinson, 1994] indicate that the ordered moment is $0.1\,\mu_B$ or less. Thus, the $\rho(T)$ data is not inconsistent with that observed for SDW systems for which an increase of $\rho(T)$ along the direction of the SDW modulation, indicating the partial gapping of the Fermi surface, should be expected. As magnetic field increases, the resistive anomaly associated with T_N is not only reduced in height but also shifts to lower temperature (Fig. 6.4 (a)). For $H > 4\,\mathrm{kOe}$ the resistive anomaly is completely suppressed and a monotonic increase of $\rho(T)$ is observed as temperature increases. Interestingly, an anomalous behavior of the resistivity in the zero temperature limit, $\rho(0)$, is observed around $8\,\mathrm{kOe}$ at which $\rho(0)$ seems to have a local maximum with varying magnetic field (see below).

Figure 6.5 (a) shows the transverse magnetoresistivity, $\rho(H)$, of sample #13 at various temperatures, data taken with a configuration; $\mathbf{H}\,\|\,[100]$ and $\mathbf{I}\,\|\,[010]$ ($\mathbf{H}\perp\mathbf{I}$). At $T = 0.02\,\mathrm{K}$ $\rho(H)$ steeply decreases with increasing magnetic field, has a local minimum near $5.6\,\mathrm{kOe}$, exhibits a hump around $8\,\mathrm{kOe}$, and then decreases with further increasing magnetic field. The broad maximum around $8\,\mathrm{kOe}$ at $T = 0.02\,\mathrm{K}$ broadens further and turns into a weak slope change as temperature increases up to $0.5\,\mathrm{K}$ above which the anomaly is no longer noticeable. The steep decrease of $\rho(H)$ as magnetic field increases from zero to $5\,\mathrm{kOe}$ can be related to the boundary of the AFM state. It is not clear at present whether the additional signature around $8\,\mathrm{kOe}$ represents a phase transition, or some kind of crossover field. For $T > T_N$ a negative MR appears, only without an $\sim 8\,\mathrm{kOe}$ hump, up to $40\,\mathrm{kOe}$. Figure 6.5 (b) shows the higher temperature MR, plotted as $[\rho(H) - \rho(0)]/\rho(0)$ vs. H. The MR decreases without any noticeable anomaly as magnetic field increases and the sign of the MR change from negative to positive for $T > 20\,\mathrm{K}$. In the high magnetic field regime ($H > 100\,\mathrm{kOe}$), quantum oscillations are visible at low temperatures. The analysis of these oscillations and discussions are presented
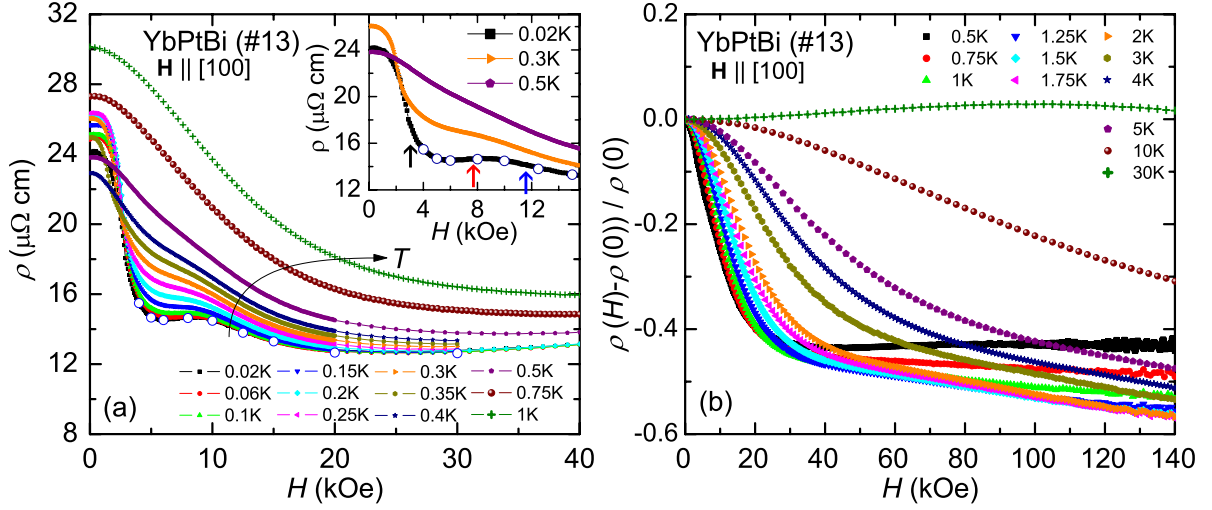
Figure 6.5 (a) Transverse magnetoresistivity of YbPtBi (sample #13) as plotted ρ vs. H at various temperatures; $\mathbf{H} \parallel [100]$ and $\mathbf{I} \parallel [010]$ ($\mathbf{H} \perp \mathbf{I}$). Inset shows a expanded plot in the low field regime for $T = 0.02$, 0.3, and $0.5\,\mathrm{K}$. Open circles in both main figure and inset represent the residual resistivity taken from the power law fit to $\rho(T)$ data (Fig. 6.4); $T^{1.5}$-fit for $H < 8\,\mathrm{kOe}$ and T^2-fit for $H \geq 8\,\mathrm{kOe}$. Vertical arrows in the inset indicate slope changes in $\mathrm{d}\rho(H)/\mathrm{d}H$ curve. (b) Transverse magnetoresistance of YbPtBi (sample #13) as plotted $[\rho(H) - \rho(0)]/\rho(0)$ vs. H at various temperatures.

in the appendix C.

The AFM phase boundary was determined from the peak position in $\mathrm{d}\rho(T)/\mathrm{d}T$ because the steep rise, seen in the zero field $\rho(T)$ below T_N, broadens as magnetic field increases. Figure 6.6 (a) shows $\mathrm{d}\rho(T)/\mathrm{d}T$ of sample #13 for selected magnetic fields. As magnetic field increases, the peak height at T_N decreases and the peak width in $\mathrm{d}\rho(T)/\mathrm{d}T$ becomes wider, indicating that the signature of the phase transition broadens. The peak in $\mathrm{d}\rho(T)/\mathrm{d}T$ is fairly sharp for $H \leq 3\,\mathrm{kOe}$ curves, whereas it is no longer visible, down to $0.02\,\mathrm{K}$, for $H \geq 4\,\mathrm{kOe}$. Thus, with increasing magnetic field, the AFM phase transition shifts to lower temperatures and vanishes at around $4\,\mathrm{kOe}$. The arrows in Fig. 6.6 (a) illustrate the criterion used to determine T_N.

Figure 6.6 (b) shows the magnetic field dependence of the derivatives, $\mathrm{d}\rho(H)/\mathrm{d}H$, obtained from the $\rho(H)$ curves presented in Fig. 6.5. The sharp peak positions of $\mathrm{d}\rho(H)/\mathrm{d}H$ were selected as the critical field of the phase transition. The sharp peak at $2.9\,\mathrm{kOe}$, shown in $0.02\,\mathrm{K}$
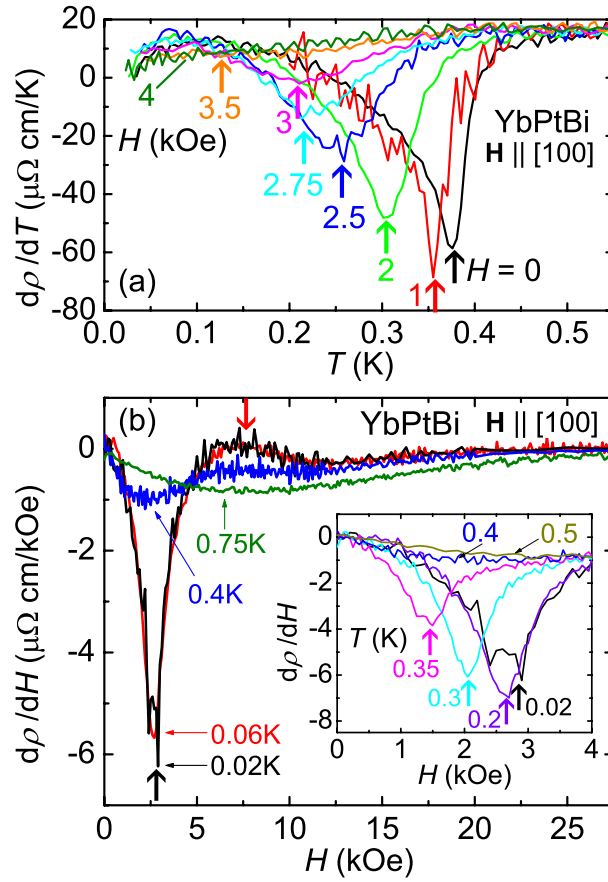
Figure 6.6 (a) $\mathrm{d}\rho(T)/\mathrm{d}T$ at various magnetic fields up to $4\,\mathrm{kOe}$. Vertical arrows indicate the determined AFM phase transition temperature. (b) $\mathrm{d}\rho(H)/\mathrm{d}H$ at various temperatures. Up-arrow indicates the AFM phase boundary and down-arrow correspond to a local maximum. Inset shows $\mathrm{d}\rho(H)/\mathrm{d}H$ up to $0.5\,\mathrm{K}$, where vertical arrows indicate the determined phase transition field.

curve, shifts to lower field as temperature increases (inset) and turns into a broad minimum for $T \geq 0.4\,\mathrm{K}$. The higher field broad maximum near $7.6\,\mathrm{kOe}$ for $0.02\,\mathrm{K}$ curve broadens as temperature increases. For $T > 0.75\,\mathrm{K}$, the lower field broad minimum and a slope change near $6\,\mathrm{kOe}$ shown for $T = 0.4\,\mathrm{K}$ curve are no longer visible and instead $\mathrm{d}\rho(H)/\mathrm{d}H$ shows a single minimum near $\sim 10\,\mathrm{kOe}$. As will be discussed below, the positions of the sharp peak and the local maximum agree with the observed anomalies in the magnetostriction, Hall resistivity, and thermoelectric power measurements.

To get further insight from the low temperature transport data from YbPtBi, $\rho(T)$ data
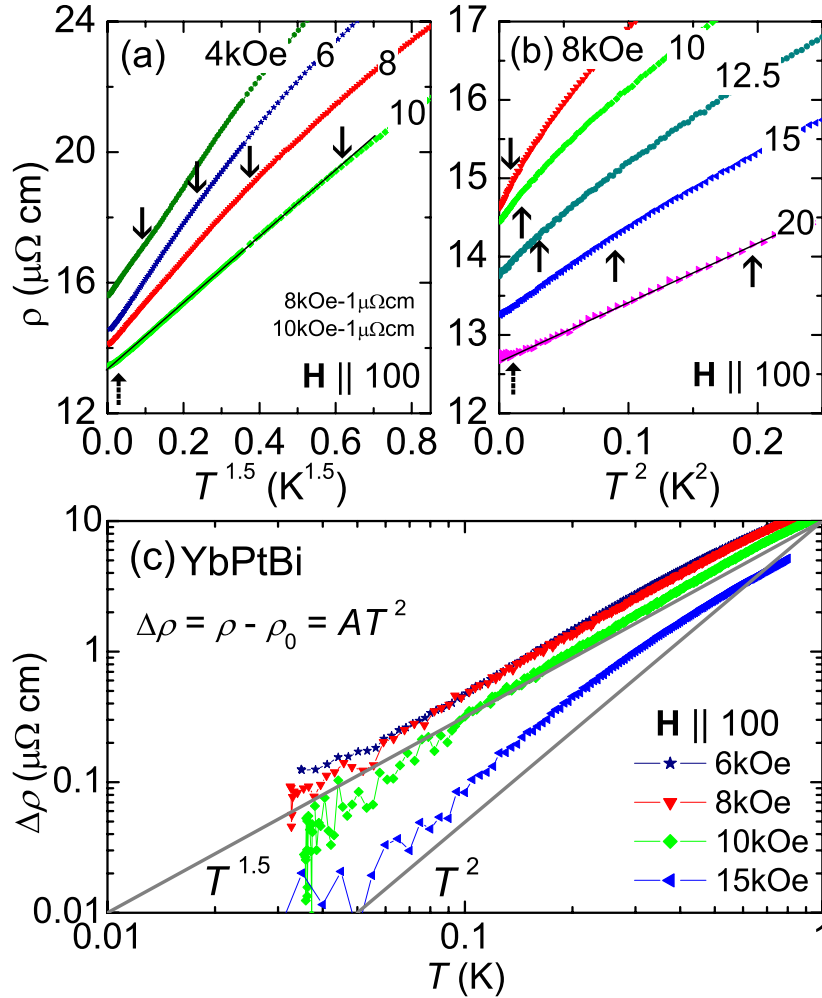
Figure 6.7   (a) $\rho(T)$ vs. $T^{1.5}$ at various magnetic fields, where $\rho(T)$ curves for $H = 8$ and $10\,\mathrm{kOe}$ are shifted by $-1\mu\Omega\mathrm{cm}$ each for clarity. Down-arrows indicate the temperature below which $\Delta\rho(T) = AT^{1.5}$, determined from a power law fit ($\Delta\rho(T) = AT^n$) to the data. For $H = 10\,\mathrm{kOe}$ the line is the fit of the power law to the data and up-arrow indicates a deviation from $T^{1.5}$-dependence of $\Delta\rho(T)$. (b) $\rho(T)$ vs. T^2 at various magnetic fields. The arrows mark the temperature where the fits ($\Delta\rho(T) = AT^2$) deviates from the data. These temperatures, T_{FL}, are plotted in the $H-T$ phase diagram (see Fig. 6.10). For $H = 20\,\mathrm{kOe}$ the line is the fit of the power law to the data and up-arrow in the low temperature side indicates a deviation from T^2-dependence of $\Delta\rho(T)$. (c) Double-logarithmic plots of $\Delta\rho(T)$ vs. T for $H = 6, 8, 10$, and $15\,\mathrm{kOe}$. The solid lines represent the temperature dependence expected for the exponent $n = 1.5$ and $n = 2$.

are analyzed by a power law; $\Delta\rho(T) = \rho(T) - \rho_0 = AT^n$, where ρ_0 is the residual resistivity and A is the coefficient. The coefficient, A, can be interpreted as the quasi-particle scattering cross-section. The exponent, n, indicates whether the system is in a Fermi Liquid (FL) regime ($n = 2$) with dominant electron-electron scattering or whether strong quantum fluctuation effects dominate, generally $n < 2$, in the vicinity of a QCP [Stewart, 2001]. Figures 6.7 (a) and (b) show plots of $\rho(T)$ vs. $T^{1.5}$ and T^2, respectively, at various magnetic fields. In Fig. 6.7 (a) $\rho(T)$ for $H = 8$ and $10\,\mathrm{kOe}$ data are shifted by $-1\,\mu\Omega\mathrm{cm}$ each for clarity. Since the anomaly in $\rho(T)$ below the SDW phase transition for $H < 4\,\mathrm{kOe}$ prevents the power law fit to the data, the fit was performed for $H \geq 4\,\mathrm{kOe}$ at which no sharp feature in $\mathrm{d}\rho(T)/\mathrm{d}T$ was observed down to $0.02\,\mathrm{K}$ (see Fig. 6.6 (a)).

For $4\,\mathrm{kOe} \leq H \leq 8\,\mathrm{kOe}$, $\rho(T)$ can be well described by a $T^{1.5}$-dependence down to the lowest accessible temperature of $0.02\,\mathrm{K}$, where the exponent n ranges between $1.45 \sim 1.6$ depending on the fit range. The maximum temperature below which $\Delta\rho(T) = AT^{1.5}$ shifts to higher temperature as magnetic field increases, indicated by down-arrows in Fig 6.7 (a). For $H = 8$ and $10\,\mathrm{kOe}$, plotted in both Figs. 6.7 (a) and (b), $\rho(T)$ can be described by a T^2-dependence at low temperatures above which $T^{1.5}$-dependence is predominant. For $H > 10\,\mathrm{kOe}$ a characteristic of FL state is clearly evidenced by the relation $\Delta\rho(T) = AT^2$ at low temperatures as indicated by the arrow in Fig. 6.7 (b). Note for $H \geq 20\,\mathrm{kOe}$ that as temperature decreases $\rho(T)$ follows T^2-dependence and then flattens, revealing the deviation of FL behavior with $n > 2$. In Fig. 6.7 (b) the up-arrow in the low temperature side on $\rho(T)$ curve for $H = 20\,\mathrm{kOe}$ curve indicates a deviation of T^2-dependence.

Since the difference of the exponent between $n = 1.5$ and 2 is very small, the results based on the power law analysis are also visualized in Fig. 6.7 (c) as log-log plot of $\Delta\rho(T)$ vs. T at selected magnetic fields. $\Delta\rho(T)$ for $H = 6\,\mathrm{kOe}$ is a straight line at least up to $0.4\,\mathrm{K}$, which is parallel to the $T^{1.5}$-line, whereas $\Delta\rho(T)$ for $H = 10\,\mathrm{kOe}$ deviates from a straight line parallel to the $T^{1.5}$-line near $0.1\,\mathrm{K}$ below which the slope is parallel to the T^2-line. Note that at low temperatures the slope in log-log plot depends on the ρ_0 value. When $\rho(T)$ is corrected by the ρ_0 value obtained from the fit of $T^{1.5}$-dependence above $\sim 0.1\,\mathrm{K}$, the slope for $H = 10\,\mathrm{kOe}$

is parallel to the $T^{1.5}$-line above $0.1\,\mathrm{K}$. For $H = 15\,\mathrm{kOe}$ curve, $\Delta\rho$ is a straight line parallel to the T^2-line below $\sim 0.25\,\mathrm{K}$, which clearly indicate a quadratic temperature dependence down to lowest temperature measured.
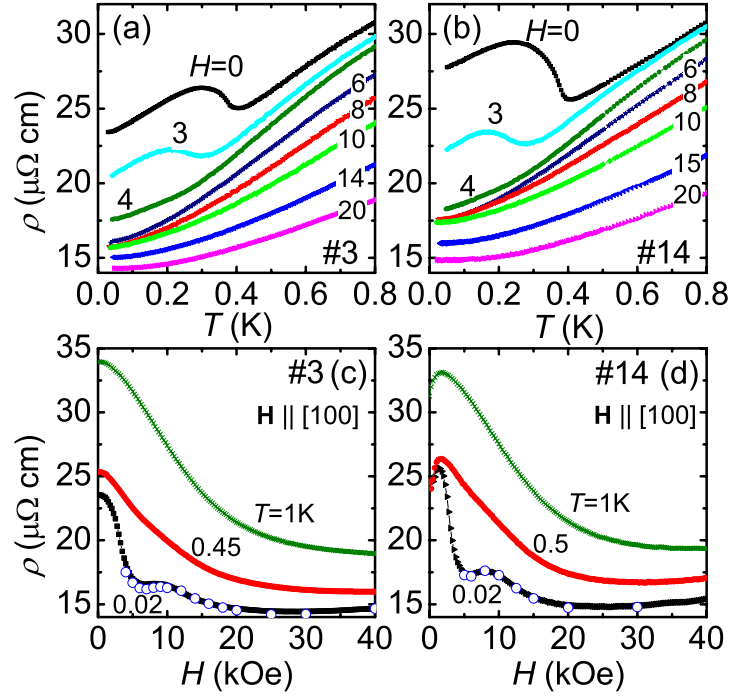
Figure 6.8 $\rho(T)$ of (a) sample #3 and (b) sample #14 at selected magnetic fields. $\rho(H)$ of (c) sample #3 and (d) sample #14 at selected temperatures. (b) Zero field $\rho(T)$ of sample #14 was shifted by $+3\mu\Omega\mathrm{cm}$ for clarity. Open circles in (c) and (d) represent the residual resistivity obtained from the power law fit to the $\rho(T)$ data.

The electrical resistivity data for samples #3 and #14 are plotted in Figs 6.8 (a)-(d), respectively, at selected temperatures and magnetic fields as representative data. For $\mathbf{H} \parallel [100]$, the overall temperature and magnetic field dependences of the resistivity for both samples #3 and #14 are the same as those for sample #13 (Figs. 6.4 and 6.5). These data were analyzed by the same methods, applied to sample #13, to determine phase transitions and power law dependences of $\rho(T)$. These results together with those of sample #13 are summarized in Fig. 6.9 and Fig. 6.10.

In Fig. 6.9 parameters of A, n, and the maximum temperature range satisfying $T^{1.5}$ and
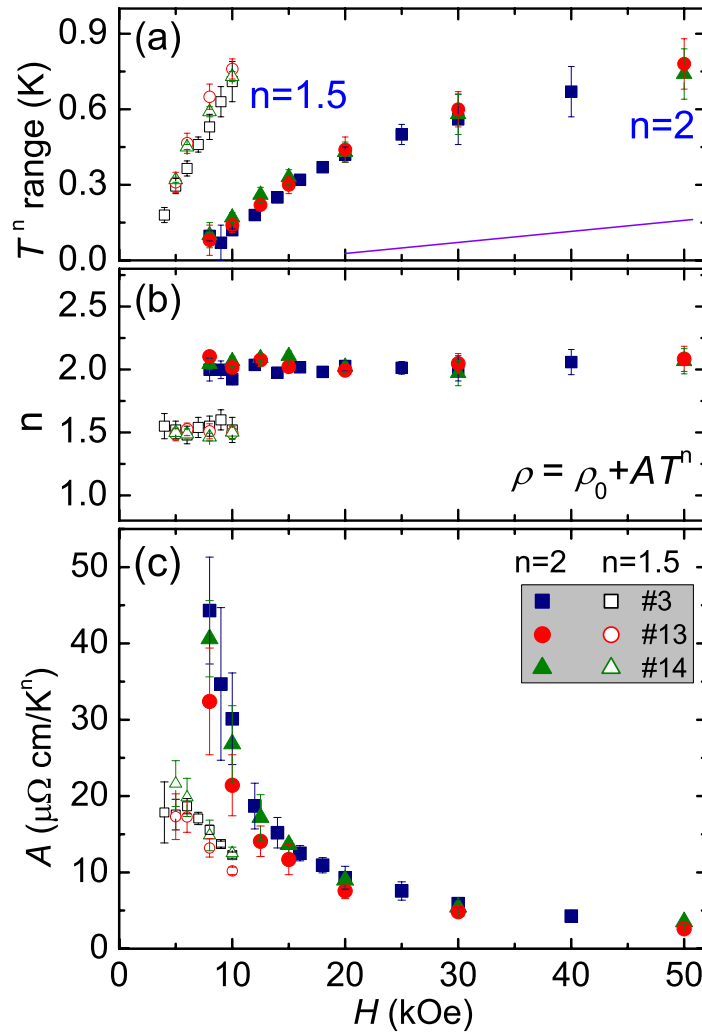
Figure 6.9   Parameters obtained from power law fits, $\rho(T) = \rho_0 + AT^n$, to the data for three different samples. Open- and solid-symbols correspond to fits with $n = 1.5$ and $n = 2$, respectively. (a) Temperatures of the fit range below which a T^n-dependence of $\rho(T)$ satisfies. For $8\,\mathrm{kOe} \leq H \leq 10\,\mathrm{kOe}$ the fit of $T^{1.5}$-dependence was performed above the temperature, satisfying T^2-dependence. The horizontal line for $H \geq 20\,\mathrm{kOe}$ indicates the temperature below which $\rho(T)$ flattens. (b) Determined exponents n from least square fits to the data. (c) Field dependencies of the coefficients, $A = (\rho(T) - \rho_0)/T^n$ with $n = 1.5$ and 2, for three different samples.

T^2, obtained from the power law fit, are summarized for $H \geq 4\,\mathrm{kOe}$. All open- and solid-symbols correspond to the fits with $n = 1.5$ and $n = 2$ (Fig. 6.9 (b)), respectively, for three different samples. For comparison with magnetoresistivity at $0.02\,\mathrm{K}$, the obtained ρ_0 values for sample #13 are plotted in Fig. 6.5 as open-circles which track well the magnetoresistivity at $T = 0.02\,\mathrm{K}$. ρ_0 values for samples #3 and #10 also track the low temperature $\rho(H)$ well (Figs. 6.8 (c) and (d), respectively). As shown in Fig. 6.9 (a) for magnetic fields above $4\,\mathrm{kOe}$ the temperature range, following $T^{1.5}$-dependences of $\rho(T)$, increases monotonically and for magnetic fields higher than $8\,\mathrm{kOe}$ the FL region, $\Delta\rho(T) = AT^2$, gradually increases. The field dependences of the coefficients, $A = (\rho(T) - \rho_0)/T^n$ with $n = 1.5$ and 2, are plotted Fig. 6.9 (c). A strong enhancement of the T^2-coefficient is observed as magnetic field approaches $8\,\mathrm{kOe}$ from higher magnetic fields.
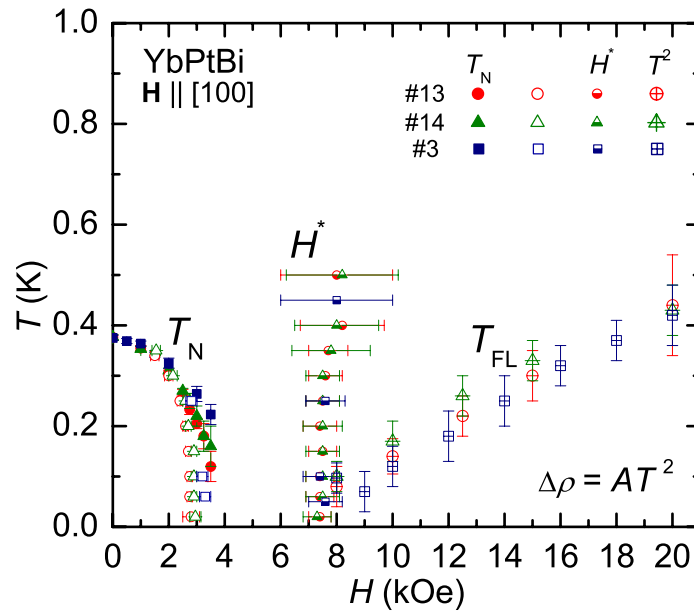
Figure 6.10 $H - T$ phase diagram of YbPtBi constructed from the $\rho(T, H)$ results for three different samples; all circles, triangles, and squares correspond to the results of samples #13, #14, and #3, respectively. T_N was derived from the sharp minimum in $\mathrm{d}\rho(T)/\mathrm{d}T$ (solid-symbols) and $\mathrm{d}\rho(H)/\mathrm{d}H$ (open-symbols). H^* was derived from the broad local maximum in $\mathrm{d}\rho(H)/\mathrm{d}H$ (Fig. 6.6). T_{FL} represents the upper limit of the T^2-dependence of $\rho(T)$.

The various characteristics observed from sample #13, together with samples #3 and #14, are collected in the $H - T$ plane and displayed in Fig. 6.10. The magnetic field dependence of T_N was determined from the sharp peak position in $\mathrm{d}\rho(T)/\mathrm{d}T$ and $\mathrm{d}\rho(H)/\mathrm{d}H$ (Fig. 6.6). The crossover scale, H^*, was obtained from the maximum of $\mathrm{d}\rho(H)/\mathrm{d}H$ (Fig. 6.6 (b)). The FL region, T_{FL}, marks the upper limit of T^2-dependence of $\rho(T)$ (Fig. 6.7). The AFM phase boundary of T_N and the crossover of H^* and T_{FL}, obtained from the results of three different samples, agree well each other. Therefore, it seems to be reasonable to assume that the strength of the anomaly developed in $\rho(T)$ below T_N is only sensitive to the strain generated through bonding agent for sample cooling (see Fig. 6.2), but the relevant physics of the samples remains the same. The AFM boundary determined from $\mathrm{d}\rho(T)/\mathrm{d}T$ does not fully agree with the one obtained from $\mathrm{d}\rho(H)/\mathrm{d}H$ at low temperatures; the AFM phase boundary below $0.2\,\mathrm{K}$ spreads significantly. It is most likely that this inconsistency is based on the criteria used to determine phase transition coordinates, but it is possible that there are two closely spaced phase boundaries.

From the $H - T$ phase diagram for the applied magnetic field parallel to the [100] direction, it is clear that the AFM ordering can be suppressed to zero for $H_c \lesssim 4\,\mathrm{kOe}$. For $H > H_c$ a field induced anomalous state, characterized by $\Delta\rho(T) = AT^{1.5}$, is established up to $\sim$ $8\,\mathrm{kOe}$, and a FL state, characterized by $\Delta\rho(T) = AT^2$, is induced for $H \geq 8\,\mathrm{kOe}$. The T_{FL} region enlarges monotonically with increasing magnetic field. It is apparent that at lowest temperature measured ($T = 0.02\,\mathrm{K}$) a crossover from $T^{1.5}$- to T^2-dependence of $\rho(T)$ occurs near $8\,\mathrm{kOe}$. At higher magnetic fields, for $H \geq 8\,\mathrm{kOe}$, a crossover from $T^{1.5}$- to T^2-dependence of $\rho(T)$ is observed with decreasing temperature. Note that for $H < 8\,\mathrm{kOe}$, because of the poor signal to noise ratio, below $0.08\,\mathrm{K}$, $\rho(T)$ can be described with the exponent $n = 2$, depending on the fit region.

As magnetic field decreases from the higher magnetic field (paramagnetic) side, the temperature range, T_{FL}, becomes smaller, while the coefficient A of T^2-dependence increases rapidly and shows a tendency of diverging as $H \to H_c$. A divergent nature of this coefficient, when approaching to the critical field from paramagnetic side, is considered strong evidence for a

field-induced quantum phase transition [Gegenwart, 2002], which will be discussed below together with the field dependence of the electronic specific heat coefficient (γ). In addition, the exponent n=1.5 near a QCP was predicted by the traditional SDW scenario of quantum criticality with $d = 3$ and $z = 2$ [Hertz, 1976; Millis, 1993]. From the phase diagram it is apparent that H^* separates T_{FL} region from the AFM phase boundary T_N.

6.2.3 Specific heat

Figure 6.11 (a) displays the temperature dependences of the specific heat, $C_p(T)$, of YbPtBi for $H = 0$ and 140 kOe, applied along the [100] direction, together with zero field $C_p(T)$ of its nonmagnetic isostructural counterpart, LuPtBi. The overall shape of $C_p(T)$ for LuPtBi is typical for a nonmagnetic systems. In particular, below 8 K it is easily described by the relation, $C_p(T) = \gamma T + \beta T^3$, in which the first term is a conventional conduction electron contribution to the specific heat with the Sommerfeld coefficient, γ, and the second term is a low temperature phonon contribution in a form of the Debye-T^3 law with the Debye temperature, Θ_D. For LuPtBi, shown in the inset of Fig. 6.11 (a), least-square fitting of this formula to the experimental data yields the $\gamma \simeq 0$ (6×10^{-5} J/mol·K^2) and from β, the Θ_D $\simeq 190$ K. Since γ is negligible, which is consistent with low a carrier density system, $C_p(T)$ of LuPtBi is dominated by the phonon specific heat.

The zero field, $C_p(T)$ of YbPtBi indicates a distinct anomaly at about 0.41 K which is consistent with earlier results [Fisk, 1991] (Fig. 6.11 (b)). Since $C_p(T)$ of YbPtBi shows a broad hump around 6 K and a peak at T_N, we were not able to extract γ and Θ_D from a fit of $C_p(T)/T = \gamma + \beta T^2$ to the data. The result of $C_p(T)$ for $H = 140$ kOe shows the development of a large, broad peak structure, centered near 10 K, probably related to the electronic Schottky anomaly. At high temperatures the $C_p(T)$ data are essentially the same for all curves shown in Fig. 6.11 (a).

The total specific heat obtained for YbPtBi can be assumed to consist of the nuclear Schottky (C_N), electronic (C_{el}), phonon ($C_{lattice}$), and magnetic (C_m) contributions. At higher temperatures, where $C_N(T)$ contribution can be ignored, $C_p(T)$ consists of C_{el}, $C_{lattice}$, and
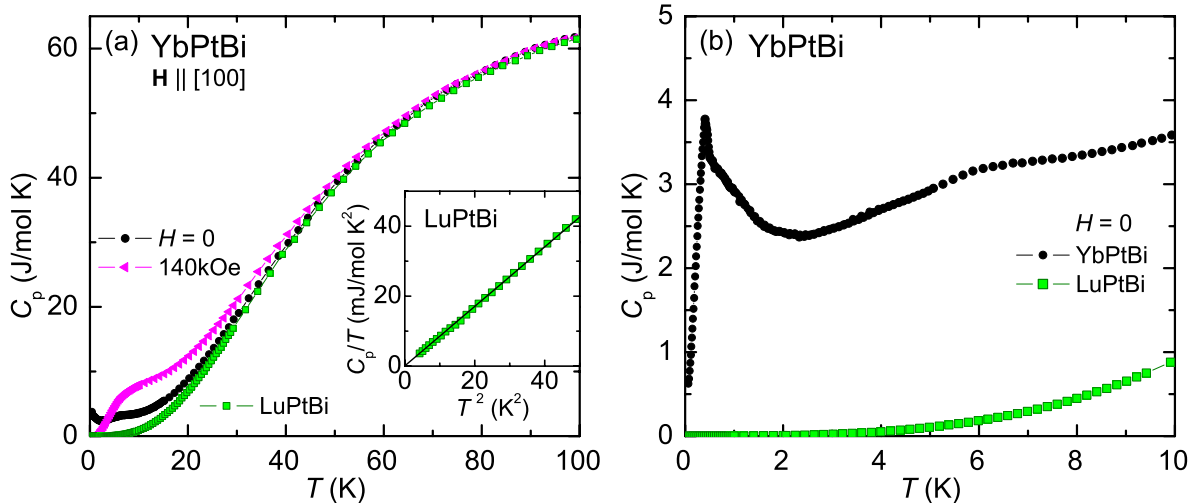
Figure 6.11   (a) Specific heat of YbPtBi as $C_p(T)$ vs. T for $H = 0$ (cir-
cles) and 140 kOe (triangles), applied magnetic field along the
[100] direction, and zero-field $C_p(T)$ of LuPtBi (squares). In-
set displays C_p/T vs. T^2 for LuPtBi. The solid line is a fit of
the equation $C_p(T) = \gamma T + \beta T^3$ to the data. (b) Zero field
specific heat for YbPtBi and LuPtBi below 10 K.

C_m contributions. Thus, $C_m(T)$ of YbPtBi was estimated by subtracting $C_p(T)$ of LuPtBi

and plotted as $C_m(T)$ vs. $\log(T)$ in Fig. 6.12 (a) for selected magnetic fields.

In zero field, in addition to a distinct anomaly at T_N, the two anomalies, which can be

expected due to the electronic Schottky contributions, are visible near 6 K and higher than

50 K. For $H > 4$ kOe which is high enough to suppress T_N, as shown by $\rho(T, H)$ results, a

broad peak is developed in the low temperature side (see $H = 10$ kOe data). The position of

the maximum of this low temperature anomaly continuously shifts to higher temperature as

magnetic field increases to 140 kOe. The anomaly, shown near 6 K in zero field, merges into

lower temperature anomaly around 40 kOe, causing significant broadening of the combined

feature. The evolutions of these two anomalies as a function of magnetic field are plotted in

the inset of Fig. 6.12 (a), where the position of maximum was determined from the Gaussian

fit to the data.

For $H = 0$ and 140 kOe, the magnetic entropy, $S_m(T)$, was inferred by integrating $C_m(T)/T$

starting from the lowest temperature measured and plotted in Fig. 6.12 (b). For $H = 140$ kOe,
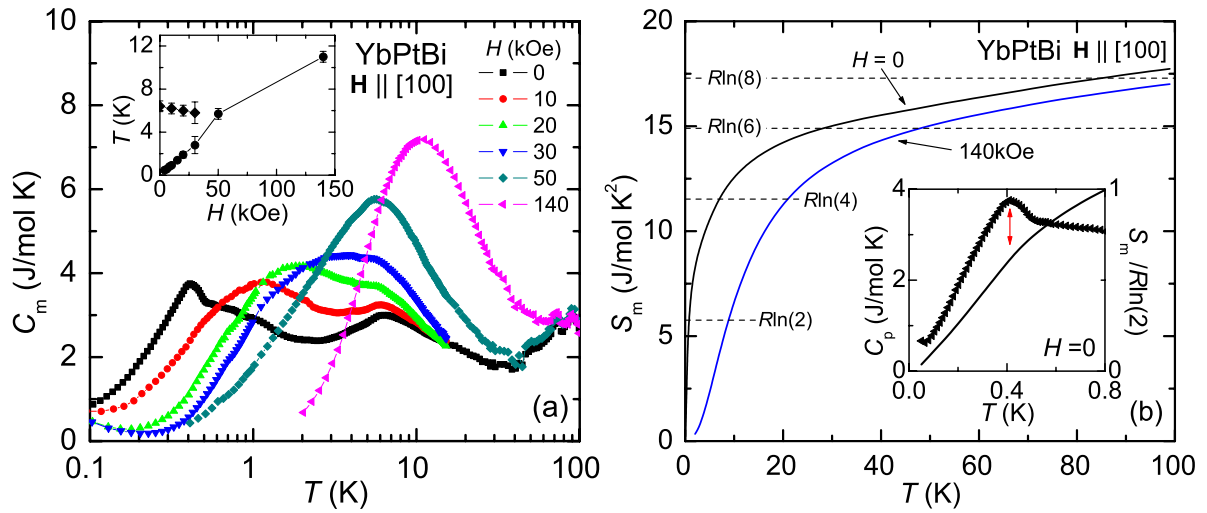
Figure 6.12   (a) Logarithmic temperature variation of the magnetic contribution $C_m(T)$ to the specific heat of YbPtBi at selected magnetic fields; $C_m(T) = C_p(T)$(YbPtBi) - $C_p(T)$(LuPtBi). Inset displays positions of maxima developed in $C_m(T)$. (b) Magnetic entropy, $S_m(T)$, for $H = 0$ and 140 kOe, inferred by integrating C_m/T starting from the lowest temperature measured. Inset shows the low temperature $C_p(T)$ of YbPtBi (left axis, symbols) and the magnetic entropy (S_m) divided by $R\ln(2)$ (right axis, line). Vertical arrow marks the peak position of the λ-shaped anomaly.

since the $C_p(T)$ data were taken above 2 K and no up-turn in $C_p(T)$ data at low temperatures was observed, the nuclear contribution was ignored to evaluate the magnetic entropy. $S_m(T)$ reaches about 55% of $R\ln(2)$ at T_N and recovers the full doublet, $R\ln(2)$, entropy by ~ 0.8 K (inset), which suggests that the ordered moment at T_N is compensated (reduced) by Kondo screening. The calculated $S_m(T)$ reaches a value of $R\ln(4)$ by 7 K and $R\ln(6)$ by 28 K, and the recovered $S_m(T)$ at $T = 100$ K is close to the full $R\ln(8)$, which suggests that the highest CEF energy levels are separated by approximately 100 K from the ground states. The inferred $S_m(T)$ data for $H = 140$ kOe is released slower than that for $H = 0$.

The results of low temperature specific heat measurements shed light on the HF state of YbPtBi, where the evolution of the quasi-particle mass can be inferred as the system is tuned by external magnetic field. The specific heat data divided by temperature are plotted in Fig. 6.13 (a) (solid symbols) as $C_p(T)/T$ vs. $\log(T)$ for $T \leq 2$ K and $H \leq 30$ kOe, where the
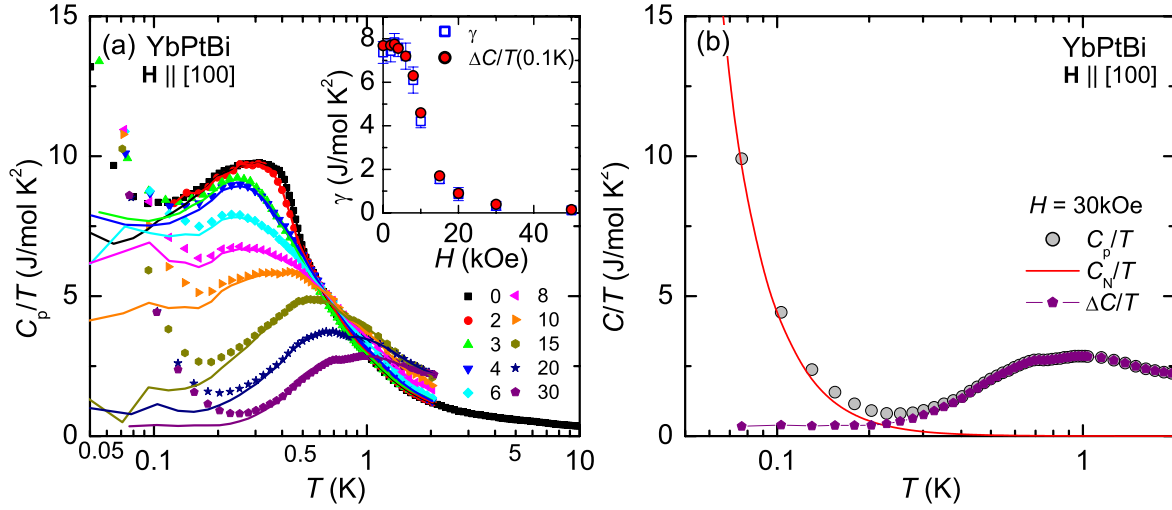
Figure 6.13 (a) Low temperature specific heat as $C_p(T)/T$ (solid symbols) and $\Delta C(T)/T$ (solid lines) vs. $\log(T)$ for YbPtBi at various magnetic fields, applied along the [100] direction; $\Delta C(T) = C_p(T)$ - $C_N(T)$, where the nuclear Schottky contribution was subtracted by using $C_N(T) \propto 1/T^2$. Inset shows the electronic specific heat coefficient, $\gamma = \Delta C(T)/T|_{T \to 0}$ (open squares), and $\Delta C(T)/T$ at $T = 0.1\,\mathrm{K}$ (solid circles) as a function of magnetic field. (b) C_p/T, C_N/T, and $\Delta C/T$ for $H = 30\,\mathrm{kOe}$, plotted in a $\log(T)$ scale.

$C(T)/T$ data for $H = 0$ are plotted below $10\,\mathrm{K}$. When magnetic field is applied, the well defined anomaly at T_N is no longer visible for $H > 3\,\mathrm{kOe}$ and instead the data show a broad maximum. This broad maximum decreases in magnitude and shifts to higher temperature with increasing magnetic field, indicating that the magnetic entropy is removed at higher temperature for larger applied magnetic fields (see for $H = 140\,\mathrm{kOe}$ curve in Fig. 6.12 (b)). At the lowest temperatures, a slight up-turn in $C_p(T)$, associated with a nuclear Schottky anomaly, is visible. This nuclear Schottky anomaly is much more pronounced in the $C_p(T)/T$ plots and becomes significant as magnetic field increases. It is expected that the anomaly correspond to AFM order for $H < 4\,\mathrm{kOe}$ may either broaden significantly or be masked by the presence of the broad peak structure as well as the nuclear Schottky contributions.

Below $2\,\mathrm{K}$, where $C_{lattice}$ contribution can be safely ignored, the electronic specific heat coefficient was estimated by subtracting nuclear contribution, using $C_N(T) \propto 1/T^2$; $\Delta C(T) =$

$C_p(T)$ - $C_N(T)$. As an example, the $C_p(T)$, the estimated $C_N(T)$, and the $\Delta C(T)$ for $H =$ 30 kOe are plotted as circles, line, and pentagons, respectively, in Fig. 6.13 (b). Above ~ 0.4 K, the $C_N(T)$ contribution to the total $C(T)/T$ is very small, however, below ~ 0.2 K, $C(T)/T$ is dominated by $C_N(T)$ contribution. The obtained $\Delta C(T)$ data for several magnetic fields are plotted as $\Delta C(T)/T$ vs. $\log(T)$ in Fig. 6.13 (a) (solid lines). In zero field, by extrapolating $\Delta C(T)/T$ to zero temperature ($\gamma = \Delta C(T)/T|_{T\to 0}$), γ is estimated to be 7.4 J/mol·K^2, which is consistent with earlier result (~ 8 J/mol·K^2 [Fisk, 1991]) and is one of the highest effective mass values observed among HF compounds. The magnetic field dependence of γ is plotted in the inset of Fig. 6.13 (a) as open squares. For comparison, the $\Delta C(T)/T$ data at $T = 0.1$ K are also plotted as solid circles, which are essentially the same as γ. At magnetic fields below 8 kOe, γ is approximately constant within about 1 J/mol·K^2. A strong decrease of γ is observed for $H \geq 8$ kOe, implied that the quasi-particle mass diverges when approaching the critical field from higher magnetic fields. For magnetic fields larger than 8 kOe, γ shows a very similar field dependence as A (see discussion below). For any of the specific heat data, measured magnetic fields up to 30 kOe, $\Delta C(T)/T$ shows no clear indication of a nFL-like behavior either as a logarithmic (-$\log(T)$) or non-analytic (-$\sqrt{T}$) temperature dependence. A -$\log(T)$ dependence of $\Delta C(T)/T$ is observed over only a limited temperature range; for example, $\Delta C(T)/T$ shows such a -$\log(T)$ dependence between $0.3 \sim 0.8$ K near 4 kOe and between $0.45 \sim 1.6$ K near 8 kOe.

6.2.4   Thermal expansion and magnetostriction

Figure 6.14 shows a linear thermal expansion coefficient, $\alpha_{100} = \mathrm{d}(\Delta L/L)/\mathrm{d}T$, where ΔL is the length variation along the [100] direction ($\Delta L/L \parallel$ [100]). At high temperatures, α_{100} gradually decreases with lowering temperature and then, below 100 K α_{100} decreases rapidly down to ~ 6 K. With further decreasing temperature, α_{100} shows a sudden enhancement below 5 K, followed by a sharp peak at $T = 0.38$ K. The observed characteristics in the temperature dependence of the zero field α_{100} are very similar to that shown in the magnetic specific heat (see Fig. 6.12). The AFM transition manifests itself as a sharp peak in α_{100} at T_N
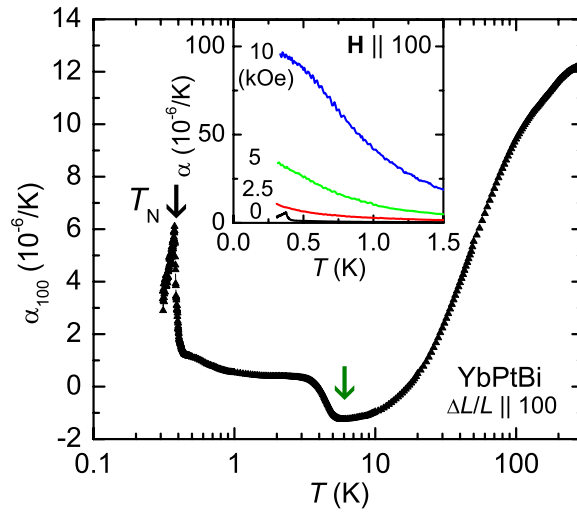
Figure 6.14   The linear thermal expansion coefficient, $\alpha_{100} = \mathrm{d}(\Delta L/L_{100})/\mathrm{d}T$, of YbPtBi, where L is the sample length along the [100] direction. The AFM ordering temperature is indicated by the arrow at 0.38 K. The arrow at 6 K represents the maximum temperature observed in specific heat. Inset shows α_{100} at selected magnetic fields ($H = 0$, 2.5, 5, and 10 kOe bottom to top), measured with a longitudinal configuration $\Delta L/L \parallel \mathbf{H} \parallel [100]$.

$= 0.38\,\mathrm{K}$, where $C_m(T)$ exhibits the AFM transition as a maximum at $T_N = 0.41\,\mathrm{K}$. If the thermal expansion, $\Delta L/L$, was composed of only the lattice contribution, it will only decrease monotonically with decreasing temperature. Thus, the two features, at which α_{100} shows a decrease with warming, at about 5 K and a saturation for $T > 100\,\mathrm{K}$, can be related to a substantial magnetic contribution associated with Yb^{3+} ions, which is in agreement with the broad peak positions centered at about 6 K and higher than 50 K in $C_m(T)$. The saturation of α_{100} for $T > 100\,\mathrm{K}$ is most likely due to CEF effects of higher energy levels combined with simple lattice effects. The anomaly near 5 K can be related to the CEF effects of the first excited state, where the lattice contribution can be ignored at low temperatures. In order to examine the magnetic field effect on α_{100} at low temperatures, the constant field, thermal expansion was measured in the magnetic field parallel to [100], i.e. $\Delta L \parallel \mathbf{H} \parallel [100]$. The results are plotted in the inset of Fig. 6.14. The peak at T_N is suppressed below 0.3 K for $H > 2.5\,\mathrm{kOe}$. Low temperature α_{100} increases with application of magnetic field.
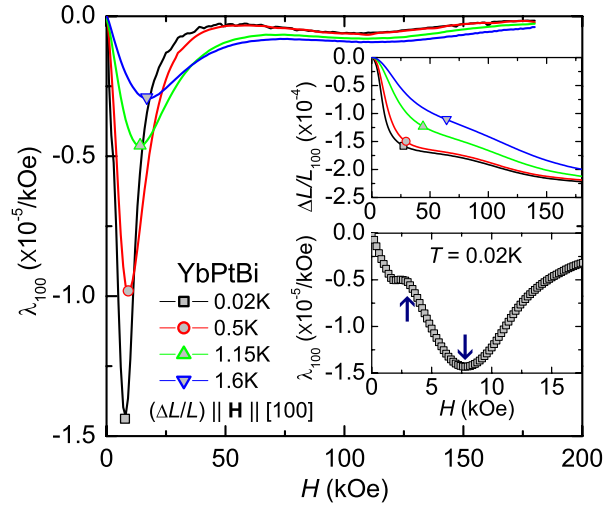
Figure 6.15   Magnetostriction and the coefficient of YbPtBi. The linear magnetostriction coefficient, $\lambda_{100} = \mathrm{d}(\Delta L/L_{100})/\mathrm{d}H$ vs. H, at selected temperatures, where L is the sample length along the [100] direction parallel to the magnetic field applied along the [100] (longitudinal configuration $\Delta L/L \parallel \mathbf{H} \parallel$ [100]). The upper inset shows the magnetic field dependence of the magnetostriction $\Delta L/L_{100}$. The lower inset shows λ_{100} at 0.02 K. The up- and down-arrow indicate the phase transition T_N and the local minimum H^*, respectively.

Figure 6.15 shows the linear magnetostriction coefficient, $\lambda_{100} = \mathrm{d}(\Delta L/L)/\mathrm{d}H$, and the linear magnetostriction, $\Delta L/L_{100}$ (upper inset), of YbPtBi for selected temperatures, where the longitudinal linear magnetostriction has been measured parallel to the [100] direction, i.e., $\Delta L \parallel \mathbf{H} \parallel$ [100]. The magnetic field was swept with a rate of between $5 \sim 10$ Oe/sec for temperatures up to 10 K. No hysteresis larger than ~ 100 Oe could be detected. In the low magnetic field regime $\Delta L/L$ at $T = 0.02$ K shows weak slope changes and then decreases rapidly as magnetic field increases, which manifests in λ_{100} as sharp slope changes below 3 kOe and a minimum around 7.8 kOe (see arrows in the lower inset). As temperature is raised, the sharp slope changes are no longer visible for $T > 0.4$ K and the minimum shifts to higher magnetic field. At high magnetic fields, there is broad features: a shoulder near 50 kOe and a minimum near 100 kOe in λ_{100}.

Figure 6.16 (a) shows a plot of the magnetic field variation of λ_{100} at selected temperatures.
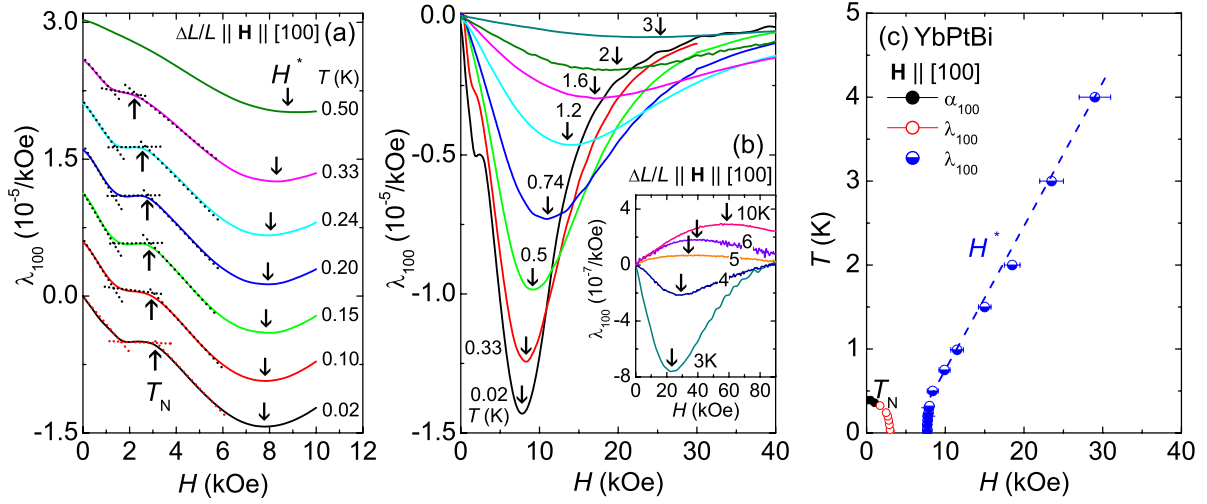
Figure 6.16   (a)   The   linear   magnetostriction   coefficient, λ_{100} $=$ $d(\Delta L/L_{100})/dH$ vs. H, at selected temperatures. For clarity the data sets are vertically shifted each by 5×10^{-5}/kOe. The up- and down-arrows indicate the phase transition T_N and the local minimum H^*, respectively. (b) λ_{100} up to 3 K. Inset shows λ_{100} up to 10 K. Arrows indicate the minimum (H^*) and maximum in λ_{100}. (c) $H - T$ phase diagram of YbPtBi, constructed form α_{100} and λ_{100}. Dashed-line is guide to eye.

For $T = 0.02$ K data, the two slope changes in λ_{100} are visible at about 1.5 and 3 kOe. These anomalies shift to lower magnetic field as temperature increases. The phase transition field was selected for the higher field slope change because the higher field one is well matched with the sharp peak position in $d\rho(H)/dH$ (see discussion below). The determined phase transition fields are indicated by up-arrow in Fig. 6.16 (a). The local minimum, observed from $T = 0.02$ K curve at $H^* \sim 7.8$ kOe, is not very sensitive to temperature up to 0.5 K ($H^* = 8.4$ kOe), whereas H^* shifts, almost linearly, to higher magnetic field with further increasing temperatures up to 10 K, which can be clearly seen when this position is plotted in the $H - T$ plane in Fig. 6.16 (c). A negative λ_{100} is observed up to 4 K and it changes to positive for $T > 5$ K, shown in the inset of Fig. 6.16 (b). Figure 6.16 (c) displays a $H - T$ phase diagram constructed from both α_{100} and λ_{100}: The AFM phase boundary, T_N, corresponds to the sharp peak position in α_{100} and the higher field slope change in λ_{100}, and a crossover scale, H^*, corresponds to the position of the minimum for $T \leq 4$ K in λ_{100}.

6.2.5 Hall effect
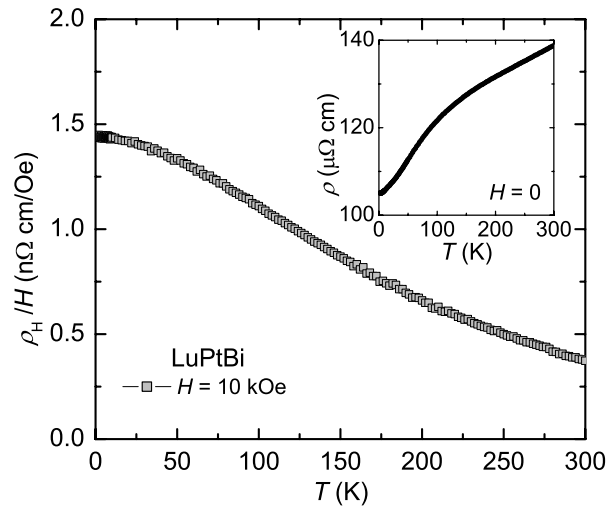
Figure 6.17   Temperature dependence of the Hall coefficient, $R_H = \rho_H/H$,
of LuPtBi for $H = 10\,\mathrm{kOe}$, applied along the [111] direction.
Inset shows the zero field resistivity.

Figure 6.17 shows the temperature-dependent Hall coefficient, $R_H = \rho_H/H$, of LuPtBi at $H = 10\,\mathrm{kOe}$, applied along the [111] direction. The positive R_H of LuPtBi, suggesting that the dominant carriers are holes, monotonically increases as temperature decreases. Assuming a single band model, the carrier concentration at $300\,\mathrm{K}$ is estimated to be $n = 1.7 \times 10^{26}$ m^{-3} ($R_H = 0.37$ nΩcm/Oe) corresponding to ~ 0.02 hole per formula unit. As shown in the inset of Fig. 6.17 $\rho(T)$ of LuPtBi decreases as temperature is lowered. Thus, LuPtBi can be characterized by a low carrier metallic (or semimetallic) system. The carrier concentration of LuPtBi is approximately 100 times smaller than that for copper [Ziman, 1960], comparable to that for earlier result of isostructural semimetal YbPtBi [Hundley, 1997], and 2 orders of magnitude larger than that of NdPtBi [Morelli, 1996] and LaPtBi [Jung, 2001]. This trend is consistent with the earlier resistivity results [Canfield, 1991] in which the resistivity systematically changes from a small gap semiconductor (or semimetal) for lighter rare-earth compounds to metallic (or semimetallic) for heavier rare-earth compounds.

Figure 6.18 displays the magnetic field-dependent Hall resistivity, ρ_H, of YbPtBi in magnetic fields up to $140\,\mathrm{kOe}$ at various temperatures. The results, obtained in this study, are

Figure 6.18   Hall resistivity, ρ_H, of YbPtBi as a function of magnetic field,
applied along the [100] direction, at various temperatures. The
arrow on 0.06 K curve near 55 kOe indicates a deviation from
linear field dependence of ρ_H. The dash-dotted line is guide
to the eye. Inset shows the low temperature and low field ρ_H
at selected temperatures.

similar to previous Hall effect measurements above 2 K [Hundley, 1997]. Here, the measurements have been extended to much higher magnetic fields, up to 140 kOe, and to much lower temperatures, down to 0.06 K, investigating the phenomena that are related to quantum criticality. Below 1 K the ρ_H data as function of temperature and magnetic field were taken with the condition that the sample was mounted on a dilution refrigerator cold stage with very thin layer of GE-varnish. At high temperatures (for $T \geq 0.5$ K), after cleaning the GE-varnish off using ethanol, the sample was mounted on the cold stage of ^{3}He option in PPMS with Apiezon N-grease and ρ_H was measured. The data, taken from a dilution refrigerator measurements, are in good agreement with the data, taken from ^{3}He setup.

The sign of ρ_H is positive for all temperatures measured which, as was the case for LuPtBi, is suggestive that hole-type carriers are dominant. Above 100 K, ρ_H follows a linear magnetic field dependence, whereas, for $T \leq 25$ K, ρ_H exhibits a non-linear magnetic field dependence. An apparent deviation from the linear magnetic field dependence of ρ_H is indicated by the heavy arrow on 0.06 K data. As highlighted in the inset, the overall features of ρ_H below
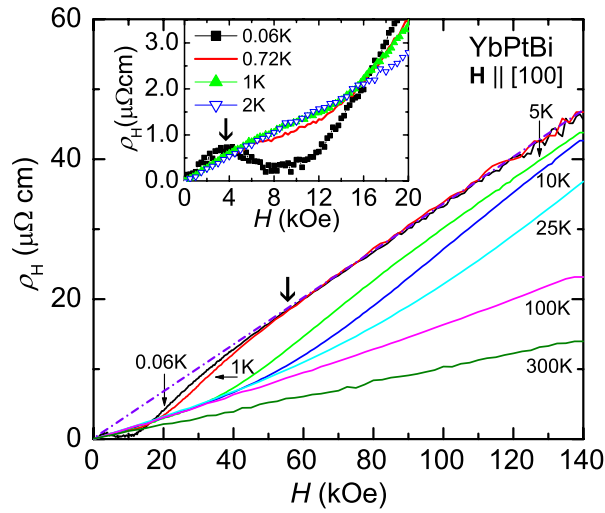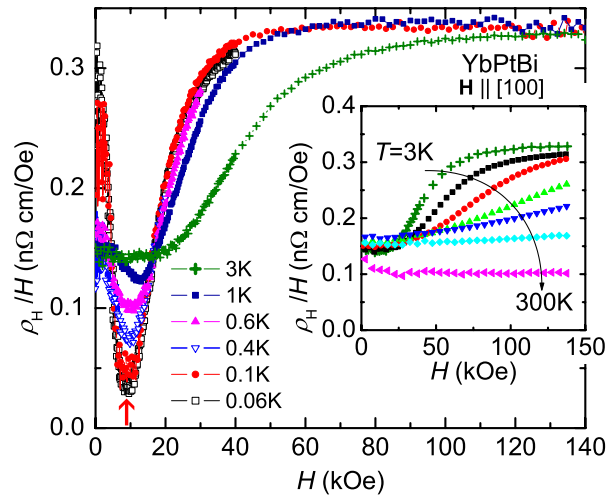
Figure 6.19   Hall coefficient, $R_H = \rho_H/H$, of YbPtBi as a function of mag-
netic field, applied along the [100] direction, at various tem-
peratures. The arrow near 8 kOe indicates the position of local
minimum shown in R_H at $T = 0.06$ K. Inset shows the high
temperature R_H for $T = 3$, 5, 10, 25, 50, 100, and 300 K (top
to bottom).

0.4 K are strongly non-monotonic as a function of magnetic field. At 0.06 K, the ρ_H manifests

distinct features: a local maximum around 4 kOe and a broad curvature (formation of local

minimum) between $4 \sim 12$ kOe. As temperature increases the local maximum broadens and

the inflection point of the broad curvature moves to higher magnetic fields.

Figure 6.19 shows R_H of YbPtBi as a function of magnetic field. At high temperatures

(inset), R_H is almost magnetic field-independent. As temperature is lowered, a broad local

minimum in R_H is developed and sharpened. An anomalous low temperature behavior of Hall

effect can be clearly seen in R_H plot. At base temperature, $T = 0.06$ K, the high magnetic

field limit of R_H ($H \rightarrow 140$ kOe) is close to the low magnetic field limit of R_H ($H \rightarrow 0$). As

magnetic field increases two features are developed as a weak slope change near 4 kOe and a

clear minimum around 8 kOe. These two features are also seen in the MR and magnetostriction

measurements. Thus, the anomaly near 4 kOe can be related to the AFM phase boundary,

however the meaning of 8 kOe anomaly is still not clear. Generally, an interpretation of the

Hall effect is difficult when multiple bands are crossing the Fermi energy.
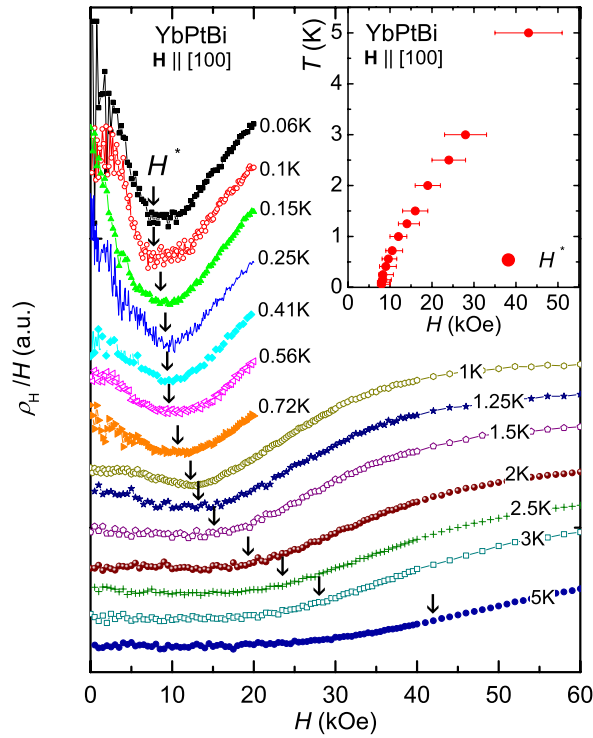
Figure 6.20 ρ_H/H at selected temperatures. For clarity, the data sets have been shifted by different amounts vertically. Arrows indicate the position of local minimum and inflection point. The positions of H^* are plotted in the $H - T$ plane in the inset.

Figure 6.20 shows R_H of YbPtBi at selected temperatures, where the data sets were shifted by different amounts vertically for clarity. Because of poor signal to noise ratio of the current data, the phase transition and the position of the characteristic feature can not be determined precisely. The local maximum in ρ_H near $4\,\mathrm{kOe}$ that is clear at $0.06\,\mathrm{K}$, (inset, Fig. 6.18) broadens significantly as temperature increases and is no longer visible for $T > 0.5\,\mathrm{K}$. The local minimum, $H^* \sim 8\,\mathrm{kOe}$ observed at $T = 0.06\,\mathrm{K}$, gradually shifts to higher magnetic fields as temperature increases. The determined positions of the local minimum are indicated by arrows in Fig. 6.20 and also plotted in the $H - T$ plane in the inset. As will be shown later, the positions of H^* agree also with the anomaly developed in MR, magnetostriction, specific heat, and TEP measurements.

In Fig. 6.21 R_H is plotted as a function of temperature at selected magnetic fields, where closed- and open-symbols are taken from temperature and magnetic field sweeps of ρ_H, re-
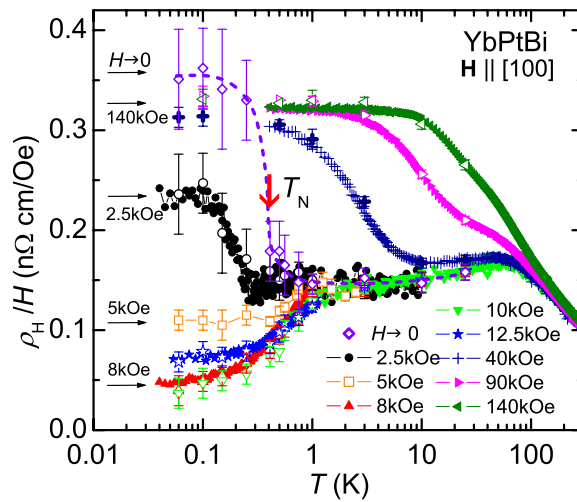
Figure 6.21 Temperature dependence of the Hall coefficient ($R_H = \rho_H/H$) of YbPtBi at various magnetic fields, applied along the [100] direction. Closed- and open-symbols are taken from temperature and field sweeps of ρ_H, respectively. The open-diamond symbols ($\diamond$) of $R_H(T \to 0)$ are obtained from the initial slope of ρ_H vs. H. The dashed-line is guide to the eye.

spectively. The data of R_H ($H \to 0$) was obtained by taking the low field limit of $d\rho_H/dH$ of which the large error bar is fundamentally due to the weak signal of ρ_H. In the low magnetic field ($H \to 0$ and $2.5\,\text{kOe}$) results, R_H clearly shows the change of scattering mechanism near $0.4\,\text{K}$ and $\sim 70\,\text{K}$. The steep increase below $0.4\,\text{K}$ in R_H ($H \to 0$) agrees with the behavior observed from resistivity measurements. The temperature dependence of R_H depends strongly on the applied magnetic field below $70\,\text{K}$, whereas above $70\,\text{K}$ R_H is basically magnetic field-independent for $H \leq 140\,\text{kOe}$.

As temperature decreases, the zero field limit R_H ($H \to 0$) data below $10\,\text{K}$ show a very weak temperature dependence and the opening of the SDW gap below $T_N = 0.4\,\text{K}$ gives rise to an abrupt enhancement of R_H ($H \to 0$). A steep increase of R_H below T_N implies a significant carrier density reduction associated with the Fermi surface gapping. For $H = 5\,\text{kOe}$ R_H becomes almost temperature-independent below $10\,\text{K}$. Similar results have been observed in URu_2Si_2 compound [Schoenes, 1987]. Below $T_0 = 17.5\,\text{K}$, R_H of URu_2Si_2 increases by factor of 5-20 because of the opening of a gap over the Fermi surface. It should be noted,

though, that since the Hall sample was mounted with GE-varnish, there is a possibility that the steep increase in R_H below $0.4\,\mathrm{K}$ may be altered by strain (as was resistivity). Thus, Hall data needs to be taken without using the GE-varnish. This may be difficult to accomplish due to the torque that needs to be secured in high magnetic fields.

6.2.6 Thermoelectric power

The TEP as a function of temperature, $S(T)$, for LuPtBi is plotted in the inset of Fig. 6.22. The positive sign of TEP indicates that holes are dominant carriers which is consistent with R_H results. As temperature increases $S(T)$ increases monotonically, after passing through a broad peak structure around $40\,\mathrm{K}$ probably due to the phonon drag, and then $S(T)$ gradually increases to $8\,\mu\mathrm{V/K}$ at $250\,\mathrm{K}$. Above $250\,\mathrm{K}$ $S(T)$ shows an essentially temperature-independent behavior up to $300\,\mathrm{K}$. The observed TEP of LuPtBi is not consistent with the behavior expected from simple metals and the origin of the strong break in slope near $40\,\mathrm{K}$ is unknown at present.
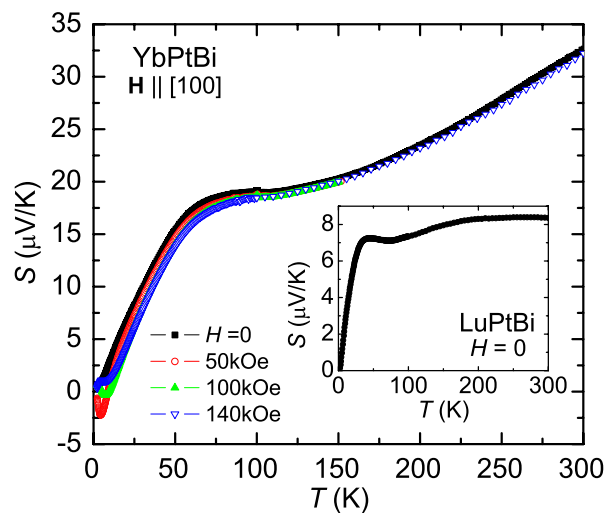
Figure 6.22 Temperature-dependent TEP, $S(T)$, of YbPtBi at selected magnetic fields, applied along the [100] direction. Inset shows the zero field $S(T)$ of LuPtBi.

Figure 6.22 shows the evolution of $S(T)$ for YbPtBi with magnetic fields applied along the [100] direction. In zero field the observed TEP is positive, indicating that holes are dominant carriers which is consistent with R_H results and with previous TEP results [Hundley, 1997]

above 2 K. However, the positive sign of TEP for YbPtBi is opposite to that generally observed in Yb-based HF systems, which is negative due to the location of a narrow Kondo resonance peak slightly below the Fermi energy [Hewson, 1993]. The emergence of a broad peak structure, centered around 70 K, can be associated with excited CEF energy levels of Yb^{3+} ions. This can be also related to the appearance of a high temperature broad maximum around 70 K in ρ_H/H and an inflection point near 85 K in $\rho(T)$. In these cases the temperature of the CEF related features corresponds to a fraction of the CEF splitting (0.4-0.6Δ_{CEF}) as evidenced in many other Ce- and Yb-based compounds and alloys [Maekawa, 1986; Bickers, 1987; Očko, 2004; Köhler, 2008].
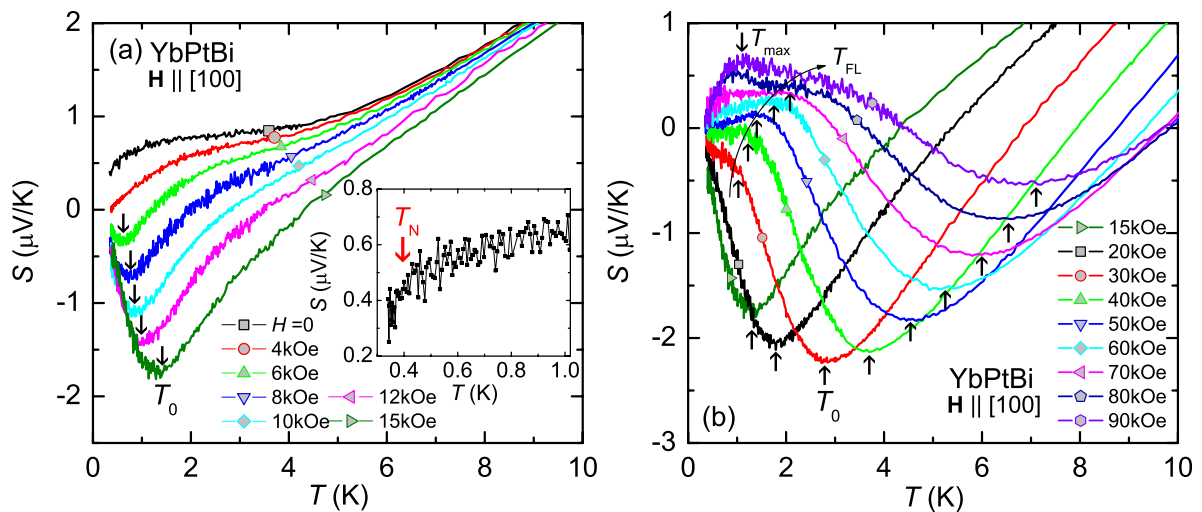
Figure 6.23   (a) Low temperature $S(T)$ of YbPtBi at selected magnetic fields for $H \leq 15$ kOe. Vertical arrows indicate a local minimum T_0. Inset shows the zero field $S(T)$ below 1 K. Vertical arrow represents the AFM ordering temperature at which the slope, $dS(T)/dT$, is changed. (b) Low-temperature $S(T)$ for $15 \leq H \leq 90$ kOe. Vertical arrows indicate the characteristic features corresponding to a local minimum temperature T_0, a linear temperature dependence of $S(T)$ below T_{FL}, and a local maximum for $H = 90$ kOe curve.

$S(T)$ changes very little with applied magnetic field for $T \gtrsim 20$ K. For $T \lesssim 20$ K $S(T)$ shows a rather complex behavior, with the emergence of new broad peak structures as magnetic field increases. In Figs. 6.23 (a) and (b), the low temperature TEP data for YbPtBi are plotted as

$S(T)$ vs. T for selected magnetic fields. In contrast to the high temperature behavior, $S(T)$ data reveal complex and strong magnetic field dependences. In zero field, the sign of TEP is positive down to 0.35 K (the base temperature of the ^{3}He system used) and $S(T)$ exhibits a broad feature around 2 K. No clear signature of the AFM phase transition near 0.4 K is observed as presented in the inset. Generally, for a SDW antiferromagnet such as Cr [Fawcett, 1988], the TEP measurements revealed a sudden enhancement due to the opening a gap below SDW state, similar to what was seen in the zero field limit Hall data ($R_H(H \rightarrow 0)$) in Fig. 6.21. Unfortunately, at 0.35 K $S(T)$ is just starting to change; low temperature measurements will be needed to fully define the zero field $S(T)$ feature. When a magnetic field is applied along the [100] direction, $S(T)$ curves shift toward a negative direction and a local minimum, T_0, develops for $H > 5$ kOe. The position of T_0 continuously shifts to higher temperature as magnetic field increases up to 90 kOe, indicated by arrows in Figs. 6.23 (a) and (b). For $H > 30$ kOe, the low temperature behavior changes significantly; the TEP shows the development of a new, broad feature, T_{FL}, and reveals complex sign reversals. The position of T_{FL} below which $S(T) \propto T$ is indicated by arrows in Fig. 6.23 (b). For $H > 70$ kOe, an additional local maximum, T_{max}, is developed in the low temperature side. The positions of both T_{FL} and T_{max} shift to higher temperature with increasing magnetic field.

In order to investigate the low temperature quasi-particle behavior, a plot of $S(T)/T$ is presented in Figs. 6.24 (a) and (b) as a function of $\log(T)$ for selected magnetic fields. In zero field, $S(T)/T$ exhibits a logarithmic temperature dependence between T_N and ~ 3 K. For $H = 2.5$ kOe the $\log(T)$ dependence of $S(T)/T$ holds below 4 K. This $\log(T)$-dependence of $S(T)/T$ has been observed from YbRh$_2$Si$_2$ [Hartmann, 2010] and YbAgGe [Mun, 2010b] in the vicinity of the QCP, as a signature of nFL-like behavior. As magnetic field increases $S(T)/T$ moves toward negative direction for $H > 4$ kOe, and the low temperature behavior changes dramatically. At higher fields for $H = 30$, 40, and 50 kOe, $S(T)$ curves are proportional to the temperature for $T < T_{FL}$ (Fig. 6.23) below which $S(T)/T = \alpha$, indicating the onset of FL behavior. For $H = 90$ kOe $S(T)/T$ deviates from a constant, indicating a deviation of FL behavior, due to the development of the local maximum, T_{max}, (see Fig. 6.23).
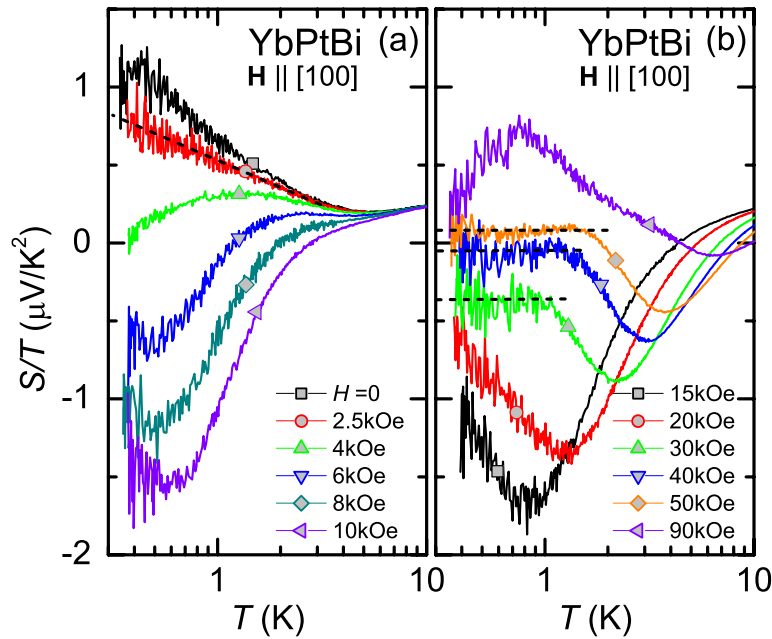
Figure 6.24 Temperature-dependent TEP divided by temperature, $S(T)/T$, in a logarithmic scale; $S(T)/T$ vs. $\log(T)$. (a) The dashed-line on the curve for $H = 2.5\,\text{kOe}$ is guide to eye, representing a logarithmic increase of $S(T)/T$ below $4\,\text{K}$. (b) Dashed-lines on the curves for $H = 30$, 40, and $50\,\text{kOe}$ indicate a saturation of $S(T)/T$ which corresponds to the linear temperature dependence of $S(T)$ below T_{FL}, shown in Fig. 6.23 (b).

Figure 6.25 shows the magnetic field dependence of TEP, $S(H)$, for YbPtBi. As magnetic field increase $S(H)$ curves initially decrease steeply and then linearly increases after passing through a minimum, H^*. For $H > 110\,\text{kOe}$ at $T = 2\,\text{K}$, the oscillatory behavior corresponds to quantum oscillations, which is consistent with Shubnikov de Haas (SdH) results. As temperature increases from $0.4\,\text{K}$, H^* shifts to higher magnetic fields and the absolute TEP value at H^* decreases up to $2\,\text{K}$ and then increases. The sign of TEP changes from positive to negative around $H_{SR} = 4.2\,\text{kOe}$ at $0.4\,\text{K}$ and recovers positive sign near $43\,\text{kOe}$; both H_{SR} values move to higher magnetic fields with increasing temperature. For $H > 100\,\text{kOe}$ and $T > 10\,\text{K}$ a sign reversal on TEP is no longer visible. At high magnetic fields, all $S(H)$ curves seem to collapse on the same line, following a linear magnetic field dependence.
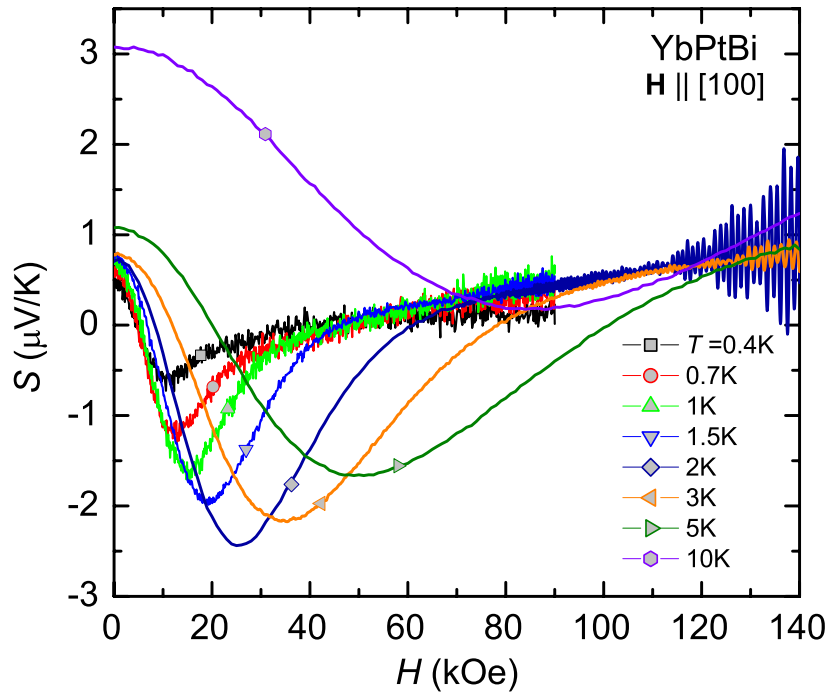
Figure 6.25 Magnetic field dependence of TEP, $S(H)$, of YbPtBi at se-
lected temperatures.

Figure 6.26 shows the low temperature $S(H)$ below $1.5\,\mathrm{K}$, where each $S(H)$ curve is shifted by $-0.3\,\mu\mathrm{V/K}$, for clarity. In addition to the lower H_{SR} and H^*, there is a slope change, H_{FL}, near $20\,\mathrm{kOe}$ above which $S(H)$ is linear in magnetic fields. The lower sign reversal (H_{SR}), the local minimum (H^*), and the slope change (H_{FL}) on $S(H)$ move to higher magnetic fields with increasing temperatures, indicated by a line, down arrows, and up arrows, respectively, in Fig. 6.26.

The features, collected from the $S(T)$ and $S(H)$ measurements, are plotted in the $H - T$ plane in Fig. 6.27. In zero field a weak signal as a small drop near $0.4\,\mathrm{K}$ is consistent with the T_N determined from resistivity (not shown in figure). The sign reversal temperatures determined from $S(T)$ is well matched with the sign reversal fields determined from $S(H)$, where the higher field sign reversal is not plotted. The line of sign reversal terminates near $4\,\mathrm{kOe}$ by simple linear extrapolation of the data below $1\,\mathrm{K}$. The H^* line determined from the local minimum in $S(H)$ is not matched with the T_0 line obtained from the local minimum in
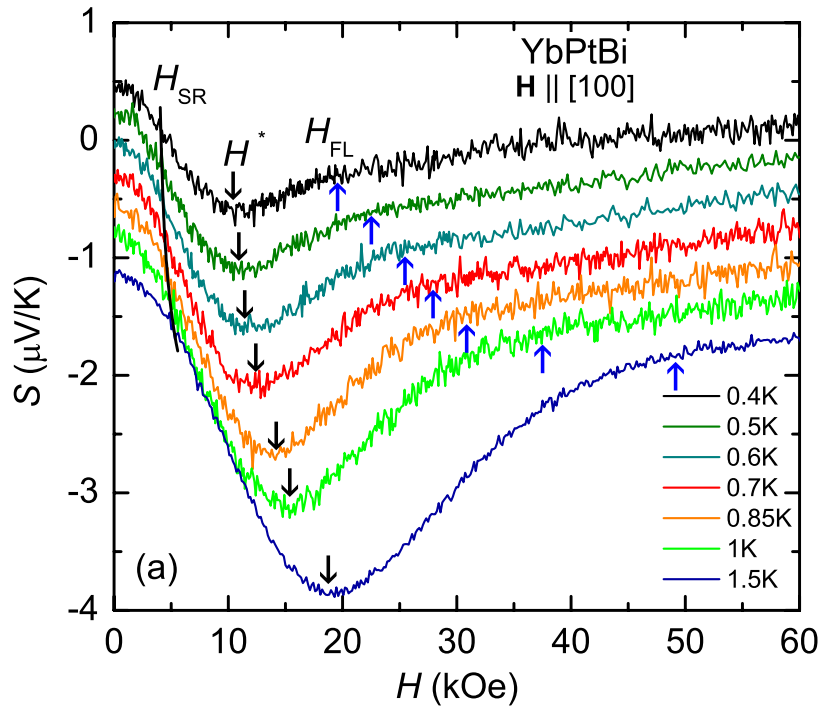
Figure 6.26 $S(H)$ of YbPtBi below $1.5\,$K. For clarity, the data sets have
been shifted by every -3μV/K vertically. Solid line H_{SR} indi-
cates a sign change of TEP from positive to negative. Down-ar-
rows H^* represent the determined position of the local mini-
mum. Up-arrows indicate a slope change, $\mathrm{d}S(H)/\mathrm{d}H$, above
which $S(H)$ follows a linear field dependence.

$S(T)$, where two lines are linearly rise with increasing magnetic field.

By carefully examining $S(T)$ and $S(H)$ data, as shown in bottom panels in Fig. 6.27, there
are signatures corresponding to H^* and T_0 in both figures even though one of features is very
weak. Below $30\,$kOe $S(H)$ for $T = 1\,$K (a horizontal cut through the $H - T$ plane) shows a
sign change at $H_{SR} = 5.6\,$kOe, a slope change near $H_0 = 11\,$kOe, and a local minimum around
$H^* = 15\,$kOe, where the signature of H_0 is very weak. Below $2.5\,$K $S(T)$ for $H = 15\,$kOe (a
vertical cut through the $H - T$ plane) indicates a slope change around $T^* = 1\,$K and a local
minimum near $T_0 = 1.3\,$K, where the signature of T^* is very weak. Thus, H^* line is sensitive
to the magnetic field sweeps and T_0 is sensitive to the temperature sweeps. Because of the
weak signal, T_0 and H^* were taken only from temperature sweeps and magnetic field sweeps,
respectively, and these are plotted in Fig. 6.27. T_0 seems to extrapolate to the origin ($T = 0$
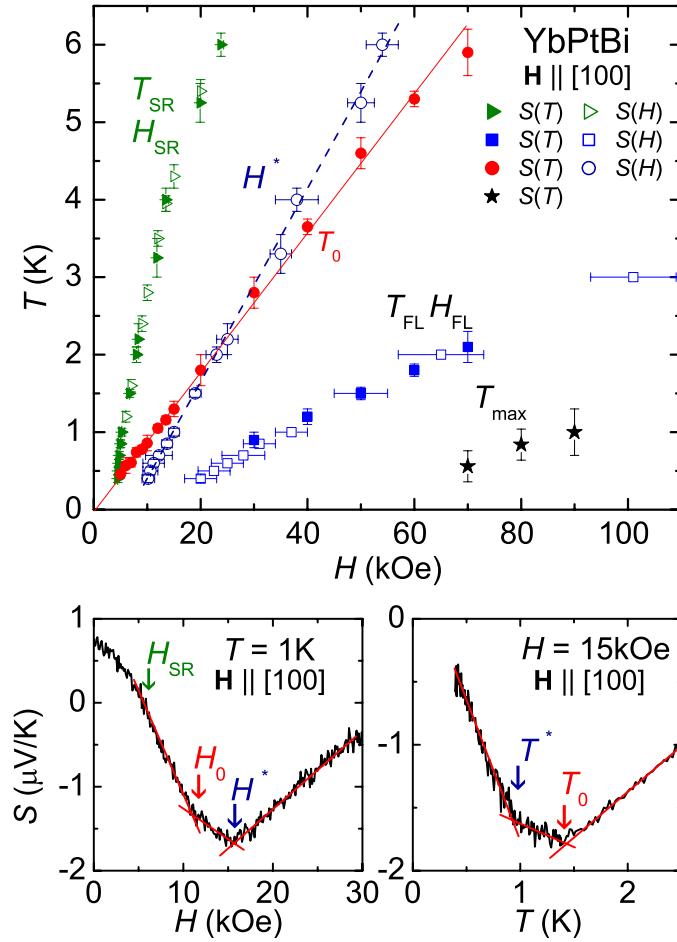
Figure 6.27   Various Characteristics observed from $S(T, H)$ measurements: T_{SR} and H_{SR} represents the sign reversal extracted from the position of $S(T, H) = 0$; H^* marks the position of the local minimum in $S(H)$; T_0 indicates the position of the local minimum in $S(T)$; T_{max} represents the position of the local maximum developed at low temperatures for $H \geq 70\,\mathrm{kOe}$; and T_{FL} and H_{FL} represent the slope change in $S(T)$ (Fig. 6.23) and $S(H)$ (Fig. 6.26), respectively. Bottom panels show the horizontal (left figure) and vertical (right figure) cut through the $H - T$ plane. Left panel: below $30\,\mathrm{kOe}$ $S(H)$ at $T = 1\,\mathrm{K}$ hits all three characteristic lines of H_{SR}, H_0, and H^*. Right panel: below $2.5\,\mathrm{K}$ $S(T)$ at $H = 15\,\mathrm{kOe}$ indicates both T^* and T_0 line. See details in the text.

and $H = 0$) of the $H - T$ plane and H^* tends toward $H = 8$ kOe at $T = 0$. The crossover T_{FL} (Fig. 6.23 and Fig. 6.26) is well overlapped with H_{FL} and is almost linear in magnetic fields above $0.4\,\text{K}$. As mentioned above for $H = 30$, 40, and 50 kOe, the TEP shows a linear temperature dependence, $S(T) = \alpha T$, which is a indication of FL behavior. Between 20 $\sim$ 30 kOe the boundary of T_{FL} is overlapped with the boundary of the FL region determined from T^2-dependence of $\rho(T)$. Therefore, TEP below $0.4\,\text{K}$ is expected to follow $S(T) = \alpha T$ for $H < 30\,\text{kOe}$. The local maximum developed in $S(T)$ for $H > 70$ kOe is plotted in Fig. 6.27 as stars. Because of the very weak TEP signal in this regime the signature is not discernible in $S(H)$ data. Since the TEP is known to be particularly sensitive to Kondo and CEF effects, the development of T_{max} can be related to the effect of further CEF splitting via Zeeman effect. In such a high magnetic field the Kondo effect with $T_K \sim 1\,\text{K}$ for YbPtBi is expected to be suppressed.

6.3 Discussion

6.3.1 Quantum criticality

The results of the low temperature thermodynamic and transport experiments are summarized in the $H - T$ phase diagram shown in Fig. 6.28. (For clarity only the resistivity data from sample #13 are used to plot AFM phase boundary.) The magnetic field dependence of the AFM phase boundary, T_N, was mainly determined from the sharp peak position in $\text{d}\rho(T)/\text{d}T$ and $\text{d}\rho(H)/\text{d}H$ (Fig. 6.10), the sharp peak position in α_{100}, and the slope change in λ_{100} (Fig. 6.16). For comparison, the temperatures of the maximum in C_p (and the minimum in $\rho(T)$) are higher than those of α_{100} and $\text{d}\rho(T)/\text{d}T$, (Fig. 6.29) but as discussed above, the position of the higher field slope change in λ_{100} is well matched with the sharp peak position in $\text{d}\rho(H)/\text{d}H$.

There is not perfect agreement between the temperature and magnetic field sweep data below $0.2\,\text{K}$ and there is an approximately $0.8\,\text{kOe}$ difference between them at $0.02\,\text{K}$. However, the field dependence of ρ_H at $0.06\,\text{K}$ shows clear feature at $H = 3.9\,\text{kOe}$ (inset of Fig. 6.18), which is close to the AFM boundary determined from the temperature sweeps. It has been
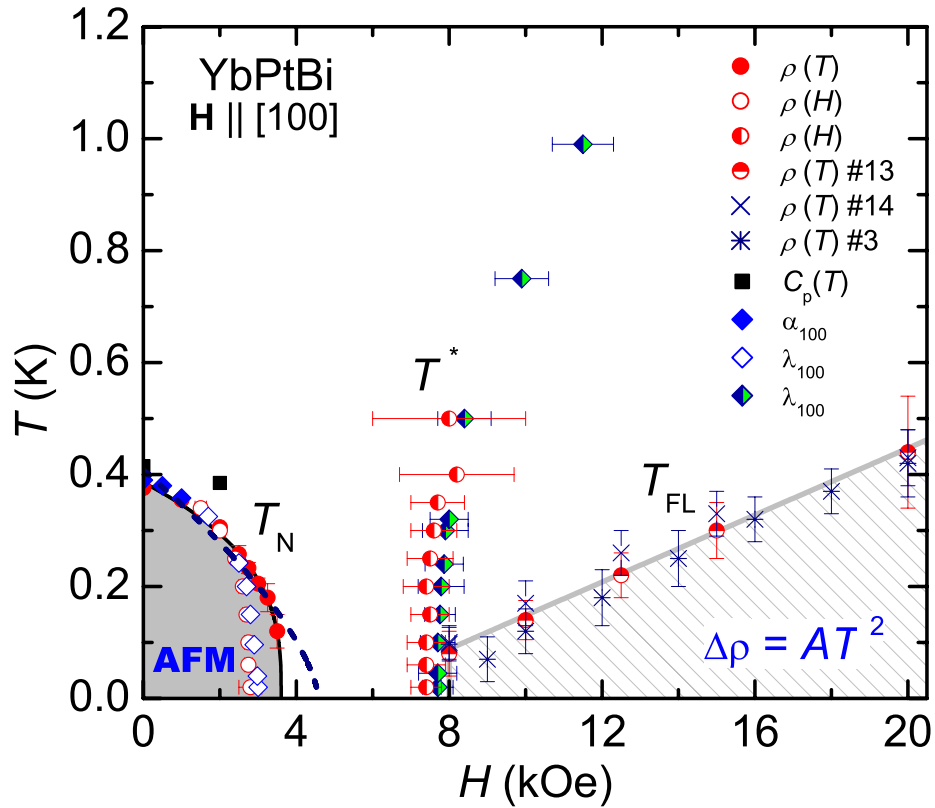
Figure 6.28 $H - T$ phase diagram for YbPtBi along $\mathbf{H} \parallel [100]$. The T_N
was derived from $d\rho(T)/dT$, $d\rho(H)/dH$, α_{100}, and λ_{100}. For
the phase boundary the $\rho(T, H)$ results for sample #13 are
only included.   The solid line on the AFM phase bound-
ary represents the fit of equation $T_N = [(H - H_c)/H_c]^{0.33}$
to the data. The dashed line represents the fit of equation
$T_N = [(H - H_c)/H_c]^{2/3}$ to the data. The T_{FL} represents the
upper limit of the T^2-dependence of $\rho(T)$, where the results of
sample #13, #14, and #3 are plotted. The solid line is guide
to the eye. The local maximum of $d\rho(H)/dH$ and the local
minimum of λ_{100} are assigned to $T^*(H)$.

shown in earlier studies that the AFM order can be suppressed by external magnetic field of 3.1 kOe [Movshovich, 1994], which is mainly based on magnetic field sweeps. It is not clear at this point that whether this discrepancy is merely based on the criteria for determining the T_N or whether the AFM order splits into two different phases below $0.2\,\mathrm{K}$ and for $H > 2\,\mathrm{kOe}$. Importantly, within any criteria used to determine phase transition, it is expected that the AFM order can be suppressed to $T = 0$ by external magnetic fields of at most $H_c = 4\,\mathrm{kOe}$.
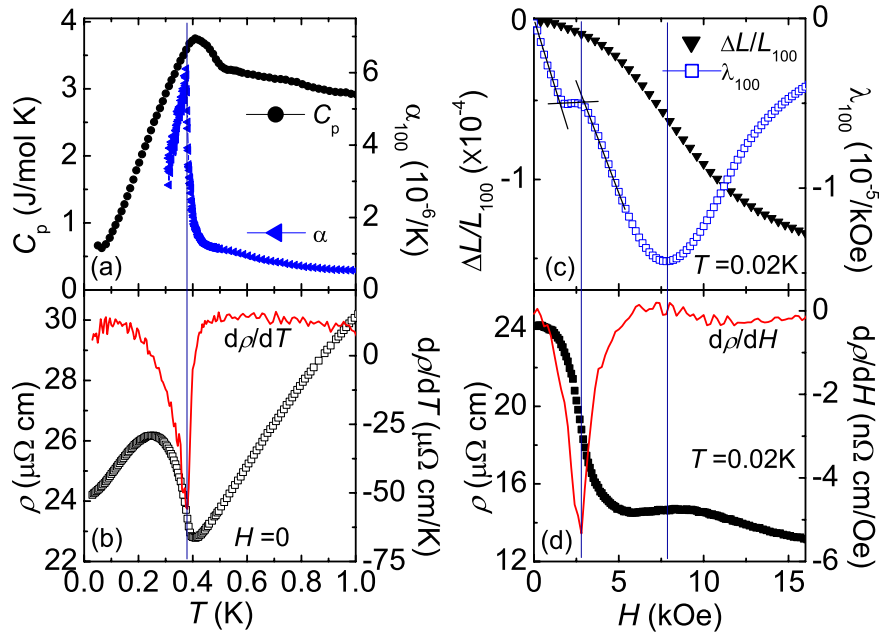
Figure 6.29 Criteria for determining T_N. (a) Zero field specific heat C_p and the coefficient of linear thermal expansion α_{100}. (b) Zero field electrical resistivity $\rho(T)$ and the derivative $\mathrm{d}\rho(T)/\mathrm{d}T$. (c) Linear magnetostriction $\Delta L/L$ and the coefficient $\lambda_{100} = \mathrm{d}(\Delta L/L)/\mathrm{d}H$ at $T = 0.02\,\mathrm{K}$. (d) Magnetoresistivity $\rho(H)$ and the derivative $\mathrm{d}\rho(H)/\mathrm{d}H$ at $T = 0.02\,\mathrm{K}$. Solid lines are guides to the eye.

Based on the scaling properties near QCP, the phase transition temperature is expected to be hold a characteristic power law dependence; $T_N \propto (\text{-}r)^\psi$, where r is the distance to the QCP and ψ is the exponent [Löhneysen, 2007]. In Fig. 6.28 the solid line on the AFM phase boundary represents the best fit of equation $T_N \propto [(H - H_c)/H_c]^\psi$ to the data with $T_N(0) =$

0.38 ± 0.02 K, $H_c = 3.6 \pm 0.2$ kOe, and $\psi = 0.33$ ($\simeq 1/3$) ± 0.03, where the error bar depends on the fitting range. For (SDW) antiferromagnets with three dimensional critical fluctuations ($d = 3$) the boundary of the ordered phase varies as $T_N \propto (-r)^{2/3}$ [Hertz, 1976; Millis, 1993]. When the exponent is fixed to $\psi = 2/3$, the fit curve is represented by dashed line (Fig. 6.28) on the phase boundary with $T_N = 0.4$ K and $H_c = 4.6$ kOe. Apparently, for YbPtBi the AFM phase boundary can be better described with $\psi \simeq 1/3$, which deviates from the theoretical prediction for a three dimensional AFM QCP of SDW scenario.
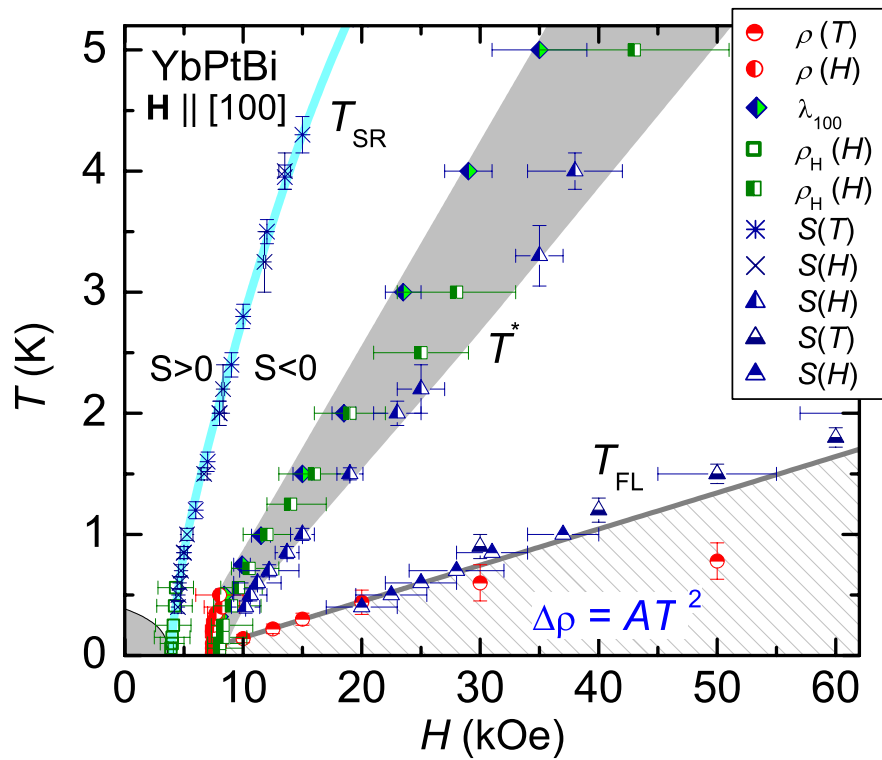
Figure 6.30 High temperature $H - T$ phase diagram for YbPtBi. The $S(T, H) = 0$ and the slope change from ρ_H/H are assigned to $T_{SR}(H)$. The local maximum in $\mathrm{d}\rho(H)/\mathrm{d}H$, the local minimum of λ_{100}, the local minimum of ρ_H/H, and the local minimum in $S(H)$ are assigned to $T^*(H)$. The T_{FL} was derived from the upper limit of the T^2-dependence of $\rho(T)$ and the upper limit of the T-dependence of $S(T)$. The slope change in $S(H)$ is also assigned to T_{FL}. All lines and shaded area are guides to the eye.

In addition to T_N, measurements indicate a crossover region of $T^*(H)$. The features in

$d\rho(H)/dH$ (Fig. 6.10), λ_{100} (Fig. 6.16), ρ_H/H (Fig. 6.20), and $S(H)$ (Fig. 6.27), associated with H^*, are assigned to $T^*(H)$ and are plotted in the $H - T$ plane as shown in Fig. 6.30. The error bars are rough estimates of the crossover widths, based on the widths of those features. The width of the T^* crossover region is wider as temperature is increased. However, in the zero temperature limit each T^* sharpens and tends to converge near $H \sim 7.8\,$kOe. For the field-induced QCP systems, Ge-doped [Custers, 2010] and parent YbRh$_2$Si$_2$ [Paschen, 2004] and YbAgGe [Bud'ko, 2005a], the similar crossover field for all of them has also been observed from various thermodynamic and transport measurements. The FL region is uniquely defined by $S(T)$ and $\rho(T)$ results below $30\,$kOe; for $H > 30\,$kOe, the FL region determined from $S(T)$ and $S(H)$ is not consistent with the one inferred from $\rho(T)$. Given that T_{FL} represents a cross over differences in its value, inferred from different data sets is not unexpected.

Even though the physical meaning behind the experimental signature is not clear and the experimental signature is very weak, there is an another crossover scale of T_{SR} (Fig. 6.30), where H_{SR} determined from $S(H)$ is assigned to T_{SR}. The lower magnetic field signature in ρ_H/H, which corresponds to the slope change in ρ_H/H emerging from H_c, is overlapped with the sign reversal in $S(T,H)$. Thus, in the $T \to 0$ limit, T_{SR} is expected to converge to H_c by tracking the ρ_H/H feature. For YbAgGe this T_{SR} crossover line has also been observed with similar behavior [Mun, 2010b].

One of the interesting issues is the magnetic field modification of the power law dependence of the resistivity (Fig. 6.7, Fig. 6.9), $\rho(T) = \rho_0 + AT^n$, which describes the low temperature quasi-particle behavior. In Fig. 6.28, for $H > H_c$, the characteristic scale of T_{FL} marks the upper limit of the observed T^2-dependence of the resistivity below which the FL state is stabilized. In Fig. 6.28 the results for sample #13, #14, and #3 are plotted and the solid line is guide to eye. The T_{FL} region shrinks quasi-linearly with decreasing magnetic field from paramagentic state. By using simple linear extrapolation, the T_{FL} line terminates at $H \sim 5.2 \pm 0.5\,$kOe, based on the results of three samples, which is close to but distinct from H_c. Below $H \sim 8\,$kOe, the $\rho(T)$ curve is better fitted to the $T^{1.5}$- than T^2-dependence, indicating nFL-like behavior ($4 < H < 8\,$kOe). A detailed analysis of $\rho(T)$ (Fig. 6.9) reveals that as magnetic

field decreases a nFL-like behavior ($\Delta\rho(T) \propto T^{1.5}$) of resistivity above the T^2-region is also observed, which shrinks progressively towards $H \sim H_c$. Although the question of whether $\rho(T) \propto T^2$ exists at very low temperature down to $H_c \sim 4$ kOe is still open (although not strongly supported by the data), a clear nFL region between 4 and 8 kOe is very clear.

The observation of these two regimes, FL and nFL, in YbPtBi raises the question of whether the FL state survives in the magnetic field range between H_c and H^* at $T = 0$ and what is the physical origin of the crossover scale T^*. The T^* line seems to block the extension of FL state below 8 kOe, but for unambiguous conclusions it will be necessary to perform high resolution measurements of the resistivity to even lower temperature. In any case, it is natural to interpret the constructed $H - T$ phase diagram as showing that T_N is suppressed to $T = 0$ for $H_c \leq 4$ kOe and the FL state is stabilized for $H > 8$ kOe. The T_{SR} and T_N line vanish at H_c and the T^* vanishes near the magnetic field of 7.8 kOe at $T \to 0$ which is not directly connected to T_N. Although we can not prove, it is expected that both T_{FL} and T^* terminate to the same magnetic field in the zero temperature limit.

Since T_{FL} seems to be detached from the T_N, it would be interesting to assess whether the quasi-particle effective mass diverges at the critical field of H_c via a strong magnetic field dependence of the FL coefficient A and γ. The coefficient A rapidly increases with decreasing magnetic field from the paramagnetic state (Fig. 6.31 (a)). Indeed, the steep variation of A value can be well described by a scaling analysis with a form of $A(H) - A_0 \propto (H - H_c)^{-\beta}$, where A_0 is the adjustable parameter, H_c is the critical field, and β is the exponent. In Fig. 6.31 (a) the solid line on A values for sample #13 represents a fit of the scaling form, where the fit was performed between 8 and 50 kOe yielding a critical field $H_c = 4.2 \pm 0.5$ kOe, an exponent $\beta = 1 \pm 0.05$, and $A_0 \simeq 0.03 \ \mu\Omega$cm/K^2. The power law dependence of A can be clearly seen, when it is plotted as A^{-1} vs. H, as shown in Fig. 6.31 (b). From a linear fit to the data the critical field is obtained to be $H_c \sim 4.4$ kOe, which is close to the critical field of power law fit. Similar critical fields for samples #3 ($H_c \simeq 4.3$ kOe) and #14 ($H_c \simeq 4.2$ kOe) with $\beta \simeq 1$ can be obtained with the adjustable parameter A_0. Note that without A_0 the critical field and the exponent, obtained from the fit to three different sets of A value, vary 3.5 kOe $\leq H_c \leq 4.7$ kOe
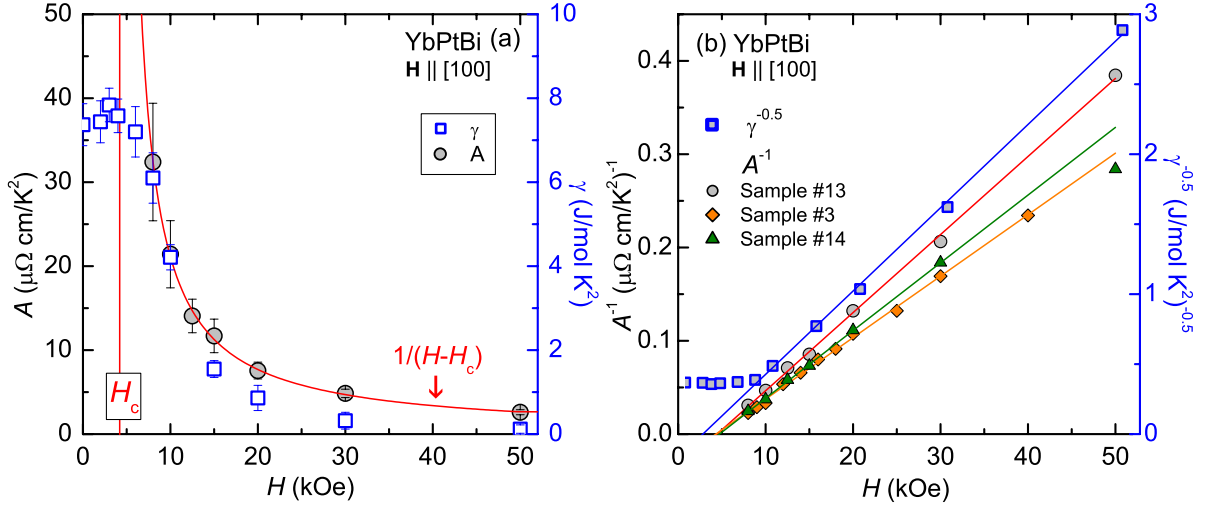
Figure 6.31 (a) Fermi liquid coefficient $A = \Delta\rho(T)/T^2$ and $\gamma = C(T)/T|_{T\to 0}$. Solid line on A values represents a fit of equation, $A - A_0 \propto 1/(H - H_c)$, performed up to $50\,\mathrm{kOe}$ with the constant offset $A_0 \simeq 0.03\ \mu\Omega\mathrm{cm/K^2}$ and $H_c = 4.2\,\mathrm{kOe}$. Vertical line represents the critical field (H_c). (b) A^{-1} (left axis) vs. H for three different samples (samples #3, #13, and #14 in Fig. 6.9) and $\gamma^{-0.5}$ (right axis) vs. H. Solid lines represent the linear fit to the data. See text for details.

and $0.92 \leq \beta \leq 1.12$, respectively, thus the adjustable parameter A_0 is necessary to allow the three data sets to converge to the same H_c and β values in the same magnetic field range, but even though A_0, the value of H_c is much closer to $H_c \sim 4.5\,\mathrm{kOe}$ than to $H^* \sim 8\,\mathrm{kOe}$ and β is close to 1.0 than to 0.5 or 1.5. Since the A value diverges at near $\sim 4\,\mathrm{kOe}$, the scattering cross-section between quasi-particles becomes singular at H_c. The observed divergence of A assigned H_c as the QCP and $\beta = 1$ as the exponent characterizing quantum criticality. A power law divergence of the A value near QCP has been observed from other field-induced QCP systems such as YbRh$_2$Si$_2$ [Gegenwart, 2002], CeCoIn$_5$ [Paglione, 2003], and CeAuSb$_2$ [Balicas, 2005] with exponent $\beta = 1$ or close to 1.

A FL state can be characterized by the Kadowaki-Woods (K-W) ratio [Kadowaki, 1986], $A \propto \gamma^2$, where γ is a direct measure of the effective mass, m^*, of quasi-particles. Thus, the dramatic variation of γ was also analyzed with a relation of $\gamma(H) - \gamma_0 \propto (H - H_c)^{-\beta}$, which is the same form as A, where γ_0 is the adjustable parameter. The power law fit to the $\gamma(H)$,

performed between 8 and 50 kOe, yields a critical field $H_c = 4.6 \pm 0.4$ kOe, an exponent $\beta = 1 \pm 0.2$, and $\gamma_0 = 0.55$ J/mol·K^2. Although this analysis gives a consistent critical field with that obtained from the fit of A, the required value of $\gamma_0 = 0.55$ J/mol·K^2 is very high. Without γ_0 the fit yields a critical field of 1.5 ± 0.5 kOe and an exponent $\beta = 2 \pm 0.4$. This result can be clearly seen in the $\gamma^{-0.5}$ vs. H plot (Fig. 6.31 (b)) which is close to the linear in H, and thus $\beta \sim 2$. In this plot, the critical field is estimated to be $H_c \sim 1.8 \pm 0.5$ kOe from the linear fit to the data. The observed exponents, $1 \leq \beta \leq 2$, are striking deviation from the K-W ratio, where the exponent $\beta = 0.5$ is expected in FL regime. It is worth noting, though, that $\gamma(H)$ diverges near or below 4.5 kOe in all cases. Note that such a deviation from the K-W ratio across the field tuned QCP has also been observed in Ge-doped YbRh$_2$Si$_2$ [Custers, 2003].
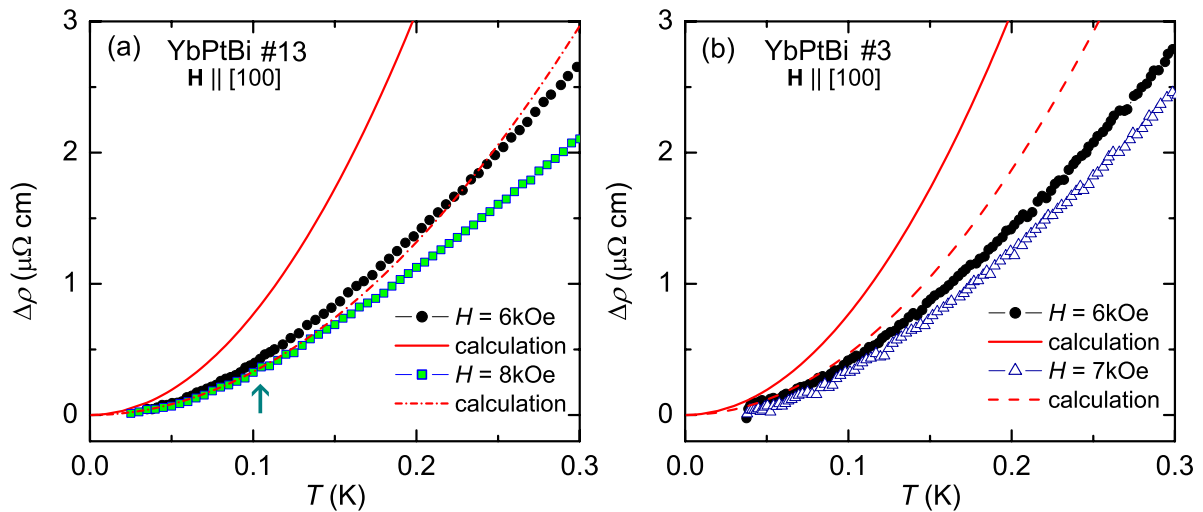
Figure 6.32   The temperature dependence of the resistivity, $\Delta\rho(T) = \rho(T) - \rho_0$, of YbPtBi for (a) sample #13 and (b) sample #3. (a) The solid and dash-dotted line represent the calculated $\Delta\rho(T)$ with $A \simeq 76.7$ $\mu\Omega$cm/K^2 for $H = 6$ kOe and with $A \simeq 32.4$ $\mu\Omega$cm/K^2 for $H = 8$ kOe, respectively. (b) The solid line and dashed line represent the calculated $\Delta\rho(T)$ with $A \simeq 76.7$ $\mu\Omega$cm/K^2 for $H = 6$ kOe and with $A \simeq 46.7$ $\mu\Omega$cm/K^2 for $H = 7$ kOe, respectively. The A values used to generate $\Delta\rho(T)$ were obtained from the power law fit ($A \propto 1/(H - H_c)$) to the A values shown in Fig. 6.31. See text for details.

To clarify the observed, anomalous power law dependence of resistivity below 8 kOe, the measured resistivity was compared to the predicted T^2-dependence of resistivity base on the

power law analysis of A values. In Fig. 6.32 the measured resistivity for samples #13 and #3, together with the calculated resistivity curves, are plotted after subtracting ρ_0 value ($\Delta\rho(T)$). For $H = 6$, 7, and 8 kOe, predicted A values, obtained from the power law fit ($A \propto 1/(H - H_c)$, Fig. 6.31) to the experimental A values, are used to generate $\Delta\rho(T)$ curves. For sample #13 as shown in Fig. 6.32 (a), the measured $\Delta\rho(T)$ for $H = 8$ kOe is in good agreement with the calculated $\Delta\rho(T)$ below ~ 0.11 K (indicated by arrow), whereas the observed $\Delta\rho(T)$ for $H = 6$ kOe can not be reproduce by the predicted $\Delta\rho(T)$ fundamentally due to the large, predicted A value used. For sample #3 (Fig. 6.32 (b)), the calculated curves for both $H = 6$ and 7 kOe shows no agreement with the measured $\Delta\rho(T)$. Therefore, there seem to be a disruption of high field FL behavior near H^* (~ 8 kOe) rather than going down to H_c (~ 4 kOe). This result is consistent with the behavior of $\gamma(H)$ which clearly shows a deviation from the power law dependence below 8 kOe (Fig. 6.31).
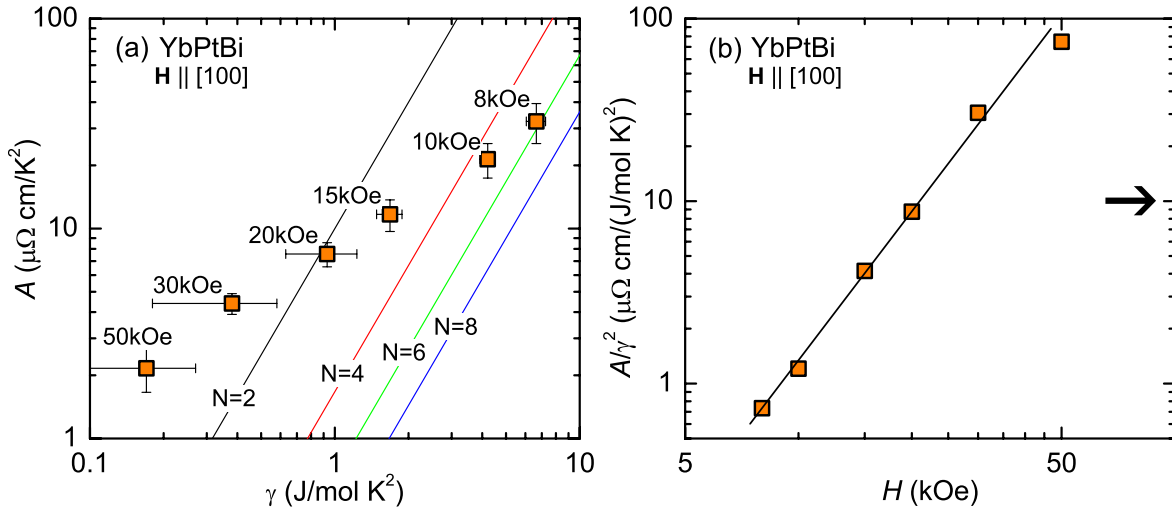
Figure 6.33 (a) $\log - \log$ plot of A vs. γ. Solid lines represent the Kadowaki-Woods (K-W) ratio for different ground state degeneracy [Tsujii, 2005] for $N = 2$ - 8. (b) A/γ^2 vs. H, where the horizontal arrow indicates the K-W ratio for $N = 2$. Solid line is guide to the eye.

It has been shown that the A/γ^2 ratio depends on the ground state degeneracy [Tsujii, 2005; Torikachvili, 2007]. A clear dependence of the A/γ^2 ratio on the degeneracy, N, is shown in Fig. 6.33 (a). The experimental A/γ^2 ratio continuously shifts from high degeneracy (near N

= 6 at 8 kOe) toward low degeneracy ($N = 2$ at 20 kOe). A clear variation of K-W ratio in the presence of magnetic field is better seen when A/γ^2 is directly plotted as a function of magnetic field (Fig. 6.33 (b)); the ratio, A/γ^2, continuously increase in log-log scale as magnetic field increases. In zero field and zero pressure, it has been shown [Torikachvili, 2007] that the K-W ratio is located close to the $N = 8$ curve (not plotted in Fig. 6.33 (a)). Because of the AFM order, the A value in zero pressure was estimated by linearly extrapolating pressure dependence of A values between 4 and 19 kbar [Movshovich, 1994a]. In this pressure range the resistivity data followed $\Delta\rho(T) = AT^2$ below 0.3 K. The observed behavior of K-W ratio suggests that the variation of A/γ^2 values is due to magnetic field induced changes in N, a supposition that seems plausible because the ground state CEF degeneracy in zero field can be lifted by applied magnetic field.

However there are several points about K-W scaling and YbPTBi that need to be considered. First, in zero field the ground state degeneracy of YbPtBi should be $N = 2$ (doublet) or $N = 4$ (quartet) in cubic CEF [Lea, 1962]. This should then N to 4, not 6 or 8. Second, the K-W ratio not only depends on the degeneracy but also on the carrier concentration, n, as $n^{-4/3}$ [Tsujii, 2005]. Thus, it is necessary to consider the carrier density for lower carrier systems. When the carrier density, 0.04 hole per formula unit (in a single band model) for YbPtBi at 300 K, is considered, the $N = 2, 4, 6$, and 8 manifold shown in Fig. 6.33 (a) shifts downward with the $N = 2$ line falling well below the data. Thus the carrier concentration within a single band model can not explain the observed behavior of K-W ratio. For YbPtBi the K-W ratio may depend on CEF splitting, low carrier density, and details of the multiple Fermi surfaces.

The multiband nature of YbPtBi is clearly evidenced from quantum oscillations (see the appendix C) and can be supported from the TEP results. Many metals, including HF compounds, have shown correlations between $C(T)/T$ and $S(T)/T$ in the zero temperature limit, linking these two quantities via the dimensionless ratio, $q = \frac{S N_A e}{\gamma T} \sim \pm 1$, where N_A is the Avogadro number and the constant $N_A e$ is called the Faraday number [Behnia, 2004]. At finite temperature, near 0.4 K, this relation seems to be not relevant for YbPtBi. Taking the values

of $S(T)/T = 1.2\ \mu$V/K at the onset of T_N and $\gamma = 7.4$ J/mol·K^2 yields $q = 0.015$. Since the dimensionless ratio holds for a single carrier per formula unit, generally a larger q value is expected when the carrier density is as low as this is; the carrier density of 0.04 hole per formula unit implies $q = $ -25. Therefore $S(T)/T \sim$ -20 μV/K^2 is expected for $\gamma = 7.4$ J/mol·K^2. As seen in Fig. 6.24 the absolute value of $S(T)/T$ up to 8 kOe is considerably lower than this value, where γ remains the same order of magnitude. Therefore, the low carrier density of YbPtBi can not, by itself, provide a natural explanation for this small magnitude of q, which points to the multiband nature of this material as a likely explanation. In order to clearly address this issue, further experimental investigations are required below 0.35 K. In multiband metals, the TEP for each band can be positive or negative, therefore, in principle, the absolute value of the weighted sum of the overall TEP could be considerably reduced, compared to the single band picture. When the same amount of entropy is carried by each type of carrier a reduction of $S(T)/T$ is expected. Therefore, in addition to the ground state degeneracy and carrier concentration, the multiband (multi-Fermi surface) effect and/or the strong anisotropy of the Fermi surfaces should be considered in the K-W ratio as well as the q value.

Based on the scaling analysis of A for magnetic field higher than H^*, the quasi-particle mass shows a power law divergence near H_c. However, the experimentally observed γ is finite for $H < 8$ kOe (close to H^*). An intriguing question to raise is whether field induced QCP in YbPtBi is connected to T_N at $T = 0$ or whether they are essentially separated. In particular, if the QCP is at H_c, what is the physical origin of the crossover line $T^*(H)$, which seems to cut off the divergence of quasi-particle mass enhancement; and why do specific heat measurements indicate no pronounced nFL behavior, -log(T) or $\sqrt{T}$, for $H \geq H_c$ down to lowest temperature measured? The resistivity results reveal a nFL behavior with $\Delta\rho(T) = T^{1.5}$ and the TEP measurements indicate a logarithmic temperature dependence, $S(T) \propto$ -log(T), for $H < H_c$ and $T > T_N$. Based on these transport results one should ask whether an extended regime of nFL state is caused by purely quantum fluctuations or whether other effects, such as magnetic field induced metamagnetic-like state or the modification of the CEF ground state, need to be considered.

A brief comparison of the $H-T$ phase diagram, corresponding to quantum criticality in field-induced QCP systems, was given in the previous chapter. As an extension of the arguments for YbAgGe, the experimental results for YbPtBi will now be compared to the other Yb-based, field-induced QCP systems; $YbRh_2Si_2$ [Gegenwart, 2002], Ge-doped $YbRh_2Si_2$ [Custers, 2010; Custers, 2003], and YbAgGe [Bud'ko, 2005a]. The schematic phase diagrams for these systems are given in Chapter 3. Each of these systems shows an AFM order being suppressed to $T=0$ by an external magnetic field and beyond a given critical field a FL state, exists below a T_{FL} crossover. However, the details of characteristic crossover scales, such as T^*, are different. For $YbRh_2Si_2$ T^* has been interpreted as a characteristic energy scale below which the quasi-particles are breakdown, involving a Fermi surface volume change from small to large across the QCP [Paschen, 2004]. The sign reversal in TEP, T_{SR}, has been observed from both $YbRh_2Si_2$ [Hartmann, 2010] and YbAgGe [Mun, 2010b] across the quantum critical region. Whereas the T_{SR} for YbAgGe emerges at the critical field and persists up to high temperature, the T_{SR} for $YbRh_2Si_2$ exists inside the AFM region and terminates at the critical field as the system is tuned through the QCP. For YbPtBi, considering these two crossovers, T^* and T_{SR}, the constructed phase diagram is similar to YbAgGe.

For both $YbRh_2Si_2$ and YbAgGe the resistivity, specific heat, and thermoelectric power in the vicinity the QCP manifest a clear $\Delta\rho(T) \propto T$, $C(T)/T \propto$ -log(T), and $S(T)/T \propto$ -log(T) behaviors as signatures of strong quantum fluctuations, which can be understood within the conventional SDW scenario with $z=2$ and $d=2$ [Hertz, 1976; Millis, 1993; Paul, 2001], and are also compatible with the unconventional Kondo breakdown scenario [Coleman, 2001; Senthil, 2004; Paul, 2008; Kim, 2010]. Note that the dimensionality of these systems needs to be clarified. For YbPtBi no strong nFL behavior is observed from thermodynamic and transport measurements, where the resistivity measurements show a $T^{1.5}$-dependence between T_{SR} and T^* in which the most strong signature is observed near T^*, the specific heat shows a -log(T) dependence over only limited temperature range, and thermoelectric power measurements shows a -log(T) dependence below the critical field. In the paramagnetic region, for Ge-doped [Custers, 2003] and parent $YbRh_2Si_2$ [Gegenwart, 2002] a divergence of the effective

mass at the QCP has been inferred from the power law analysis of the FL coefficients of A. For YbPtBi a power law analysis of the A-coefficient shows an indication of divergence at the critical field, however the specific heat remains finite (and near constant) for $H < H^*$ at which the divergence nature of the effective mass is essentially cut off. For YbAgGe the power law dependence of these coefficients has not been analyzed.

The biggest difference between YbRh$_2$Si$_2$ and YbAgGe is that the crossover scales, T^* and T_{FL}, are detached from AFM phase boundary (T_N) for YbAgGe, whereas T_N, T^*, and T_{FL} terminate at the QCP for YbRh$_2$Si$_2$ (see schematic phase diagram in Chapter 3). Interestingly the T^* for Ge-doped YbRh$_2$Si$_2$ is also detached from T_N. When the nFL region is considered, a wide nFL region, determined from $\Delta\rho(T) \propto T$, is robust for YbAgGe [Niklowitz, 2006] and Ge-doped YbRh$_2$Si$_2$ [Custers, 2010], in contrast to the field-induced QCP in YbRh$_2$Si$_2$ of which the FL behavior is recovered when $T_N \to 0$. From this point of view the constructed $H - T$ phase diagram of YbPtBi is similar to that of YbAgGe and Ge-doped YbRh$_2$Si$_2$. For YbAgGe, the two crossover scales, T_{SR} and T^*, are evidenced from thermodynamic and transport measurements, where the wide nFL region has been seen between these two crossovers, which is similar to that of YbPtBi. Note the for Ge-doped YbRh$_2$Si$_2$ the T_{SR} has not been identified.

However, there are remaining questions when YbAgGe is compared to other systems. In the zero temperature limit, both T^* and T_{FL} terminate to the same field for Ge-doped and pure YbRh$_2$Si$_2$, whereas T_{FL} for YbAgGe is detached from T^*. For YbPtBi it is reasonable to assume that both T^* and T_{FL} terminate at or near the same field at $T = 0$. In a simple point of view, YbPtBi is very similar to YbAgGe with regards to the crossover scales of T_{SR} and T^* and is close to that of Ge-doped YbRh$_2$Si$_2$ with regards to the T^* and T_{FL}. Therefore, YbPtBi can be located between YbAgGe and Ge-doped YbRh$_2$Si$_2$ (closer to the Ge-doped YbRh$_2$Si$_2$) in the extended Doniach-like diagram [Custers, 2010] (see figure in Chapter 3). As discussed in the previous chapter about YbAgGe, if there are two QCP (characterized by two crossover scales) in YbPtBi, the frustration effect, caused by the faced centered cubic structure, may gives rise to the spin liquid state. Thus, the T_{SR} line could be related to the magnetic QCP

caused by the SDW instabilities and the T^* line can be related to the second QCP caused by the suppression of the Kondo effect.

Quantum criticality can be identified by either the strong quantum fluctuations at low temperatures or the tracking of the Kondo temperature at finite temperatures. It has been inferred from the claimed breakdown of the Kondo scale from the magnetization and specific heat data for YbRh$_2$Si$_2$ [Tokiwa, 2005]. However, for YbPtBi the Kondo scale can not be defined because thermodynamic and transport measurements do not show any clear signature. The fundamental reason of this is expected to be due to the comparable energy scales of T_K, T_N, and the small CEF level splitting. Also this may cause the broadening the specific heat which hides the nFL behavior.

6.3.2   Antiferromagnetic order

In zero field the observed $\rho(T)$ below T_N depends on the measurements conditions, but the T_N remains approximately the same temperature for all cases. Similar behavior has been reported in Ref. [Movshovich, 1994], where $\rho(T)$ data for several rod-shaped samples show either an increase or a decrease below T_N. The different relative height of $\rho(T)$ below T_N was explained due to the partial gapping of the Fermi surface. In addition, the results of $\rho(T)$, measured by Montgomery arrangement [Montgomery, 1971], reveal anisotropy for current directions between along the high temperature [100] and [010] directions, which indicated a broken cubic symmetry below T_N. In this study, for testing the anisotropy with respect to the different current directions, several pieces of resistivity samples were cut from a plate-shaped sample with a wire-saw both parallel to the [100] and [010] crystallographically equivalent direction. The results indicate that the anisotropy of $\rho(T)$ below T_N does not depend on the different current directions but highly depend on the sample mounting conditions. In the earlier studies it has been speculated that the anisotropy was caused either by the highly oriented domains or by internal stress developed during material growth [Movshovich, 1994]. In this study, however, the anisotropy is caused by the external parameters and expected to be due to the external stress (anisotropic pressure), which is consistent with earlier specific heat

results [Lacerda, 1993]. Note that the sample used in this study was annealed at 600°C for 100 hr before decanting the crystals. Similar results have been found in the cubic chromium (Cr) [Fawcett, 1988; Bastow, 1966], which is the canonical example of SDW material with T_N = 311 K, that magnetic field cooling and compressive stress cooling profoundly change the magnetic structure [Bastow, 1966]. The application of a uniaxial stress ($\sim$ 0.07 kbar) to a single crystal of Cr, while cooling through T_N, prohibits the development of domains with a SDW vector ($\overrightarrow{q}$) parallel to the direction of stress, where the shifts of T_N and magnitude of the $\overrightarrow{q}$ vector were detected [Bastow, 1966]. In YbPtBi, for stress cooling through T_N, it is suspected that the anisotropic distortion of the Fermi surface under external strain can cause the radical variation of the resistivity below T_N.

One of the interesting aspects of antiferromagnetism in YbPtBi is the rapid suppression of T_N by the application of hydrostatic pressure [Movshovich, 1994], where a pressure as low as 1 kbar suppresses the signature of the phase transition in resistivity measurements. On the other hand, the specific heat measurements has been shown [Lacerda, 1993] that the phase transition feature, shown in $C(T)/T$ for the single crystal samples, is completely smeared out for the pressed pellet samples, prepared from single crystals, which was mixed with GE-7301 varnish. In addition to the resistivity results in this study, the drastic difference of the specific heat results between single crystals and pressed pellet samples suggests that the results of the pressure dependence of resistivity are caused mainly by the external stress applied and also possibly non-hydrostatic components in pressure experiments.

The temperature dependence of the electrical resistivity shows a sharp rise below T_N which is reminiscent of a SDW antiferromagnet Cr [Fawcett, 1988] and URu$_2$Si$_2$ [Schoenes, 1987]. From a simple point of view, we expect that parts of the high temperature Fermi surface disappears when the gap is opened. As shown in Fig. 6.21, the opening of the SDW gap below T_N gives rise to an abrupt enhancement of R_H ($H \rightarrow 0$), enhanced roughly factor of two compared to the value above T_N. From the earlier study of the electrical resistivity and specific heat [Movshovich, 1994], it has been shown by the analysis of these data, based on BCS theory, that the Fermi surface is removed roughly 16 % by the formation of the SDW state. Thus,

the steep increase of R_H below T_N implies a carrier density reduction with Fermi surface nesting of highly renormalized bands. Previously, although neutron scattering experiments have not confirmed AFM order [Robinson, 1994], the μ-SR experiments have been seen tiny ordered moment [Amato, 1992]. Therefore, a SDW ground state is supported by compelling evidence from $\rho(T)$, $C_p(T)$, and $R_H(T)$ as well as the microscopic measurements. Note that very similar results have been observed in URu$_2$Si$_2$ [Schoenes, 1987]. The carrier concentration of URu$_2$Si$_2$ estimated from R_H is 0.05 holes per formula unit which is close to the value of YbPtBi, and about 40 % of the Fermi surface, calculated from specific heat, is removed by the formation of the hidden ordered state at $T_0 = 17.5\,\mathrm{K}$ [Maple, 1986]. Below T_0, R_H of URu$_2$Si$_2$ increases by factor of 5-20 because of the opening of a gap over the Fermi surface. Recently ρ_H measurements in pulsed magnetic field show that the steep enhancement of R_H below T_0 is completely suppressed across the QCP by order of 40 Tesla [Oh, 2007]. Similarly the sharp rise of R_H for YbPtBi is completely suppressed near H_c (Fig. 6.21).

6.4 Summary and Conclusion

The $H - T$ phase diagram of YbPtBi has been constructed by low temperature thermodynamic and transport measurements. In zero field the strength of the anomaly developed in $\rho(T)$ below T_N is sensitive to the strain, but the relevant physics of the samples remains the same for magnetic field applied along $\mathbf{H} \parallel [100]$ up to $140\,\mathrm{kOe}$. The AFM order can be suppressed to $T = 0$ by external magnetic field of $H_c \leq 4\,\mathrm{kOe}$ and the temperature dependence of the resistivity indicates the recovery of the FL state (clearly) for $H \geq 8\,\mathrm{kOe}$. The two well separated crossover scales, T_{SR} and T^*, have been found, where these crossover lines show a tendency of converging toward to $H_c \sim 4\,\mathrm{kOe}$ and $H^* \sim 7.8\,\mathrm{kOe}$ in the zero temperature limit. Although no clear nFL behavior is observed in the specific heat measurements in the vicinity of the critical field, the electrical resistivity shows anomalous temperature dependence, $\rho(T) \propto T^{1.5}$, as a signature of nFL behavior, between these two crossovers and $S(T)/T$ exhibits a logarithmic temperature dependence for $H < H_c$ above the AFM ordering temperature. The observed γ is finite below $H \sim 8\,\mathrm{kOe}$ and the quasi-particle scattering cross-section, A,

indicates a power law divergence as $A \propto 1/(H - H_c)$ upon approaching the critical field from paramagnetic state. As magnetic field decrease from higher field side the power law dependence of both A and γ show a disruption below $H^* \sim 8\,\mathrm{kOe}$. The constructed $H - T$ phase diagram and the details of the quantum criticality in YbPtBi turn out to be complicated.

CHAPTER 7.   Summary and an outlook on future work

The motivation of this dissertation was to advance the study of Yb-based heavy fermion (HF) compounds especially ones related to quantum phase transitions. One of the topics of this work was the investigation of the interaction between the Kondo and crystalline electric field (CEF) energy scales in Yb-based HF systems by means of thermoelectric power (TEP) measurements. In these systems, the Kondo interaction and CEF excitations generally give rise to large anomalies such as maxima in $\rho(T)$ and as minima in $S(T)$. The TEP data were use to determine the evolution of Kondo and CEF energy scales upon varying transition metals for YbT_2Zn_{20} (T = Fe, Ru, Os, Ir, Rh, and Co) compounds and applying magnetic fields for YbAgGe and YbPtBi. For YbT_2Zn_{20} and YbPtBi, the Kondo and CEF energy scales could not be well separated in $S(T)$, presumably because of small CEF level splittings. A similar effect was observed for the magnetic contribution to the resistivity. For YbAgGe, $S(T)$ has been successfully applied to determine the Kondo and CEF energy scales due to the clear separation between the ground state and thermally excited CEF states. The Kondo temperature, T_K, inferred from the local maximum in $S(T)$, remains finite as magnetic field increases up to $140\,\text{kOe}$.

For YbT_2Zn_{20} systems, the zero temperature limit of $S(T)/T$ scaled well with the electronic specific heat coefficient, γ, which is reflected by a strong correlation via the quasi-universal ratio, $q = N_A eS/\gamma T$, and confirms the validity of Fermi-liquid descriptions. For YbAgGe, the ratio of q was investigated in the paramagnetic regime and found to be anisotropic for different heat flow directions. At high magnetic fields, for $H > 70\,\text{kOe}$, the enhanced value of $S(T)/T$ is indicative of the HF state, supporting previous specific heat and resistivity results. In contrast to YbAgGe, the estimated q value for YbPtBi is much less than the theoretically predicted

value, $|q| = 1$, and continuously varies as magnetic field increases. The small magnitude of q can not be explained just by considering the low carrier nature of YbPtBi, indicating that multiband effects in this low carrier density HF will have to be considered.

Furthermore, TEP investigations for YbAgGe were shown to be a useful tool to probe and refine the $H-T$ phase diagram and provided complementary information to the study of quantum criticality in this system. The TEP measurements reproduced the earlier $H-T$ phase diagram; identified an additional dome-like phase between ~ 45 and $\sim 70\,\mathrm{kOe}$; and confirmed, clarified, and extended the two characteristic crossover lines to high temperature. Importantly, the power law analysis of resistivity indicates a strong nFL behavior, $\rho(T) \propto T$, in the dome-like area, located between the two crossover lines. For $H = 70\,\mathrm{kOe}$ data, $S(T)/T$ exhibits clearly a logarithmic temperature dependence in agreement with earlier specific heat results $C(T)/T \propto -\log(T)$. The present TEP results, combined with earlier specific heat and resistivity results, provide strong evidence of a quantum critical point at $H \simeq 70\,\mathrm{kOe}$.

The study of YbPtBi compound was aimed at providing a new material to serve as a canonical example for magnetic field tuned quantum criticality. This compound offered the possibility of studying the interplay between a well defined ground state, which shows an (spin density wave, SDW) antiferromagnetic (AFM) ordering below $0.4\,\mathrm{K}$, and a low Kondo temperature of order of $T_K \sim 1\,\mathrm{K}$, which give rise to an enormous γ at low temperatures. The $H-T$ phase diagram of YbPtBi for $\mathbf{H} \parallel [100]$ has been constructed by low temperature thermodynamic and transport measurements down to $0.02\,\mathrm{K}$ and up to $140\,\mathrm{kOe}$.

The AFM order can be suppressed to $T = 0$ by external magnetic field of $H_c \leq 4\,\mathrm{kOe}$ and the temperature dependence of the resistivity indicates the recovery of the FL state (clearly) for $H \geq 8\,\mathrm{kOe}$. The two separated crossovers have been found in this study, which were also seen for YbAgGe. Although no clear nFL behavior is observed in the specific heat measurements in the vicinity of the critical field, the electrical resistivity shows anomalous temperature dependence, $\rho(T) \propto T^{1.5}$, as a signature of nFL behavior, between these two crossovers and $S(T)/T$ exhibits a logarithmic temperature dependence for $H < H_c$ above the AFM ordering temperature. The observed γ is finite below $H \sim 8\,\mathrm{kOe}$ and the quasi-particle scattering

cross-section, A, indicates a power law divergence as $A \propto 1/(H - H_c)$ upon approaching the critical field from paramagnetic state. For YbPtBi, the constructed $H - T$ phase diagram and low temperature physical properties in the vicinity of the critical field are complicated, but not as complicated as, for example, YbAgGe.

In this dissertation we have examined the heavy quasi-particle behavior, found near the field tuned AFM quantum critical point (QCP), with YbAgGe and YbPtBi. Although the observed nFL behaviors in the vicinity of the QCP are different between YbAgGe and YbPtBi, the constructed $H - T$ phase diagram including the two crossovers are similar. For both YbAgGe and YbPtBi, the details of the quantum criticality turn out to be complicated. We expect that YbPtBi will provide an additional example of field tuned quantum criticality, but clearly there are further experimental investigations left and more ideas needed to understand the basic physics of field-induced quantum criticality in Yb-based systems.

To date, there is no universal scenario to reconcile all of the experimental results for AFM QCP, partly due to the absence of unambiguous experimental tools to probe quantum critical scenarios and partly due to the limited experimental examples. With this said important questions for future experiments can be pointed out. Based on the conventional (SDW) and unconventional (Kondo breakdown) scenarios, it seems to be important to make a connection between the underlying magnetic phase (local moment AFM order or SDW) and the nFL behavior. If this is the way to distinguish the mechanism of quantum criticality, YbPtBi may be the best material to address this issue by comparing between the local moment AFM ordering for YbAgGe and/or YbRh$_2$Si$_2$ and the SDW ordering for YbPtBi. Therefore, local probes such as neutron scattering experiments, to explicitly identify the nature of the AFM order, as well as low ultra temperature investigations, with high resolution thermodynamic and transport measurements, are necessary for YbPtBi. Since the strain, externally applied to the sample, can affect the signatures of the AFM phase transition, transport and thermodynamic measurements need to be performed carefully down to $20\,\mathrm{mK}$ or below.

In metallic compounds the interpretation of physical quantities requires careful consideration of the Fermi surface, especially at a QCP. The question this raises is, "What is the

evolution of the Fermi surface at the QCP ?" If the Fermi surfaces have different shapes or are completely reconstructed across the QCP, then a Lifshitz transition [Lifshitz, 1960], associated with a reconstruction of the Fermi surface, must separate the two phases between AFM and paramagnetic. Because most of the HF compounds have multiple Fermi surfaces, the natural question is, "What is the experimental tool to probe such Lifshitz transition at extremely low temperatures in a multiband material ?" The transport measurements can address this issue clearly for a system with a single band, however it may not be true for multiband systems. The quasi-particle mass seems to diverge at the QCP with a power law for YbPtBi. Quantum oscillations for YbPtBi confirms the multi-band nature of this system. It needs to be clarified if the power law divergence of quasi-particles is derived from a particular Fermi surface with the other Fermi surfaces remaining essentially unaffected.

In the vicinity of a SDW instability, it has been predicted that HF compounds can show a superconductivity mediated by AFM spin fluctuations [Scalapino, 1986]. One example of this is thought to be $CePd_2Si_2$ [Mathur, 1998] when pressure induced superconductivity is observed in the $P - T$ diagram near an inferred critical pressure. In YbPtBi, no signature of superconductivity was detected down to $20\,mK$ in zero field as well as in the vicinity of the critical field. Possible causes could be that no superconductivity is intrinsically present in YbPtBi system, the sample is not clean enough (unlikely given SdH oscillations), the T_c is too low to observe, or the external magnetic field needed to induce a QCP exceeds $H_{C2}(0)$ of the superconductivity, in which case the control parameter may need to be changed.

The details of quantum criticality may depend on control parameter used. So far, the $CeCu_6$ system is the only one whose quantum criticality has been tested by all three available control parameters: $\mathbf{x}$, $\mathbf{H}$, and $\mathbf{P}$. Thus, the quantum criticality for both YbAgGe and YbPtBi also need to be tested by using other control parameters.

APPENDIX A.   Experimental Setup for the Measurement of the Thermoelectric Power in Zero and Applied Magnetic Field

Introduction

Since its discovery in 1821 by Thomas Johann Seebeck, relatively few studies of the magnetic field dependence of the thermoelectric power (TEP) were carried out, mostly in pure metals [Blatt, 1976]. However, over the past few decades, the magnetic field-dependent TEP studies of many materials ranging from magnetic multilayers [Sakurai, 1991] to high T_c superconductors [Wang, 2001], to the electron-topological transition and to strongly correlated electron systems [Sakurai, 1995; Benz, 1999; Izawa, 2007] have provided useful information. Intensive efforts also have been made in the search for highly efficient thermoelectric materials. This being said, the measurement of the intrinsic TEP is particularly difficult even in simple metals such as copper or gold. This is due to the small magnitude of TEP at low temperatures and its sensitivity to the presence of small concentrations of impurities, where magnetic impurities can enhance the TEP below certain temperatures by means of the Kondo effect [Blatt, 1976].

Few experimental details have been given in the literature concerning the measurement setups and the procedure for calibration of lead (as in contacting the sample, not Pb) wires [Resel, 1996; Burkov, 2001; Choi, 2001]. Detailed descriptions of the measurement techniques at low temperatures and high magnetic fields can be found in Refs. [Resel, 1996; Choi, 2001]. In this article, we describe the development of an experimental setup for TEP measurement in a Quantum Design (QD), Physical Property Measurement System (PPMS). The PPMS sample puck provides both thermal and electrical contacts to the sample. The merits of this technique are (i) it is easy to implement using two commercial, Cernox thin-film, resistance cryogenic

temperature sensors and two strain gauge heaters and (ii) it is easy to control the temperature and magnetic field of the system using the PPMS platform. Using the PPMS temperature-magnetic field $(T - H)$ environment and the two heaters and two thermometers, an alternating heating method allows for measurements of the TEP of materials over a temperature range from 2 to 350 K and magnetic fields up to 140 kOe. The alternating heating method we use improves the resolution by a factor of two and provides a reliable temperature gradient. For the measurement, the sample is mounted directly between the two Cernox thermometers each of which is heated by a strain gauge heater with constant DC current. An important component of this technique involves the use of phosphor-bronze lead wires to reduce the background TEP and magneto-thermoelectric power (MTEP) associated with the lead wires.

Experimental Setup

In this section we will describe our specific sample holder (sample stage) and explain the data acquisition process. This measurement setup was designed to fit PPMS cryostat used to control the temperature and magnetic field of the system. All instruments (current sources, voltmeters, switch system and PPMS) were controlled by National Instruments LabVIEW software. The sample holder can be easily modified and adapted to other cryogenic systems, including those with higher magnetic fields and lower temperatures.

Sample Holder

Figures A.1 (a) and (b) show a schematic diagram of the sample stage built on the PPMS sample puck and a photograph of actual sample stage. The magnetic field is applied perpendicularly to the plane of the heaters, thermometers and puck platform. Two sample stages are attached to a circular copper heat sink positioned on the 23 mm diameter PPMS sample puck that, when in use, is shielded by a gold plated copper cap (not shown). We use Cernox sensors (CX-1050-SD package) as thermometers that provide high sensitivity at low temperatures, good sensitivity over a broad range and low magnetic field-induced errors. The dimensions of this package ($1.9{\times}1.1{\times}3.2$ mm^3) are large enough to attach a heater and sample simultane-
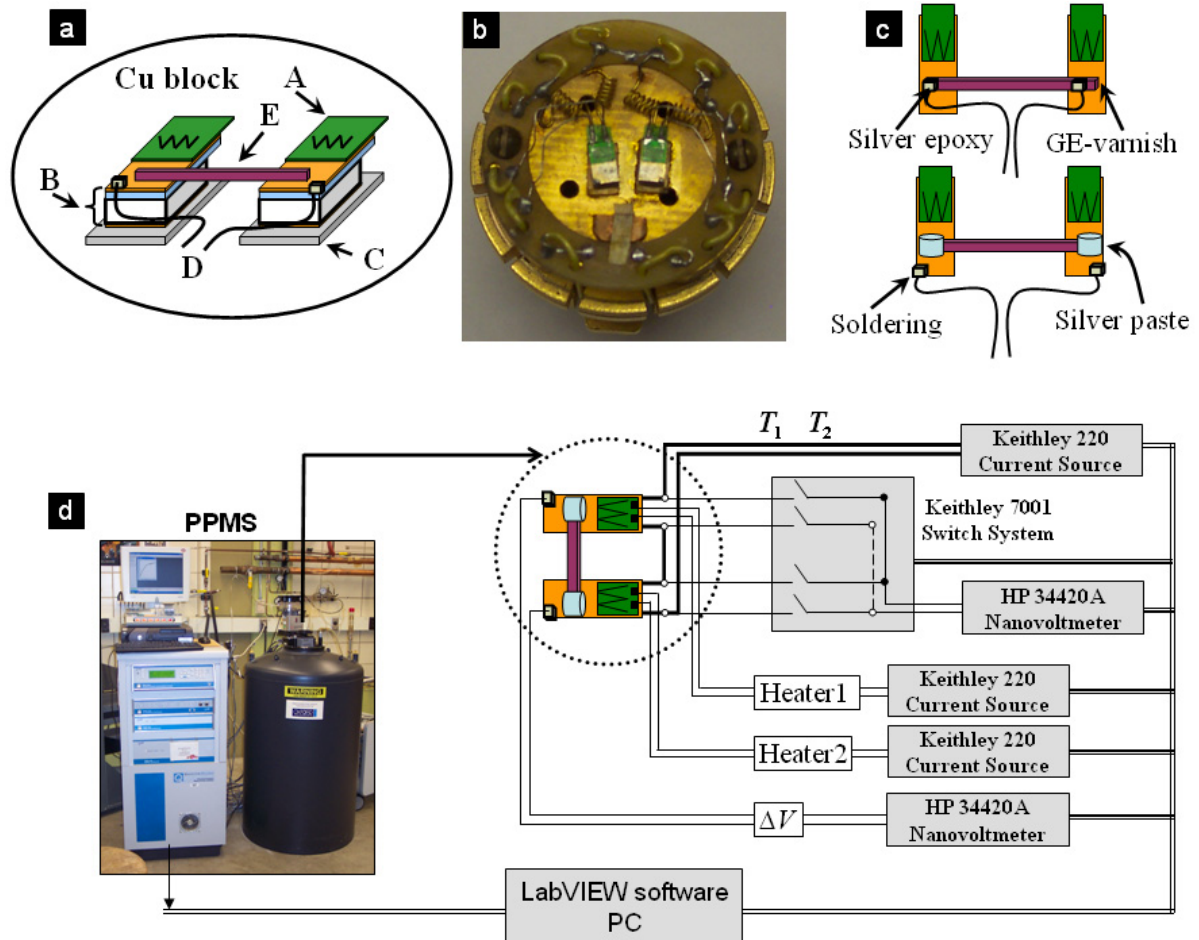
Figure A.1   (a) Schematic diagram of sample stages. A: Strain gauges for heater, B: Thermometers (Cernox), C: G-10 for thermal insulation from heat sink, D: Voltage probe wires, E: Sample. (b) A photo of the measurement cell. (c) Sample mounting method using GE-varnish (top) and silver paste (bottom). (d) Block diagram of measurement system. The system temperature and magnetic field is controlled by PPMS. All instruments shown in the block diagram including PPMS is operated by LabVIEW software. The details of the use of the instruments are explained in the text.

ously to the package surface. Strain gauges (heaters), 0.2×1.4 mm^2 and typically $R \sim 120$ Ω, are glued to the top of the Cernox thermometers using Stycast 1266 epoxy. In order to insure thermal isolation, the heat sink (PPMS puck) and the sample stage was separated by a thin (1 mm thickness) G-10 plate. This G-10 plate was glued to the bottom of the Cernox thermometer using the Stycast 1266 epoxy. From several test runs we observed that the two Cernox wires and two heater wires provided enough cooling power to the sample stage since the strain gauge and Cernox each have low thermal mass. Each sample stage including heater, thermometer and G-10 plate, was glued to the copper heat sink with GE 7301 varnish, so that it could be easily removed by dissolving the GE-varnish with ethanol. Because of the constraint of the PPMS sample puck, the distance between two stages can be varied from $\sim$1.5 mm to $\sim$ 6 mm. Large flexibility with respect to the sample size can therefore be gained since the precise configuration of the thermal stage can be easily adjusted. If the sample length is smaller than 1.5 mm, it is hard to establish a temperature difference (ΔT) because both thermal stages are isolated from the heat sink. Typically, samples with length varying from 2 to 7 mm can be measured. All wires on the measurement cell are thermally anchored to the heat sink. The TEP measurement was made with the PPMS operating in the high vacuum mode with pressure $\sim 10^{-5}$ torr.

For mounting the sample, and measuring the voltage, two different configurations were tested (Fig. A.1 (c)). First, samples were mounted on the two sample stages with GE-varnish. The voltage difference ΔV is measured using 25 μm diameter copper wire or phosphor-bronze wire attached to the sample using silver epoxy as shown in the top of Fig. A.1 (c). Alternatively, samples were directly mounted to the sample stages using DuPont 4929N silver paste. The silver paste provides good thermal and electrical contact between the sample and the gold plated layer on the surface of the Cernox package (bottom of Fig. A.1 (c)). The copper wire or phosphor-bronze lead wire is soldered to this gold plated layer. In this case the voltage difference is obtained by measuring the voltage difference between two sample stages. Since the data was taken in a steady state, by assuming the temperature of the gold layer is the same as silver paste, the TEP contribution of the sample stage can be ignored. Since the

silver paste can be dissolved in hexyl acetate, the sample can be easily detached by carefully adding small amount of this solvent without degrading Stycast or GE-varnish. We ran several test measurements to compare thermal coupling between sample and thermometers by using silver paste and GE-varnish. We found it to be essentially the same for both cases. In general the TEP measurement was performed with the silver paste configuration, because the sample mounting and removal were easier than GE-varnish. The GE-varnish configuration is preferred mainly when good electrical contact between the sample and the gold layer of the thermometer with silver paste can not be established. For example, when we measure the TEP of the $Bi_2Sr_2CaCu_2O_{8+\delta}$ (Bi2212) high T_c samples for calibration it was hard to get good electrical contact (see next section).

Determination of ΔT, ΔV, T_{av} and S

A block diagram of the TEP measurement is shown in Fig. A.1 (d). Since the PPMS sample puck provides only 12 wires, they had to be used frugally: Six wires total were used for the two Cernox sensors, which were connected in series, four wires were used for the heaters (2 each), and two wires were used for the TEP voltage. The resistance of each Cernox is measured with a Hewlett Packard 34420A nanovoltmeter via a Keithley 7001 switch system with a Keithley 7059 low voltage scanner card. The current was supplied to the Cernox thermometers by a Keithley 220 programmable current source. A temperature difference (ΔT) across the sample was established by applying a DC current with two Keithley 220 programmable current source alternately through one of the strain gauges at a time, while the voltage difference (ΔV) across the sample was monitored independently with a Hewlett Packard 34420A nanovoltmeter.

When we apply a small temperature difference across the sample, the temperatures ($T_1(t)$, $T_2(t)$) and a voltage ($V(t)$) are recorded as a function of time, as illustrated in Fig. A.2. T_1 and T_2 are the temperatures of the two Cernox thermometers that the sample spans. t_i represents the time just before alternating power to the heaters (e.g. #1 on and #2 off) and t_f indicates the time just before the next power switch (e.g. #1 off and #2 on). As shown in Figs. A.2 (c) and A.2 (d) in particular, from a linear fit of the measured voltage and temperature
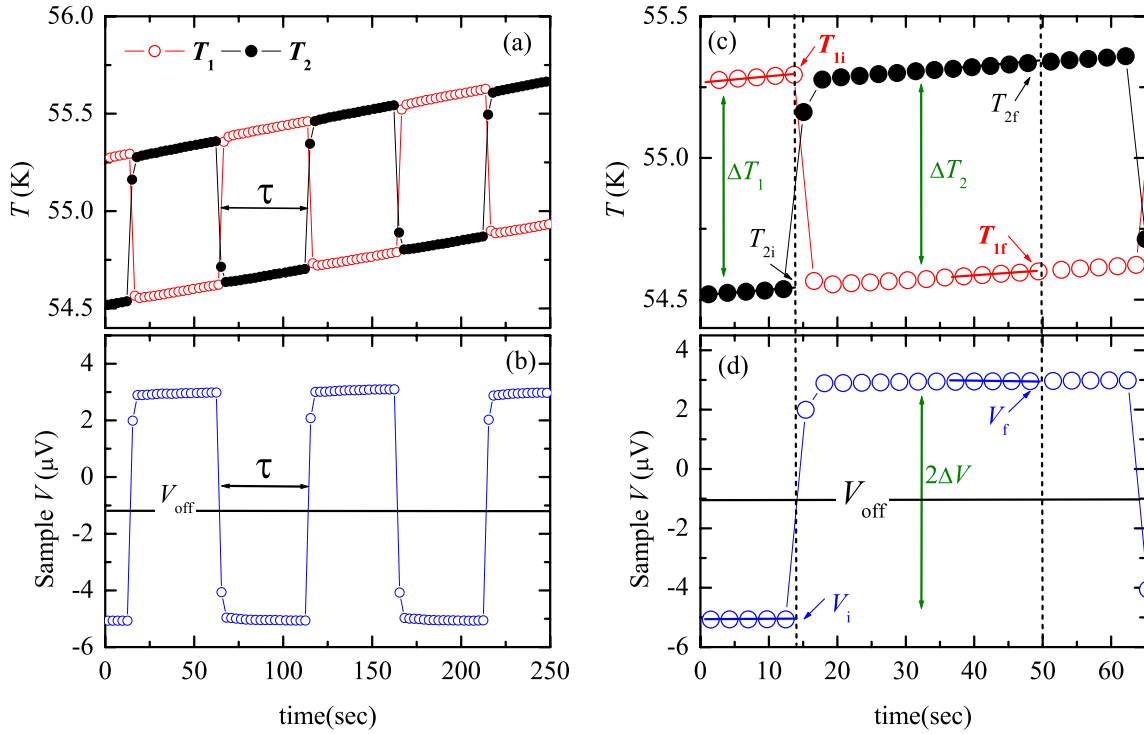
Figure A.2 Measurement procedure to extract the TEP from data corresponding to the measurement performed near 55 K on Pt-wire *versus* phosphor-bronze wire. Actual time period (τ) between subsequent cycles, used to calculate TEP, was 50 sec. (a) Measured temperatures of both thermometers (T_1 and T_2) and (b) sample voltage (V) as a function of time. Note small (~ 0.1 K/min) drift superimposed on data. (c) (d) One cycle of measurement to determine parameters ΔT, ΔV: initial temperature T_i, final temperature T_f, initial voltage V_i, final voltage V_f and offset voltage V_{off}. The solid lines represent the linear fit to the measurement data. The temperature difference for T_1 (T_2) is determined by $\Delta T_1 = T_{1i} - T_{2i}$ ($\Delta T_2 = T_{2f} - T_{1f}$) so that $2\Delta T = \Delta T_1 + \Delta T_2$. The voltage difference is calculated $2\Delta V = V_f - V_i$ (see text).

as a function of time, ΔT and ΔV, respectively, the sample temperature T_{av} and the TEP ($S = -\Delta V/\Delta T$) are calculated using the following equations.

$$2\Delta T = (T_{2f} - T_{1f}) + (T_{1i} - T_{2i})$$

$$2\Delta V = V_f - V_i$$

$$T_{av} = \frac{(T_{2f} + T_{1f}) + (T_{2i} + T_{1i})}{4}$$

Since the temperature difference is generated by alternately applying power to one of the heaters, the measured voltage corresponds to $2\Delta V$. Thus, the TEP of sample is calculated by $S = -2\Delta V/2\Delta T$. Figure A.2 shows the data corresponding to a measurement performed near 55 K on a platinum (Pt) wire sample, using phosphor-bronze lead wires. The puck temperature was ramped at the rate of 0.1 K/min. A complete cycle, used to determine ΔT and ΔV, took a time period (τ) of 50 sec. The parameters (T_{1i}, T_{1f}, T_{2i}, T_{2f}, V_i and V_f) were determined by a linear fit of the data as a function of time as shown in Fig. A.2 (c) and (d).

The heater current (I) and time period (τ), needed to generate given ΔT, are not easy to estimate a prior, because of the temperature dependence of multiple parameters, such as the thermal conductivity and heat capacity of the sample, sample stage and all electrical wiring of the apparatus. Therefore, the current and measurement time for given ΔT were determined empirically at several temperatures by applying constant power to one of the heaters. For determining the final temperature and voltage, after switching the power from one heater to the other, the number of data point for linear fit was selected within constant temperature and voltage region as a function of time. Although it depends on the sample under investigation, typical values of $\tau \sim 45$ sec at 2 K and $\tau \sim 150$ sec at 300 K for this setup allowed an accurate determination of the final values of T_f and V_f. Typical values of the heater current were $I \sim 0.8$ mA to generate $\Delta T \sim 0.2$ K at 2 K, and $I \sim 5$ mA to generate $\Delta T \sim 1.0$ K at 300 K.

By utilizing two heaters and an alternating gradient ΔT, we avoid problems associated with offset voltages. V_i and V_f represent the thermal voltages in the circuit, which include spurious voltages and the TEP of lead wires. In fact, for very low values of the TEP, it is often necessary to consider an offset voltage (V_{off}) in the system and circuit. A common source of spurious voltage, for example, is the wiring of the system from the voltmeter to the sample

space since there is a thermal gradient and several soldering points between various wires. We found that the value of V_{off} for this setup depended on temperature; it was $\sim$0.5 μV around 300 K and $\sim$ -1.5 μV around 10 K. If we suppose that V_{off} is independent of the small ΔT across the sample and has a small temperature dependence as a function of time (adiabatic approximation) V_{off} can be easily canceled out using two heaters as shown in Fig. A.2 (d).
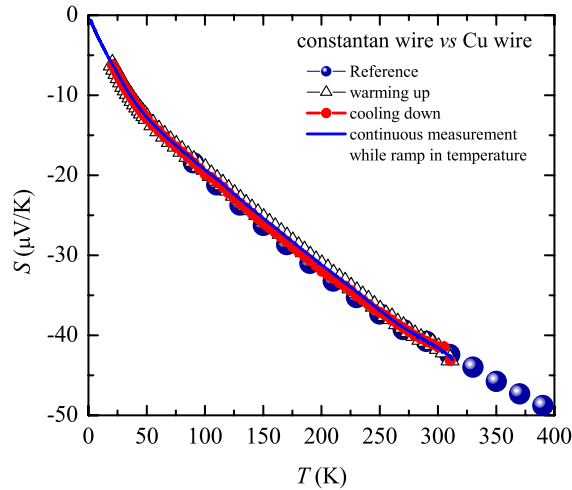

Figure A.3   TEP of constantan wire *versus* copper wire. Warming up and cooling down indicate the measurement data using the stable temperature method. The solid line shows the TEP values using the alternating heating method by slowly drifting system temperature. The detailed explanations are in the text. We used the reference data provided from MMR Technologies with constantan as a standard.

In the early stage of testing this measurement setup, the process of collecting data was checked by measuring the constantan wire (100 μm diameter) against copper wire ($\sim$ 20 μm diameter). Since constantan wire has been known to have large TEP value compared to copper wire, the system can be tested without correcting the contribution of copper wire as shown in Fig. A.3. In this test run, we used the following two protocols. Firstly, a stable temperature method was applied; in this measurement the sample puck was held at a constant temperature and the TEP of the constantan wire using either one heater or two heaters was measured and found to be basically same within error bar of this measurement setup. However, the TEP data for the constantan wire showed a small hysteresis upon cooling and warming between 50

and 260 K with a maximum difference of about 2 %. The origin of this hysteresis is not clear, we expect this that it is based on different relaxation times to stablize the temperatures of the system.

Secondly we adopted an alternate method which was to measure the TEP while slowly warming the system temperature with the ramp rate of 0.1 K/min below 10 K and of 0.45 K/min above 100 K (shown for a measurement of Pt wire in Fig. A.2 (a) for $T \sim 55$ K). As temperature increases higher than 10 K, the ramp rate was increased for certain temperature range, for instance 0.2 K/min up to 20 K and 0.3 K/min up to 100 K. It is worth noting that if the system temperature is slowly warming, it is necessary to carefully consider the time dependence of the sample temperatures and voltages. In this case we calculated ΔT and ΔV from a linear fit of the data. Continuous measurements while ramping temperature provide a high density of data and reduce the measurement time. In general it takes 16 hours to run from 2 to 350 K. This is in contrast to our finding that the relaxation time to stablize a sample stage completely under high vacuum at a single temperature is longer than one hour. Figure A.3 shows the TEP of Constantan wire based on these two protocols. In this test run the agreement between measured results and the reference data [1] is reasonable. The TEP extracted by the second protocol (slow drift of the system temperature) lies between the data taken on warming and cooling using the stable temperature method.

System Calibration and Sample TEP

Since the wires attached to the sample are either copper or phosphor-bronze, a second thermal voltage is also generated. The measured TEP is then

$$S_{measured} = S_{sample} - S_{wire} \tag{A.1}$$

Here S_{wire} represents the sum of the wire and all system contributions. When measuring an unknown sample the TEP is then the sum of S_{wire} and $S_{measured}$.

The TEP of copper is strongly dependent on magnetic impurities below 100 K due to the Kondo effect [Blatt, 1976] and therefore no reliable (or universal) reference data set is

---

[1]The reference data came from MMR Technologies with constantan wire as a standard.
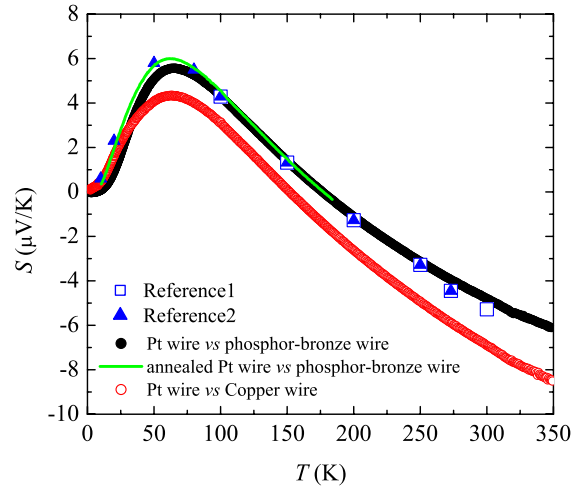
Figure A.4   TEP of Pt-wire *versus* phosphor-bronze wire and Pt-wire *versus* copper wire. Circles and solid line represent the measured data from this work without any corrections. Both reference 1 (open squares) and reference 2 (solid triangles) data are from Ref. [Blatt, 1976].

available for low temperatures. On the other hand, a superconducting material is a suitable reference because $S = 0$ in superconducting state. In the present study Pt-wire and Bi2212 high T_c superconductors were each, separately, mounted between the two sample stages and calibration measurements were performed. These were sufficient for determining the lead wire contribution S_{wire}. For the high temperature region pure Pt-wire (~ 50 μm diameter) was used as a reference. Figure A.4 shows the TEP of the Pt-wire *versus* copper wire and Pt-wire *versus* phosphor-bronze wire. The result of Pt-wire *versus* phosphor-bronze wire is in good agreement with the absolute TEP value of Pt [Blatt, 1976] which implies that the absolute TEP value of phosphor-bronze wire is negligible. Note that below 100 K the Pt-wire manifests slightly different TEP responses depending on the heat treatment (annealing) of wire. At low temperatures we employed two superconducting Bi2212 compounds with T_c about ~ 82 K and ~ 92 K, where the different T_c values may be due to the heating of sample in air. The results of the TEP measurement for Bi2212 against copper and phosphor-bronze wire are shown in Fig. A.5. In this calibration measurement samples were mounted on the two sample stages with GE-varnish. The copper and phosphor-bronze wire were attached to the sample using silver

epoxy (top configuration of Fig. A.1 (c)). Here we used Bright Brushing Gold to attach the wire to the Bi2212 because using only silver epoxy provided a poor electrical contact, usually on the order of 10^3 Ω. After painting on the Bright Brushing Gold, the sample was heated up to 400 ^{o}C quickly, held for 5 min and air quenched to room temperature, where the contact resistance was reduced to below 100 Ω.
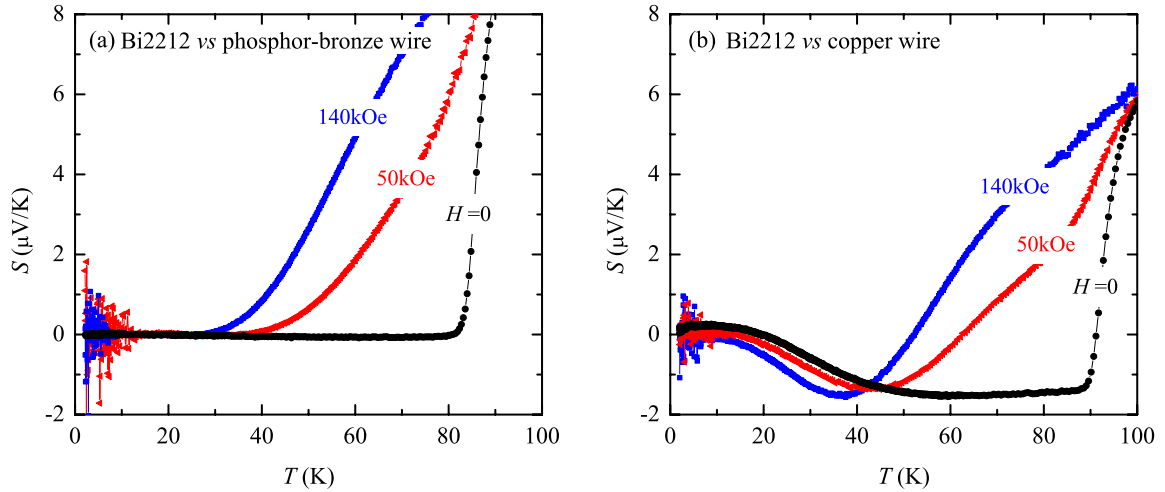

Figure A.5   Calibration measurements of lead wires. (a) TEP of Bi2212 *versus* phosphor-bronze wire and (b) Bi2212 *versus* copper wire as a function of temperature at several constant magnetic fields.

The absolute TEP of copper and phosphor-bronze wire we measured and of copper, from the literature, is shown in Fig. A.6. Because $S = 0$ in the superconducting state, the observed TEP is the absolute TEP of copper and phosphor-bronze wire. From Fig. A.6 (a) it is dramatically clear that the absolute TEP value of phosphor-bronze wire is very small, $S \ll 0.5$ μV/K, up to 80 K. For copper wire the agreement between measured results and the literature data is reasonable. The inset of Fig. A.6 (b) shows the low temperature TEP of copper wire. For the copper wire measured against phosphor-bronze, no correction was added. These data indicate a fairly good agreement with the data taken from Fig. A.5 (b). The estimated uncertainty for the copper wire is about 0.3 μV/K. In addition to the subtraction errors, we believe that this disagreement is due to a difference in quality of the copper wire in Ref. [Blatt, 1976] and that used in this measurement.
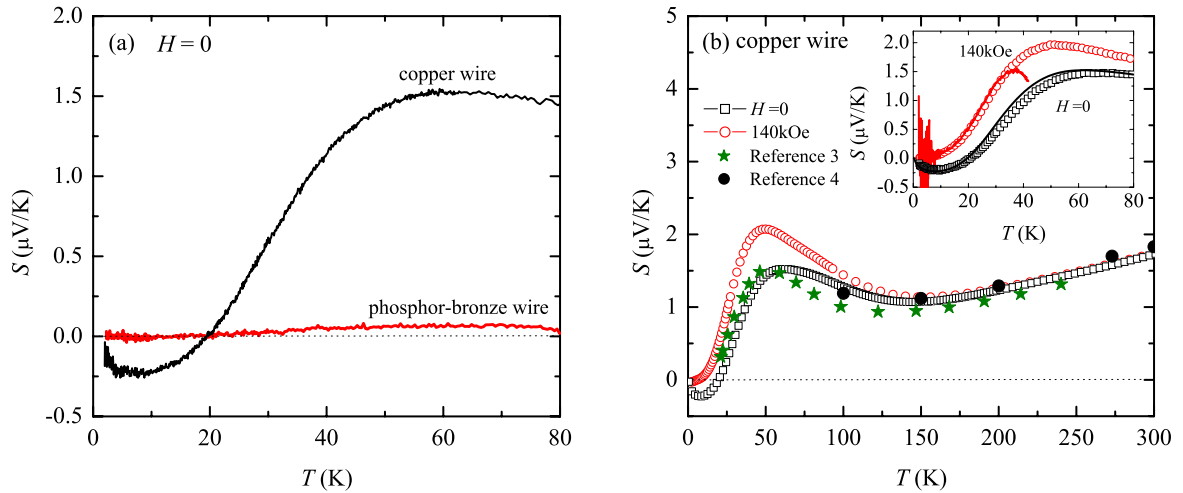
Figure A.6   (a) Absolute TEP of copper and phosphor-bronze wire below 80K. The data are taken from Fig. A.5. (b) Calibrated TEP curve of copper wire at H=0 (open square) and 140 kOe (open circle). Both closed circles (reference 3) and stars (reference 4) were taken from Ref. [Blatt, 1976]. Inset: expanded view for low temperature range. The symbols present the measured TEP of copper wire against to phosphor-bronze wire. No correction was added. Solid lines are taken from Fig. A.5 (b).

As an aside, it should be noted that the low temperature, oscillatory behavior of the Bi2212 sample for H >0 (Fig. A.5) is reproducible. Although similar behavior was observed in the Nernst signal and associated with the plastic flow of the vortices [Wang, 2006], the origin of this phenomena is still somewhat unclear.

Previous TEP measurements at low temperatures and in high magnetic fields have had to take into account the significant contribution of background voltage. By using well-known elemental metal wires of copper or gold and superconducting materials, these background contributions can be accounted for, correcting the background contribution. For small single crystals an alternating AC current technique, utilizing a thermocouple, has been used to measure TEP under high magnetic fields for a wide range of temperatures [Resel, 1996; Choi, 2001]. Although the thermocouple wire provides a good sensitivity for relative temperatures, an accurate determination of ΔT in high magnetic fields becomes difficult and large efforts are needed to calibrate the field dependence of the thermocouple wire.

In order to exclude the difficulties due to the magneto-thermoelectric power (MTEP) measurement based primarily on the field dependence of S_{wire} and thermometer calibrations, we selected phosphor-bronze wire and Cernox. Whereas the TEP of copper (Cu) wire is not small and shows a field dependence, phosphor-bronze wire provides essentially zero TEP over wide temperature range and is almost temperature and field independent [Wang, 2003] as shown in Figs. A.5 and A.6. Therefore, in this measurement setup the magnetic field dependence of TEP of samples, including the quantum oscillation (de Haas-van Alphen oscillation) at low temperatures, can be reliably measured.

The accuracy of this technique was estimated by using the measurement of Pt and Cu wire. The estimated uncertainty of this system over all temperature ranges falls within a maximum ± 1 $\mu V/K$, and the relative accuracy is within a maximum of 10 %. In the high temperature region, roughly above 100 K, the main uncertainty originates from inaccurate determination of the ΔT due to the relatively low sensitivity of the Cernox. The absolute and relative temperature of Cernox was observed within a resolution of 4 mK at low temperatures, the relative error at high temperatures falls within $\sim$ 200 mK. For materials having low thermal conductivity, the error may be larger due to the temperature difference between sample and thermometer. For materials having small TEP, less than 0.5 $\mu V/K$, the error can also be larger due to noise. More contributions to the error need to be considered for TEP measurements in the magnetic field. For instance, due to the heat conducting environment which is mainly caused by induced current by applying magnetic fields ($d\Phi/dt$), it is very important to make sure that the ramp rate of magnetic field should be slow enough to avoid additional heating and reduce the induced voltage due to the open loop. Alternatively, the TEP can be measured stepping the magnetic field with the magnet in persistent mode for each value of the field.

Summary of Technical Parameters and Reference Information

- Operation range: temperature range from 2 to 350 K and magnetic fields up to 140 kOe.

- Sample dimension: the length of the sample is between 1.5 and 7 mm.

- ΔT: from 0.1 to 2.5 K, depending on the temperature and the absolute TEP value of sample.

- Ramp rate of system temperature: it can be varied up to 1 K/min. For example, in the calibration measurement, it was selected 0.1 K/min up to 10 K, 0.35 K/min up to 100 K and 0.45 K/min above 100 K.

- Estimated accuracy: maximum of ± 1 μV/K and 10% depending on the temperature and sample. The limit of accuracy is mainly imposed by the limitations in the thermometery and the thermal contact between the sample and the thermal stage. If the absolute TEP of the sample is smaller than 0.5 μV/K the fluctuation of the sample voltage was observed.

- Copper wire: 0.025 mm diameter, Puratronic, 99.995% (metals basis), Alfa Aesar. Detected impurity elements are Fe, Ag, O, S (as provided by supplier).

- Phosphor-Bronze wire: $Cu_{0.94}Sn_{0.06}$ alloy, 0.025 mm diameter, GoodFellow.

- Platinum wire: 0.05 mm diameter, 99.95% (metals basis), Alfa Aesar.

- Silver epoxy: H20E, Epotek.

- Strain gauge : FLG-02-23, 0.2×1.4 mm^2 grid made from Cu-Ni alloy and 3.5×2.5 mm^2 thin epoxy backing, Tokyo Sokki Kenkyujo Co., Ltd.

- Silver paste: DuPont 4929N silver paint, DuPont, Inc.
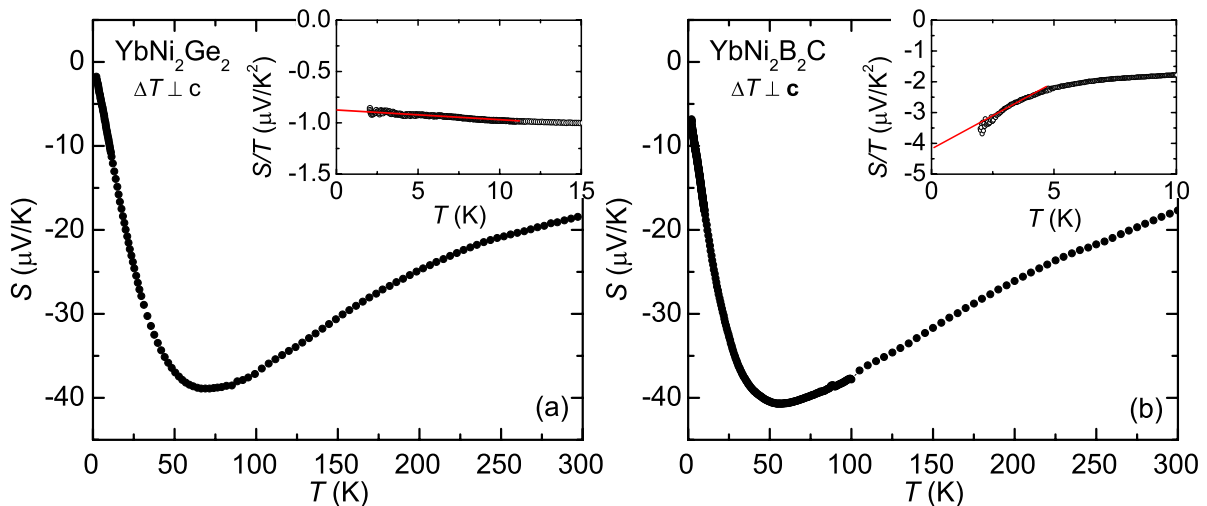
- Stycast 1266: Emerson & Cuming, Inc.

APPENDIX B.   TEP of $YbNi_2Ge_2$ and $YbNi_2B_2C$

Figure B.1   TEP of (left) $YbNi_2Ge_2$ and (right) $YbNi_2B_2C$ as a function of temperature between 2 and 300 K for $\Delta T \perp \mathbf{c}$. Insets show the $S(T)/T$ vs. T. Solid lines are guides to the eye.

Zero field $S(T)$ data of $YbNi_2Ge_2$ and $YbNi_2B_2C$ compounds are plotted in Fig. B.1. At high temperatures, the $S(T)$ for both exhibit a large, negative minimum (approximately -40 μV/K in both cases) and $S(T)$ is negative for both samples over the measured temperature range. A negative sign with a highly enhanced value of the TEP over the temperature region measured is typical of those found in Yb-based Kondo lattice systems [Foiles, 1981; Andreica, 1999; Deppe, 2008]. The inset of Fig. B.1 (a) presents $S(T)/T$ of $YbNi_2Ge_2$ below 15 K. The zero temperature limit of $S(T)/T$ was estimated by extrapolating $S(T)$ from 10 K to $T = 0$ (solid line), where the inferred $S(T)/T|_{T\rightarrow 0}$ is approximately -0.88 μV/K^2. For $YbNi_2B_2C$, the estimated $S(T)/T|_{T\rightarrow 0}$ value is found to be $\sim$-4.2 μV/K^2 by using a linear extrapolation below 5 K as shown in Fig. B.1 (b).

APPENDIX C.   Quantum oscillations - YbPtBi

Shubnikov-de Haas (SdH) quantum oscillations have been observed throughout the magnetoresistance (MR) measurements at low temperatures and high magnetic fields. Figure C.1 shows the MR at $T = 0.1\,\mathrm{K}$ for magnetic field applied along [100] and [111] directions, where samples are mounted on a dilution refrigerator cold stage with GE-varnish. At high magnetic fields a broad local extrema in MR is observed for both magnetic field directions. This behavior may be due to the change of scattering processes with CEF levels, or it may be the oscillatory component corresponding to extremely small Fermi surface area in which the small frequency has been observed for RPtBi ($R =$ La, Ce, and Nd) [Goll, 2002; Wosnitza, 2006; Morelli, 1996] in the paramagnetic state (see below discussion). For YbPtBi though this is not likely to be the case because the frequency is so small that it would have an amplitude that would make it hard to observe in SdH measurements. What is intriguing are the unambiguous quantum oscillations at high magnetic fields.

Before analyzing data in detail, it should be noted that the measurements are susceptible to torque effects at high magnetic fields. At $T = 0.5\,\mathrm{K}$ MR curves for the sample #13 are plotted in the inset of Fig. C.1, where open circle indicates the data taken from hanging the sample in vacuum and open square indicates the data taken from gluing the sample to the heat sink using Apiezon N-grease. The MR data shows significantly different behavior for $H > 40\,\mathrm{kOe}$. At higher magnetic fields along $\mathbf{H} \parallel [100]$, quantum oscillations are discernible for both curves, but the fast Fourier transform (FFT) spectra indicate a frequency difference between the two data sets. The observed difference of MR is most likely due to the torque. Note that the MR curve for hanging the sample in vacuum indicates no hysteresis. Thus, only for measurements performed with the sample attached to the cold stage using GE-varnish, are the SdH oscillation
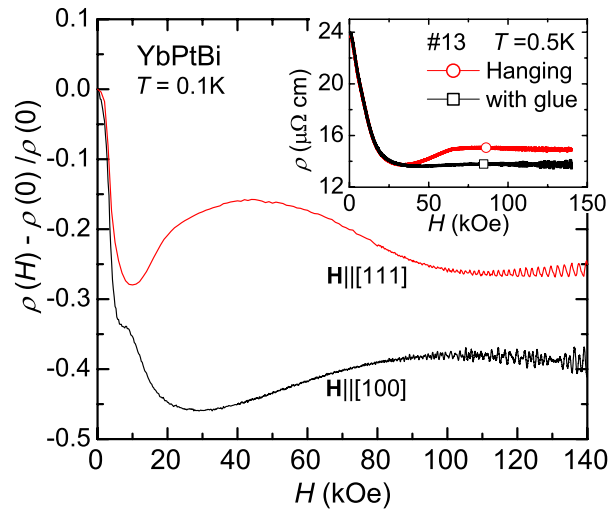
Figure C.1 Magnetoresistance (MR), plotted as $[\rho(H) - \rho(0)]/\rho(0)$ vs. H, of YbPtBi at $T = 0.1\,\mathrm{K}$ along $\mathbf{H} \parallel [100]$ and $\mathbf{H} \parallel [111]$. Inset shows MR for sample #13 at $T = 0.5\,\mathrm{K}$ along $\mathbf{H} \parallel [100]$. Open circles are taken data with hanging the sample in vacuum and open squares are taken data with mounting the sample to the cold stage using GE 7301 varnish. At high magnetic fields quantum oscillations are discernible for both curves.

analyzed up to $2\,\mathrm{K}$. To analyze the SdH frequency, the magnetic field range, $80\,\mathrm{kOe} \leq H \leq 140\,\mathrm{kOe}$, was used.

In Figs. C.2 (a) and (c) typical SdH data sets for YbPtBi, after subtracting the background contributions, are displayed as a function of $1/H$ at selected temperatures. The amplitude of the oscillations decreases as temperature increases. Since the signals are comprised of a superposition of several oscillatory components, the data are most easily understood by taking the FFT of these data as shown in Fig. C.2 (b) for $\mathbf{H} \parallel [100]$ and (d) for $\mathbf{H} \parallel [111]$. The FFT spectra at $T = 0.06\,\mathrm{K}$ show several frequencies, including second harmonics with very small amplitudes. The observed frequencies are summarized in Table C.1.

Quantum oscillations are observed in magnetic fields as low as $60\,\mathrm{kOe}$ at the lowest temperature measured and in temperatures as high as $3\,\mathrm{K}$, which confirms the very high quality samples as well as very small effective mass of conduction carriers. The frequencies in FFT spectra do not shift with temperature and most of the first harmonics of the frequencies are clearly observed as high as $2\,\mathrm{K}$. The cyclotron effective mass, m^*, of the carriers from the vari-
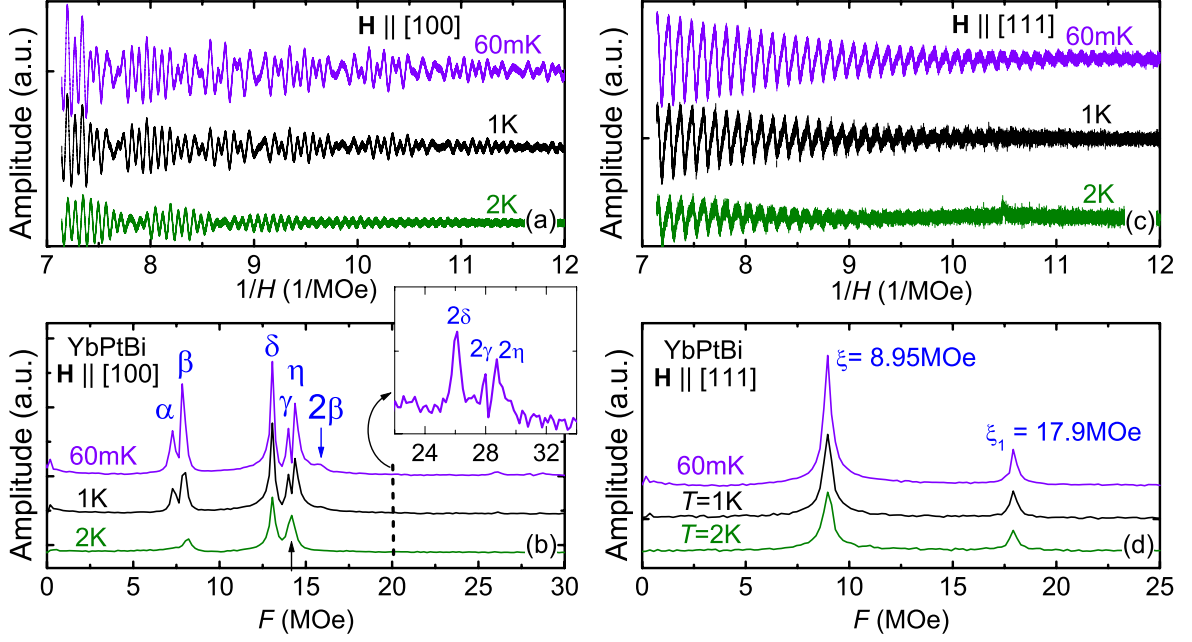
Figure C.2   SdH of YbPtBi at $T = 0.06$, 1, and 2 K, plotted after subtract-
ing the background MR, for (a) $\mathbf{H} \parallel [100]$ and (c) $\mathbf{H} \parallel [111]$.
FFT spectra of SdH data at $T = 0.06$, 1, and 2 K for (b)
$\mathbf{H} \parallel [100]$ and (d) $\mathbf{H} \parallel [111]$.

ous orbits were determined by fitting the temperature-dependent amplitude of the oscillations
to the Lifshitz-Kosevich (L-K) formula [Shoenberg, 1984] for each frequency:

$$\rho = C \, F(H) F(T_D) F(X) F(s) \sin\left(\frac{2\pi f}{H} + \phi\right) \tag{C.1}$$

where C is a constant, and $F(H)$ is a function of only H, which will vary from case to case.
$F(T_D)$ is the Dingle reduction factor, $F(T_D) = \exp(-2p\pi^2 k_B T_D/\beta H)$, with $\beta = e\hbar/m^*c$ and
Dingle Temperature $T_D = \hbar/2\pi k_B \tau$; $F(X)$ is the temperature reduction factor, $F(X) = X/\sinh(X)$, with $X = 2p\pi^2 k_B T/\beta H$; and $F(s)$ is the damping factor (spin splitting factor)
de-phasing by Zeeman splitting ($E = \pm g\mu_B H$), $F(s) = \cos(p\pi g m^*/2m_e)$. The various sym-
bols have the following meanings: p is the harmonics of the frequency (f), ϕ is the phase of
oscillations, τ is the relaxation time, e is the negative electronic charge, m^* is the effective
(cyclotron) mass, m_e is the bare electron mass, g is the spin-splitting factor, μ_B is the Bohr
Magneton, and $\hbar$ is the Plank's constant.

The oscillation amplitudes and the fit curves using the temperature reduction factor are

Table C.1 Frequencies f and effective masses m^* obtained from the SdH oscillations. m_e is the bare electron mass.

$\mathbf{H} \parallel [100]$		f (MOe)	m^*/m_e
	α	7.27	1.41
	β	7.83	1.59
	δ	13.06	0.83
	γ	13.99	0.80
	η	14.37	0.97
	2β	15.67	
	2δ	26.13	
	2γ	27.99	
	2η	28.74	
$\mathbf{H} \parallel [111]$			
	ξ	8.95	1.22
	ξ_1	17.90	0.49

plotted in Fig. C.3 (a) and (b). The calculated effective masses range from $m^*(\alpha) \sim 1.41\, m_e$ to $m^*(\xi_1) \sim 0.49\, m_e$, where m_e is the bare electron mass. The estimated effective masses are summarized in Table C.1. We were not able to estimate the effective masses, associated with the second harmonic frequencies due to the small amplitude of the signals. Although the frequency ξ_1 is integer-multiple of ξ, $\xi_1 \simeq 2\xi$, it is not a higher harmonic of ξ because of the inconsistent effective masses. In addition, if these frequencies are originating from the same extremal orbit, the phase difference between two frequencies can not be explained; the oscillation curves are generated by L-K formula with the phase term, $A_1 \sin(2\pi\xi/H + \pi/1.95)$ $+ A_2 \sin(2\pi\xi_1/H - \pi/7.7)$, as shown in Fig. C.3 (c). Therefore, ξ_1 is independent frequencies, coming from different area of extremal orbit. The frequency of the orbit η is almost twice of the frequency of the α, however these orbits are also expected to be came from different Fermi surfaces. If the orbit η is the second harmonics of the α, the oscillation amplitude of the η should be smaller than that of α, but the amplitude of these frequencies are almost the same for both. Therefore, the orbit η is not the second harmonics of the α. Note that the frequency, observed near $14\,\mathrm{MOe}$ at $2\,\mathrm{K}$ along $\mathbf{H} \parallel [100]$, seems to split from one component into two component of γ and η with decreasing temperature, as indicated by up arrow in Fig. C.3 (b). At present it is not clear whether two frequencies of γ and η are originating from
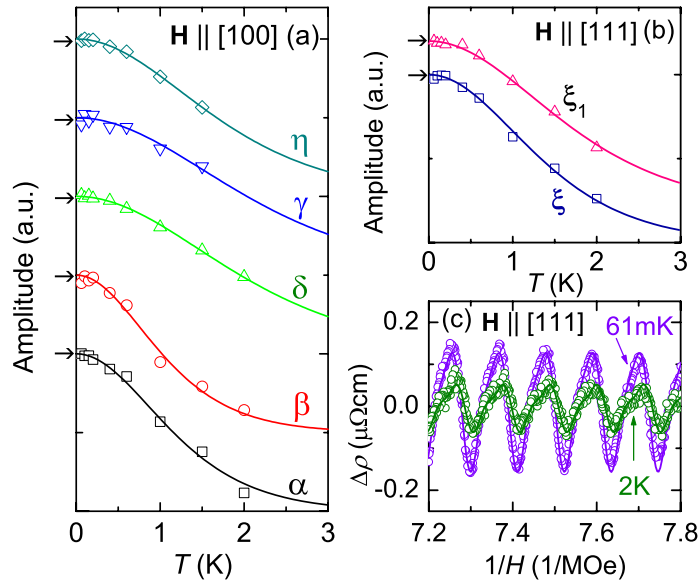
Figure C.3   (a) and (b) Temperature dependence of the SdH amplitudes. Solid lines represent the fit curves to the Lifshitz-Kosevich (L-K) formula. All data and fit curves are normalized to 1, indicated by horizontal arrows, and shifted for clarity. (c) Resistivity along $\mathbf{H} \parallel [111]$ at $T = 0.06$ and $1\,\mathrm{K}$, plotted as a function of $1/H$ after subtracting the background MR, where the solid lines represent the fit curves based on the L-K formula with the frequency ξ and ξ_1.

the same extremal orbit, thus it needs to be clarified by further detailed measurements. From the observed frequencies quite simple Fermi surfaces are expected. It would be necessary to measure frequencies as a function of angle between the crystallographic axes in order to make estimates of the Fermi surface topology.

The low carrier density for YbPtBi implies a Fermi surface occupying a small portion of the Brillouin zone, which is consistent with the results of quantum oscillations. The frequency of the quantum oscillations is proportional to the extremal cross-section, A_{FS}, of the Fermi surface; $f = (\hbar/2\pi e)A_{FS}$ [Shoenberg, 1984]. In the paramagnetic region direct evidence for small Fermi surfaces comes from SdH measurements, where several small extremal orbits, implying a small portion of occupation of the Brillouin zone, are observed. Quantum oscillations have also been observed for LaPtBi and CePtBi [Goll, 2002; Wosnitza, 2006] from the

electrical resistivty measurements in pulsed magnetic fields up to 50 Tesla. The oscillation frequencies for LaPtBi are approximately 10 times smaller, 0.65 MOe for $\mathbf{H} \parallel [100]$ increasing to 0.95 MOe for $\mathbf{H} \parallel [110]$, than for YbPtBi. For CePtBi the anomalous temperature dependence of SdH frequency, $f = 0.6$ MOe, was observed along $\mathbf{H} \parallel [100]$ and a very low SdH frequency of ~ 0.2 MOe, which is independent of temperature, was found along $\mathbf{H} \parallel [111]$. In addition to the unusual temperature dependence of the SdH frequency for CePtBi, the disappearance of the oscillations was observed above about 25 Tesla at which the magnetic field-induced band structure change was proposed [Wosnitza, 2006]. Since the SdH frequencies for YbPtBi are not changed by temperature or magnetic field, within the temperature and magnetic field range of our measurements, such a band structure modification is not expected. The band calculations for LaPtBi [Oguchi, 2001] and CePtBi [Goll, 2002], assuming localized $4f$ states, were found to be semimetals. In these calculations, two hole-like Fermi surface are found around zone center, which are similar to the measured angular dependence of the Fermi surface cross-section area of LaPtBi. A number of small electron-like pockets are also predicted in the band calculations which are too small to observe experimentally. The effective masses for both LaPtBi and CePtBi have been estimated to be $\sim 0.3\,m_e$ [Wosnitza, 2006], which is somewhat smaller than for YbPtBi. The observed trend of SdH frequencies suggested larger Fermi surface sheets for YbPtBi than LaPtBi, and these are consistent with earlier resistivity results of RPtBi [Canfield, 1991], where the resistivity varied from metallic (semimetallic) to small gap semiconductor when rare-earth changes from Lu to La; $\rho(T)$ of LuPtBi decreases and $\rho(T)$ of LaPtBi increases as temperature decreases, where the carrier density for LuPtBi is approximately two order of magnitude bigger than that for LaPtBi.

In order to compare the experimental observations of SdH frequencies to the topology of the Fermi surfaces, we calculated the zero field band structure of paramagnetic YbPtBi. For the Fermi surface calculation, we have used a full-potential Linear Augmented Plane Wave (fp-LAPW) [Blaha, 2001] method with a local density functional [Perdew, 1992]. The structure data was taken from reported experimental results [Robinson, 1994]. To obtain the self consistent charge density we chose 1204 k-points in the irreducible Brillouin zone and set

$R_{MT} \cdot K_{max}$ to 9.0, where R_{MT} is the smallest muffin-tin radius and K_{max} is the plane-wave cutoff. We used muffin-tin radii 2.5 for all Yb, Bi, and Pt atoms. The calculation was iterated with 0.0001 electrons of charge and 0.01 mRy of total energy convergence criteria. Although there was a discussion about $4f$ electron pinning at the Fermi energy [Oppeneer, 1997] and we were aware that Fermi surface is quite different under $4f$ electrons influence [McMullan, 1992] we treated $4f$ electrons as core-electrons since we were interested in the high magnetic field, paramagnetic state. To obtain SdH frequencies we calculated 2-dimensional Fermi surfaces and integrated the Fermi surface area. We chose planes which were perpendicular to k_z-axis and had 0.01 $(2\pi/a)$ interval. Each plane ($-1 \leq k_x, k_y \leq 1$) were divided with 100×100 mesh. For a 3-dimensional Fermi surface, we used 2300 k-points in the irreducible Brillounin zone and a graphic program called XcrysDen [XcrysDen].
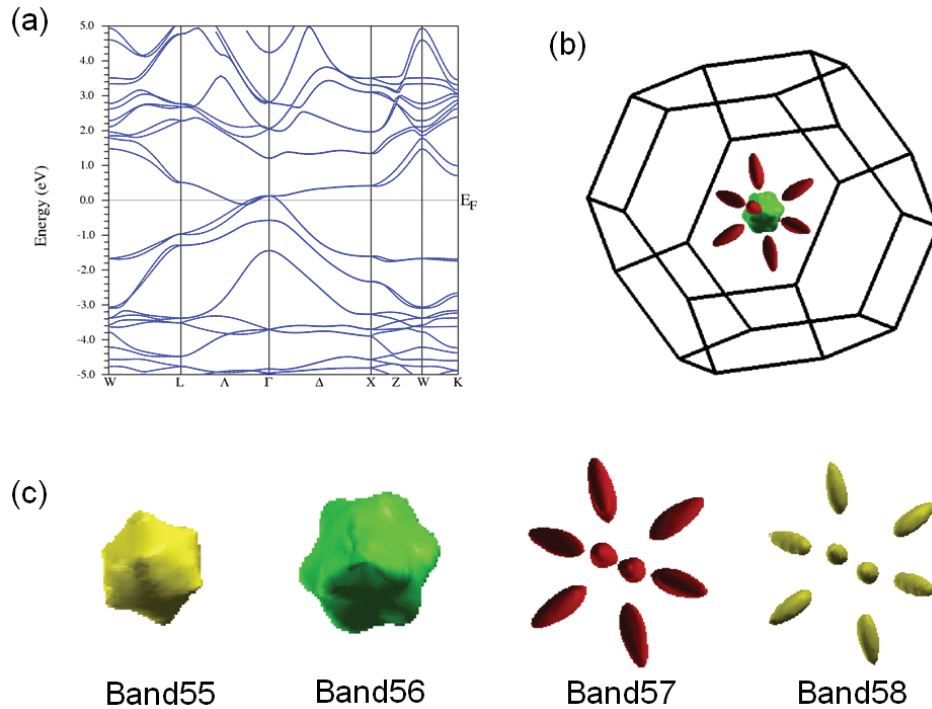

Figure C.4 (a) Band structure of nonmagnetic YbPtBi, calculated for localized $4f$ states. (b) Calculated Fermi surface in the fcc Brillouin zone. Two three dimensional pockets (bands 55 and 56), located in the zone center, are surrounded by sixteen cigar shaped pockets (bands 57 and 58). (c) Enlarged Fermi surface for band 55, 56, 57, and 58.

The results of band structure calculations are shown in Fig. C.4 (a). The overall features are very similar to the results of LaPtBi, however with more Fermi surface occupation in the Brillouin zone. Around zone center two hole-like Fermi surface (band 55 and 56) are surrounded by sixteen small electron-like pockets (band 57 and 58). These calculated Fermi surfaces of YbPtBi are plotted in Fig. C.4 (b) and (c). The SdH frequencies of these four bands are calculated to be 2.4, 3.5, 0.79, and 0.65 MOe from the maximum area perpendicular to the k_z, where there are orbits very close to 2.4 and 3.5 MOe due to the 3-dimensional shape of the Fermi surfaces at the zone center. These values are much larger than the predicted value for LaPtBi and CePtBi [Goll, 2002; Wosnitza, 2006], however four times smaller than the frequencies determined from experimental results.

The Fermi surfaces of YbPtBi are highly sensitive to the $4f$ electron contributions as predicted in Ref. [McMullan, 1992]. When the $4f$ electrons are included in the band calculations, the six hole-like pockets are located zone center in which the predicted frequencies range from ~ 27 to ~ 164 MOe [McMullan, 1992], which is much higher than the experimental observations. So treating $4f$ electrons as included in core levels appears to be reasonable. If the Fermi level is shifted to lower energy, the experimentally observed frequencies can be matched to the hole-like pockets at the zone center, whereas the electron-like pocket surrounding the zone center will not be detected. As a conjecture, the effective masses and frequencies of the orbit α and β along [100] direction, linked to the ξ along [111] direction, are almost the same, expected that these two orbits are came from the band 55. Similarly the orbits δ, γ, and η, connected to the ξ_1, all came from the 3-dimensional shape of the band 56.

Without an angular dependence of the SdH measurements, the Fermi surface topology can not be determined unambiguously and further theoretical work is needed to unravel the discrepancies in the precise extremal orbit sizes. Since we have observed only small effective masses for YbPtBi, it is expected that the hybridization between $4f$ and conduction electrons has been suppressed for these high magnetic fields. This is consistent with the specific heat results; the enormous value of $\gamma \sim 8$ J/mol·K^2 for $H = 0$ is suppressed to $\gamma \sim 0.15$ J/mol·K^2 for $H = 50$ kOe.

Note that if there are still significant $4f$ electron contributions in this magnetic field range, up to $140\,\mathrm{kOe}$, it required much lower temperatures to observe heavy electrons in SdH measurements. This is a standing problem in HF physics, in order to detect the heavier effective masses, higher magnetic fields are needed, however the mass enhancement can be suppressed due to the application of these larger magnetic fields. Thus, lower measurement temperatures, crystals with extremely low scattering in terms of Dingle temperature, and materials with higher T_K values are necessary to detect heavier effective mass of carriers. Measuring de Haas-van Alphen (dHvA) oscillations as a complementary to SdH oscillations may be another experimental approach since oscillation amplitudes have different dependence of m^* in dHvA and SdH. However, this task can be challenging due to high paramagnetic background signal.

BIBLIOGRAPHY

[Aeppli, 1986] G. Aeppli, H. Yoshizawa, Y. Endoh, E. Bucher, J. Hufnagl, Y. Onuki and T. Komatsubara, Phys. Rev. Lett. **57**, 122 (1986).

[Alami, 1999] K. Alami-Yadri, D. Jaccard, and D. Andreica, J. Low Temp.Phys. **114**, 135 (1999).

[Amato, 1987] A. Amato, D. Jaccard, J. Flouquet, F. Lapierre, J. L. Tholence, R. A. Fisher, S. E. Lacy, J. A. Olsen, and N. E. Phillips, J. Low Temp. Phys. 68, 371 (1987).

[Amato, 1992] A. Amato, P. C. Canfield, R. Feyerherm, Z. Fisk, F. N. Gygax, R. H. Heffner, D. E. MacLaughlin, H. R. Ott, A. Schenck, J. D. Thompson, Phys. Rev. B **46**, 3151 (1992).

[Andreica, 1999] D. Andreica, K. Alami-Yadri, D. Jaccard, A. Amato, and D. Schenck, Physica B **259-261**, 144 (1999).

[Andres, 1975] K. Andres, J. E. Graebner, and H. R. Ott, Phys. Rev. Lett. **35**, 1779 (1975).

[Aoki, 1998] Y. Aoki, T. D. Matsuda, H. Sugawara, H. Sato, H. Ohkuni, R. Settai, Y. Ōnuki, E. Yamamoto, Y. Haga, A. V. Andreev, V. Sechovsky, L. Havela, H. Ikeda, and K. Miyake, J. Magn. Magn. Mater. **177-181**, 271 (1998).

[Auerbach, 1986] A. Auerbach and K. Levin, Phys. Rev. B **34**, 3524 (1986).

[Balicas, 2005] L. Balicas, S. Nakatsuji, H. Lee, P. Schlottmann, T. P. Murphy, and Z. Fisk, Phys. Rev. B **72**, 064422 (2005).

[Bastow, 1966] T. J. Bastow and R. Street, Phys. Rev. **141**, 510 (1966).

[Baym, 1991] G. Baym and C. Pethick, *Landau Fermi-Liquid Theory*: concept and applications (1991, Wiley, New York).

[Bednorz, 1986] J. G. Bednorz and K. A. Müller, Z. Phys. B **64**, 189 (1986).

[Behnia, 2004] K. Behnia, D. Jaccard, and J. Flouquet, J. Phys.: Condens. Matter **16** 5187 (2004).

[Behnia, 2004a] The zero temperature limit of S/T and γ for YbCuAl, YbInAu$_2$, YbAl$_3$, YbCu$_2$Si$_2$, YbAgCu$_4$, YbCu$_{4.5}$ and Pd are taken from the table of Ref. [Behnia, 2004]. S/T and γ of Yb$_2$Pt$_6$Al$_{15}$ are taken from Ref. [Deppe, 2008]. γ value of YbNi$_2$B$_2$C and YbNi$_2$Ge$_2$ are taken from Ref. [Li, 2006] and Ref. [Bud'ko, 1999], respectively. The TEP data of YbNi$_2$B$_2$C and YbNi$_2$Ge$_2$ are presented in the appendix B.

[Benz, 1999] J. Benz, C. Pfleiderer, O. Stockert, and H.v. Löhneysen, Physica B **259-261**, 380 (1999).

[Bhattacharjee, 1976] A. K. Bhattacharjee and B. Coqblin, Phys. Rev. B **13**, 3441 (1976).

[Bickers, 1985] N. E. Bickers, D. L. Cox, and J. W. Wilkins, Phys. Rev. Lett. **54**, 230 (1985).

[Bickers, 1987] N. E. Bickers, D. L. Cox, and J. W. Wilkins, Phys. Rev. B **36**, 2036 (1987).

[Bitko, 1996] D. Bitko, T. F. Rosenbaum, and G. Aeppli, Phys. Rev. Lett. **77**, 940 (1996).

[Blaha, 2001] P. Blaha, K. Schwarz, G. K. H. Madsen, D. Kvasnick, and J. Luitz, WIEN2k, An augmented Plane wave + Local Orbitals Program for Calculation Crystal Properties (K. Schwarz, TU wien, Austria, 2001).

[Blatt, 1974] F. J. Blatt, A. D. Caplin, C. K. Chiang, and P. A. Schroeder. Solid State Commun. **15**, 411 (1974).

[Blatt, 1976] F. J. Blatt, P. A. Schroeder, C. Foiles and D. Greig, *Thermoelectric Power of Metals* (Plenum, New York, 1976).

[Bogenberger, 1995] B. Bogenberger and H. v. Löhneysen, Phys. Rev. Lett. **74**, 1016 (1995).

[Brice, 1986] J. C. Brice, *Crystal growth processes* (Halsted Press, 1986).

[Bud'ko, 1999] S. L. Bud'ko, Z. Islam, T. A. Wiener, I. R. Fisher, A. H. Lacerda, P. C. Canfield, J. Magn. Magn. Mater. **205**, 53 (1999).

[Bud'ko, 2004] S. L. Bud'ko, E. Morosan, and P. C. Canfield, Phys. Rev. B **69**, 014415 (2004).

[Bud'ko, 2005] S. L. Bud'ko, E. Morosan, and P. C. Canfield, Phys. Rev. B **71**, 054408 (2005).

[Bud'ko, 2005a] S. L. Bud'ko, V. Zapf, E. Morosan, and P. C. Canfield, Phys. Rev. B **72**, 172413 (2005).

[Burdin, 2000] S. Burdin, A. Georges, and D. R. Grempel, Phys. Rev. Lett. **85**, 1048 (2000).

[Burkov, 2001] A. T. Burkov, A. Heinrich, P. P. Konstantinov, T. Nakama, and K. Yagasaki, Meas. Sci. Technol. **12**, 264 (2001).

[Canfield, 1991] P. c. Canfield, J. D. Thompson, W. P. Beyermann, A. Lacerda, M. F. Hundley, E. Peterson, Z. Fisk, and H. R. Ott, J. Appl. Phys. **70**, 5800 (1991).

[Canfield, 1992] P. C. Canfield and Z. Fisk, Philos. Mag. B **65**, 1117 (1992).

[Canfield, 2001] P. C. Canfield and I. R. Fisher, J. Crystal Growth **225**, 155 (2001).

[Canfield, 2008] P. C. Canfield, *Plenary Lecture, the 25th Rare Earth Research Conference* (2008).

[Canfield, 2010] P. C. Canfield, *Solution growth of intermetallic single crystals: a beginner's guide* (Book Series on Complex Metallic Alloys 2010, 93-111, World Scientific Publishing Co. Pte. Ltd.).

[Castro Neto, 1998] A. H. Castro Neto, G. Castilla, and B. A. Jones, Phys. Rev. Lett. **81**, 3531. (1998).

[Chaikin, 1995] P. M. Chaikin, and T. C. Lubensky, *Principles of Condensed Matter Physics* (Cambridge University, New York, 1995).

[Choi, 2001] E. S. Choi, J. S. Brooks, J. S. Qualls, and Y. S. Song, Rev. Sci. Instrum. **72**, 2392 (2001).

[Chubukov, 2005] A. V. Chubukov, D. L. Maslov, S. Gangadharaiah, and L. I. Glazman, Phys. Rev. B **71**, 205112 (2005).

[Coleman, 2001] P. Coleman, C. Pépin, Q. Si, and R. Ramazashvili, J. Phys.: Condens. Matter **13**, R723 (2001).

[Coleman, 2007] P. Coleman, *Handbook of Magnetism and Advanced Magnetic Materials* (John Wiley & Sons, Inc., Vol. 1, Heavy Fermions: electrons at the edge of magnetism, 2007)

[Coleman, 2008] P. Coleman, from lecture note, APS Boulder Summer School, (2008). Most of contents are in Ref. [Coleman, 2007].

[Coleman, 2010] P. Coleman, Phys. Status Solidi B **247**, 506 (2010).

[Continentino, 1989] M. A. Continentino, G. M. Japiassu, and Amós Troper, Phys. Rev. B **39**, 9734 (1989).

[Coqblin, 1969] B. Coqblin and J. R. Schrieffer, Phys. Rev. **185**, 847 (1969).

[Cowan, 2005] B. Cowan, *Topics in Statistical Mechanics* (Imperial College Press, 2005).

[Custers, 2003] J. Custers, P. Gegenwart, H. Wilhelm, K. Neumaier, Y. Tokiwa, O. Trovarelli, C. Geibel, F. Steglich, C. Pépin, and P. Coleman, Nature **424**, 524 (2003).

[Custers, 2010] J. Custers, P. Gegenwart, C. Geibel, F. Steglich, P. Coleman, and S. Paschen, Phys. Rev. Lett. **104**, 186402 (2010).

[deHaas, 1934] W. J. de Haas, J. H. de Bore, G. J. van den Berg, Physica **1**, 1115 (1934).

[Dagotto, 1994] E. Dagotto, Rev. Mod. Phys. **66**, 763 (1994).

[Das Sarma, 1996] S. Das Sarma and A. Pinczuk, 1996, Eds., *Perspectives in Quantum Hall Effects*: Novel Quantum Liquids in Low- Dimensional Semiconductor Structures (Wiley, New York).

[Deppe, 2008] M. Deppe, S. Hartmann, M. E. Macovei, N. Oeschler, M. Nicklas, and C. Geibel, New J. Phys. **10**, 093017 (2008).

[Doniach, 1977] S. Doniach, Physica B & C **91B**, 231 (1977).

[Elliott, 1972] R. J. Elliott, *Magnetic Properties of Rare Earth Metals* (Plenum press, London and New York, 1972).

[Fåk, 2005] B. Fåk, D. F. McMorrow, P. G. Niklowitz, S. Raymond, E. Ressouche, J. Flouquet, P. C. Canfield, S. L. Bud'ko, Y. Janssen, and M. J. Gutmann, J. Phys.: Condens. Matter **17**, 301 (2005).

[Fåk, 2006] B. Fåk, Ch. Rüegg, P. G. Niklowitz, D. F. McMorrow, P. C. Canfield, S. L. Budko, Y. Janssen, and K. Habicht, Physica B **378-380**, 669 (2006).

[Fawcett, 1970] E. Fawcett, J. P. Maita, and J. H. Wernick, 1970, Int. J. Magn. **1**, 29 (1970).

[Fawcett, 1988] E. Fawcett, H. L. Alberts, V. Yu. Galkin, D. R. Noakes, and J. V. Yakhmi, Rev. Mod. Phys. **60**, 209 (1988).

[Fawcett, 1994] E. Fawcett, H. L. Alberts, V. Yu. Galkin, D. R. Noakes, and J. V. Yakhmi, Rev. Mod. Phys. **66**, 25 (1994).

[Feldman, 1993] J. Feldman, J. Magnen, V. Rivasseu, and E. Trubowitz, Europhys. Lett. **24**, 437 (1993).

[Fisk, 1989] Z. Fisk, J. P. Remeika, in: K. A. Gschneidner and L.R. Eyring (Eds.), *Handbook of Physics and Chemistry of Rare Earths*, Vol. **12** (North-Holland, Amsterdam, 1989, p. 53).

[Fisk, 1991] Z. Fisk, P. C. Canfield, W. P. Beyermann, J. D. Thompson, M. F. Hundley, H. R. Ott, E. Felder, M. B. Maple, M. A. Lopez de la Torre, P. Visani, and C. L. Seaman, Phys. Rev. Lett. **67**, 3310 (1991).

[Foiles, 1981] C. L. Foiles, J. Appl. Phys. **52**, 2217 (1981).

[Friedemann, 2009] S. Friedemann, T. Westerkamp, M. Brando, N. Oeschler, S. Wirth, P. Gegenwart, C. Krellner, C. Geibel and F. Steglich, Nature Phys. **5**, 465 (2009).

[Gegenwart, 1998] P. Gegenwart, C. Langhammer, C. Geibel, R. Helfrich, M. Lang, G. Sparn, F. Steglich, R. Horn, L. Donnevert, A. Link, and W. Assmus, Phys. Rev. Lett. **81**, 1501 (1998).

[Gegenwart, 2002] P. Gegenwart, J. Custers, C. Geibel, K. Neumaier, T. Tayama, K. Tenya, O. Trovarelli, and F. Steglich, Phys. Rev. Lett. **89**, 056402 (2002).

[Gegenwart, 2007] P. Gegenwart, T. Westerkamp, C. Krellner, Y. Tokiwa, S. Paschen, C. Geibel, F. Steglich, E. Abrahams, and Q. Si, Science **315**, 969 (2007).

[Gegenwart, 2008] P. Gegenwart, Q. Si, and F. Steglich, Nat. Phys. **4** 186 (2008).

[Goll, 2002] G. Goll, J. Hagel, H. v. Lohneysen, T. Pietrus, S. Wanka, J. Wosnitza, G. Zwicknagl, T. Yoshino, T. Takabatake, and A. G. M. Jansen, Europhys. Lett. **57**, 233 (2002).

[Gratz, 2001] E. Gratz and A. S. Markosyan, J. Phys.: Condens. Matter 13, R385 (2001).

[Grenzebach, 2006] C. Grenzebach, F. B. Anders, Gerd Czycholl, and T. Pruschke, Phys. Rev. B **74**, 195119 (2006).

[Grier, 1984] B. H. Grier, J. M. Lawrence, V. Murgai, R. D. Parks. Phys. Rev. B **29**, 2664 (1984).

[Griffiths, 1969] R. B. Griffiths, Phys. Rev. Lett. **23**, 17 (1969).

[Gruner, 1994] G. Grüner, Rev. Mod. Phys. **66**, 1 (1994).

[Gruner, 1994a] G. Grüner, *Density Waves in Solids* (Addison Wesley, Reading, MA, 1994).

[Hartmann, 2010] S. Hartmann, N. Oeschler, C. Krellner, C. Geibel, S. Paschen, F. Steglich, Phys. Rev. Lett. **104**, 096401 (2010).

[Hewson, 1993] A. C. Hewson, *The Kondo Problem to Heavy Fermions* (Cambridge: Cambridge University Press, 1993)

[Hertz, 1976] J. A. Hertz, Phys. Rev. B **14**, 1165 (1976).

[Heuser, 1998] K. Heuser, E.-W. Scheidt, T. Schreiner, and G. R. Stewart, Phys. Rev. B **57**, R4198 (1998). K. Heuser, E.-W. Scheidt, T. Schreiner, and G. R. Stewart, Phys. Rev. B **58**, R15959 (1998).

[Hirst, 1978] L.L. Hirst, Adv. Phys. **27**, 231 (1978).

[Houghton, 1987] A. Houghton, N. Read, and H. Won Phys. Rev. B **35**, 5123 (1987).

[Hundley, 1997] M. F. Hundley, J. D. Thompson, P. C. Canfield, and Z. Fisk, Phys. Rev. B **56**, 8098 (1997).

[Huo, 2001] D. Huo, J. Sakurai, O. Maruyama, T. Kuwai, and Y. Isikawa, J. Magn. Magn. Mater. **226-230**, 202 (2001).

[Izawa, 2007] K. Izawa, K. Behnia, Y. Matsuda, H. Shishido, R. Settai, Y. Onuki, and J. Flouquet, Phys. Rev. Lett. **99**, 147005 (2007).

[Jacko, 2009] A. C. Jacko, J. O. Fjærestad, and B. J. Powell, Nature Phys. **5**, 422 (2009).

[Jia, 2007] S. Jia, S. L. Bud'ko, G. D. Samolyuk, and P. C. Canfield, Nat. Phys. **3**, 334 (2007).

[Jia, 2008] S. Jia, N. Ni, G. D. Samolyuk, A. Safa-Sefat, K. Dennis, Hyunjin Ko, G. J. Miller, S. L. Bud'ko, and P. C. Canfield, Phys. Rev. B **77**, 104408 (2008). Note that the Debye temperatures used in this paper are recalculated; Θ_D (YFe_2Zn_{20}) = 350 K and Θ_D (YCo_2Zn_{20}) = 344 K.

[Julian, 1996] S.R. Julian, C. Pfleiderer, F. M. Grosche, N. D. Mathur, G. J. McMullan, A. J. Diver, I. R. Walker, and G. G. Lonzarich, J. Phys.: Condens. Matter **8**, 9675 (1996).

[Julian, 1998] S. R. Julian, F. V. Carter, F. M. Grosche, R. K. W. Haselwimmer, S. J. Lister, N. D. Mathur, G. J. McMullan, C. Pfleiderer, S. S. Saxena, I. R. Walker, N. J. W. Wilson, and G. G. Lonzarich, J. Magn. Magn. Mater. **177-181**, 265 (1998).

[Jung, 2001] M. H. Jung, T. Yoshino, S. Kawasaki, T. Pietrus, Y. Bando, T. Suemitsu, M. Sera, and T. Takabatake, J. Appl. Phys. **89**, 7631 (2001).

[Kadowaki, 1986] K. Kadowaki and S. B. Woods, Solid State Commun. **58**, 507 (1986).

[Kambe, 1996] S. Kambe, S. Raymond, H. Suderow, J. McDonough, B. Fåk, L. P. Regnault, R. Calemczuk, and J. Flouquet, Physica B **223-224**, 135 (1996).

[Kamihara, 2008] Y. Kamihara, T. Watanabe, M. Hirano, and H. Hosono, J. Am. Chem. Soc. **130**, 3296 (2008).

[Kasuya, 1956] T. Kasuya, Prog. Theor. Phys. **16**, 45 58 (1956).

[Katoha, 2004] K. Katoha, Y. Manoa, K. Nakanoa, G. Teruia, Y. Niidea, and A. Ochiai, J. Magn. Magn. Mater. **268**, 212 (2004).

[Kim, 2008] K. S. Kim, A. Benlagra, and C. Pépin C Phys. Rev. Lett. **101** 246403 (2008).

[Kim, 2010] K.-S. Kim and C. Pépin, Phys. Rev. B **81**, 205108 (2010).

[Kittel, 1996] C. Kittel, *Introduction to Solid State Physics*, 7th ed. (Wiley, New York, 1996).

[Köhler, 2008] U. Köhler, N. Oeschler, F. Steglich, S. Maquilon, and Z. Fisk, Phys. Rev. B **77**, 104412 (2008).

[Kondo, 1964] J. Kondo, Prog. Theor. Phys. **32**, 37 (1964).

[Kontani, 2003] H. Kontani, Phys. Rev. B **67**, 014408 (2003).

[Kontani, 2004] H. Kontani, J. Phys. Soc. Jpn. **73**, 515 (2004).

[Kontani, 2005] H. Kontani, Physica B **359-361**, 202 (2005).

[Kontani, 2008] H. Kontani, Rep. Prog. Phys. **71**, 026501 (2008).

[Kriegisch, 2008] M. Kriegisch, J. Custers, C. Geibel, G. Hilscher, C. Krellner, M. Mller, F. Steglich, and S. Paschen, Physica B **403**, 1295 (2008).

[Kroha, 2010] J. Kroha, M. Klein, A. Nuber, F Reinert, O Stockert, and H. v. Löhneysen, J. Phys.: Condens. Matter **22**, 164203 (2010).

[Kubo, 2010] H. Kubo, K. Umeo, K. Katoh, A. Ochiai, and T. Takabatake, J. Phys.: Conf. Ser. **200**, 012098 (2010).

[Lacerda, 1993] A. Lacerda, R. Movshovich, M. F. Hundley, P. C. Canfield, D. Arms, G. Sparn, J. D. Thompson, Z. Fisk, R. A. Fisher, N. E. Phillips, and H.-R. Ott, J. Appl. Phys. **73**, 5415 (1993).

[Landau, 1957a] L. D. Landau, 1957, Sov. Phys. JETP **3**, 920.

[Landau, 1957b] L. D. Landau, 1957, Sov. Phys. JETP **5**, 101.

[Landau, 1959] L. D. Landau, 1959, Sov. Phys. JETP **8**, 70.

[Lassailly, 1985] Y. Lassailly, A. K. Bhattacharjee, and B. Coqblin, Phys. Rev. B **31**, 7424 (1985).

[Lea, 1962] K. R. Lea, M. J. M. Leask, and W. P. Wolf. J. Phys. Chem. Solids **23**, 1381 (1962).

[Lee, 1986] P. A. Lee, T. M. Rice, J. W. Serene, L. J. Sham, and J. H. Wilkins, Comments in solid State Physics **12**, 99 (1986).

[Lee, 2004] M. Lee, A. Husmann, T. F. Rosenbaum, and G. Aeppli, Phys. Rev. Lett. **92**, 187201 (2004).

[Li, 2006] S. Li, M. C. De Andrade, E. J. Freeman, C. Sirvent, R. P. Dickey, A. Amann, N. A. Frederick, K. D. D. Rathnayaka, D. G. Naugle, S. L. Bud'ko, P. C. Canfield, W. P. Beyermann, M. B. Maple, Philos. Mag. B **86**, 3021 (2006).

[Lifshitz, 1960] I. M. Lifshitz, Sov. Phys. JETP **11**, 1130 (1960).

[Löhneysen, 1994] H. v. Löhneysen, T. Pietrus, G. Portisch, H. G. Schlager, A. Schröder, M. Sieck, and T. Trappmann , Phys. Rev. Lett. **72**, 3262 (1994).

[Lohneysen, 1996] H. v. Löhneysen, J. Phys.: Condens. Matter **8**, 9689 (1996).

[Löhneysen, 1998] H. v. Löhneysen, S. Mock, A. Neubert, T. Pietrus, A. Rosch, A. Schröder, O. Stockert, and U. Tutsch, J. Magn. Magn. Mater. **177-181**, 12 (1998).

[Löhneysen, 2001] H. v. Löhneysen, C. Pfleiderer, T. Pietrus, O. Stockert, and B. Will, Phys. Rev. B **63**, 134411 (2001).

[Löhneysen, 2007] H. v. Löhneysen, A. Rosch, M. Vojta, and P. Wölfle, Rev. Mod. Phys. **79**, 1015 (2007).

[Ma, 1976] S. K. Ma, *Modern Theory of Critical Phenomena*, Frontiers in Physics (W. A. Genjamin Inc., Reading, Massachusetts, 1976).

[Maekawa, 1986] S. Maekawa, S. Kashiba, M. Tachiki, and S. Takahashi, J. Phys. Soc. Jpn. **55**, 3194 (1986).

[Mahan, 1997] G. D. Mahan, Phys. Rev. B **56**, 11833 (1997).

[Maple, 1986] M. B. Maple, J. W. Chen, Y. Dalichaouch, T. Kohara, C. Rossel, M. S. Torikachvili, M. W. McElfresh, and J. D. Thompson, Phys. Rev. Lett. **56**, 185 (1986).

[Maple, 1998] M. B. Maple, J. Magn. Magn. Mater. **177**, 18 (1998).

[Mathur, 1998] N. D. Mathur, F. M. Grosche, S. R. Julian, I. R. Walker, D. M. Freye, R. K. W. Haselwimmer, G. G. Lonzarich, Nature **394**, 39 (1998).

[Matsumura, 2004] T. Matsumura, H. Ishida, T. J. Sato, K. Katoh, Y. Niide, and A. Ochiai, J. Phys. Soc. Jpn. **73**, 2967 (2004).

[McMorrow, 2008] D. F. McMorrow *et al.*, oral presentation, 25th International Conference on Low Temperature Physics, Amsterdam 2008.

[McMullan, 1992] G. J. McMullan and M. P. Ray, J. Phys: Condens. Matter **4** , 7095 (1992).

[Miyake, 1989] K. Miyake, T. Matsuura, and C. M. Varma, Sold State Commun. **71**, 1149 (1989).

[Miyake, 2005] K. Miyake and H. Kohno, J. Phys. Soc. Jpn. **74**, 254 (2005).

[Millis, 1993] A. J. Millis, Phys. Rev.B **48**, 7183 (1993).

[Montgomery, 1971] H. C. Montgomery, J. Appl. Phys. **42**, 2971 (1971).

[Moriya, 1985] T. Moriya, 1985, *Spin Fluctuations in Itinerant Electron Magnetism* (Springer, Berlin).

[Moriya, 1995] T. Moriya and T. Takimoto, J. Phys. Soc. Jpn. **64**, 960 (1995).

[Moriya, 1973] T. Moriya and A. Kawabata, J. Phys. Soc. Jpn. **34**, 639 (1973). J. Phys. Soc. Jpn. **35** 669 (1973).

[Morelli, 1996] D. T. Morelli, P. C. Canfield, and P. Drymiotis, Phys. Rev. B **53**, 12896 (1996).

[Morosan, 2004] E. Morosan, S. L. Bud'ko, P. C. Canfield, M. S. Torikachvili, and A. H. Lacerda, J. Magn. Magn. Mater. **277**, 298 (2004).

[Movshovich, 1994] R. Movshovich, A. Lacerda, P. C. Canfield, J. D. Thompson, and Z. Fisk, Phys. Rev. Lett. **73**, 492 (1994).

[Movshovich, 1994a] R. Movshovich, A. Lacerda, P. C. Canfield, J. D. Thompson, and Z. Fisk, J. Appl. Phys. **76**, 15 (1994).

[MPC] Materials Preparation Center, Ames Laboratory, U.S. DOE, Ames, Iowa (www.mpc.ameslab.gov).

[Mun, 2010] E. Mun, S. L. Bud'ko, M. S. Torikachvili, and P. C. Canfield, Meas. Sci. Technol. **21**, 055104 (2010).

[Mun, 2010a] In zero-field, the resistivity data for YbT_2Zn_{20} compounds are taken from Ref. [Torikachvili, 2007]. The resistivity data for $LuFe_2Zn_{20}$ and $LuCo_2Zn_{20}$ compounds were taken from: S. Jia, N. Ni, S. L. Bud'ko, and P. C. Canfield, Phys. Rev. B **80**, 104403 (2009). The resistivity data for LuT_2Zn_{20} (T = Ru, Os, Ir, and Rh) are unpublished. The TEP data of $YbNi_2B_2C$ and $YbNi_2Ge_2$ are presented in the appendix B.

[Mun, 2010b] Eundeok Mun, the thermoelectric power measurements for YbAgGe will be published.

[Mun, 2010c] Data are not included in this thesis.

[Mydosh, 1993] J. A. Mydosh, *Spin Glasses*: *An Experimental Introduction* (Taylor & Francis, London, 1993).

[Myers, 1999] K. D. Myers, S. L. Bud'ko, I. R. Fisher, Z. Islam, H. Kleinke, A. H. Lacerda, and P. C. Canfield, J. Magn. Magn. Mater. **205**, 27 (1999).

[Nakatsuji, 2008] S. Nakatsuji, K. Kuga, Y. Machida, T. Tayama, T. Sakakibara, Y. Karaki, H. Ishimoto, S. Yonezawa, Y. Maeno, E. Pearson, G. G. Lonzarich, L. Balicas, H. Lee, and Z. Fisk, Nature Phys. **4**, 603 (2008).

[Newns, 1987] D. M. Newns and N. Read, Adv. Phys. **36**, 799 (1987).

[Norman, 2003] M. R. Norman, Q. Si, Y. B. Bazaliy, and R. Ramazashvili, Phys. Rev. Lett. **90**, 116601 (2003).

[Niklowitz, 2006] P. G. Niklowitz, G. Knebel, J. Flouquet, S. L. Bud'ko, and P. C. Canfield, Phys. Rev. B **73**, 125101 (2006).

[Očko, 2004] M. Očko, J.L. Sarrao, and Ž. Šimek, J. Magn. Magne. Mater. **284**, 43 (2004).

[Oguchi, 2001] T. Oguchi, Phys. Rev. B **63**, 125115 (2001).

[Oh, 2007] Y. S. Oh, K. H. Kim, P. A. Sharma, N. Harrison, H. Amitsuka, and J. A. Mydosh, Phys. Rev. Lett. **98**, 016401 (2007).

[Okamoto, 2000] H. Okamoto, *Desk Handbook phase Diagrams for Binary Alloys* (ASM international, 2000).

[Okane, 2009] T. Okane, T. Ohkochi, Y. Takeda, S.-i. Fujimori, A. Yasui, Y. Saitoh, H. Yamagami, A. Fujimori, Y. Matsumoto, M. Sugi, N. Kimura, T. Komatsubara, and H. Aoki, Phys. Rev. Lett. **102**, 216401 (2009).

[Onuki, 1987] Y. Ōnuki and T. Komatsubara, J. Magn. Magn. Mater. **63-64**, 281 (1987).

[Oppeneer, 1997] P. M. Oppeneer, V. A. Antonov, A. N. Yaresko, A. Ya. Perlov, and H. Eschrig, Phys. Rev. Lett. **78**, 4079 (1997).

[Orenstein, 2000] J. Orenstein and A. J. Millis, Science **288**, 468 (2000).

[Otsuki, 2007] J. Otsuki, H. Kusunose, P. Werner and Y. Kuramoto, J. Phys. Soc. Jpn. **76**, 11 (2007).

[Ott, 1983] H. R. Ott, H. Rudigier, Z. Fisk, and J. L. Smith, Phys. Rev. Lett. **50**, 1595 (1983).

[Overhauser, 1962] A. W. Overhauser, Phys. Rev. **128**, 1437 (1962).

[Paglione, 2003] J. Paglione, M. A. Tanatar, D. G. Hawthorn, E. Boaknin, R. W. Hill, F. Ronning, M. Sutherland, L. Taillefer, C. Petrovic, and P. C. Canfield, Phys. Rev. Lett. **91**, 246405 (2003).

[Pamplin, 1975] B. R. Pamplin, *Crystal growth* (Oxford, 1975).

[Paschen, 2004] S. Paschen, T. Lühmann, S. Wirth, P. Gegenwart, O. Trovarelli, C. Geibel, F. Steglich, P. Coleman, and Q. Si, Nature **432**, 881 (2004).

[Paschen, 2006] S. Paschen, Physica B **78-380**, 28 (2006).

[Paul, 2001] I. Paul and G. Kotliar, Phys. Rev. B **64**, 184414 (2001).

[Paul, 2007] I. Paul, C. Pépin, and M. R. Norman, Phys. Rev. Lett. **98**, 026402 (2007).

[Paul, 2008] I. Paul, C. Pépin, and M. R. Norman, Phys. Rev. B **78**, 035109 (2008).

[Perdew, 1992] J. P. Perdew and Y. Wang, Phys. Rev. B **45**, 13244 (1992).

[Petrovic, 2001] C. Petrovic, P. G. Pagliuso, M. F. Hundley, R. Movshovich, J. L. Sarrao, J. D. Thompson, Z. Fisk, and P. Monthoux, J. Phys.: Condens. Matter **13**, L337 (2001).

[Pfleiderer, 2001] C. Pfleiderer, S. R. Julian, and G. G. Lonzarich, Nature (London) **414**, 427 (2001).

[Pietrus, 1995] T. Pietrus, B. Bogenberger, S. Mock, M. Sieck, and H. v. Löhneysen, Physica B **206-207**, 317 (1995).

[Pobell,1996] F. Pobell, *Matter and Methods at Low Tempertures* (Springer, 1996).

[Rajan, 1983] V. T. Rajan, Phys. Rev. Lett. **51**, 308 (1983).

[Ramesh, 2007] R. Ramesh and N. A. Spaldin, Nature Materials **6**, 21 (2007).

[Rasul, 1984] J. W. Rasul and A. C. Hewson, J. Phys. C: Solid State Phys. **17**, 2555 (1984).

[Ray, 1972] A. E. Ray and K. J. Strnat, IEEE Trans. Magn., vol. **MAG-8**, 518 (1972).

[Rech, 2006] J. Rech, P. Coleman, G. Zarand, and O. Parcollet, Phys. Rev. Lett. **96**, 016601 (2006).

[Resel, 1996] R. Resel, E. Gratz, A. T. Burkov, T. Nakama, M. Higa, and K. Yagasaki, Rev. Sci. Instrum. **67**, 1970 (1996).

[Rice, 1968] Rice, M. J. Phys. Rev. Lett. **20**, 1439 (1968).

[Robinson, 1994] R. A. Robinson, A. Purwanto, M. Kohgi, P. C. Canfield, T. Kamiyama, T. Ishigaki, J. W. Lynn, R. Erwin, E. Peterson, R. Movshovich, Phys. Rev. B **50**, 9595 (1994).

[Rosch, 1997] A. Rosch, A. Schröder, O. Stockert, and H. v. Löhneysen, Phys. Rev. Lett. **79**, 159 (1997).

[Rosch, 1999] A. Rosch, Phys. Rev. Lett. **82**, 4280 (1999). Physica B **280**, 341 (2000).

[Ruderman, 1954] M. A. Ruderman and C. Kittel, Phys. Rev. **96**, 99 (1954).

[Sachdev, 1999] S. Sachdev, *Quantum Phase Transitions* (Cambridge University Press, Cambridge, England, 1999).

[Sachdev, 2000] S. Sachdev, Science **288**, 475 (2000).

[Sagawa, 1984] M. Sagawa, S. Fujimura, M. Togawa, H. Yamamota, and Y. Matsuura, J. Appl. Phys. **55**, 2083 (1984). J. J. Croat, J. F. Herbst, R. W. Lee, and F. E. Pinkerton, J. Appl. Phys. **55**, 2078 (1984). D. J. Sellmyer, A. U. Ahmed, and G. C. Hadjipanayis, J. Appl. Phys. **55**, 2088 (1984).

[Sakurai, 1991] J. Sakurai, M. Horie, S. Araki, H. Yamamoto, and T. Shinjo, J. Phys. Soc. Jpn. **60**, 2522 (1991).

[Sakurai, 1995] J. Sakurai, Y. Takamatsu, T. Kuwai, Y. Isikawa, K. Mori, T. Fukuhara, and K. Maezawa, Physica B **206**, 834 (1995).

[Sakurai, 2002] J. Sakurai, A. Iwasaki, Q. Lu, D. Huo, Y. Isikawa, J. R. Fernández, and J. C. Gómez Sal, J. Phys. Soc. Jpn. **71**, 2829 (2002).

[Samolyuk, 2006] G. D. Samolyuk, S. L. Bud'ko, E. Morosan, V. P. Antropov, and P. C. Canfield, J. Phys.: Condens. Matter **18**, 1473 (2006).

[Scalapino, 1986] D. J. Scalapino, E. Loh, and J. E. Hirsch, Phys. Rev. B **34**, 8190 (1986).

[Scheidt, 1999] E. -W. Scheidt, T. Schreiner, K. Heuser, and G. R. Stewart, Physica B **259-261**, 388 (1999).

[Schmiedeshoff, 2006] G. M. Schmiedeshoff, A. W. Lounsbury, D. J. Luna, S. J. Tracy, A. J. Schramm, S. W. Tozer, V. F. Correa, S. T. Hannahs, T. P. Murphy, E. C. Palm, A. H. Lacerda, S. L. Bud'ko, P. C. Canfield, J. L. Smith, J. C. Lashley, and J. C. Cooley, Rev. Sci. Instrum. **77**, 123907 (2006).

[Schmiedeshoff, 2010] G. M. Schmiedeshoff, private communication.

[Schoenes, 1987] J. Schoenes, C. Schönenberger, J. J. M. Franse, and A. A. Menovsky, Phys. Rev. B **35**, 5375 (1987).

[Schröder, 1998] A. Schröder, G. Aeppli, E. Bucher, R. Ramazashvili, and P. Coleman, Phys. Rev. Lett. **80**, 5623 (1998).

[Schröder, 2000] A. Schröder, G. Aeppli, R. Coldea, M. Adams, O. Stockert, H. v. Löhneysen, E. Bucher, R. Ramazashvili, and P. Coleman, Nature (London) **407**, 351 (2000).

[Shankar, 1994] R. Shankar, Rev. Mod. Phys. **66**, 129 (1994).

[Senthil, 2003] T. Senthil, S. Sachdev, and M. Vojta, Phys. Rev. Lett. **90**, 216403 (2003).

[Senthil, 2004] T. Senthil, M. Vojta, and S. Sachdev, Phys. Rev. B **69**, 035111 (2004).

[Shoenberg, 1984] D. Shoenberg, *Magnetic Oscillations in Metals* (Cambridge University Press, Cambridge, England, 1984).

[Si, 2001] Q. Si, S. Rabello, K. Ingersent, and J. L. Smith, Nature (London) **413**, 804 (2001).

[Si, 2003] Q. Si, S. Rabello, K. Ingersent, and J. L. Smith, Phys. Rev. B **68**, 115103 (2003).

[Sondheimer, 1948] E. H. Sondheimer, Proc. R. Soc. Lond. A **193**, 484 (1948).

[Sondhi, 1997] S. L. Sondhi, S. M. Girvin, J. P. Carini, and D. Shahar, Rev. Mod. Phys. **69**, 315 (1997).

[Steglich, 1979] F. Steglich, J. Aarts, C. D. Bredl, W. Lieke, D. Meschede, W. Franz and H. Schäfer, Phys. Rev. Lett. **43**, 1892 (1979).

[Stewart, 1984] G. R. Stewart, Rev. Mod. Phys. **56**, 755 (1984).

[Stewart, 2001] G. R. Stewart, Rev. Mod. Phys. **73**, 797 (2001). and Rev. Mod. Phys. **78**, 743 (2006).

[Stockert, 1998] O. Stockert, H. v. Löhneysen, A. Rosch, N. Pyka, and M. Loewenhaupt, Phys. Rev. Lett. **80**, 5627 (1998).

[Stockert, 2007] O. Stockert, M. Enderle, and H. v. Löhneysen, Phys. Rev. Lett. **99**, 237203 (2007).

[Takabatake, 2006] T. Takabatake, E. Matsuoka, S. Narazu, K. Hayashi, S. Morimoto, T. Sasakawa, K. Umeo, and M. Sera, Physica B **383**, 93 (2006).

[Thiede, 1998] V. M. T. Thiede, W. Jeitschko, S. Niemann, and T. Ebel, J. Alloys and Compd. **267**, 23 (1998).

[Tokiwa, 2005] Y. Tokiwa, P. Gegenwart, T. Radu, J. Ferstl, G. Sparn, C. Geibel, and F. Steglich, Phys. Rev. Lett. **94**, 226402 (2005).

[Tokiwa, 2006] Y. Tokiwa, A. Pikul, P. Gegenwart, F. Steglich, S. L. Bud'ko, and P. C. Canfield, Phys. Rev. B **73**, 094435 (2006).

[Torikachvili, 2007] M. S. Torikachvili, S. Jia, E. D. Mun, S. T. Hannahs, R. C. Black, W. K. Neils, D. Martien, S. L. Bud'ko, and P. C. Canfield, Proc. Natl. Acad. Sci. U.S.A. **104**, 9960 (2007).

[Trovarelli, 2000] O. Trovarelli, C. Geibel, S. Mederle, C. Langhammer, F. M. Grosche, P. Gegenwart, M. Lang, G. Sparn, and F. Steglich, Phys. Rev. Lett. **85**, 626 (2000).

[Tsujii, 2003] N. Tsujii, K. Yoshimura, and K. Kosuge, J. Phys.: Condens. Matter **15**, 1993 (2003).

[Tsujii, 2005] N. Tsujii, H. Kontani, and K. Yoshimura, Phys. Rev. Lett. **94**, 057201 (2005).

[Umeo, 2004] K. Umeo, K. Yamane, Y. Muro, K. Katoh, Y. Niide, A. Ochiai, T. Morie, T. Sakakibara, and T. Takabatake, J. Phys. Soc. Jpn. **73**, 537 (2004).

[Vojta, 2003] M. Vojta, Rep. Prog. Phys. **66**, 2069 (2003).

[von Helmolt, 1993] R. von Helmolt, J. Wecker, B. Holzapfel, L. Schultz, and K. Samwer, Phys. Rev. Lett. **71**, 2331 (1993).

[Wang, 2001] Y. Wang, Z. A. Xu, T. Kakeshita, S. Uchida, S. Ono, Y. Ando, and N. P. Ong, Phys. Rev. B **64**, 224519 (2001).

[Wang, 2003] Y. Wang, N. S. Rogado, R. J. Cava, and N. P. Ong, Nature **423** 425 (2003), Supplimentary Information.

[Wang, 2006] Y. Wang, L. Li, and N. P. Ong, Phys. Rev. B **73**, 024510 (2006).

[Weigman, 1983] P. B. Weigman and A. M. Tsvelik, J. Phys. C: Solid State Phys. **16**, 2281 (1983), J. Phys. C: Solid State Phys. **16**, 2321 (1983).

[White, 1983] R. M. White, *Quantum theory of magnetism* (Springer-Verlag, Berlin, Heidelberg, New York, 1983).

[Wilhelm, 2004] H. Wilhelm and D. Jaccard, Phys. Rev. B **69**, 214408 (2004).

[Wosnitza, 2006] J. Wosnitza, G. Goll, A. D. Bianchi, B. Bergk, N. Kozlova, I. Opahle, S. Elgazzar, Manuel. Richter, O. Stockert, H. v. Löhneysen, T. Yoshino, and T. Takabatake, New J. Phys. **8**, 174 (2006).

[XcrysDen] http://www.xcrysden.org

[Yeh, 2002] A. Yeh, Y.-A. Soh, J. Brooke, G. Aeppli, T. F. Rosenbaum, and S. M. Hayden, Nature (London) **419**, 459 (2002).

[Yoshiuchi, 2009] S. Yoshiuchi, M. Toda, M. Matsushita, S. Yasui, Y. Hirose, M. Ohya, K. Katayama, F. Honda, K. Sugiyama, M. Hagiwara, K. Kindo, T. Takeuchi, E. Yamamoto, Y. Haga, R. Settai, T. Tanaka, Y. Kubo, and Y. Onuki, J. Phys. Soc. Jpn. **78**, 123711 (2009).

[Yosida, 1957] K. Yosida, Phys. Rev. **106**, 893 (1957).

[Yuan, 2006] H. Q. Yuan, M. Nicklas, Z. Hossain, C. Geibel, and F. Steglich, Phys. Rev. B **74**, 212403 (2006).

[Ziman, 1960] J. M. Ziman, *Electrons and Phonons* (Clarendon Press, Oxford, 1960).

[Ziman, 1972] J. M. Ziman, *Principles of the Theory of Solids* (Cambridge, Cambridge University Press, 1972)

[Zlatić, 2003] V. Zlatić, B. Horvatić, I. Milat, B. Coqblin, G. Czycholl, and C. Grenzebach, Phys. Rev. B **68**, 104432 (2003).

[Zlatić, 2005] V. Zlatić and R. Monnier, Phys. Rev. B **71**, 165109 (2005).

[Zlatić, 2007] V. Zlatić, R. Monnier, J. K. Freericks, and K. W. Becker, Phys. Rev. B **76**, 085122 (2007).